New Carbon-Based Materials for Energy Storage

Andreas Bliersbach

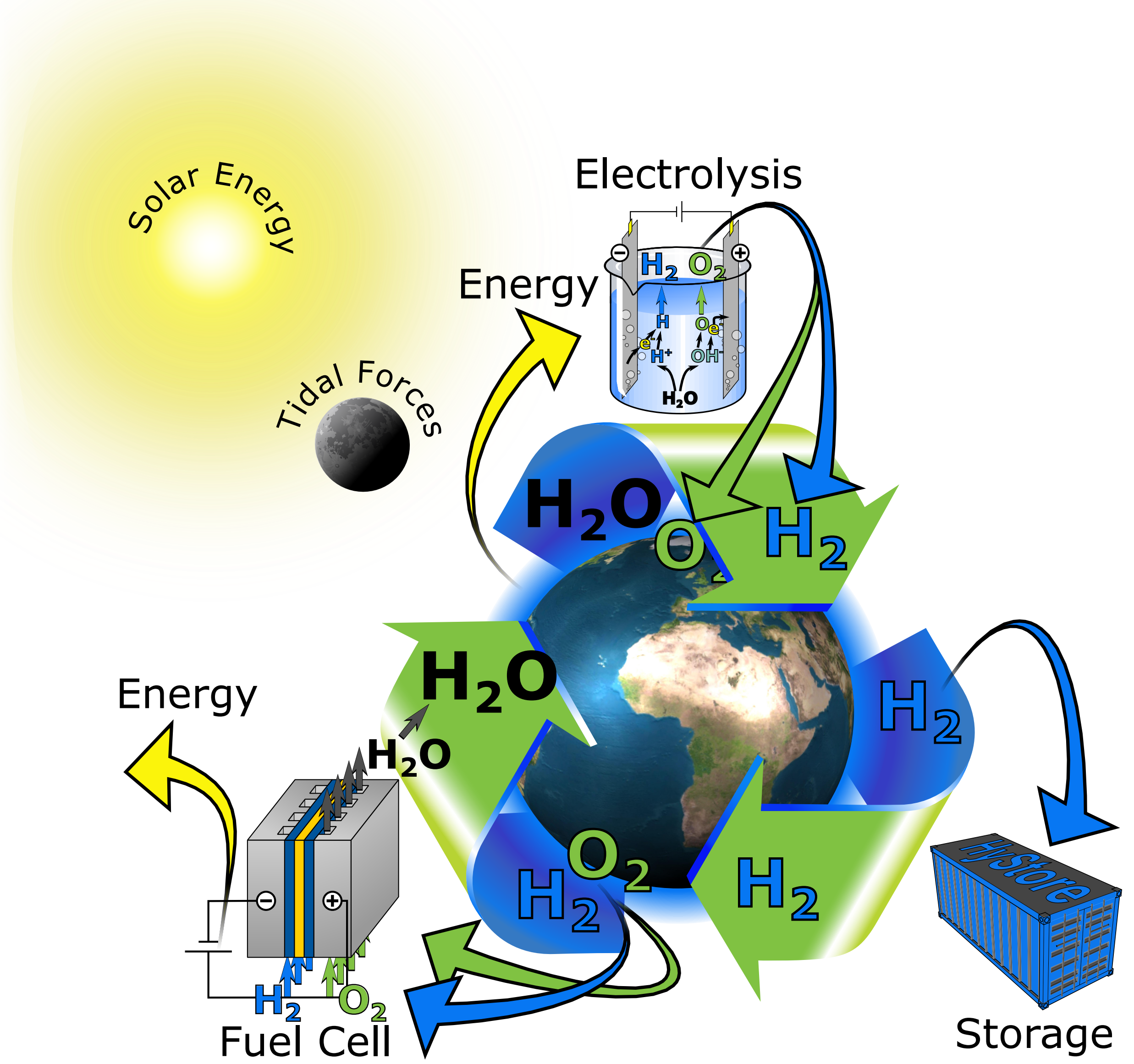

EMPA
Materials Science & Technology

Universität Zürich UZH

New Carbon-Based Materials for Energy Storage

Dissertation

zur

Erlangung der naturwissenschaftlichen Doktorwürde
(Dr. sc. nat.)

vorgelegt der

Mathematisch-naturwissenschaftlichen Fakultät

der

Universität Zürich

von

Andreas Bliersbach

aus

Deutschland

Promotionskomitee

Prof. Dr. Karl-Heinz Ernst (Vorsitz)
Prof. Dr. Peter Hamm
Prof. Dr. Jürg Osterwalder
Prof. Dr. Anthony Linden

Zürich, 2015

The presented thesis work was conducted at the Swiss Federal Laboratories for Materials Science and Technology (Empa), a part of the ETH domain. The doctorate was carried out under the supervision of Prof. Dr. Karl-Heinz Ernst during the period of December 2011 through January 2015.

This dissertation was submitted at the Faculty of Science of the University of Zurich, Switzerland, after recommendation of independent reviewers (listed below). It is part of the compulsory requirements for awarding the doctoral degree Dr. sc. nat.. A public thesis defense was held on Tuesday, 27 January 2015, prior to an examination by the members of the doctoral committee:

Chairman:	Prof. Dr. Karl-Heinz Ernst (University of Zurich)
Examiners:	Prof. Dr. Peter Hamm (University of Zurich)
	Prof. Dr. Jürg Osterwalder (University of Zurich)
	Prof. Dr. Anthony Linden (University of Zurich)
Thesis reviewer:	Prof. Dr. Karl-Heinz Ernst (University of Zurich)
	Dr. Arndt Remhof (Empa)
	Prof. Dr. Torben Jensen (Aarhus University)

Abstract

In the context of hydrogen for energy storage purposes it has long been debated that lightweight, compact, affordable and safe hydrogen storage can only be realized within an absorber. Tremendous efforts have been made to develop novel materials with high hydrogen densities as well as with rapid, reversible and energetically economical sorption properties. However, even 149 years after the discovery of the first metal hydride (PdH) currently no material satisfies all requirements. Hydrogen forms compounds with nearly every other element on the periodic table and generally has a dramatic impact on the chemical and physical properties of the host. Consequently, the number of possible combinations that can be investigated is extensive. In this thesis, novel, nanoscale, carbon-based materials have been investigated for their structure and energy storage related properties. Three different types of materials have been synthesized and were characterized by means of a multitude of experimental techniques, i.e. volumetric gas sorption, Raman-, EEL-, X-ray photoelectron- and FT-IR spectroscopy, X-ray and neutron powder diffraction, SQUID magnetometry, electrochemical cycling tests, electron microscopy and muon spin repolarization. The impressive impact of the carbon structure and the metal doping on hydrogen storage capacities reported here for metal decorated thermally exfoliated graphites and metal intercalated fullerenes clearly motivates future investigations of similar materials. In addition important preliminary work was done on the storage of Li-Ions on corannulene derivatives. The results indicate that the strategy is working and is worth pursuing further in the future.

Keywords: energy storage, hydrogen storage, Li-Ion, battery, nanoscale carbon, fullerene, fulleride, graphene, corannulene, metal enhancement, intercalation, metal decoration, doping, characterization

Kurzfassung

Es ist seit langem bekannt, dass zur kompakten, kostengünstigen und sicheren Speicherung von Wasserstoff ein Absorber benötigt wird. Der Grund hierfür liegt darin, dass Wasserstoff in seiner flüssigen und seiner gasförmigen Phase entweder zu geringe Speicherdichten oder zu hohe Sicherheitsrisiken aufweist. Die Entdeckung des ersten Metallhydrids (PdH) liegt fast einhundertfünfzig Jahre zurück und seither sind Jahrzehnte intensiver Forschung an Wasserstoffspeichermaterialien vergangen. Trotz dieser großen wissenschaftlichen Anstrengungen ist noch kein Speichersystem entwickelt worden, welches allen Anforderungen nach schnellen, reversiblen und energetisch wirtschaftlichen Sorptionseigenschaften genügt. Da Wasserstoff mit fast jedem Element des Periodensystems Bindungen eingeht und dabei oft gleichzeitig die physikalischen sowie chemischen Eigenschaften des Trägers massiv beeinflusst, existieren unzählige Kombinationen von möglichen Speichersystemen. Viele dieser Systeme sind weiterhin unbekannt. In dieser Doktorarbeit wurden neuartige, auf Kohlenstoff basierte Nanomaterialien bezüglich ihrer Struktur- und Energiespeichereigenschaften untersucht. Drei unterschiedliche Materialien wurden synthetisiert und mittels einer Vielzahl von experimentellen Methoden charakterisiert. Unter anderem wurden die Proben mittels volumetrischer Gassorption, Raman-, EEL-, Röntgen-Photoelektronen- und FT-IR Spektroskopie, Röntgen- und Neutronen-Pulverdiffraktometrie, SQUID Magnetometrie, Elektronenmikroskopie und Myonen-Spin-Repolarisation untersucht. Anhand von Messungen an metalldekorierten Graphenen und metallinterkalierten Fullerenen wurde der Einfluss der Kohlenstoffstruktur sowie der Metalldotierung auf die Interaktion des Absorbers mit molekularem sowie atomarem Wasserstoff verdeutlicht. Die vorgelegten Resultate sind hoch motivierend und fordern weitere Untersuchungen an vergleichbaren Materialien. Des Weiteren wurden wichtige erste Messungen zur Lithiumspeicherung an Corannulene-Derivaten durchgeführt. Die vorläufigen Ergebnisse bestätigen die Messstrategie und eröffnen weitreichende Möglichkeiten für zukünftige Messungen.

Schlüsselwörter: Energiespeicherung, Wasserstoff, Wasserstoffspeicherung, Lithium-Ionen, Batterie, Kohlenstoff Nanopartikel, Fulleren, Fullerit, Graphen, Corannulene, Interkalation, Dotierung, Charakterisierung

Contents

List of abbreviations

Abbreviation	Full Name
μSR	Muon Spin Repolarization
LF-μSR	Longitudinal Field - μSR
ZF-μSR	Zero Field - μSR
TF-μSR	Transversal Field - μSR
%At.Conc.	Atomic Concentration in %
a.u.	arbitrary units
B.E.	Binding Energy
BET	Brunauer,Emmett,Teller (theory or instrument)
CB	Carbon Black
CMC	Carboxymethylcellulose
Dr. sc. nat.	Doctor Scientiarum Naturalium
EC:DEC	Ethylene Carbonate:Diethylcarbonate
EELS	Electron Energy Loss Spectroscopy
Empa	Swiss Federal Laboratories for Materials Science and Technology
FEC	Fluoroethylene Carbonat
FFT	Fast Fourier Transform
FLL	Flux Locked Loop
FT-IR	Fourier Transform - Infrared Spectroscopy
FWHM	Full Width at Half Maximum
HHV	Higher Heating Value
HRPT	High Resolution Powder Diffractometer
K.E.	Kinetic Energy
LHV	Lower Heating Value
MFC	Mass Flow Controller
NP	Nano Particle
pcT	pressure-composition Temperature instrument
PP	Polypropylen
PSI	Paul Scherrer Institute

Abbreviation	**Full Name**
PVDF	Polyvinylidene Fluorid
Rel.Conc.	Relative Concentration
SAED	Selected Area Electron Diffraction
SEI	Solid Electrolyte Interface
SINQ	Swiss Spallation Neutron Source
SNSF	Swiss National Science Foundation
SPM	Superparamagnetism or Superparamagnetic
SS	Stainless Steel
SSA	Specific Surface Area
SQUID	Superconducting Quantum Interference Device
DC-SQUID	Direct Current - SQUID
FC-SQUID	Field Cooled - SQUID
ZFC-SQUID	Zero Field Cooled - SQUID
TEGO	Thermally Exfoliated Graphite Oxide
G	Graphite
GO	Graphite Oxide
TEM	Transmission Electron Microscopy
HRTEM	High Resolution TEM
STEM	Scanning TEM
HAADF-STEM	High Angle Annular Dark Field STEM
THF	Tetrahydrofuran
XPS	X-ray Photoelectron Spectroscopy
XRD	X-ray Diffraction

1

Introduction

One of the greatest challenges of mankind in the 21st century is to satisfy an ever growing hunger for energy and materials by sustainable means. Never before in our history have we been able to accommodate a greater number of people with such an unsurpassed standard of living and at the same time produced labor with higher efficiency. The success of the many, their prosperity and wealth are closely related to the conversion of resources and the therewith associated work. It does not seem possible to conserve or increase our standard of living without producing and consuming energy on the way. This correlation goes so far that for the developed world the gross domestic product grows proportionally to the consumption of energy [23]. While past generations have depleted resources and overburdened our environment on a global scale to accumulate the wealth we are living in today, the current generation and the generations to come have to provide solutions to the same problems but with an added acknowledgment of global warming, limited resources, our impact on the environment and finally our own health. In addition growing political unrest and questionable economic dependencies of so-called petrostates demand the reevaluation of the status quo. These ever growing demands of a modern society, propelled by tremendous media coverage, change our Zeitgeist and cause a paradigm shift towards sustainability. Undoubtedly, manifold partial solutions need to be found to address such a universal and faceted problem and cheap, pollution free energy can solve a majority of these.

On the energy production side, the feasibility of renewable energy has been proven over and over again, and the first countries have set admirable goals for a 100% renewable electric-energy society [90, 30, 48, 34, 134, 78]. The trend clearly goes toward the utilization of renewable energy sources and away from fossil energy vectors such as natural gas, coal and crude oil derivatives. This solves the problems of greenhouse gas emission as well as political and economical dependencies simultaneously. While the present global market share of renewables is small, the potential is enormous and a large fraction of the contemporary energy demand can be quenched by implementing an already existing portfolio of technologies such as photovoltaics, photothermics, geothermics, wind- and hydropower. These technologies do not depend on government subsidies to achieve grid parity, in stark contrast with some conventional sources such as nuclear power and in opposition to common misconception [7, 12, 74].

One of the roadblocks for most renewable energy sources and the biggest drawback is that the generated electric power and the power demand rarely coincide. On each particular production site, the solar irradiation, wind speeds, ocean tides and waves show inconstant intensities and can vary greatly over time. The power produced thereby varies correspondingly in the same time intervals. The peaks and gaps in power production need to be bridged and the generated but unused electric power needs to be stored such that it is readily available at a later point in time when demand surpasses supply [30]. This demand/supply deficiency can be on the timescale of hours, days or even seasons. The problem of efficiently utilizing renewable energy sources thus condenses to an energy storage problem. The different timescales involved and the distinct requirements on the storage system make a one-fits-all solution highly unlikely. Many different energy storage technologies are already available, and on the market. However, there are no market competitive products for large scale stationary energy storage, to bridge the previously mentioned gaps between demand and supply, and for energy storage systems applicable in electric mobility.

1.1 The hydrogen cycle

A pollution free and sustainable solution for many energy storage problems would be a hydrogen-based energy economy. There are logical reasons why hydrogen is an appropriate medium to store energy and release it at a later point in time. Hydrogen is the most abundant chemical element in our universe and 74 mass% of baryonic matter is made up of it. Hydrogen, is furthermore one of the most abundant chemical elements in the Earths lithosphere, with the majority chemically bound as water or in hydrocarbons. The price of hydrogen will therefore never be determined by scarcity of the chemical element and it is freely available everywhere on the globe. Hydrogen is not only extremely abundant but also has the highest heating value per mass of all chemical elements and common fuels (higher heating value (HHV) $\approx$ 142.2 MJ/kg, see table 1.1). Since hydrogen is rarely found in its stable molecular form, H_2, it needs to be liberated from chemical compounds for use as a fuel. Figure 1.1 shows the most common possible feedstocks and process alternatives for hydrogen production. Which production technology is utilized is often based on a benefit-cost ratio and necessarily depends on the local availability of the feedstock, the development state of the technology, properties of the hydrogen-demanding application, political considerations and various other determining issues. However, the end price of produced hydrogen is mainly determined by the sophistication and state-of-the-art of the production technology, quite the contrary to fossil or nuclear fuels.

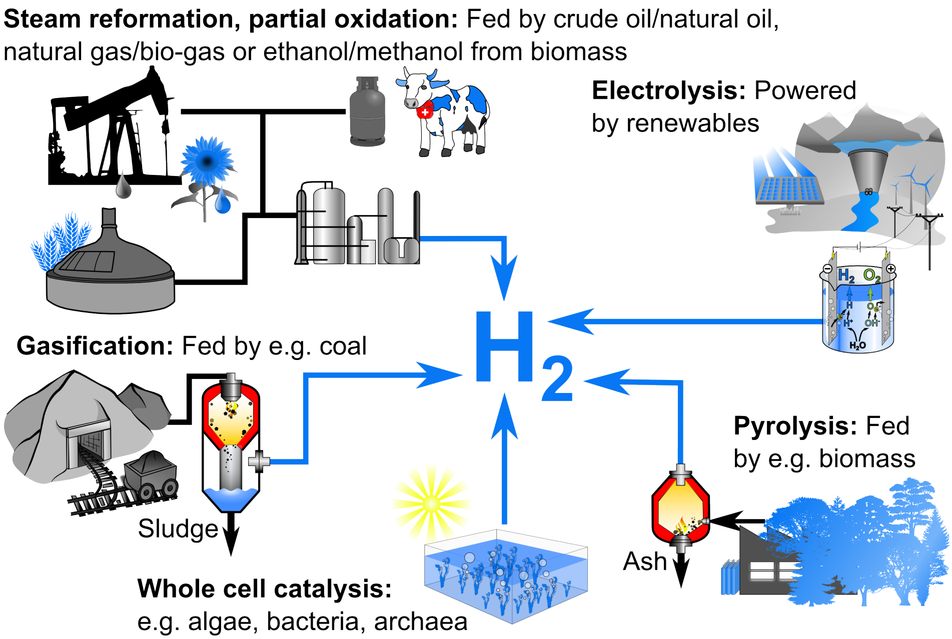

Figure 1.1: Hydrogen can be produced by various production technologies using corresponding feedstocks. A detailed overview can be found elsewhere [56, 87].

Liberated and stored hydrogen has great advantages over alternative energy storage solutions; among others, hydrogen can be used for a wide variety of applications and troublesome end products can be avoided. Hydrogen can be used to generate pollution free heat by means of catalytic burning with the final product being pure water. On the other hand, hydrogen can be directly transformed into electric power by means of a fuel cell. This avoids the production of large amounts of excess heat and thus does not limit efficiency due to heat management issues, as would be the case for any type of heat engine [73]. A broad scale hydrogen economy could thus close the cycle between sustainable production and pollution free, sophisticated utilization, leaving only end products that in turn can be used to produce hydrogen again (see figure 1.2).

With appropriate reaction paths hydrogen can be reversibly utilized within a contained cycle. For this so-called Hydrogen Cycle the main aspects are the production of hydrogen, hydrogen storage and the later usage of the thus stored energy. There are many different ways to produce hydrogen (see figure 1.1); however, perhaps the cheapest way is to use hydrogen as a buffer to accommodate peaks in the power production of renewables, i.e. when the oversupply of power needs to be handled to maintain grid-stability. The main energy sources providing the necessary power for hydrogen production could be photovoltaics, solar thermal, biomass, wind- and water-power (all stemming finally from solar energy through nuclear fusion), geothermal heat (nuclear fission) and tidal range (gravity).

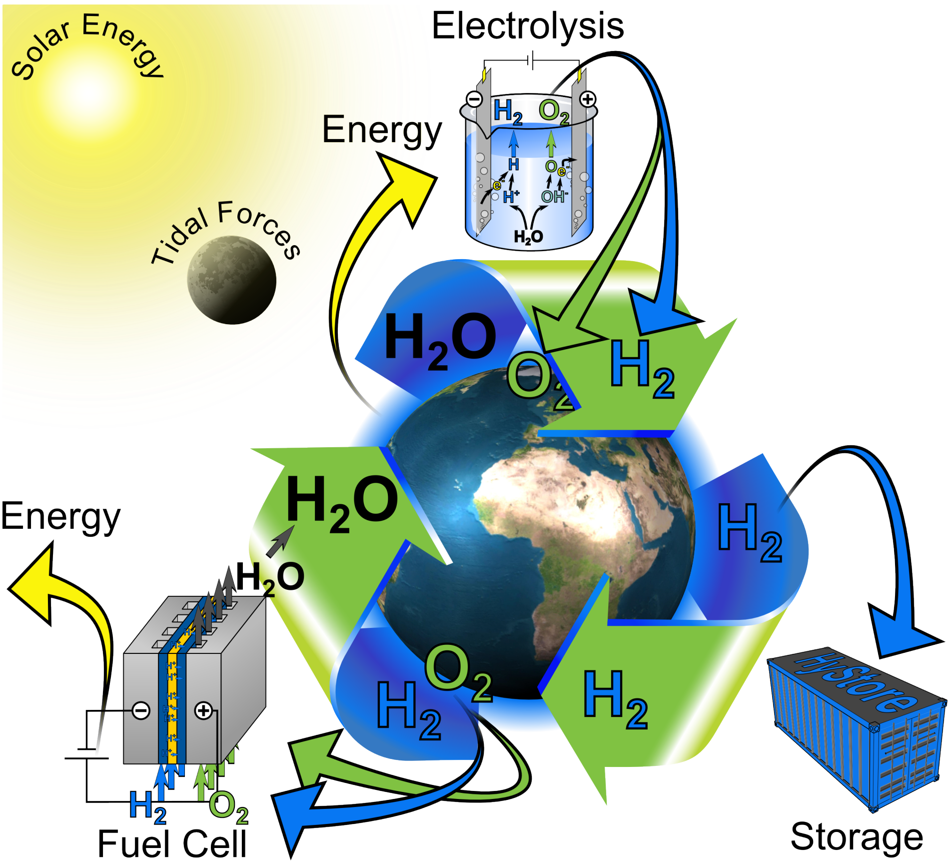

Figure 1.2: The Hydrogen Cycle is a closed, sustainable, pollution free life cycle for hydrogen. The key aspects are the production of hydrogen, hydrogen storage and the later consumption of the stored energy. To liberate hydrogen from a chemical compound, energy is required and the main sources can be temporary overproduction via renewable energy sources such as: solar energy, tidal range and geothermal heat. Hydrogen can thereafter be stored as gaseous or liquid hydrogen or in a solid medium. The stored hydrogen can be used to generate heat by catalytic burning, to generate heat and work by simple combustion in a heat engine, or to generate electric power for instance in a fuel cell. Within the Hydrogen Cycle, energy is produced and consumed by forcing hydrogen into different chemical states without the creation of harmful byproducts or greenhouse gasses. In the presented cycle, hydrogen is liberated from water by electrolysis ($2H_2O \rightarrow 2H_2 + O_2$) and utilized by the reverse reaction within a fuel cell.

If hydrogen is produced by electrolysis, oxygen is generated as a side product, which in turn can either be stored and used or safely released into the environment. The gained hydrogen needs to be stored and depending on the later application, various different viable storage solutions are already on the market such as metal hydride hydrogen storage in MgH_2 [82], or gaseous hydrogen storage either in composite tanks for mobile applications or through injection into the natural gas grid [111, 35, 133]. While currently available storage techniques are already capable of solving this part of the problem, stored hydrogen has the potential to rival or supercede currently utilized storage solutions such as Li-ion batteries or, in the near future with rising oil prices and climate levies, even gasoline for mobile applications [123].

1.2 Carbon-based energy storage

Carbon, no matter if used for the purpose of energy storage or not, is of great interest for any available and prospective technology since it is first and foremost a lightweight, highly abundant, conveniently accessible and thus cheap element. Carbon is, due to its valency, extremely versatile in its structure and exists in many different allotropes such as graphite, diamond, amorphous carbon, graphene, nanotubes and fullerenes, among others. Associated with these structural differences are dramatic differences in physical properties. While graphite is black, highly electrically conducting and soft enough to be used for writing on sheets of paper, diamond is transparent, a poor electric conductor and exhibits the highest hardness of any bulk material. In addition, carbon does not only form a large number of pure element allotropes, but also vast numbers of chemical compounds, de facto more than any other chemical element. The high adaptability of carbon with its structural versatility and the ability to adjust physical as well as chemical properties on a broad scale enables the creation of application-specific, tailored compounds. Carbon is the basis of all known living organisms and composes most of our comestibles. Hydrocarbons, especially methane, crude oil and coal, are valuable energy vectors. Carbon-based cellulose is not only thought to be the most abundant organic polymer on Earth but also shows great commercial potential starting from wool, over paper production, linen and hemp to filler materials in drugs [58]. All currently available plastics are made from carbon polymers, often including oxygen and nitrogen in the polymeric structure. Carbon steel, diamond-like-carbon (DLC) coatings, various lubricants and pigments, pencils, neutron moderators in nuclear reactors, gem quality diamond for jewelry and industrial diamonds for drilling, cutting or polishing, carbon-fiber-reinforced polymers as extremely tough but light structural elements, activated carbon as absorber and adsorber filter materials, carbon-fiber brushes for electric motors and carbon-based electrode materials for batteries are but a few of many applications of carbon.

In terms of energy storage, currently the most widely used class of energy vectors is without a doubt hydrocarbons in the form of fossil fuels. The main advantages of hydrocarbons are their natural availability and high volumetric as well as gravimetric energy density (see table 1.1). The low present-day price of oil, natural gas and coal, extracted from natural deposits, is surely one of the main reasons for the success of hydrocarbons, making them the status quo of today's energy storage. As such, a new and competing storage technology has a difficult task since it must rival its predecessor in all regards: energy density, convenience and price. While hydrogen can be used in fuel cells to generate electric power or in catalytic burners for heat, both of which produce only water as the end product, hydrocarbons are burned in conventional heat engines, oxidizing all constituents, not only hydrogen. Burning hydrocarbons has therefore the major disadvantage of producing unwanted or even adverse end products, e.g. gasoline, diesel or LPG usage in commercial combustion engines produces CO_2 in large quantities and due to the high temperatures in common heat engines, the exhaust-gas needs to be reformed in catalytic converters to reduce the amount of carbon monoxide and nitrogen oxides, all of which are highly toxic compounds. Natural coal, burned in coal power plants for electric power generation, not only causes environmental disasters and humanitarian misery during mining, but the contained pollutants such as sulfur, mercury, uranium, thorium, arsenic and other heavy metals are freed into the environment if not properly filtered. In perspective, European coal power plants alone are estimated to cause more than 18200 premature deaths, 8500 cases of chronic bronchitis and account for over 4 million lost working days every year [52]. The attributed economic costs of the health impacts are estimated to be 42.8 billion € per year [52]. Similar analysis can be conducted on all kinds of products and fuels to estimate the overall impact and the attributed costs. Although it is difficult to verify the accuracy of these kind of studies, it becomes evident that an honest and real-world benefit-cost analysis and comparison between hydrocarbons and hydrogen needs to include these adverse effects, and the corresponding cost of handling them, in their calculations. This is commonly not done, causing a tremendous market distortion where the burdens are imposed on society instead of the polluter.

While this reflects poorly on carbon-based energy storage technologies, there are many reasons why carbon persists to be of great interest in specific therms. Carbon-based compounds do not necessarily need to be fully oxidized and hydrogen, although energetically less favorable, can be liberated and used separately.

In general there are certain factors determining the success of any energy storage solution:

1. Volumetric energy density
2. Gravimetric energy density
3. Abundance/availability of the storage material
4. Appropriate working conditions
5. If reversible: capacity retention and cyclability
6. Safety aspects of the technology

Depending on the application, some of these points are more important than others and any of the above can be a key factor in making a technology unfeasible. There is no doubt that for instance the use of heavy metal hydrides for mobile hydrogen applications is unreasonable while they find use in stationary applications. In the same way it is clear that it would be pointless to exchange modern Li-ion batteries in smartphones with little combustion engines running on gasoline. Applications clearly determine which storage solution is suitable. Methane (CH_4), for example, consists of about 25.1 mass% hydrogen, which is an amount well above typical demands on a viable hydrogen storage solution, if gravimetric as well as volumetric storage densities would be the only important parameters (The US DoE target for mobile storage is 7.5 mass% H_2 [87]). Unfortunately, hydrogen is strongly, covalently bound to the carbon and the average bond-dissociation energies of C-H in CH_4 is very high ($E_{\text{dis.}} = 414$ kJ mol^{-1}) [65]. Non-catalytic thermal cracking to liberate hydrogen requires temperatures above 1400 K to achieve a reasonable turnover rate, making it highly impractical [1]. The development of appropriate energy storage technologies is clearly a complex problem with many determining parameters; but, owing to their previously mentioned adaptability, carbon-based compounds are sufficiently flexible to satisfy all these demands.

Undoubtedly the energy necessary to liberate hydrogen depends on the nature of the chemical bond and can thus vary drastically. With the reasonable assumption that there is no activation barrier for H_2 adsorption, the enthalpy of formation, in equilibrium, is determined by $\Delta H \approx T\Delta S$, where T is the temperature and S the entropy. Considering typical entropy values for H_2 one can estimate the ideal range of H_2 binding energies [65, 70]. Below a binding energy of 20 kJ mol^{-1}, H_2 complexes are not bound strong enough to achieve substantial capacities under ambient conditions. For physisorption on carbon materials for instance, the binding energy is approximately 3–10 kJ mol^{-1} H_2 and cryogenic temperatures are required to store considerable amounts of hydrogen at near atmospheric pressures [101, 64].

Physisorption of hydrogen under cryogenic temperatures is, however, energetically demanding. While this rules out physisorption for significant hydrogen storage in general, high specific surface area carbon materials, with more than 3000 $m^2\ g^{-1}$, can be used as an additive in pressurized gas tanks, leading to higher overall volumetric storage densities while still being relatively light weight [77, 136].

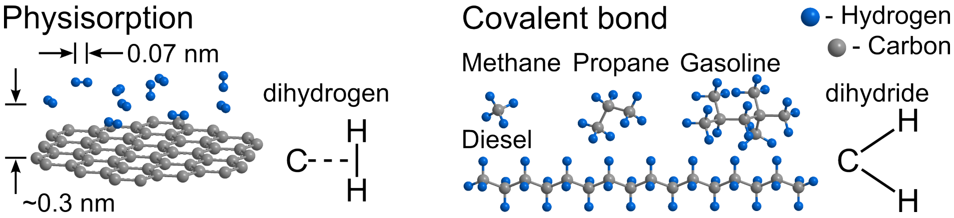

Figure 1.3: **(left)** A molecular model of hydrogen physisorbed on a graphene sheet. Physisorbed hydrogen is weakly bound by van der Waals forces, leaving the dihydrogen molecules intact. The weak binding energy (≈ 5 kJ mol^{-1} H_2) results in very low storage capacities at ambient pressures and room temperature. **(right)** The same is not the case for covalently bound hydrogen, as found in hydrocarbons, where the typical C-H bond energies are in the order of > 400 kJ mol^{-1} [65]. Molecular models of four common fuels are depicted, namely methane (CH_4), propane (C_3H_8) and a typical gasoline (C_8H_{18}) and diesel molecule ($C_{16}H_{34}$).

With binding energies above 40 kJ mol^{-1} H_2, hydrogen is likely bound too strongly, such that elevated temperatures or pressures are required for adsorption and desorption. Chemical bonds between carbon and atomic hydrogen are often too strong, as shown for methane with an average bond-dissociation energy of 414 kJ mol^{-1}. In hydrogenated fullerenes (e.g. $C_{60}H_x$), hydrogen is covalently bound to carbon, as in hydrocarbons. Theoretical calculations for $C_{60}H_{36}$, however, predict an average C-H bond energy of 295 kJ mol^{-1}, which is significantly lower than the typical C-H bond energies of hydrocarbons and a demonstration of the impressive impact of structure. Unfortunately this bond energy is still an order of magnitude too high [96, 65].

Binding energies of H_2-complexes in the range of 20–40 kJ mol^{-1} H_2 as well as a dramatic reduction of the enthalpy of reaction and the activation energies for H-complexes as compared to common hydrocarbons would both be ideal for practical applications [70]. Naturally occurring complexes with such energies are, however, uncommon and need to be specifically synthesized. Starting with the lower end of the range, the binding energy of H_2 needs to be enhanced which can be achieved by the introduction of additional attractive forces between the hydrogen molecule and the material. One way of achieving this is by introducing the Kubas interaction in which H_2 acts as a neutral two electron σ donor to a transition metal center with the back-donation of electrons from a filled metal d-orbital to the anti-bonding σ^* orbital of the hydrogen molecule [59]. If σ donation and simultaneous back-donation into σ^* are in the right balance, i.e. there is no hydride formation through heterolytic cleavage ($[\mathrm{M{-}H}]^- + \mathrm{H}^+$) or oxidative addition $\left(\mathrm{M} <^{\mathrm{H}}_{\mathrm{H}}\right)$, the hydrogen–hydrogen bond is stretched but the molecule essentially persists. A diagram of the orbitals involved in the bond is depicted in figure 1.4. For hydrogen bound via Kubas interactions, H_2 is not bound to the carbon atoms in the structures but to transition metal centers strategically incorporated into the material. The carbon matrix acts as the host material, preventing the metal from aggregating. Theoretical calculations of metal doped carbon materials predict Kubas interactions with bond energies in the desired range [59, 138, 18, 113, 63, 68]. Another possibility for increasing the bond energy is the addition of attractive electrostatic interactions by the introduction of charge on the host material (see figure 1.4). Analogously it was predicted that excess charge on differently sized fullerenes leads to a dramatic increase in binding energy to about 17–31 kJ mol^{-1} H_2 [141].

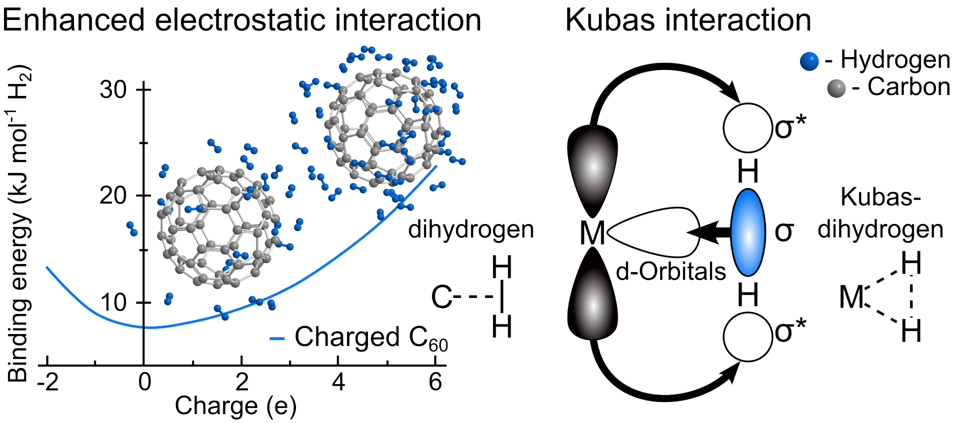

Figure 1.4: **(left)** Charged fullerenes are predicted to show enhanced electrostatic interaction and bind large quantities of H_2 with comparatively high binding energies. This enhanced interaction is attributed to the high electric field, caused near the surface by the added charge, polarizing the hydrogen molecules. The curve shows a schematic of the H_2 binding energy versus the charge state of C_{60}; corresponding literature values can be found elsewhere [141, 148]. **(right)** A molecular orbital diagram of H_2 bound via Kubas interaction to a transition metal atom. For reasons of simplicity only the metal d-orbitals that take part in the H_2 bonding are indicated for the metal center, M.

A different potential pathway for hydrogen storage is via hydrogen spillover where a dispersed active catalytic site, for instance a metal center, supported by a host material (often simply called the support), can facilitate the dissociation of hydrogen under conditions that are thermodynamically unfavorable for the pristine host. Subsequent to the dissociation of H_2 and adsorption of atomic hydrogen on the metal, H atoms migrate from the metal onto the support and diffuse away, the so-called spiltover hydrogen. The presence of the catalytic center decreases the activation energy needed for the molecule to dissociate and adsorb on the support, an effect that is well known in the field of catalysis. If this works in both sorption directions, the mechanism can enable hydrogenation as well as dehydrogenation under preferable conditions [93, 94]. While theory endorses hydrogen spillover the topic is still heavily debated. In figure 1.5 a comparison between hydrogen spillover on a carbon nanotube and a typical metal hydride is depicted.

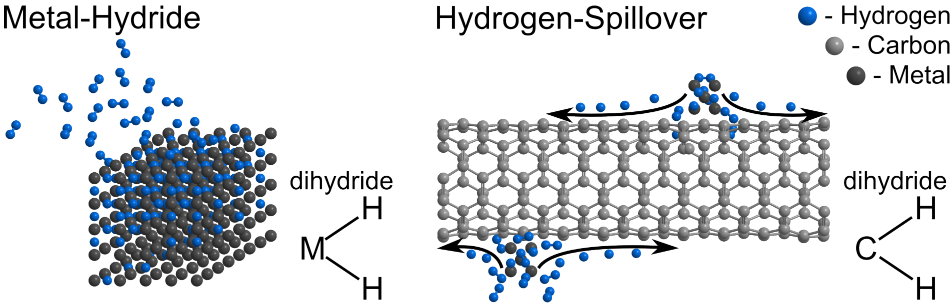

Figure 1.5: The different steps in hydrogen absorption for metal hydrides are: H_2 adsorption on the metal, dissociation of H_2, absorption of H and subsequent diffusion into the metal host lattice. The same steps occur for hydrogen spillover, followed by the transition from the metal onto the underlying support, a carbon nanotube in this case, and further diffusion on the support. The main difference between metal hydrides and hydrogen spillover is that the majority of hydrogen is bound to the support in the case of spillover, and not to the metal. The metal dramatically reduces the effective activation energy for absorption and thus hydrogen can bind to the support under conditions energetically not feasible in its absence.

By sophisticated tailoring of carbon materials it is thus possible to attain hydrogen storage materials satisfying the demands on a modern storage technology.

Table 1.1: *Common fuels and their corresponding gravimetric and volumetric higher and lower heating values (HHV and LHV) [88].*

	Fuel	Higher Heating Value		Lower Heating Value	
		MJ/kg	MJ/l	MJ/kg	MJ/l
Gasous[a]	Hydrogen (101 kPa)	142.2	0.013	120.2	0.011
	Hydrogen (70 MPa)	142.2	5.6	120.2	4.7
	Natural Gas (101 kPa)	52.2	0.041	47.1	0.037
Liquid	Liquid Hydrogen	141.8	10.0	120.1	8.5
	Crude oil	45.5	38.6	42.7	36.1
	Gasoline	46.5	34.7	43.4	32.4
	Diesel	45.8	38.3	42.8	35.8
	Methanol	22.9	18.2	20.1	16.0
	Ethanol	29.8	23.6	27.0	21.3
	Acetone	31.9	24.9	29.6	23.2
	Liq. petroleum gas	50.2	25.5	46.6	23.7
	Liq. natural gas	55.2	23.6	48.6	20.8
	Dimethyl ether	31.7	21.1	28.9	19.2
	Methyl ester	40.2	35.7	37.5	33.3
	Propane	50.2	25.5	46.3	23.5
Solid	Coal[b]	24.0		22.7	
	Coking coal[b]	29.9		28.6	
	Farmed trees[c]	20.6		19.6	
	Herbaceous matter[c]	18.1		17.2	

[a]: At 273 K, [b]: Wet basis, [c]: Dry basis

1.3 This thesis

In the previous introductory sections, the driving forces for a change towards renewable energy sources and away from fossil fuels for heat and electric power generation have been described. Energy storage was identified as one of the major roadblocks; caused by the irregularity of energy production, based on fluctuating sources. Hydrogen was proposed as an ideal energy storage medium with appealing properties such as abundance, the existence of closed life cycles, the highest heating value of all chemical compounds and the possibility of its use without causing pollution. The disadvantage of hydrogen as a storage medium is the fact that it is highly combustible in gaseous form and has a very low boiling point at ambient pressures (≈ 21 K) leading to low volumetric densities at ambient conditions. Storing hydrogen in compounds such as metal hydrides dramatically increases the volumetric density but at the cost of gravimetric density. Finding a suitable compromise between these two along with suitable thermodynamics, i.e. practical sorption temperatures and kinetics leading to fast and reversible cycling, is an ongoing scientific and engineering endeavor. The ideal binding energy for H_2 is thought to be between 20–40 kJ mol^{-1} H_2, which requires careful attention to the nature of the bond [70]. A second viable approach is to reduce possible energy barriers for absorbed atomic hydrogen, such as large bond dissociation energies. Modified carbon structures were commended in these terms and the low weight, abundance and variability of carbon were highlighted. On this basis, the research performed in the course of this thesis has focused on novel nano-structured carbon materials with prospectively high energy storage capacities.

The research described herein was conducted on three different classes of carbon materials. Owing to their differences and different possible applications, this thesis is structured such that it is not intended to be read cover to cover but rather chapter by chapter. A comprehensive overview of theory and experimental methods relevant to this thesis as a whole is given in chapters 2.1 and 2.2, respectively. Each following chapter is a treatise of a particular class of materials. The materials include metal decorated graphenes (chapter 3), metal intercalated fullerenes (chapter 4) and corannulene derivates (chapter 5). The first two materials are of interest as potential, lightweight and cheap hydrogen storage materials while the latter are found to exhibit large lithium capacities and are thus potential candidates for Li-ion battery anode materials.

In chapter 3 investigations on thermally exfoliated graphite oxide (TEGO) and lithium and nickel decorated derivatives of TEGO (Li- and Ni-TEGO) are presented. The preparatory introduction elucidates why this novel class of materials deserves special attention followed by a description of the synthesis of the different samples. The focus of the conducted research rests on their structural identification and evaluation of a possible hydrogen storage utilization. Nickel decorated graphene was studied in particular depth and besides a thorough characterization, muon spin relaxation and volumetric hydrogen gas sorption measurements are presented. Both techniques give insight into the hydrogen storage capacity of Ni-TEGO which is dramatically increased as compared to the undecorated TEGO. Li-TEGO was found to be unstable and was only present with oxidized lithium species; hence, no hydrogenation experiments were conducted on these samples.

The investigations of assorted metal intercalated fullerenes are reported in chapter 4. Similar to metal decorated graphenes, theory predicts significant interaction of the material with hydrogen, which is the focus of the corresponding introductory section. The main focus of this chapter lies on the investigations of pure, sodium and lithium intercalated fullerenes in view of their potential as lightweight hydrogen storage materials. Hydrogen and deuterium sorption measurements show a dramatic capacity increase of the fullerides compared to pristine C_{60} and significantly reduced absorption and desorption temperatures. X-ray and neutron powder diffraction on the hydrogenated and dehydrogenated samples show the appearance of minor NaH (NaD) and LiH (LiD) reflections. The hydrogenation/dehydrogenation is thus accompanied by a deintercalation and corresponding reintercalation of minor quantities of sodium and lithium, all well below the common decomposition temperatures of the separate species.

Besides investigations on novel hydrogen storage materials, corannulene, a small, corrugated fraction of C_{60}, and the derivative decakis(phenylthio)corannulene was investigated by means of galvanostatic lithium cycling measurements. Both materials have been shown to exhibit significant lithium intercalation capacities and are thus believed to be promising candidates for future Li-ion battery anode materials. However, the preliminary results presented in chapter 5 call these assumptions into question.

2 Methods

The materials used in the here reported work are either novel materials, in every respect, or novel with respect to hydrogen storage. To be able to draw unambiguous conclusions it is therefore crucial to study the materials characteristics thoroughly, prior and post hydrogen sorption. Consequently a large part of the here reported work was conducted in the area of materials characterization. To gain a holistic view of the structure, hydrogen mediated structural changes and physical as well as chemical properties of any given material, the application of a variety of complementary measurement techniques is required.

The majority of the here utilized experimental setups and techniques belong to the standard toolbox of modern science and only a brief description is given rather than a detailed analysis of the underlying method. Two experiments are, however, more unusual, namely SQUID magnetometry on superparamagnetic nanoparticles as well as muon spin repolarization. Hence, a more comprehensive overview is given below.

2.1 Theory

2.1.1 Superparamagnetism in nanoparticles

If ferromagnetic particles are sufficiently small, the energy cost of forming or maintaining domain walls is higher than the resulting savings in demagnetization energy. In such a case the particles are in a single-domain, also called monodomain, state. All magnetic moments within a single-domain particle point in the same direction and the particle is therefore magnetically saturated in the absence of an external field. The magnitude of this moment can be written as $\mu = VM_s$, where V is the volume of the particle and M_s the saturation magnetization. Multi-domain particles of soft magnetic material can adjust easily to external magnetic fields, by moving the domain walls with relative ease and thus showing a low coercivity. Contrary single-domain particles respond to external magnetic fields by simultaneous rotation of all internal magnetic moments as one and thus, show a much larger coercivity. A phenomenon that strongly increased the interest in the study of magnetic nanoparticles. As one delves deeper into the theoretical description of an ensemble of magnetic nanoparticles two major difficulties become apparent. Firstly the magnetic dipole-dipole interaction between the particles and secondly the intricate nature of the characteristic anisotropy of each particle.

The dipolar coupling between two nanoparticles with magnetic moments $\vec{\mu}_1$ and $\vec{\mu}_2$ is dependent on the mean distance r between them and the mutual alignment. The potential energy can be written as [10]:

$$E = \frac{\mu_0}{4\pi r^3}\left[\vec{\mu}_1 \cdot \vec{\mu}_2 - \frac{3}{r^2}\left(\vec{\mu}_1 \cdot \vec{r}\right)\left(\vec{\mu}_2 \cdot \vec{r}\right)\right] \tag{2.1}$$

with μ_0 the vacuum permeability. Since the magnetic moments are dependent on the volume of the particles one finds that the dipolar coupling is proportional to $E \propto V/r^3$. Thus, in a sufficiently dilute system the influence of dipolar interactions are small compared to typical anisotropy energies.

Amongst others the spin-orbit coupling of electrons is influenced by the crystal lattice, thus, it is clear that the crystal can induce directionality in the spins. This leads to preferred directions in which it is particularly easy to magnetize the crystal, the so-called easy axes. To magnetize the crystal into a less preferred direction a certain energy barrier must be overcome, the anisotropy energy barrier. The effective anisotropy K_{eff} of individual particles is a more complex matter and usually several, very different, contributions need to be considered. For nanoparticles in particular, in contrast to bulk crystals, the crystal structure plays a much less dominant role in defining the preferential direction of magnetization such that amongst others shape, stress and surface effects have non negligible contributions to the anisotropy.

- **Magnetocrystalline anisotropy:** To magnetize a crystal along certain crystallographic directions can be easy or hard (easy axis / hard axes). Nickel, as an example, shows cubic magnetocrystalline anisotropy with a negative anisotropy constant and eight equivalent $\langle 111 \rangle$ easy magnetization directions along the diagonals of the unit cell.

- **Magnetostriction - stress anisotropy:** Stress can alter the lattice and lead to changes of the hybridized orbitals or overlap of orbitals of neighboring atoms. Since the exchange interaction strongly depends on these, induced strain can alter the overall magnetic energy density and thus the anisotropy.

- **Surface effects:** While surface effects do not play a fundamental role for large crystals, the small size of nanoparticles leads to a large fraction of the crystals atoms being at the surface. The distinction between surface and core atoms is due to the different environment caused for instance by the lower amount of nearest neighbors, atomic vacancies, changes in atomic coordination, dangling bonds and lattice disorder. In certain cases surface defects can be so dominant as to cause ferromagnetic behavior in nanoparticles that are otherwise diamagnetic [114], e.g.cerium oxide [69, 36] or niobium nitride [108].

- **Magnetostatic - shape anisotropy:** To counteract the magnetization of a particle and reduce the corresponding dipolar energy, demagnetizing fields arise that in sufficiently large particles force the formation of domain walls. While dipolar energy is saved, the formation of domain walls requires energy such that at some point an equilibrium is reached. For single domain particles this mechanism of domain wall creation versus dipolar energy stops to work since no further domains can be created due to the high cost in energy. However, the shape of the particle itself can lead to large dipolar energy along certain directions and lower energy in others. In thin films for example the magnetization favors an in-plane preferential orientation while in prolate ellipsoids the magnetization will be along the polar axis. The later is the case for the nickel nanoparticles present on one of the investigated samples.

The description of an ensemble of differently sized magnetic nanoparticles with slight alternations in shape is exceedingly difficult. In the course of this thesis the magnetic properties of single-domain nickel nanoparticles have been investigated and the focus of this theoretical discussion is thus on cubic, single-domain, particles. These simplifications narrow down the complex description significantly. Previous studies on the influence of size distribution but also shape distribution have concluded that for assemblies of cubic magnetic nanoparticles the total energy is easily dominated by the shape and surface anisotropy [125]. In an easy approximation alternations in shape of generally spherical particles are of ellipsoidal nature and the combined anisotropy can thereafter be well described by an uniaxial anisotropy with the polar axis (see figure 2.1 (a)) of the ellipsoid being the easy magnetization axis. So even though the nanoparticles show cubic magnetocrystalline anisotropy, the overall effective anisotropy of a randomly oriented dilute assembly of nanoparticles is comparable to that of pure uniaxial magnetic anisotropy. This is an assumption often found in literature, however, while vital to the further description of a magnetic system a justification for this assumption can be rarely found.

Let us now consider a dilute assembly of ferromagnetic, single-domain nanoparticles with prolate spheroidal shape that, as described above, show uniaxial anisotropy. Figure 2.1 (a) shows a schematic image of such a particle. The equatorial axis is a, the polar axis is denoted c and assumed to be the easy axis for magnetization. The anisotropy energy density of such particles follows $E_\mathrm{a}/V = K_\mathrm{eff}\sin^2\alpha$, where V is the volume of the particle and α is the angle between the magnetization M and the easy axis (see figure 2.1 (b) and (c)). The energy has two minima at 0 and at π which correspond to the two directions along the easy axis. A magnetic moment of a particle will hence experience an energy barrier $\Delta E_B = K_\mathrm{eff}V$ between the two minima that needs to be overcome for the particle to flip its magnetization state from one direction of c to the other.

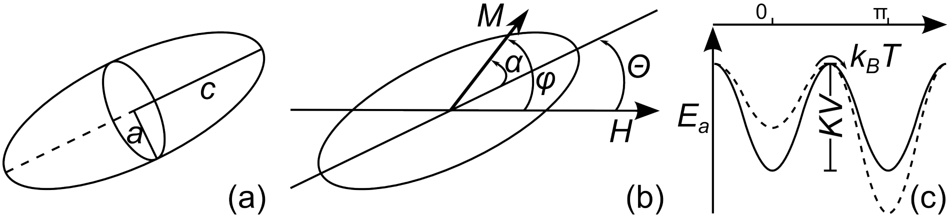

Figure 2.1: **(a)** Prolate spheroid with the polar and easy axis c and the equatorial axis a. **(b)** Two dimensional representation of the prolate spheroid in (a)in an external field H. Θ is the angle between H and c, angle α is the angle between M and c and ϕ is the angle between M and H. **(c)** Schematic representation of the energy density of an uniaxial crystal with its two minima at 0 and π. The dashed line shows the same energy density but while an external field is applied along the direction of the second minima.

For very small particles $K_{\text{eff}}V$ becomes small enough, so that thermal energy of the form $E_T = k_BT$, with k_B the Boltzmann constant and T the temperature, suffices to overcome the barrier and the magnetization reverses spontaneously. When $K_{\text{eff}}V \ll k_BT$ the assembly will, hence, behave like a paramagnet, however, instead of atomic spins, readily alignable with a sufficiently large external field, the whole ensemble of spins within each particle will align. Since nanoparticles have already hundreds if not thousands of atoms this state was aptly named superparamagnetic. Superparamagnetism (SPM) should not be wrongly regarded as a special case of the paramagnetism that ferro- and ferrimagnetic materials show above the Curie temperature. SPM is exclusively observed below the Curie temperature of ferromagnetic material and thus needs its own theoretical background.

The field activated alignment of the the magnetic moments is countered by thermally induced fluctuations causing misalignment (see dashed line in figure 2.1 (c)). As a thermally activated process the characteristic relaxation time τ follows an Arrhenius law. The theory describing this time and temperature dependence is often called the Néel-Brown or Néel-Arrhenius theory motivating the well known equation [86, 15, 5]:

$$\tau = \tau_0 \exp\left(\frac{\Delta E}{k_BT}\right) \tag{2.2}$$

with τ_0 the fluctuation time or inverse fluctuation frequency and typically around 10^{-9} s. Solving equation 2.2 for K_{eff} one gets:

$$K_{\text{eff}} = \ln\left(\frac{\tau}{\tau_0}\right)\frac{k_BT}{V}. \tag{2.3}$$

Equation 2.2 clearly demonstrates the dependency on temperature and the energy barrier but does not directly show the dependency on the experimental measurement time t. t is different for the various existing techniques and for DC-SQUID, as used in this thesis, a typical value is around $t = 100$ s.

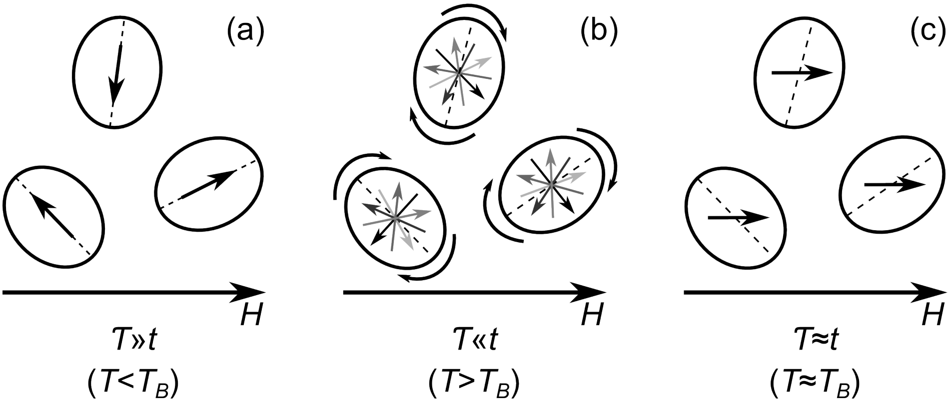

Figure 2.2: Schematic illustration of nanoparticles in a small external field H. **(a)** shows the blocked state where $\tau \gg t$ and H is to small to force the magnetic moments into alignment. **(b)** depicts the particles freely fluctuating in the superparamagnetic state $\tau \ll t$. The thermal energy is much larger than H and the net magnetization is zero. **(c)** shows how the particles align with the applied external field within the observation period t. The easy axes of the particles are indicated by dashed lines, their magnetic moments by arrows.

Through experimental measurements t and τ are coupled and the outcome of each measurement can be divided into different scenarios as follows:

- **$\tau \gg t$:** If the relaxation time is much larger than the observation period the particles will not have had the time to flip before the measurement is concluded. The particles can be thought of as in a blocked state (see figure 2.2 (a)).

- **$\tau \ll t$:** If the time a particle resides in a certain magnetic state is short compared to the measurement time, it is in a superparamagnetic state. The particle will be easily aligned with a sufficiently large field, and in the absence of such a field they will thermally fluctuate such that the average magnetization of the ensemble equals zero (see figure 2.2 (b)).

- **$\tau \approx t$:** The probably most interesting case is when the measurement time is roughly as long as it takes for the magnetic moments to relax. The magnetic moments will have a certain probability to align with an applied field in time while not yet enough time has passed to flip out of the induced state again (see figure 2.2 (c)).

N.B. due to the logarithmic dependency of τ/τ_0 even large variations of the time scales involved, for instance if measuring with different instruments, will only lead to fractional changes in the results. Instead of differentiating the scenarios by their time one can without loss of generality divide them by their respective temperatures. A visualization of the different regimes is purposed in figure 2.2.

Stoner and Wohlfarth established their theory on magnetic hysteresis in heterogeneous alloys in 1948, where they describe their calculations on particles similar to ours. In contrast to the Néel-Brown theory the Stoner-Wohlfarth model can be used to calculate the magnetization curve for single-domain particles. With the two equatorial axes equal, the sum over all spheroid axes gives $2N_a + N_c = 4\pi$. The energy induced by the applied magnetic field can be written as:

$$E_H = -HM\cos\left(\phi\right) \tag{2.4}$$

The energy associated with the demagnetization field is [112]:

$$E_\mathrm{D} = \frac{1}{2}M^2\left(N_c\cos^2(\alpha) + N_a\sin^2(\alpha)\right) \tag{2.5}$$

with $N_{a,c}$ the demagnetization coefficients along the corresponding axes. Substituting $\cos^2(\alpha)$ with $1 - \sin^2(\alpha)$ and plugging this into equation 2.5 one gets:

$$E_\mathrm{D} = \frac{1}{2}M^2 N_c + \frac{1}{2}M^2(N_a - N_c)\sin^2(\alpha) \tag{2.6}$$

The second part of this equation can be identified as the angle-dependent part of the anisotropy energy for uniaxial systems and thus the shape-anisotropy constant K_s is given by:

$$K_s = \frac{1}{2}M^2(N_a - N_c) \qquad \text{and for SI units:} \qquad K_s = \frac{1}{2}\mu_0 M^2(N_a - N_c) \tag{2.7}$$

When the particle becomes spherical ($N_a = N_c$) the shape anisotropy vanishes as expected and with the previously chosen assumptions the relevant total energy E_tot of a dilute assembly of prolate spheroid particles in an external field can be described by the sum of the equations 2.5 and 2.4:

$$E_\mathrm{tot} = E_D + E_H = \frac{1}{2}M^2 N_c + K_s\sin^2(\alpha) - HM\cos\left(\phi\right) \tag{2.8}$$

2.1.2 Muons, unstable elementary particles

Muons are elementary particles, very similar to electrons. Like electrons they belong to the class of leptons, further including the tauon and a corresponding neutrino for each of the three heavy leptons. For every lepton exist anti-leptons and the basic properties for the muon (μ^-) and anti-muon (μ^+) are listed in table 2.1 below.

Table 2.1: *Basic properties of muons and anti-muons.*

Symbol	$\mu^\pm$
El. Charge	$\pm 1\ e$
Mass	105.7 MeV/c^2, 0.112 m_p, 207 m_e
Spin S_μ	1/2
Gyeomagnetic factor	−2
Mean lifetime	2.2 μs

Muons are created during the interaction of cosmic radiation with matter in the outer shells of the earths atmosphere. However, to produce muons in a controlled way a high energy proton beam and thus a particle accelerator is necessary. When a high energy proton beam is channeled on a target (usually graphite) pions are created via:

$$p + p \to p + n + \pi^+ \tag{2.9}$$

$$p + n \to n + n + \pi^+ \tag{2.10}$$

Pions have a mean lifetime of only 26 ns and will subsequently decay via a two body process mediated by weak interaction:

$$\pi^+ \to \mu^+ + \nu_\mu \tag{2.11}$$

The weak interaction is the only fundamental interaction that breaks parity-symmetry. Parity violation implies that only left-handed neutrinos exist. Their spins are always antiparallel to their linear momentum. In a likewise manner only right-handed anti-neutrinos are found in nature. Taking a closer look at equation 2.11 one discerns that while the pion is spinless both products have spin 1/2 which must therefore be directed antiparallel for reasons of conservation. Considering that the pion is at rest prior to decay, which is the case at the research facility of concern in this thesis, momentum conservation dictates that the muon and the neutrino must have equal and opposite momentum. As a result all emitted muons are 100 % spin polarized with a spin antiparallel to their direction of motion.

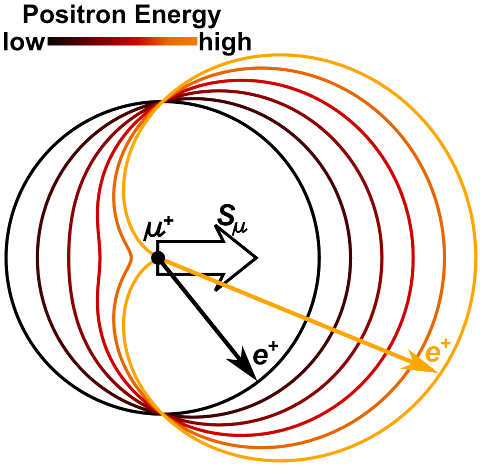

Figure 2.3: Angular distribution of the positrons emitted in the decay of μ^+ as determined by equation 2.14. The angular distribution varies depending on the energy of the positron. In general positrons are preferentially emitted parallel to the spin of the muon.

With a mean lifetime of 2.2 μs muons have one of the longest lifetimes of all unstable subatomic particles. The subsequent decay of the muon is a three particle process and as well mediated exclusively by weak interaction. For every muon decay an electron is produced, of the same electrical charge as the muon, and two neutrinos. Equation 2.12 and 2.13 describe the decay processes for muon and anti-muon respectively.

$$\mu^- \rightarrow e^- + \overline{\nu_e} + \nu_\mu \tag{2.12}$$

$$\mu^+ \rightarrow e^+ + \nu_e + \overline{\nu_\mu} \tag{2.13}$$

Parity is violated again, as was the case for the pion decay. However, this time it is a tree instead of a two body process and the resulting $e^\pm$ are emitted anisotropic. The probability of measure a positron at an angle Θ towards the direction of the muon spin can be expressed by an angular distribution function following:

$$W(\Theta) = 1 + \alpha \cos(\Theta), \tag{2.14}$$

where $0 \leq \alpha \leq 1$ monotonically increases with the energy of $e^\pm$. The preferential direction of emission of electron or positron is therefore parallel to the spin of the muon. This preferential emission can be used to track any changes towards the muons spin before the decay, however, requires large quantities of positrons for satisfying statistics.

As reported in table 2.1 muons have a mass of about 105.7 MeV/c^2 or approximately a ninth of a proton and 200 times that of the electron. As a result of their higher mass and the lower amount of emitted bremsstrahlung upon injection, muons penetrate matter much deeper than electrons of the same velocity. Within condensed matter the implanted muon interacts with its host in a variety of ways that can be used to deduce information of the host. One particular measurement technique, μSR, is reported in section 2.2.4.

2.2 Experimental

This section presents a brief description on the experimental methods and setups used to gather the data that is analyzed and discussed in this thesis. The focus does not rest on reevaluating established measurement techniques and the discussion is limited to a clarification of the use setups rather than on an explanation of the underlying principles.

2.2.1 Powder diffraction

Powder diffraction techniques are commonly used for the detection of crystalline structures within samples. While diffraction occurs when ever a propagating wave encounters an object or a slit the method used here takes place on periodic structures. These periodic structures cause the incident beam to diffract into specific directions. Unlike in single crystal diffraction, where the incident beam is diffracted on only one crystallographic direction, ideally all possible crystalline orientations are present equally in a powder sample and will contribute to the diffracted beam. To attain true randomness and counter possible texturing the orientation of the powder samples are generally rotated.

As a result the three dimensional reciprocal space of a corresponding single crystal is projected onto a single dimension for a powder sample. This becomes especially apparent when the diffraction patterns on a two dimensional detector plate are compared. While for single crystal well defined Laue spots are observed, powder samples generate rings caused by the average orientation of the crystallites. The angle, commonly called scattering angle, between the incident $\overrightarrow{k_i}$ and the diffracted beam $\overrightarrow{k_o}$ is denoted as 2Θ (see figure 2.4). Following the Laue condition constructive interference only occurs if the vector $\overrightarrow{k_o} - \overrightarrow{k_i} = \Delta\overrightarrow{K}$ equals a reciprocal lattice vector $\overrightarrow{G}$; in which case $\Delta\overrightarrow{K}$ is called scattering vector. Therefore each ring detected in a powder diffraction experiment corresponds to a family of reciprocal lattice vectors of the same length.

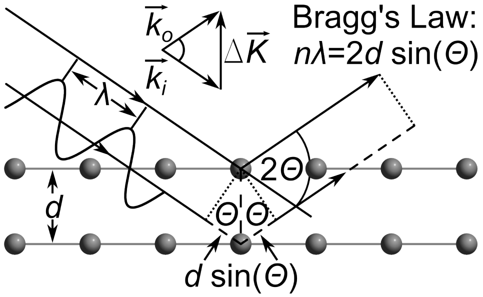

Figure 2.4: Representation of Bragg's law in real space. The spheres represent atoms on periodic lattice positions. An incident beam $\overrightarrow{k_i}$ of wavelength λ is scattered on the lattice planes of distance d. Constructive interference occurs under the Bragg condition $n\lambda = 2d\sin(\Theta)$. The scattering angle 2Θ is the angle between incident $\overrightarrow{k_i}$ and diffracted beam $\overrightarrow{k_o}$.

Powder diffraction experiments are generally presented in so-called diffractograms where the recorded intensity of the diffracted beam is depicted as a function of either the scattering angle 2Θ or the length of the scattering vector $\Delta\overrightarrow{K}$. The latter has the advantage that it is independent of the wavelength of the used radiation. This can be of particular usefulness since different radiation sources, for instance neutrons or various kinds of x-rays, have different wavelength. Within this thesis X-ray and neutron powder diffractograms are presented and so the different used setups are explained below.

2.2.1.1 X-ray powder diffraction

The interaction of X-rays with condensed matter is based on the scattering of X-ray photons with the electron cloud of the sample under investigation. The scattering amplitude therefore increases proportional to the atomic number Z. Heavy, electron rich, elements are easier to detect than light elements which can cause problems when investigating samples made up by weak scatterers.

Powder X-ray diffraction (XRD) was performed on a laboratory Bruker D8 Advanced diffractometer operating in parallel beam geometry. The Bruker D8 was equipped with a copper target ($\lambda_{\mathrm{Cu}K_\alpha} = 0.1541$ nm) and Göbel X-ray mirror, to parallelize the incident beam. The diffracted beam was detected by a one-dimensional position sensitive VÅNTEC-1 gas detector.

Sample preparation was conducted under inert atmosphere within argon filled glove boxes. Generally the powder samples where filled into 0.5 mm quartz capillaries, with a wall thickness of 0.01 mm, sealed by melt off. This allowed contamination free handling and measurements, which were performed at room temperature. Capillaries were subsequently mounted via a goniometer head to a rotation stage at the center of the circle described by X-ray tube and detector.

For Rietveld refinement a software called TOPAS from Bruker was used. The origin of the refined crystal structures is always mentioned.

2.2.1.2 In situ neutron powder diffraction

One of the most fundamental results of quantum physics is the wave-particle duality. Neutrons can behave like waves and scatter and diffract akin with X-rays. The wavelength of thermal neutrons is in fact similar to that of X-rays resulting in very similar scattering angles. However, the main difference between XRD and neutron diffraction is that unlike X-rays, neutrons are scattered by nuclei (strong nuclear force) instead of electrons (electromagnetic force). Since neutrons interact by strong interaction with the potential of the nucleus the scattering cross sections vary for different elements and even for different isotopes of the same element. While hydrogen and deuterium is basically transparent for X-ray radiation neutrons are heavily scattered. At the same time the cross section for hydrogen is over 10 times higher than that for deuterium but mostly due to incoherent scattering, which is why commonly deuterium is used for neutron diffraction.

All in situ neutron powder diffraction measurements were conducted at the high resolution powder diffractometer (HRPT) of the Swiss Spallation Neutron Source (SINQ) at the Paul Scherrer Institute (PSI) in Villingen, Switzerland. The facility provides a continuous beam of thermal neutrons created in a spallation source. The moderated neutrons passed a collimator after which they were filtered by a silicon crystal and subsequently passed through a monochromator before entering the sample. The neutron flux was constantly recorded and possible fluctuations have been accounted for in the analyzed data. Neutron detection was performed with a large position sensitive ^{3}He detector with a high resolution of ($\delta d/d < 0.001$). For the conducted experiments a radiation type furnace was installed which permitted heating of the sample in a range of 300–700 K. A gas-handling system, similar to the setup discussed in section 2.2.3.2, was used for the in situ neutron scattering experiments. This enabled measurements at different gas pressures and, combined with the furnace, variable temperature.

2.2.2 X-ray photoelectron spectroscopy

The surface properties of a material can dramatically influence catalytic activity, adhesion, corrosion rates, the contact potential, wettability, chemisorption kinetics and many more factors. Since all condensed matter interact with their surroundings by means of their surfaces, surface characterization is paramount for a full understanding of these processes. X-ray photoelectron spectroscopy (XPS), also known as electron spectroscopy for chemical analysis (ESCA), is one of the most commonly used experimental techniques for the determination of specific surface characteristics. As a quantitative, surface sensitive spectroscopic technique XPS is able to accurately measure the elemental composition and the chemical and electronic state of the first few nanometers of the sample under investigation. XPS is rooted in the photoelectric effect. When photons of sufficiently high energy $E = h\nu$ hit a material the electrons within can interact with the photon and absorb the energy carried by the wave package. Is this energy larger than the work function W of the material the electron has sufficient energy to eject from its bond partner into a state at rest in the vacuum. The experimental quantity measured is the kinetic energy of the electrons detected in the spectrometer. Since this is dependent on the frequency of the X-rays it is not an intrinsic material property. The quantity of real interest is the binding energy (B.E.) of the electron, which can be determined by:

$$E_{\text{B.E.}} = h\nu - E_{\text{K.E.}} - W \tag{2.15}$$

where $h\nu$ is the photon energy, $E_{\text{K.E.}}$ is the kinetic energy measured with the spectrometer and W is the analyzer work function, i.e. the minimum energy required to remove an electron from the solid and into the analyzer.

The XPS measurements presented in this thesis were performed on a modified VG EscaLab spectrometer. Photoelectrons were detected using a Specs PHOIBOS 100 hemispherical energy analyzer. The X-ray source was operated with an aluminum target. Since the so generated X-ray light is polychromatic the outlet of the X-ray gun was spanned by a sub-μm, high purity, aluminum foil. This foil dramatically reduces the Bremsstrahlungs quantity of the X-ray spectrum, blocks ejected electrons from entering the XPS chamber and additionally feeds low energy photoelectrons to the sample surface. The latter is of particular use since long periods of photoelectron generation will leave a samples surface slightly electron depleted, even a well grounded one, which is compensated in this way. As a result the X-ray light that illuminated the sample consisted mainly of the well defined, characteristic K_α lines of aluminum. The base pressure of the UHV system was below $< 10^{-7}$ Pa. A particularity of the instrument is the directly connected Ar filled glove box. This way the samples could be prepared within the confines of inert atmosphere and subsequently transferred via the connected XPS load lock without exposure of contaminants. All prepared powder samples were pelletized in a hand worked pettel press. The resulting pellets were securely placed onto copper sample holders of a diameter slightly smaller than the sample pallet to prevent any photoelectron creation from the sample holder.

Data analysis was performed using CasaXPS and specifics of the curve fits are explained in the corresponding section.

2.2.3 Gas sorption measurements

2.2.3.1 pcT measurements

Most hydrogen and deuterium sorption measurements were conducted on in-house build dynamic pcT (pressure-composition Temperature) instruments. The main difference of this type of instruments to the more commonly used ones, employing the Sieverts method, is that the latter work at near-equilibrium conditions while the dynamic pcT does not. The dynamic pcT instrument measures the supplied amount of hydrogen by means of thermal mass flow controllers (MFC) instead of calculating it via pressure changes. Hydrogen MFCs measure the amount of H_2 by means of the specific heat capacity of the gas. This is done in a simple procedure. First the gas temperature is measured at the inlet of the device. The gas will subsequently pass a heating stage before exiting at the outlet where the temperature is measured again. The difference in ΔT can be used to calculate the amount of passed through gas; which is directly proportional. A review of the dynamic pcT instrument and the underlying method can be found elsewhere [8].

Sample handling prior to mounting to the dynamic pcT instrument was conducted in the inert atmosphere of an argon filled glove box. The sample holders consist of elongated stainless steel cylinders that can be sealed by means of gas tight valves. After transfer from the glove box and subsequent mounting to the dynamic pcT instrument the gas line between the dynamic pcT and the valve was evacuated. The external piping and the sample holder were outgassed at around 523 K for typically 16 h after which a base pressure of < 0.08 Pa was reached. During this whole procedure the temperature was monitored in situ and controlled by a JUMO Imago 500 multichannel process controller.

2.2.3.2 BET measurements

Various sorption measurements have been conducted on a BELSORP-max by BEL JAPAN INC.. Three types of measurements have been performed with this system that can be separated into adsorption measurements with helium, hydrogen and nitrogen gas. The instrument is fully automatic and works by the Sievert's method. In short, the sample, at known pressure and volume, is connected to a reservoir of well known volume and pressure. An automatic valve isolates the reservoir from the sample volume and by opening this isolation valve a new equilibrium is established. The amount of sorbed gas is thereafter determined via the equation of state for gas and the gas pressure change of the old and new equilibrium.

Sample preparation was conducted within an argon filled glove box. A cylindrical glass sample vial was filled with a precise amount of sample. A glass rod was subsequently inserted to reduce the dead volume of the vial after which a closing valve was inserted. This valve functioned as both a filter, preventing powder to enter the BET instrument in case of rapid pressure changes and turbulences, as well as a closing valve which only opened upon insertion into the instrument and closed upon extraction. This way the samples never needed to be exposed to contaminants.

Nitrogen adsorption was used to determine the Brunauer–Emmett–Teller (BET) specific surface area of thermally exfoliated graphite oxide. Measuring BET specific surface areas is the main purpose of the instrument, which is why it is often simply called BET instrument. The underlying theory of Brunauer, Emmett, and Teller aims to explain physisorption of gas molecules on solid surfaces and in particular addresses multilayer adsorption [16]. The main assumptions made during the derivation of the theory are:

- Adsorption takes place on well-defined adsorption sites
- Each adsorbed molecule provides a new adsorption site for another molecule
- E_1 is the unique energy of adsorption of the first monomolecular layer
- Every additional layer has the same constant energy equaling the heat of condensation E_L
- Each individual layer does not interact with any other layer
- The uppermost molecular layer is in equilibrium with the gas phase
- At the saturation pressure the number of adsorbed layers is infinite

These assumptions can restrict the use of the BET theory and careful examination is necessary to determine if it is a viable approach. The thus derived BET isotherm equation can be written as

$$\frac{p}{V\left(p_0-p\right)}=\frac{1}{V_{\mathrm{mon}}C}+\frac{C-1}{V_{\mathrm{mon}}C}\left(\frac{p}{p_0}\right), \tag{2.16}$$

where p and p_0 are the pressure and the vapor pressure of the adsorbate at the measurement temperature, V is the volume of adsorbed adsorbate, V_{mon} is the volume corresponding to the amount of adsorbate required to form a monolayer and C is the BET constant. It is important to note that the volume is not a temperature and pressure independent value and hence has to be defined at special conditions. The standard state, defined by BEL JAPAN INC., is $T = 273.15$ K and $p = 101.3$ kPa, and the same standard state was used for all BET analysis. The BET constant C is defined as

$$C=\exp\left(\frac{E_1-E_{\mathrm{L}}}{RT}\right), \tag{2.17}$$

with E_1 the heat of adsorption of the first layer, $E_L = E_2 = E_3 = ...$ the heat of adsorption for all subsequent layers, R the gas constant and T the temperature.

With a y-axis of

$$\frac{p}{V\left(p_0 - p\right)}$$

and an x-axis depicting p/p_0 the BET adsorption isotherm described in equation 2.16 resembles a straight line in the range of $0.05 \leq p/p_0 \leq 0.35$. Plotting the data in this way enables an easy linear fit yielding the slope s and the y-axis intercept i. Both can be used to calculate V_{mon} and the BET constant C via

$$V_{\mathrm{mon}} = \frac{1}{s+i} \tag{2.18}$$

$$C = \frac{s}{i} + 1 \tag{2.19}$$

In a final step the BET specific surface area a_{BET} can be calculated by

$$a_{BET} = \frac{V_{\mathrm{mon}} N_A \sigma}{V_{\mathrm{mol}} m_s}, \tag{2.20}$$

with $N_{\mathrm{A}} = 6.022 \cdot 10^{23} \mathrm{mol}^{-1}$ the Avogadro constant, $V_{\mathrm{mol}} = 22.414 \cdot 10^{-3}\ \mathrm{m}^3\ \mathrm{mol}^{-1}$ the molar volume of the adsorbate at standard conditions, m_s the specific mass of the measured sample and σ the cross-sectional area of an adsorbate molecule. As a particularity of the measurement setup the BELSORP-max already normalizes the y-axis data $\left(p/\left[V\left(p_0 - p\right)\right]\right)$ with m_s and gives it in units of g cm^{-3}. It is therefore not necessary to divide equation 2.20 by m_s again and it was just mentioned here for completeness.

2.2.4 Muon spin repolarization

Muon spin spectroscopy is an experimental technique based on the injection of 100 % spin polarized muons into matter. For an introduction on the elementary particle see section 2.1.2. Subsequent to the implantation the muon spin will be influenced by the materials properties, i.e. local magnetism, superconductivity and molecular dynamics. In analogy to other resonance techniques such as electron spin resonance (ESR) or nuclear magnetic resonance (NMR) a common abbreviation is μSR; standing for muon spin rotation, relaxation, repolarization or resonance depending on the conducted experiment.

Subsequent to the implantation of μ^+ into condensed matter they will lose their remaining kinetic energy by means of Coulombic interactions in a fraction of nanoseconds ($\approx 0.1 - 1$ ns). The influence of thermalization on the muons spin is very limited and no significant loss of polarization takes place. Although strictly speaking leptons, thermalized μ^+ behave like light protons and will generally occupy interstitial sites within the host. For metallic samples the positive charge is immediately screened by the free electrons in the conduction band. The muon is essentially free in a so called diamagnetic state. For semiconductors or insulators no rapid screening is possible due to the lack of free, delocalized electrons. After deposition of the kinetic energy the positive muon will usually capture an electron to form a neutral hydrogen-like state called muonium (Mu= $\mu^+ + e^-$). The analogy goes so far that besides a very similar Bohr radius the electronic structure nearly equals that of equivalent hydrogen centers, except effects caused by the reduced mass of the muon. As a consequence of local magnetic interactions the polarized spins will evolve and precess. For this muons have only a limited amount of time.

This time window is the muons lifetime after which they decay in a three body process (see equation 2.13). To date the only particle, of the three resulting, that is sensible to detect is the positron (for instance by means of a scintillation counters and photomultipliers). Since also the decay of the muon is mediated by weak interaction the decay violates parity and the positron is more likely to be emitted parallel to the muons spin than in any other direction (see figure 2.3). If the muon decays immediately its spin will have had no time to interact and a positron will be emitted preferentially into a backward detector where it will be counted. If the muon decays later and its spin does half a precession due to interactions, the emitted positron will be registered in a forward directed detector. The time evolution of registered positrons in forward and backward direction are expressed by the functions $N_\mathrm{F}(t)$ and $N_\mathrm{B}(t)$ respectively. The normalized difference of the muons spin polarization can thus be expressed by the asymmetry $A(t)$ given by:

$$A(t) = \frac{N_\mathrm{B}(t) - \alpha N_\mathrm{F}(t)}{N_\mathrm{B}(t) + \alpha N_\mathrm{F}(t)}, \tag{2.21}$$

where α is a calibration factor determined prior to the actual experiment. $A(t)$ is characteristic for all influences the spin was exposed to prior to the muons decay. A schematic illustration of the instrumental setup for zero field (ZF) and longitudinal field (LF) μSR is shown in figure 2.5. The former is basically a measurement proportional to $A(t)$ and very sensitive to weak internal magnetic fields. For the latter an external magnetic field is applied; parallel to the direction of the initial muon spin polarization. This way one can decouple the spin from any sample internal field and by knowing the applied field deduce information on the internal magnetism.

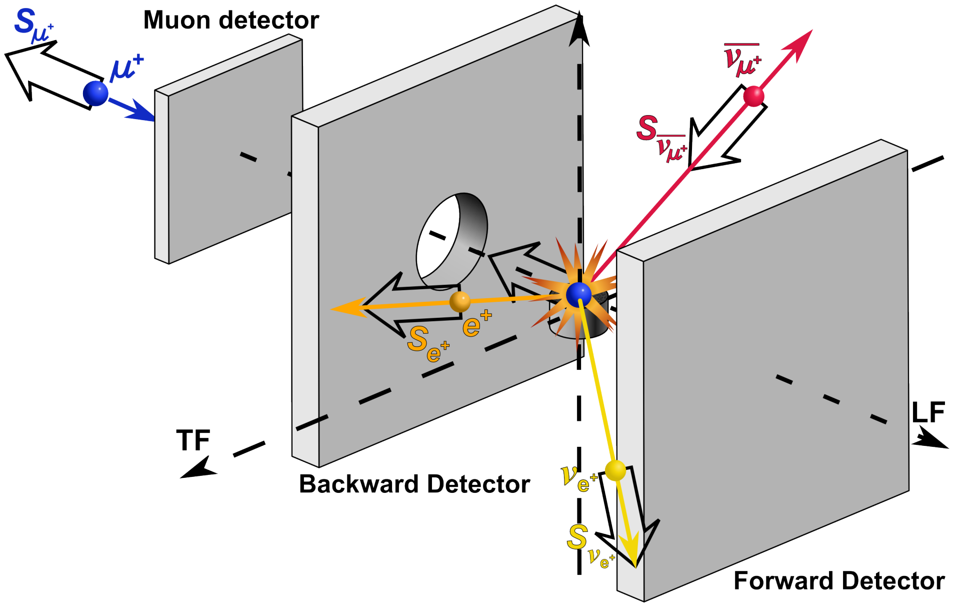

Figure 2.5: Schematic of the instrumental setup used for ZF and LF μSR experiments. A pulsed 100 % spin polarized μ^+ beam is directed onto the sample. Before implantation the beam penetrates a trigger detector which activates all other detectors. This dramatically reduces the background and noice from caused by accidental counts. By means of forward and backward positron detectors the time evolution of the decay products $\left(e^+\right)$ are mapped. For a LF-μSR experiment a static magnetic field is applied parallel to the initial spin of the muons.

In summary muons are used in a technique called μSR by implanting a fully spin polarized beam of muons into the sample of interest. Within the sample the spins of the muons will react to any internal or externally applied magnetic field, be it constant or fluctuating. As a result of these interactions the spins are redirected from their original direction and upon decay positrons are emitted preferentially parallel to the redirected spins. Forward and backward detectors count the emitted positrons and the time it took from implantation to detection. Resulting data will therefore include the asymmetry $A(t)$, the corresponding time and the measures of any applied external magnetic field. A more thorough collection of information on spin polarized muons in condensed matter can be found elsewhere ([9, 26, 97]).

2.2.5 DC-SQUID magnetometry

A superconducting quantum interference device (SQUID) is a highly sensitive magnetometer based on the quantum mechanical tunneling effect within a superconducting Josephson junction. Owed to their stunning sensitivity SQUID magnetometers have become one of the most widely used types of instruments in current magnetometry. The DC-SQUID has two parallel Josephson junctions in a superconducting ring.

A single Josephson junction can be explained as two separate superconducting regions isolated from each other by a thin non-superconducting slab. Cooper pairs can tunnel through the junction resistance free and without any voltage difference over the junction. If the superconducting regions are totally isolated the wavefunctions of the Cooper pairs within each region will have unrelated phases; while the phases are coherent for each region. If ϕ_1 is the phase of the Cooper pairs in one region and ϕ_2 the phase of the other region than the current over the junction is:

$$\begin{aligned} I &= I_{\max} \sin\left(\phi_2 - \phi_1\right) \\ &= I_{\max} \sin\left(\Delta\phi\right), \end{aligned} \tag{2.22}$$

where $I_{\max}$ is the maximal, Cooper pair based, current or critical current and dependent on the thickness of the junction. Equation 2.22 is also called DC Josephson current. The maximum current flows across the junction when the phase difference is a multiple of $\pi/2$ and $I = I_{\max}$.

For a typical DC-SQUID two such junctions are placed in a superconducting ring and the critical current of the junctions is much lower than the critical current of the rest superconducting ring. A schematic of this can be seen in in figure 2.6.

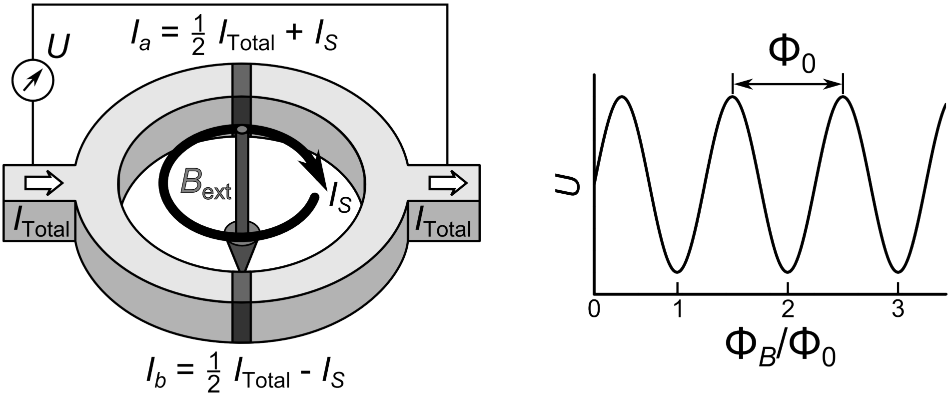

Figure 2.6: Left: Simplified illustration of a superconducting DC-SQUID ring with two Josephson junctions (dark grey). An applied external magnetic field B_{ext} (grey round arrow) induces a circular screening current I_S. Right: The voltage measured between the two electrodes of the SQUID ring versus the normalized flux Φ_{B}/Φ_0 at constant bias current I_{Total}.

In the absence of magnetic fields or currents the phase of all Cooper pairs takes the same value ϕ throughout the superconducting ring. If the Josephson junctions equal each other precisely an applied input current I_{Total} will split equally over both branches. If now an external magnetic field B_{ext} is applied perpendicular to the ring, for instance by magnetic moments of a sample place in the ring, the phenomenon of flux quantization takes place. A flux contained in a closed loop is quantized in units of single magnetic flux quanta $\Phi_0 = \frac{h}{2e} \approx 2.07 \times 10^{-15}$ Wb; where h is Planck's constant and e is the elementary electronic charge. The phase around the closed ring is now not equal for all Cooper pairs any longer and due to flux quantization it changes over a closed loop by $2\pi n$, where n is the number of the enclosed flux quanta [25]. The phase change can thus be expressed by:

$$\Delta\phi_{B_{\text{ext}}} = 2\pi \frac{\Phi_B}{\Phi_0}, \tag{2.23}$$

where Φ_B is the flux produced by the applied magnetic field. Since Φ_B does not necessarily equal an integer number of flux quanta a small current is generated to produce a final phase change of $2\pi n$. This generated current is often called screening current I_S. The phase change created by the screening current can either add or subtract to the phase change of the magnetic flux to give a final integer value and thus is modulated periodically with the period of one flux quantum. The separate currents over each branch become:

$$I_a = \frac{1}{2} I_{\text{Total}} \pm I_S \tag{2.24}$$

$$I_b = \frac{1}{2} I_{\text{Total}} \mp I_S \tag{2.25}$$

with the signs alternating with the same periodicity as the modulated current. This is the origin of the working principle behind DC-Squids.

If the applied current I_{Total} to the DC-SQUID is slightly larger than the critical current across the junctions the excess current generates a voltage U that can be read out between the electrodes of the ring. While an internal current is modulated by any applied magnetic flux the voltage will be modulated correspondingly and is therefore a direct function of the flux Φ_B. The voltage U is in a minimum state when the current has its maximum and vice versa. In this mode the superconducting ring of the DC-SQUID acts as a magnetic flux to electric voltage transducer. Due to the periodicity of the voltage SQUIDs measure fluctuations of fluxes rather than absolute values of magnetic field strength.

In an actual SQUID the superconducting ring is isolated from all external fields and the sample. This way possible disturbances from strong magnetic fields are countered in addition to a much easier thermal management. The SQUID is coupled via an input coil to a pick-up coil which in turn is exposed to the sample and possible external magnetic fields. A change in the magnetic field at the pick-up coil induces a field in the input coil. The SQUID, inductively coupled to the input coil, can thereafter detect a change in the relative magnetic flux. While the periodicity of a current biased SUID, as has been explained before, is one flux quantum this is not necessarily the limiting resolution. In analogy to a phase-locked-loop (PLL) a flux-locked-loop (FLL) can be used to operate the DC-SQUID.

The FLL operates by using the measured periodic voltage to drive a coil close to the superconducting ring. The coil is placed in such a way that it will generate a magnetic flux of equal strength and opposite polarity to the unknown flux one wants to measure. This will effectively cancel out the flux within the SQUID, such that it operates in a locked zero magnetic flux condition. By measuring the necessary current to drive the opposing coil one has a measure of the magnitude of the unknown flux; matched by the opposing flux within a fraction of the flax quantum.

2.2.6 Raman and infrared spectroscopy

When photons impinge on a molecule they can elastically or inelastically scatter. The latter is called Raman scattering and in the process the frequency of the incident photons can either red or blue shift, i.e. decrease or increase respectively. Is part of the photon energy deposited onto the target by addition to the internal energy, the resulting photon appears red shifted. One speaks of Stokes scattering. In the reverse process, the photon increases its energy by absorption of internal energy of the target, the process is called Anti-Stokes scattering. With the photon energies used in common Raman and Fourier transform infrared spectroscopy (FT-IR) the internal energy is related to vibrational energy of the target. In this context Raman and FT-IR spectroscopy are very similar but yield complementary information.

In Raman spectroscopy the detected photons correspond to the scattered and thus shifted photons. Usually monochromatic laser light is used for illumination. The measurement requires the determination of the energy of the scattered photons rather than the intensity. The recorded photons appear at energies shifted from that of the incident light and directly corresponding to the excitation energy. FT-IR commonly works in transmission and thus the photons that have not interacted with the sample are collected. The used radiation is polycromatic infrared light and the whole wavelength spectrum is measured simultaneously. The recorded transmittence or absorbance is subsequently plotted versus the wavelength or wavenumber. The latter is the result of a Fourier transform.

The main difference between Raman and FT-IR spectroscopy is based on the different nature of the transitions taking place. In general, molecular vibrations symmetric with regard to the center of symmetry of the molecule are forbidden for in the FT-IR spectrum. On the other hand antisymmetric vibrations, again with regard to the center of symmetry of the molecule, are forbidden in the Raman spectrum. This particularity of Raman and IR spectroscopy is called rule of mutual exclusion. Raman and FT-IR give therefore complementary information on the possible vibrational transitions. The selection rules are a more precise formulation of the previously mentioned symmetry considerations. For an infrared detectable transition the dipole moment in a molecule must undergo a change during vibration. For a transition to be Raman active, the polarizability in a molecule must change during vibration. As a result of this infrared spectroscopy provides information about functional groups whereas Raman spectroscopy is used to study the carbon backbone of the sample investigated in this thesis.

The here presented Raman measurements were conducted on a Bruker Senterra Raman spectrometer equiped with a 532 nm laser. Infrared measurements were conducted on a Bruker Alpha FT-IR spectrometer with an Attenuated Total Reflectance (ATR) module and equipped with a diamond crystal suitable for powder samples.

3

Metal decorated graphene

3.1 Introduction

The possibility of scalable production of graphene and functionalized graphene generated an incredible surge in interest in this class of materials [24]. Pristine graphene has the largest specific surface area of all graphitic materials (2630 m^2 g^{-1} [92]) making it attractive for gas adsorption. Fully hydrogenated graphene, called graphane, has a hydrogen content of 7.7 mass% [89]. As hydrogen is covalently bound to graphene the absorption and desorption of H requires elevated temperatures making a commercial use of graphane as a hydrogen storage material technically unfeasible. In section 1.2 several ways to improve the interaction between carbon and hydrogen were mentioned. Amongst others enhanced electrostatic binding of H_2 on C, Kubas interaction on metal doped carbon and hetero-catalytic dissociation of hydrogen and subsequent spillover from the catalytic site to the carbon support. In addition that lattice defects can play a fundamental role in the dissociation of H_2 and act as trapping centers [97]. The latter can be of importance since the applied synthesis method for graphene, thermal exfoliation of graphite oxide, produces a material with properties of graphene but also very different from it, particularly a high defect density and markedly less surface area. First principle calculations of lithium, calcium and titanium decorated graphene propose hydrogen adsorption via Kubas interaction and hydrogen storage capacities between 9.5–15.4 mass% with a binding energy of approximately 20 kJ mol^{-1} H_2 [53, 54, 63, 68, 144]. Other works, both experimental as well as theoretical, present evidence for hydrogen spillover on calcium and platinum decorated graphene with the possibility of full hydrogenation under preferable conditions and thus an accessible hydrogen content of 7.7 mass% [91, 66, 31, 41]. From a technical point of view working with metal and alkali-metal functionalized graphene proves challenging. The main difficulty in studying this kind of material lies in the need for an appropriate synthesis approach, performed in the absence of oxidizing agents, and the subsequent handling under inert conditions, all of which is necessary to prevent unwanted reactions and oxidation of the material. This is critical since dealing with novel materials and interpreting evidence can only be achieved if the experiments are repeatable and the materials properties remain equivalent for all measurements.

In the following chapter novel materials, functionalized thermally exfoliated graphite oxide, are discussed. Nickel and lithium decorated TEGO derivatives have been produced by a two-step, oxygen and water free, synthesis approach. The crystallinity of the samples have been investigated by means of X-ray powder diffraction (XRD), Raman spectroscopy, high resolution and high-angle annular dark-field scanning transmission electron microscopy (HRTEM and HAADF-STEM), electron energy loss spectroscopy (EELS) and selected area electron diffraction (SAED). Information on the chemical composition and the magnetic properties were gathered using X-ray photoelectron spectroscopy (XPS) and a superconducting quantum interference device (SQUID) respectively. Helium and nitrogen adsorption experiments were conducted to measure the skeletal density and the Brunauer-Emmet-Teller specific surface area (BET-SSA) of the samples. For the determination of the interaction with atomic as well as molecular hydrogen muon spin repolarization (μSR) and volumetric H_2 gas adsorption measurements have been performed respectively.

3.2 Experimental

3.2.1 Sample synthesis

The basis for the investigations on metal decorated graphenes was thermally exfoliated graphite oxide, which is also called graphene in this context. There are various different methods to synthesize graphene on a gram scale and the following is an explanation of the procedure used to produce the TEGO that was studied in the cause of this thesis. Prior to exfoliation pure graphite powder (SGL Carbon, RW-A grade) was oxidized using Brodie's method [14]. The oxidation of graphite leads to an out of plain expansion of the graphite lattice. This expansion is caused by the addition of functionalized groups between the plains. The resulting graphite oxide (GO) is, unlike its hydrophobic parent material, hydrophilic. This property was utilized and GO was diluted and washed in distilled water whereby residual traces of the solvents, used during oxidation, were removed. A subsequent drying at 333 K under air for about 24 h produced a green graphite oxide powder. The out of plain expanded lattice and the many introduced functional groups in between the plains facilitate thermal exfoliation of the lattice. To achieve this a propellant gas between the layers needs to be formed, leading to an overpressure and thus forcing the interplanar bonds to break. This can be achieved by sudden heating of GO causing the detachment of the functional groups from the plains.

To increase the efficiency of exfoliation a thorough oxidation is necessary. Furthermore a large difference between the build up pressure of the propellent gas and the external pressure is needed.

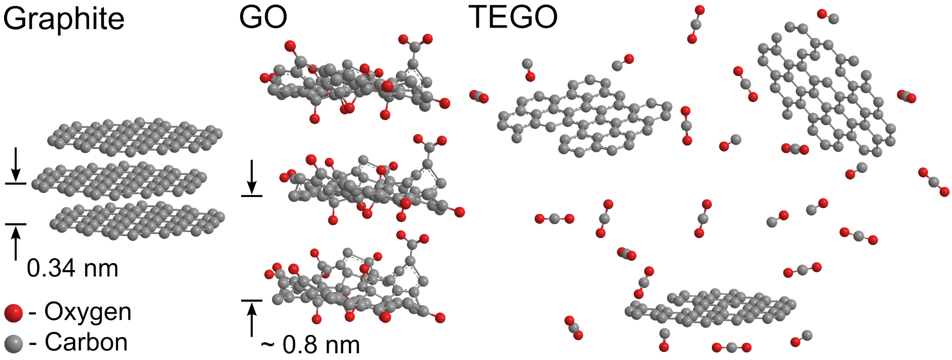

Figure 3.1: Schematic visualization of the steps involved to synthesize TEGO from graphite. (Graphite) Pristine graphite with an interplanar distance of 0.34 nm prior to oxidation. (GO) Graphite oxide with increased interplanar distance due to the formation of various different functional groups (e.g. hydroxide, peroxide, epoxy, carboxyl etc.). The exact distance is dependent on the oxidation state. (TEGO) Highly defective thermally exfoliated graphite oxide flakes are produced. The freed groups often remove their respective carbon atoms from the lattice and leave lattice defects behind. The amount of defects can be reduced by thermal annealing.

This was realized by placing GO at the end of a long quartz vial (see figure 3.2(a)). The vial was evacuated to high vacuum 10^{-3} Pa and subsequently flash heated up to a temperature of 1423 K under dynamic high vacuum. At this temperature the sample was kept for 30 minutes. By quickly placing the quartz vial into the hot furnace, instead of heating it up conjointly, a heating rate of $\gg 500\,\mathrm{K/min}$ can be reached. The dynamic high vacuum ensured that the freed propellent gas was quickly removed, preserving the needed large pressure difference for exfoliation. Under these conditions thermal exfoliation takes place in the first few seconds after the sample is placed in the furnace. For further annealing and healing of defects the sample was kept at at a high temperature for an extended period of time. The quartz tube was afterward quickly cooled down to room temperature. Pictures of the dramatic sample volume difference prior and post thermal treatment can be seen in figure 3.2. As-synthesized TEGO was removed from the quartz tube under inert conditions in a Ar-glove box (H_2O and O_2 < 0.5 ppm). A more detailed description on the synthesis of TEGO can be found elsewhere [81].

Different nominal stoichiometries of lithium and nickel decorated TEGOs were synthesized by means of wet chemical methods. TEGO was mixed with either lithium azide (LiN_3) or nickel(II) acetylacetonate ($Ni(acac)_2$) and subsequently the sample containing vial was evacuated below 10^{-3} Pa. The vial was slowly submerged in liquid nitrogen and previously degassed anhydrous tetrahydrofuran (THF, Alfa Aesar) was introduced. Due to the cryogenic temperatures the THF condensed and completely soaked the reagents.

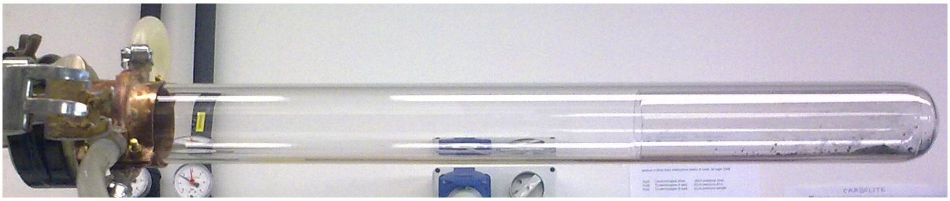

(a) Quartz vial prior to thermal exfoliation. The GO can be seen to the right where it appears as dark flakes. The pump line is situated to the left.

(b) After thermal exfoliation the resulting TEGO shows a dramatic volume increase compared to GO.

Figure 3.2: Pictures taken from the quartz vial used for thermal exfoliation 3.2(a) prior and 3.2(b) post thermal treatment. The pictures were taken by Dr. Marcello Mazzani and are adapted with kind permission.

To ensure absolute impregnation of TEGO with the precursor (LiN_3 or $Ni(acac)_2$) the vial was removed from the liquid nitrogen bath and kept at 323 K for 12 h under constant stirring with a teflon coated magnetic stirrer. The solvent was removed and a uniform black powder remained in the vial. The product was slowly heated up to 573 K under high dynamic vacuum $\left(10^{-4}\ \text{Pa, heating ramp of } 60\ \text{K/h}\right)$ upon which the precursors thermally decomposed. The Li- and Ni-TEGO show up as uniform black powder with a higher volumetric mass density than TEGO. The samples described in this chapter were synthesized by Dr. Mattia Gaboardi at the University of Parma.

3.2.2 Experimental procedure and setups

All samples were exclusively kept under vacuum or anaerobic conditions and in between measurements they were only handled in argon filled glove boxes (H_2O and O_2 levels < 0.5 ppm). This preserved unsaturated defects and dangling bonds for as long as possible and at the same time prevented moisture build up, oxidation and other contamination.

In case of high resolution transmission electron microscopy (HRTEM), high angle annual dark field scanning transmission electron microscopy (HAADF-STEM), selective area electron diffraction (SAED) and electron energy loss spectroscopy (EELS) small amounts of Ni-TEGO were exposed to air and quickly dispersed in isopropanol. These samples have been discarded after the measurements due to very probable contamination. Small droplets of this suspension were deposited onto carbon coated copper grids and then loaded into the respective instrument. Two differently equipped JEOL JEM-2200FS microscopes were used. One was stationed at IIT (Istituto Italiano di Tecnologia) in Genova and the other at IMEM-CNR (Istituto Materiali per Elettronica e Magnetismo - Consiglio Nazionale delle Ricerche) in Parma, Italy. The microscope of the Parma facility was equipped with with a Schottky gun working at 80 and 200 kV (resolution of 0.3–0.19 nm respectively), an in-column energy filter (JOEL, Ω-type), a high resolution CCD camera, an EDS and STEM detectors. HAADF-STEM (200 kV) and HRTEM (80 kV) images were acquired on this instrument. The microscope stationed at the IIT in Genova was used to record SAED patterns and HRTEM images of deposited nickel nanoparticles; fitted with a Schottky gun working at 200 kV and a CEOS 3rd order aberration corrector in the objective lens, capable of a resolution of 0.1 nm. The EEL spectra were measured on a FEI Tecnai G2 microscope equipped with a Gatan Enfinium SE spectrometer (model 976) at IIT in Genova, Italy.

For Raman spectroscopy and X-ray diffraction the samples were filled into $\varnothing = 0.7$ and 0.5 mm quartz capillaries with a wall thickness of 0.01 mm respectively. The capillaries were sealed by melt off. Raman spectroscopy was measured with a 532 nm laser and an output power of 10 and 20 mW at a magnification of 10x and a resulting spectral resolution of 3.5 cm^{-1}. The X-ray diffractometer and the Raman spectrometer are explained in sections 2.2.1.1 and 2.2.6 respectively.

DC-SQUID magnetometry was carried out on a MPMSXL-5 SQUID magnetometer at the university of Parma, Italy. About 12 mg of sample was sealed in 5 cm long quartz tubes under a helium pressure of 10 Pa. Hysteresis loops were measured at 2 and 300 K temperature with an applied field range of ±5 T. For the zero-field-cooled (ZFC) and field-cooled (FC) SQUID measurements a magnetic field of $\mu_0 H = 3 \cdot 10^{-3}$ T was applied in the temperature range of 2–400 K.

Zero field and longitudinal field muon spin repolarization (ZF and LF µSR) measurements were carried out on the EMU spectrometer at the ISIS-Rutherford Appleton Laboratory, England. The detectors of this facility have the longest data accumulation time of all muon spin facilities (about 15–20 μs) and are therefore superior in terms of recording the evolution of the muon spin at long timescales. The muon beams are pulsed and 100 % spin-polarized. For the measurement about 350 mg of Ni-TEGO was pressed in an airtight silver coated aluminum cell and sealed with kapton windows. A transversal field (TF) measurement was performed at 300 K on a pure silver plate to estimate the full asymmetry of 21.7(1) %. In order to obtain the baseline of 9.25(6) % a second measurement was performed on a quartz sample for which 100 % of the muons form muonium.

Hydrogen sorption was measured volumetrically with a pcT instrument at 77, 93 and 103 K and in a pressure range of 0–4 MPa H_2. Due to the exceptionally low bulk density of the synthesized samples only about 100–200 mg could be compressed inside the airtight stainless steel sample holders. After transfer from the glove box, where the sample holder was filled, to the pcT instrument the gas line and subsequently the sample holder was outgassed at 523 K for about 16 h after which a base pressure of < 0.08 Pa was reached; the temperature was monitored in situ and controlled by a JUMO Imago 500 multichannel process controller. Subsequently the sample was submerged in a bath of liquid nitrogen (LN_2) where it cooled down to 77 K. Particular care was given to the filling level of LN_2, which was kept constant over the entire measurement time. To enable temperature control the sample holder was embedded in an oven, capable of heating the sample while submerged in LN_2. High purity hydrogen gas (99.999 % H_2) was introduced to the system upon reaching of thermal equilibrium. The effective adsorbed and subsequently desorbed amount of hydrogen was determined via the mass flow method were the hydrogen mass, supplied to or from the sample, is measured with a thermal mass flow controller [8]. As a reference sample a commercial, non-absorbing, silicon (Sigma-Aldrich) was used. Desorption was performed under vacuum (< 0.1 Pa). Additionally measurements at 77 K and up to 0.1 MPa of hydrogen were performed on a Sieverts-type apparatus (BET) from BELSORP-max (BEL, Japan). Compared to the pcT the BET instrument has the advantage of a higher sensitivity at very low pressure but has the drawback of a small pressure range. The BET was furthermore used to measure the BET specific surface area via nitrogen adsorption at 77 K and the skeletal density via the expansion of helium at room temperature from a known volume into the sample volume, once with and once without the sample. A description on the instrumentation can be found in section 2.2.3.

X-ray photoelectron spectroscopy (XPS) was measured on a modified VG EscaLab spectrometer. The XPS had a base pressure of $< 1 \cdot 10^{-7}$ Pa and a specially designed load lock connected to an argon filled glove box. The load lock enabled the sample transfer from inert conditions directly into the instrument and vice versa, effectively preventing contamination of the sample. The used X-ray source provided radiation of the $K\alpha_1$ line of aluminum which was recorded by means of a Specs PHOIBOS 100 analyzer.

The μSR experiment and subsequent data analysis was carried out by Dr. Mattia Gaboardi and Prof. Dr. Mauro Riccó. Raw data acquisition of HRTEM, SAED, HAADF-STEM and EELS was carried out by Dr. Giovanni Bertoni. Data acquisition of SQUID magnetometry was performed by Dr. Mattia Gaboardi. All pcT, BET, XRD, Raman and XPS measurements presented in this chapter were conducted in the course of this thesis. All data analysis and discussion presented in this chapter was conducted in the course of this thesis if not otherwise stated.

3.3 Structural investigation

3.3.1 Crystallinity

X-ray powder diffraction measurements were conducted to determine to which degree the different samples show signs of crystallinity, possibly originating from layers of unexfoliated graphite oxide or metal crystallites larger than the detection limit. The XRD data of as-synthesized TEGO is presented in figure 3.3.

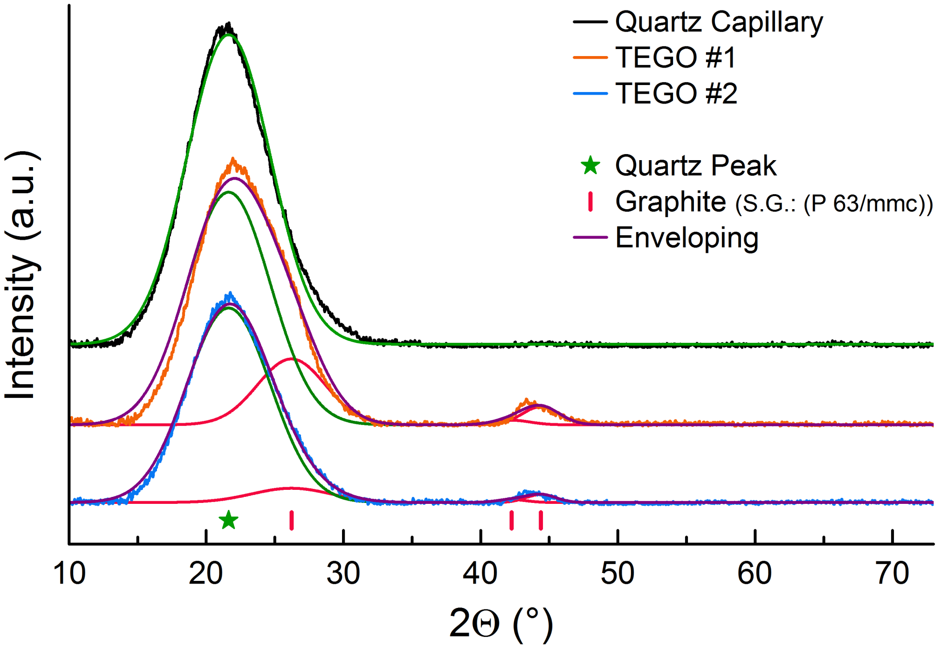

Figure 3.3: Normalized and y-axis shifted X-ray powder diffraction data of two separate batches of as-synthesized thermally exfoliated graphite oxide and a reference measurement of an empty 0.5 mm quartz capillary. Reflections of graphite are indicated by red bars [51]; The main peak of the quartz capillary is indicated by a green star.

The broad peak around $2\Theta = 21°$ originates for the most part from the quartz capillary and naturally shows up in all recorded patterns. For remaining multilayers of unreacted graphite oxide (GO) or graphite (G) reflections from the out-of-plane stacking of planes in the [002] direction are expected. These phases are known to be around $2\Theta_{GO} \approx 10 - 15°$ and $2\Theta_G \approx 26°$ respectively [50, 49]. While no graphite oxide phase is detectable, a minute shoulder on the broad $2\Theta = 21°$ quartz peak can be identified. Decomposition of this peak, by fitting a reference measurement of an empty capillary and using the same center and FWHM, unravels a broad, low intensity, reflection at 26°. An initial attempt was made to fit a Voigt profile, however, the Lorentzian contribution was negligible and for reasons of simplicity it was decided to solely fit the

XRD data with Gaussian functions. Besides the most prominent reflection in the graphite spectrum, from the out-of-plane periodicity, graphite patterns show reflections for the in-plane periodicity, two of which can be seen around 42.3° and 44.4° in figure 3.3. While the out-of-plane distance fits well to literature values, the in-plane distances are altered and thus the corresponding reflections are shifted. The shifts result from the high density of defects of the synthesized TEGO and naturally hamper the quality of any single curve fit. The overall intensity of the measured data is limited by the small scattering volume, the low degree of order and the weak X-ray reflection of the light carbon atoms. However, the (002) reflection are dominant enough to not only take it as proof of the existence of graphite but also to do a rough estimation of the mean size of the ordered domains, i.e. the average number of layer repetitions. An important equation in crystallography is the Scherrer equation which can be used to determine the size of particles, crystallites and ordered domains. The equation can be written as:

$$L = \frac{K\lambda}{\beta \cos\Theta}, \tag{3.1}$$

where L is the mean size of the ordered domain, K is a dimensionless shape factor called Scherrer constant, λ is the wavelength of the incident radiation, β is the FWHM measured in radians (after subtracting instrumental broadening) and Θ is half the scattering angle of the investigated reflection. Applying equation 3.1 to the results for sample #1 and #2, with a fitted $FWHM_{\#1\,(002)} = 5.82°$ and $FWHM_{\#2\,(002)} = 6.76°$, a Scherrer constant for graphite of $K_{\text{out-of-plane}} = 0.9$ and the Cu Kα radiation of wavelength $\lambda = 0.1541$ nm, an estimate for the thickness of $L \approx 1.59$ and 1.37 nm can be calculated respectively [105]. This corresponds to regions of roughly 4 – 5 layers thickness on average. The (100) and (101) planes share the same $FWHM$ and have been determined for both samples to $FWHM_{\#1\,(100)(101)} = 3.21°$ and $FWHM_{\#2\,(100)(101)} = 2.56°$. The Scherrer constant for these planes is $K_{\text{in-plane}} = 1.84$ with which the in-plane domain size can be estimated accordingly [105]. For the results of sample #1 and #2 the Scherrer equation yields average in-plane domain sizes of 5.2 and 6.5 nm respectively. The in-plane values,however, should be considered with care and it is important to note that a relatively large error for them is expected; not least due to the very low signal to noise ratio of the (100) and (101) reflections, large overlap and thus poor decomposition.

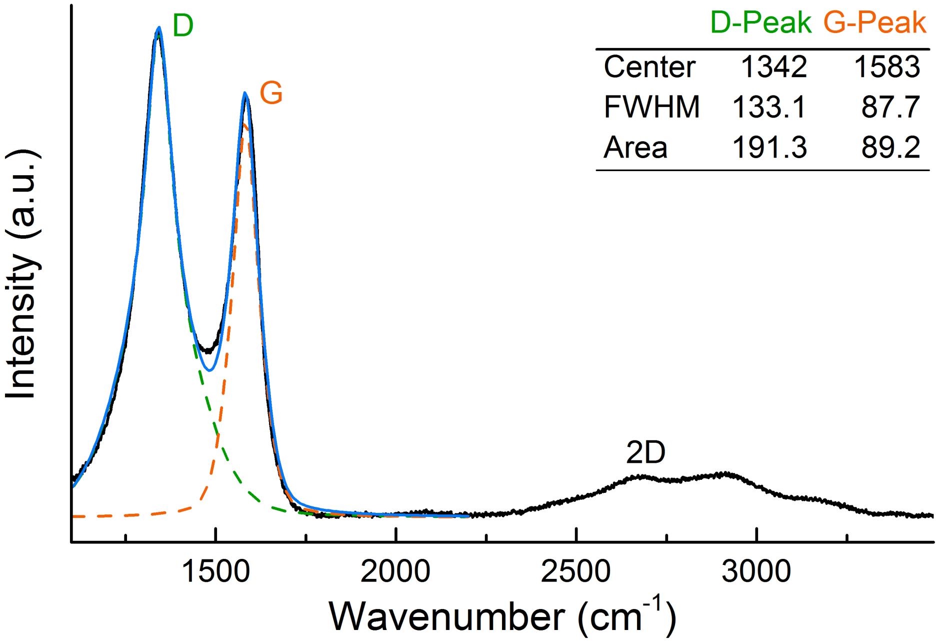

Figure 3.4: Normalized Raman spectrum of as-synthesised TEGO and a laser excitation wavelength of 532 nm. Fits of pseudo Voigt profiles for both D- and G-band are shown in green and orange dashed lines with the composed peak depicted as a solid blue line. Fit results are presented in a table in the top right corner. The figure is representative for all measured TEGO and metal decorated TEGO samples and only minor variations have been recorded.

Raman spectroscopy is a widely used technique to study the crystallinity of carbonaceous materials and can in addition be used to quantify the average sp^2 domain size. In the case of graphene and graphite the sp^2 domains correspond to the in-plain domains which have been previously estimated by means of XRD. The Raman spectrum of as-synthesized TEGO is shown in figure 3.4. The spectrum displays several notable features denoted as the D- (1350 cm^{-1}), G- (1580 cm^{-1}), D'- (1620 cm^{-1}) and 2D-band (2690 cm^{-1}) [21]. The G- and 2D-band, are both caused by induced in-plane vibrations, the latter as a second-order overtone of the D-Band. D- and D'-band are associated with structural defects and disorder and will be weak or vacant in spectra of highly crystalline graphite. Cançado et al. showed empirically that the inverse ratio of the integrated peak area of the D- and G-band, $(I_{\mathrm{D}}/I_{\mathrm{G}})^{-1}$, is proportional to the crystallite size L_a of nanographite materials. The relation can be written as [17]:

$$L_a(\mathrm{nm}) = 2.4 \cdot 10^{-10} \lambda_{\mathrm{laser}}^4 \left(\frac{I_{\mathrm{D}}}{I_{\mathrm{G}}}\right)^{-1}, \tag{3.2}$$

With an average ratio of $I_\mathrm{D}/I_\mathrm{G} = 2.1 \pm 0.2$ the calculated average sp^2 domains have a size of $L_a = 9.1 \pm 0.8$ nm. This is slightly larger than the domain sizes calculated by means of the Scherrer equation but still in excellent agreement considering the previously mentioned uncertainties of the XRD analysis.

Both X-ray powder diffraction as well as Raman spectroscopy are measurement techniques helpful in understanding bulk properties of the investigated materials. To solidify the morphological picture of a given sample it is oftentimes beneficial to study a small part of it with imaging techniques and compare the so gained local information with the bulk data to get a more comprehensive picture of the whole. Utilizing high resolution transmission electron microscopy very thin regions of relative order surrounded by a thicker interconnected network of disorder can be identify. The corresponding images can be seen in figure 3.5 (a). FFT of the central domain in figure 3.5 (c) shows sharp spots from a hexagonal ordered structure corresponding to the sp^2 graphene structure. The morphology and size of these graphene like ordered domains, highlighted in yellow in fig. 3.5 (b), varies significantly. However, the average diameter can be estimated and is roughly 6.5 ± 3.5 nm. This is in good agreement with the data collected by both Raman and XRD measurements. The out-of-plane periodicity of the entire region in figure 3.5 (a) can be probed using EEL spectrometry. Comparing the EEL spectrum in figure 3.6 with the profiles and plasmon positions published in literature a good agreement can be found with the results for $1-5$ layers of graphene. This stands again in excellent agreement with the results of the X-ray powder diffraction data. Like the XRD data these values are only an average measure of the thin/ordered and thick/disordered regions. Electron diffraction on selected areas (SAED) of the sample was performed to clarify if the ordered regions are indeed single layers of graphene. By analyzing the intensity ratio of a set of reflections as a function of incidence angle it is possible to estimate the thickness of the selected area under investigation. At a tilt of 0° and 20° between incident beam and normal a reflection intensity ratio of ≈ 1.5 and ≈ 1.4 was measured respectively. A ratio > 1 is believed to be a clear indication for single layer graphene and the fact that the intensity ratio does not strongly vary with the tilt angle is further proof that the ordered domains are indeed monolayers [47, 83].

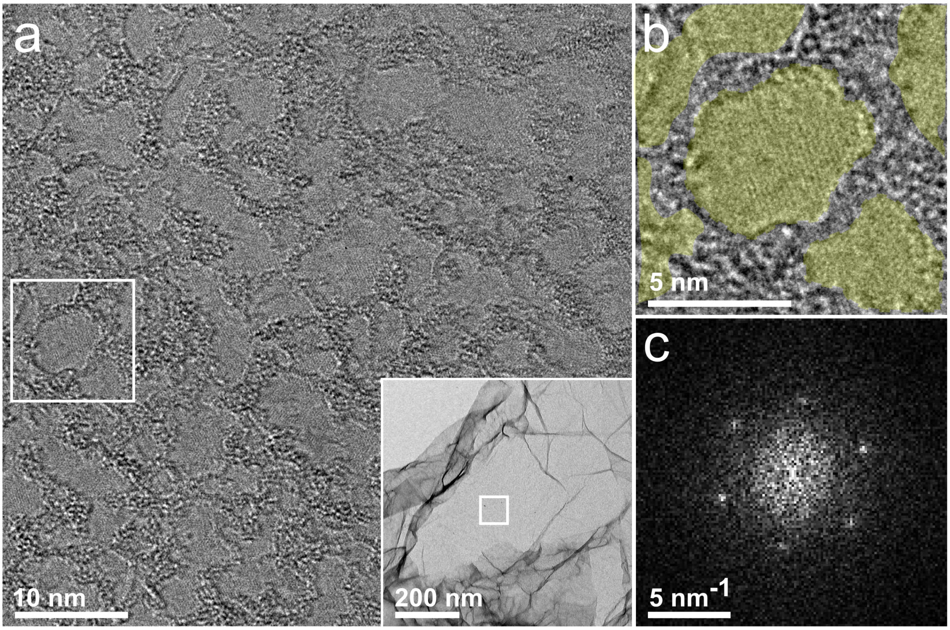

Figure 3.5: **(a)** HRTEM image, recorded with an 80 kV electron beam, of the flat region indicated in the inset. **(b)** Magnified image of the region indicated in (a). The ordered regions are highlighted in yellow and consist of sp^2 domains. **(c)** FFT of the centered domain in (b). The sharp spots originate from the hexagonal crystal structure of graphene.

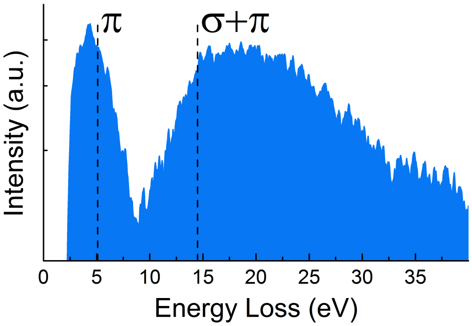

Figure 3.6: Average EEL spectrum of the whole region in figure 3.5 (a) after background subtraction. Literature values for the π and $\sigma + \pi$ plasmon locations are indicated by dashed lines [72, 33]. The superposition of signal from single layer areas and the thicker unordered network gives an average spectrum comparable to the results for 1-, 2- and 5-layers of graphene as published by Eberlein et al. [33].

Metal decoration of TEGO samples leads to the formation of very different metal phases depending on the synthesis parameters while no evidence for an altered TEGO structure was found. Three different types of lithium decorated and equally many nickel decorated graphene samples were synthesized as described in section 3.2.1. The corresponding X-ray data is shown in figure 3.7 (Li-TEGO) and 3.8 (Ni-TEGO). The decoration with lithium and subsequent sample handling proved challenging and all samples that have been investigated showed traces of oxidation and the formation of different undesired phases. Depicted in figure 3.7 Li_2O (S.G.: $(Fm\bar{3}m)$), $Li_2(CO_3)$ (S.G.: (C2/c)), Li (S.G.: $(Im\bar{3}m)$) and LiOH (S.G.: (P4/nmm)) reflections are marked for the different Li-TEGO samples. As a result of the strong signals for oxide phases it was decided against further investigation of the interaction with hydrogen of these samples.

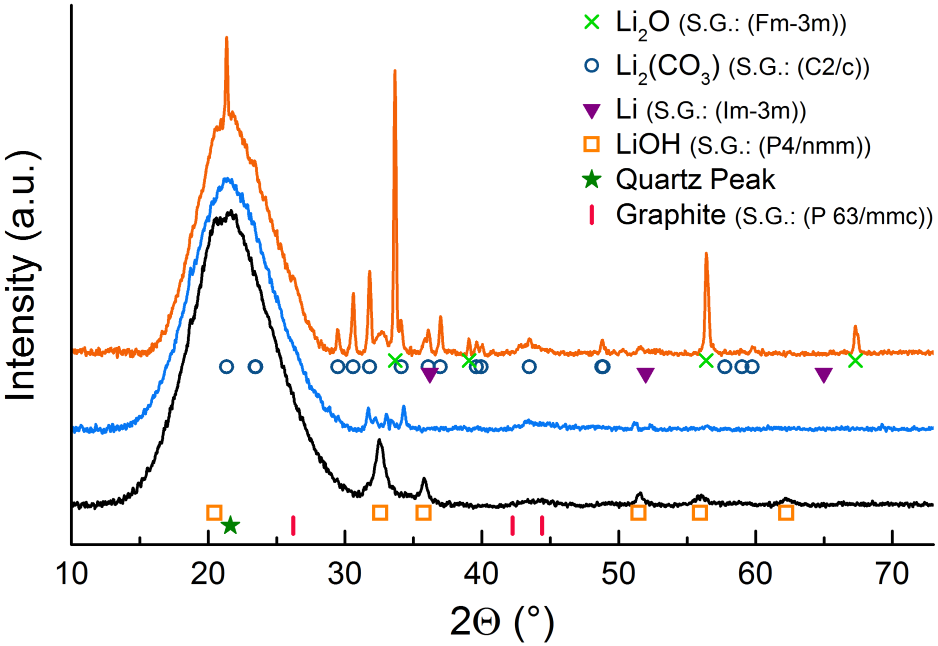

Figure 3.7: Normalized and y-axis shifted X-ray powder diffraction data of three different batches of Li-TEGO. Very strong and defined reflections can be assigned to various oxide phases. Reflections of Li_2O (light green x, [147]), $Li_2(CO_3)$ (dark blue circles, [55]), Li (violet triangles, [84]), LiOH (orange rectangles, [76]) and graphite (red bars, [51]) are indicated by their respective symbols; The main peak of the quartz capillary, as determined in figure 3.3, is indicated by a green star.

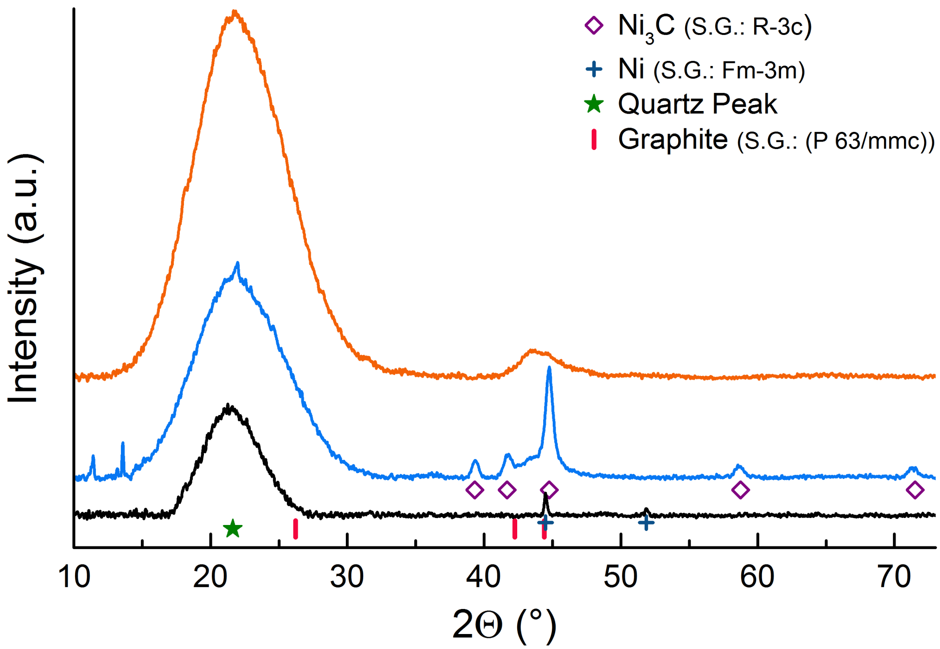

Figure 3.8: Normalized and y-axis shifted X-ray powder diffraction data of three different batches of Ni-TEGO. While for the batches depicted in black and blue crystalline phases can be assigned, the orange Ni-TEGO does not show any sharp reflections. The latter was later used for the investigation of hydrogen interaction. Reflections of Ni_3C (violet diamonds, [85]), Ni (dark blue pluses, [115]) and graphite (red bars, [51]) are indicated by their respective symbols; The main peak of the quartz capillary, as determined in figure 3.3, is indicated by a green star.

For the Ni-TEGO samples two separate phases could be identified, a cubic fcc nickel phase with the space group $Fm\bar{3}m$ and, in a different sample, a nickel carbide phase of the space group $R\bar{3}c$. No mixed phases or traces of strong oxidation could be detected and the last batch, drawn in orange in figure 3.8, shows no evidence of large periodic structures. The absence of impurity phases was a strong reason to select this sample for further investigation and later on for the study of the interaction with hydrogen. In the cause of studying the metal decoration HAADF-STEM images were recorded. HAADF-STEM has the advantage of a large contrast between elements of varying atomic number Z due to a proportionality of the signal to $\approx Z^2$. The HAADF-STEM image in figure 3.9 (a) clearly indicates metal decoration in the form of particles in the nanometer regime. Bright field HRTEM images of single nanoparticles can be seen in figure 3.9 (c) and (d). Subsequently FFT was performed on selected regions of these NPs which uncovered reflections compatible with cubic fcc structure and S.G.:$Fm\bar{3}m$. It should be noted that the particles did not show up in the XRD pattern of the same sample shown in orange in figure 3.8. The absence of signal in XRD is most likely caused by the very low nickel concentration in the sample, such that broad reflections caused by nanoparticles will not be visible over the superimposed data of the capillary and TEGO. The statistical analysis of the particle diameter shown in figure 3.9 (b) was performed on about 350 particles recorded in different regions with HAADF-STEM. The average diameter is $\bar{d}$ = 17 nm and has a standard deviation of σ = 4 nm. Figure 3.9 (e) and (f) depict EEL spectra of a nickel nanoparticle of 20 nm diameter. The C-K and Ni-$L_{2,3}$ ionization edges, originating from the underlying TEGO and the particle itself, are clearly visible. No traces of possible nickel oxidation can be detected. The fine structure of the Ni-$L_{2,3}$ ionization edge (Fig. 3.9 (f)) equals that of metalic fcc nickel and compares through all collected spectra of different Ni NPs [11, 37].

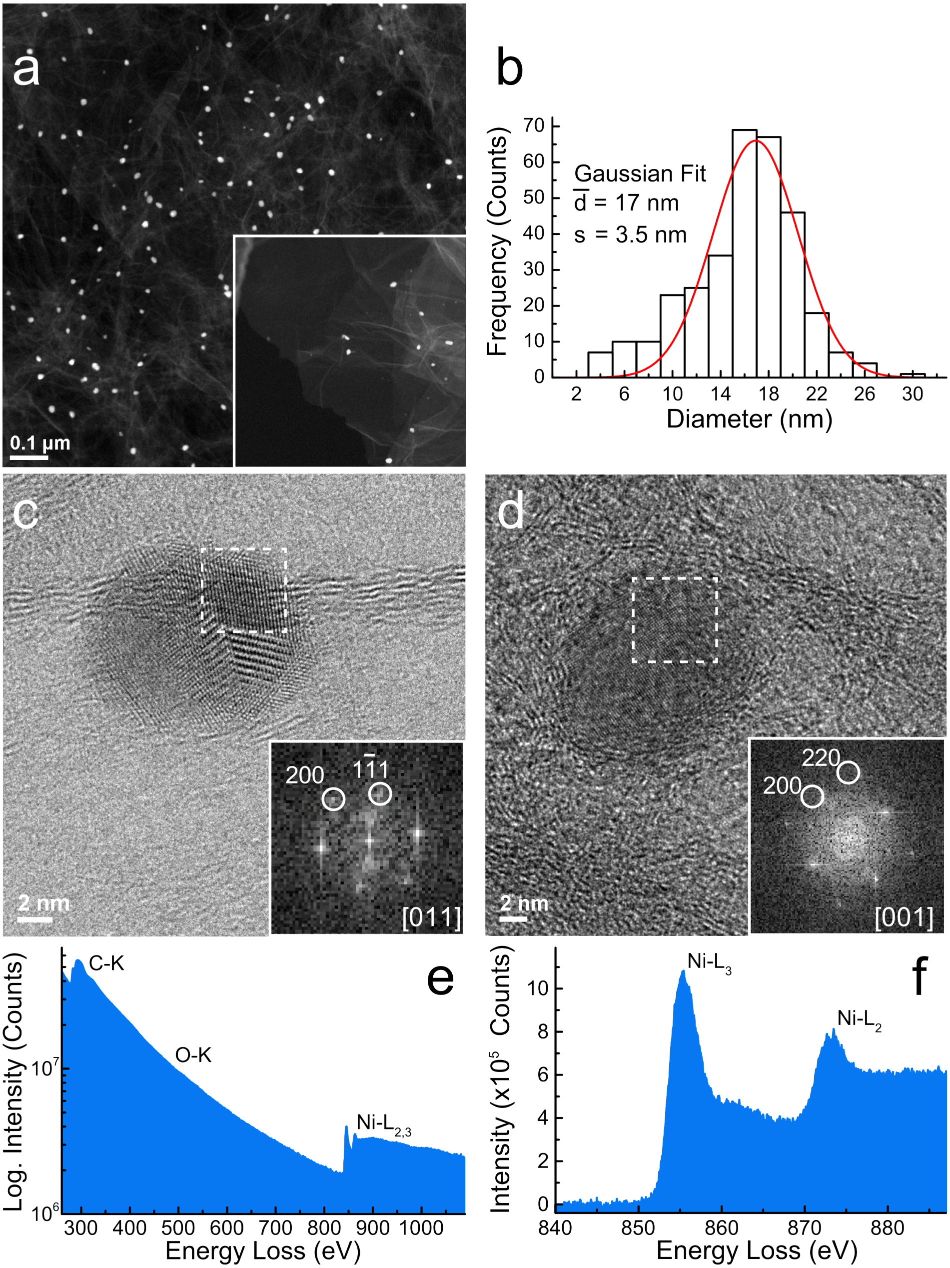

Figure 3.9: **(a)** HAADF-STEM image of Ni-TEGO. The Ni-NPs ($Z = 28$) show up bright before dark TEGO background of carbon ($Z = 6$). The inset shows an image of a single layer graphene region. **(b)** Particle size distribution of about 350 Ni NP that have been measured in several STEM images. **(c)** and **(d)** show representative HRTEM images of nickel NPs. The insets show FFTs of the marked regions with fcc reflections. **(e)** EEL spectrum of a Ni NP on TEGO with the C-K and Ni-$L_{2,3}$ ionization edges of the TEGO and nickel respectively. Note the absence of a O-K ionization edge. **(f)** Background subtracted EEL spectrum of the Ni-$L_{2,3}$ ionization edge. The profile is compatible with metallic fcc nickel reported in literature [11, 37].

3.3.2 Chemical composition

Naturally not all types of chemical impurities show up in X-ray diffraction patterns for reasons of quantity, lack of order or simply because the signal is to weak. The conducted Raman spectroscopy shows only Raman active species and the utilized microscopic techniques are local measurements that lack universality. X-ray photoelectron spectroscopy on the other hand is a well suited method to detect possible surface impurities and can furthermore be applied to study the composition of the first few nanometers of irradiated materials, in particular metal decorated graphenes with their few nanometer thin surface like structure. XPS, the sample preparation and the experimental conditions are described in section 2.2.2.

Data analysis was done using CasaXPS, a standard software and commonly used for XPS analysis. A Shirley algorithm background was subtracted. This type of background shows a dependent intensity that is, at any given binding energy, proportional to the intensity of the total area under the peak from the current binding energy to lower binding energies and is one of the most generally used backgrounds for XPS data analysis. All peaks, besides the main feature in the carbon 1s peak (description below), were fitted by a symmetric 70 % Gaussian and 30 % Lorentzian product function (GL(30)). In principle the Gaussian contribution accounts for the measurement process (i.e. instrumental response, x-ray line-shape, Doppler and thermal broadening) while the Lorentzian contribution accounts for the natural broadening due to the variation in lifetime of the different ejected electrons [129].

An as-synthesized TEGO sample served as the basis for the investigation of the metal decorated samples and a full survey scan can be seen in figure 3.10. The relative atomic concentrations (%At Conc.) have been calculated with CasaXPS and are a measure of the integrated area under the peaks (C 1s, O1s etc.) weighted by their corresponding relative sensitivity factors (R.S.F.). A carbon content of 97 %At Conc. and only about 3 %At Conc. of oxygen are excellent values for thermally exfoliated graphite oxide and indicate the good deoxygenation of the synthesis. When taking a closer look at the carbon 1s peak an asymmetry towards higher binding energies can be seen. This is typical for samples with a high sp^2 content and has a strictly physical origin. In short, when an x-ray photon is absorbed in a material it will not only be able to excite the electronic but also the atomic structure, for instance by means of induced vibrations. This is the basis of many spectroscopic techniques such as Raman and IR-spectroscopy. In x-ray photoelectron spectroscopy this induced vibrations will alter the line shape of the photoelectron peak. The kinetic energy of an ejected photoelectron is therefore not only determined by the energy lost by exciting the electron out of its initial core level state but can also be influenced by the energy loss of the photon caused by induced atomic or molecular oscillations and vibrations. Consequently, the ejected photoelectron will have less kinetic energy and thus be registered at higher binding energies. One finds, that while sp^2 carbon will cause a broad, asymmetric tail towards higher binding energies sp^3 and functionalized carbon will show a more symmetric line-shape [4]. This asymmetry was addressed by adding a tail modification to the GL(30) line-shape of the main feature of the C1s peak, denoted CC peak in the corresponding figures. A detailed description of the Gaussian and Lorentzian product function and the tail modifier function (T) can be found elsewhere [129]. The tail modification for all CC peaks was modest and of the form GL(30)T(1.6).

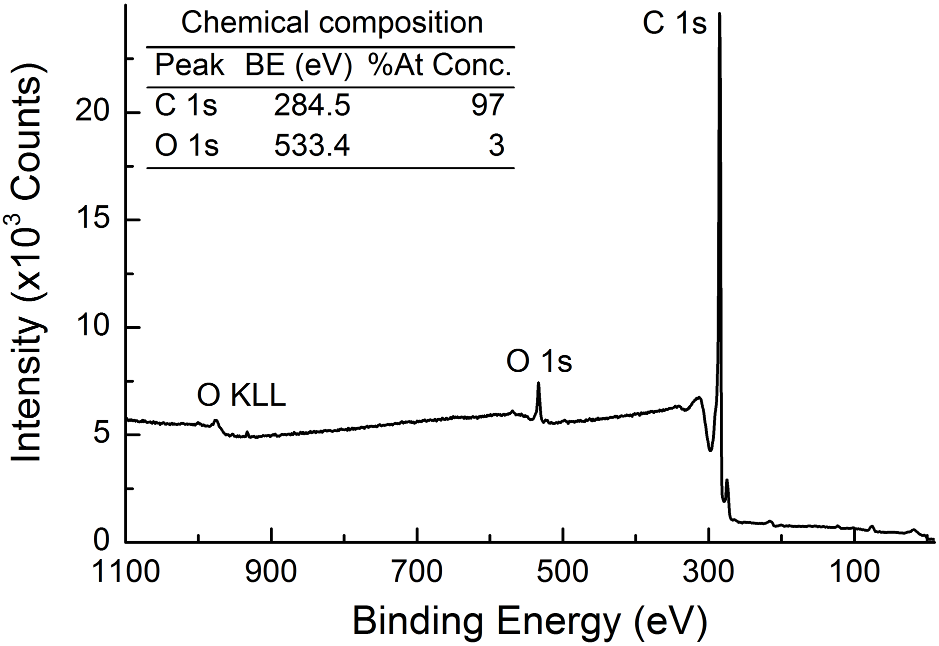

Figure 3.10: Full survey spectrum of as-synthesized TEGO with indicated peak positions of the different detected elements. In the top left corner a quantification table is depicted, indicating the binding energies of the main peaks and the relative atomic concentration of the corresponding elements. Minute peaks from the copper sample holder can be seen but account for far less than 1 %At Conc. and have therefore been neglected.

The combined fit of the carbon 1s spectrum of TEGO is presented in figure 3.11. Three components are necessary to model the peak and the largest, slightly asymmetric, is the above mentioned CC peak. CC consists mainly of contributions from sp^2 bound carbon with a weak contribution, at slightly higher binding energies, from sp^3 carbon (lattice defects). Due to the broadness of the peak and the small contribution of sp^3 a deconvolution is not feasible.

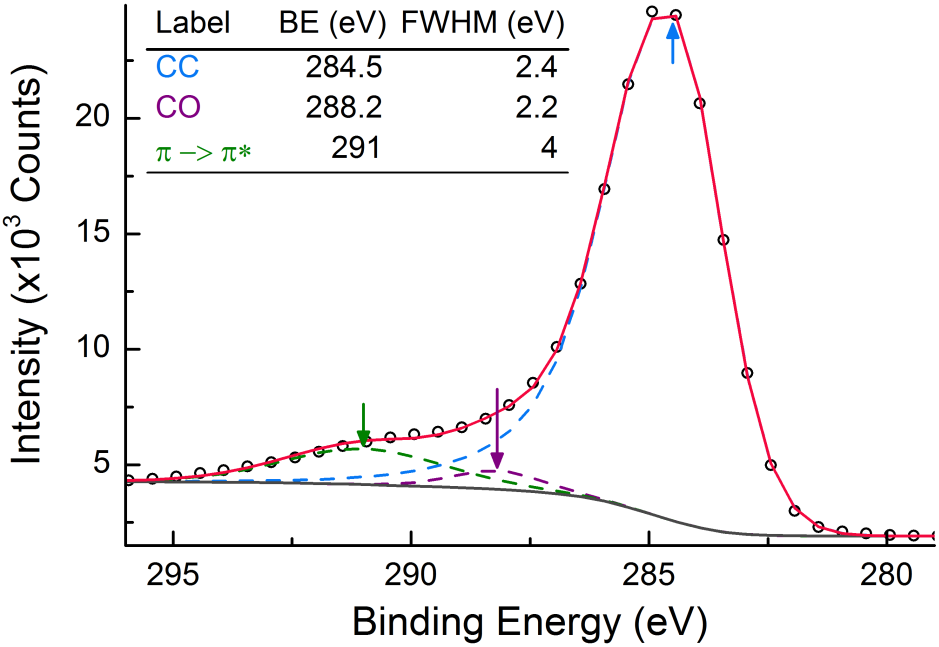

Figure 3.11: Fitted XPS of the C 1s peak of as-synthesized TEGO. In the top left corner a table denotes the proposed peak origin and the center and FWHM of the corresponding fits. The fitted components are depicted in dashed lines, the colors correspond to the labels in the table, centers are marked by arrows.

The survey spectrum was calibrated such that this peak centers at 284.5 eV, a typical literature value for the carbon-carbon bond in graphite and graphene systems [135, 102, 19]. The peak centered at 288.2 eV, denoted as CO, is shifted from CC to higher binding energies. The intensity ratio between CC at 284.5 and CO at 288.2 eV is as large as the relative atomic concentration between carbon and oxygen and CO can therefore be safely assigned to carbon bound to oxygen atoms. The generally higher FWHM of CO is an indication that the peak is a convolution of multiple smaller peaks since different contributions from different types of carbon-oxygen bonds, with slightly different chemical shifts, are to be expected. Literature draws a rather controversial picture on specific peak assignments but it is generally agreed that for higher temperatures during exfoliation and annealing, comparable to temperatures used to synthesize the here discussed samples, certain impurities and defects heal out. A. Ganguly et al. for example interpret their high resolution XPS data on the thermal deoxygenation of graphene oxide by a generally healed graphene sheet with evidence for oxygen bound to aromatic carbon by phenol groups (C-OH) around 286 eV and carbonyl groups (>C=O) at ≈ 288 eV [40]. The last fitted peak in the C 1s spectrum centers around 290.7 eV and can be identified as the $\pi \rightarrow \pi*$ transition (shake-up).

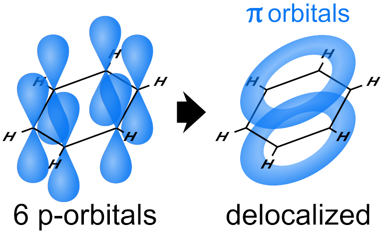

Figure 3.12: Schematic example of the hybridization of 6 p orbitals,in a benzene ring, forming a delocalized π conjugation. The delocalized π electrons cause a shake-up signal in XPS spectra at B.E..

The signal is a result of the change in kinetic energy of the C 1s photoelectrons after inelastic scattering. Subsequent to a loss in kinetic energy the photoelectron will be registered at seemingly higher binding energies. As the name suggests the scattering excites an electron from the bonding π orbital to the antibonding $\pi*$ orbital and is hence only of relevance in systems with overlapping sp^2 orbitals. The intensity of the shake-up peak is naturally related to the amount of scattering centers, i.e. the amount of π orbitals, and particularly pronounced for delocalized π conjugated systems with their connected p-orbitals and delocalized electrons. Figure 3.12 shows a model of the hybridized p-orbitals of benzene and a visualization of their overlap, causing the electrons to become delocalized in a conjugated state. A well detectable shake-up signal in thermally exfoliated graphite oxide is hence a qualitative measure for the quality and crystallinity of the sheets.

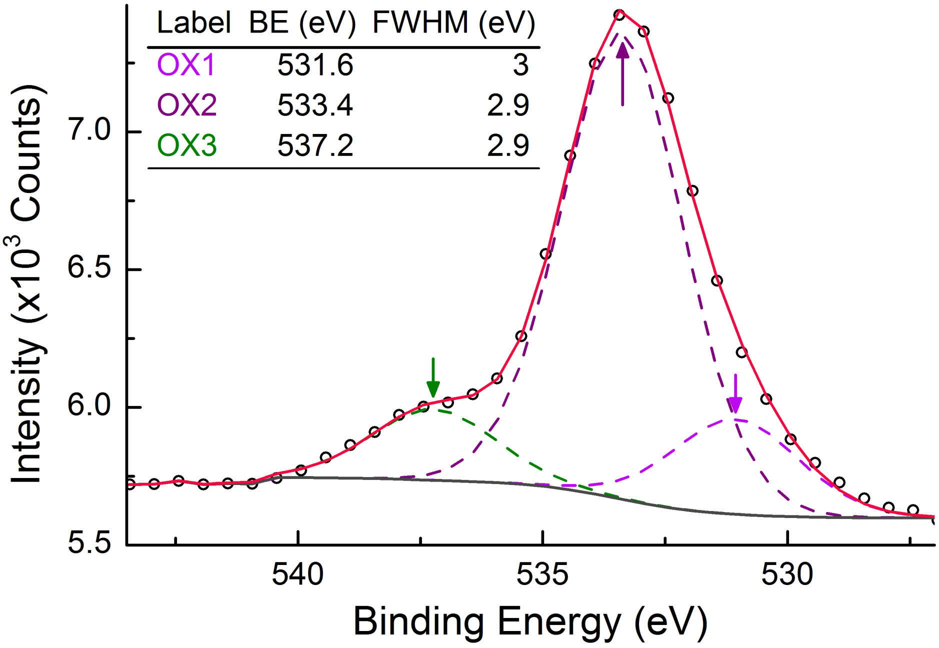

Label	BE (eV)	FWHM (eV)
OX1	531.6	3
OX2	533.4	2.9
OX3	537.2	2.9

Figure 3.13: Fitted XPS of the O 1s peak of as-synthesized TEGO. Three peaks are needed to fit the data satisfactory. The centers, marked by arrows, and FWHM of the GL(30) line-shapes are located in a table in the top left corner.

Figure 3.13 shows the oxygen 1s spectrum of TEGO. O 1s can be modeled by three distinct features denoted OX1, OX2 and OX3 which are centered at 531.6, 533.4 and 537.2 eV respectively. According to the previously mentioned carbonyl and phenol groups, located in the O 1s spectrum at 531.1 eV and 533.4 eV [40], one can assign OX1 and OX2 to oxygen bound in carbonyl and phenol groups respectively [4]. While the CO peak, around 288 eV, indicates a larger fraction of carbon doubly bond to oxygen in carbonyl groups the main feature in the O 1s peak is OX2, so the oxygen bound in phenol groups. The origin of this divergence between the two spectra is currently not known but a high resolution XP spectrum is most likely able to resolve this question. The third feature in the O 1s spectrum, OX3, is centered at an unexpectedly large chemical shift of about 6 eV above OX1. Such a high chemical shift is puzzling in particular since no other elements than carbon and oxygen have been registered in the survey spectrum. However, the 6 eV shift correspond precisely to the 6 eV shift recorded for the $\pi \rightarrow \pi*$ transition in carbon and hence it is possible, that the photoelectrons, modeled by OX3, originate from inelastic scattering on the bonding π orbital of carbon, analogous to the shake-up peak seen in the C 1s spectrum. All modeled species in the TEGO O 1s peak appear with a broader FWHM than the ones reported for the carbon peak. This is a physical response since as the binding energy gets higher there are more available states, with lower binding energies, that the ejected photoelectron can scatter on, thus, broadening the peaks.

Besides the as-synthesized TEGO a lithium and a nickel decorated graphene sample was selected for further investigation. The chosen samples correspond to the top most lines depicted in orange in the figures 3.7 and 3.8. In the survey spectrum, shown in the top of figure 3.14, the elemental concentrations for lithium, carbon, nitrogen and oxygen of Li-TEGO are depicted. While a small Cu 2p peak can be seen at a binding energy of 932 eV, caused by a minute part of the copper sample holder not covered by the sample pallet, much less than 1 %At Conc. are observed. This is below the expected error and not further relevant for the analysis. The detection of nitrogen in the spectrum is a clear indicator that the annealing of lithium azide ($Li\text{-}N_3$), used during metal decoration, was not fully successful. Moreover an oxygen content of about 9 %At Conc. is another obvious indication for an unsatisfying synthesis and, in addition to the evidence gathered with XRD, this lead to the disregarding of this sample in context of the investigation with hydrogen.

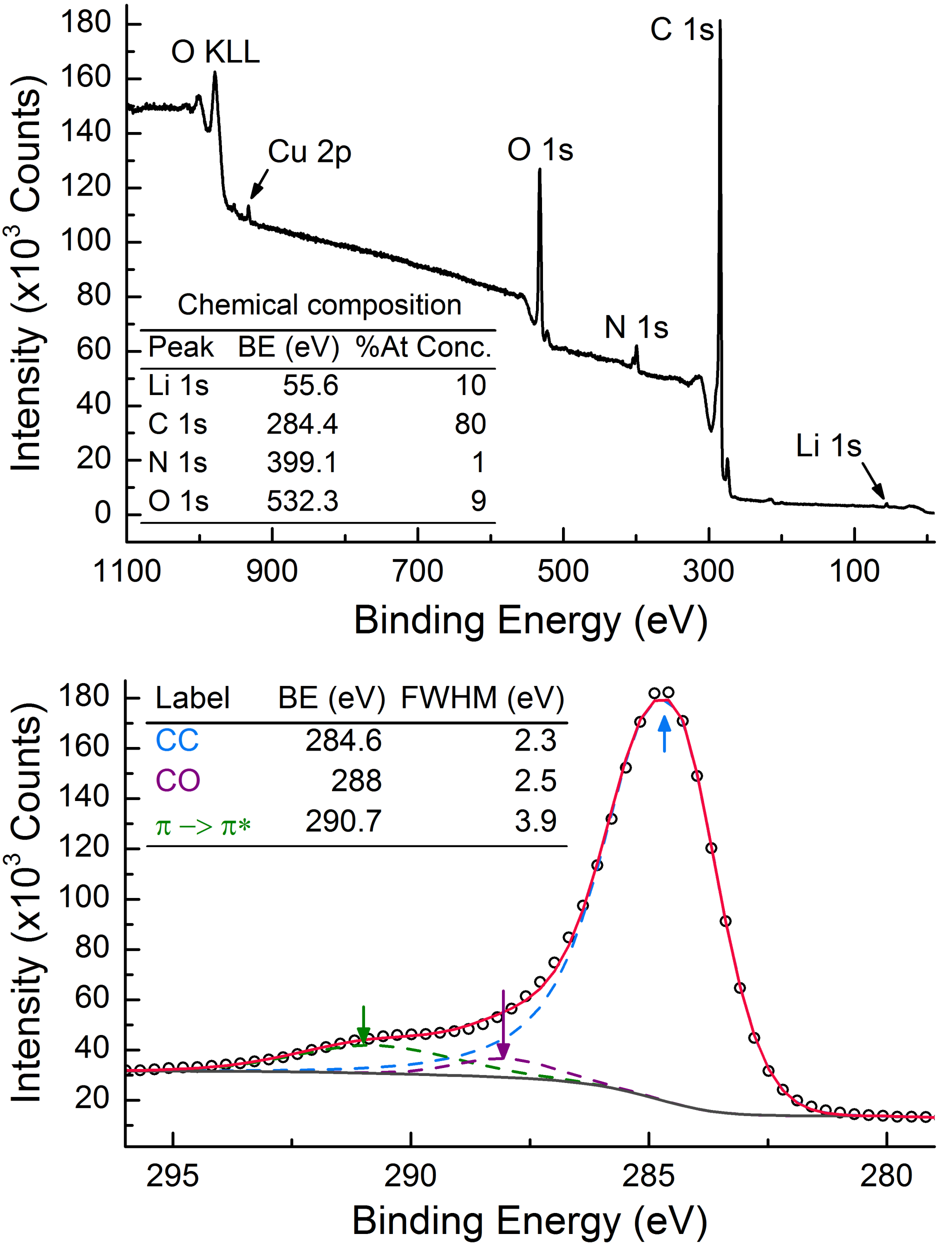

Figure 3.14: **(top)** Full survey spectrum of lithium decorated graphene with indicated peak positions of the different detected elements. In the lower left corner a quantification table is depicted, indicating the average binding energies of the peaks and the relative atomic concentration of the corresponding elements. **(bottom)** Fitted XPS of the corresponding C 1s peak. The centers, marked by arrows, and FWHM of the fitted line-shapes are located in a table in the top left corner. The fitted features are depicted in dashed lines, the colors correspond to the labels in the table.

Figure 3.14 (bottom) shows the C 1s, figure 3.15 the O 1s XPS spectrum of Li-TEGO and their corresponding proposed fits. The modeling was done in analogy to the above described spectra of TEGO and for the C 1s peak the same three component model fits very well. In contrast to the previously discussed O 1s peak of TEGO, the O 1s peak of Li-TEGO appears as one broad feature without the distinguished shoulder at higher binding energies that can be seen for TEGO. Applying the same 3 component fit will not model the peak and a large additional feature was needed to appropriately characterize the peak. The peak is denoted OLi in reference to its possible origin from oxygen bound to lithium. As has been seen in the XRD pattern of this sample oxidized lithium was detected in different species and thus OLi is most likely a superposition of the different contributions. The relative intensity of OLi compared to the other components of O 1s indicates that most oxygen is bound to lithium and not to the TEGO backbone. Nitrogen and lithium have been fitted with a single Gaussian-Lorentzian product function GL(30) and the graphs can be found in figure 3.16(a) and 3.16(b).

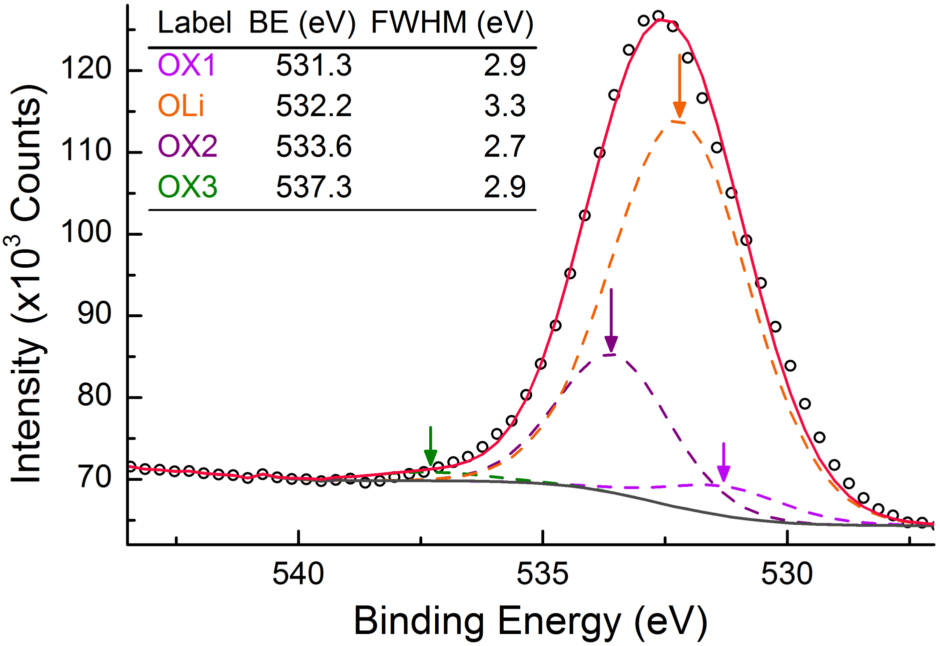

Figure 3.15: Fitted XPS of the O 1s peak of Li-TEGO. The center, marked by an arrow, and FWHM of the GL(30) line-shape is denoted in a table in the top left corner.The fitted features are depicted in dashed lines, the colors correspond to the labels in the table.

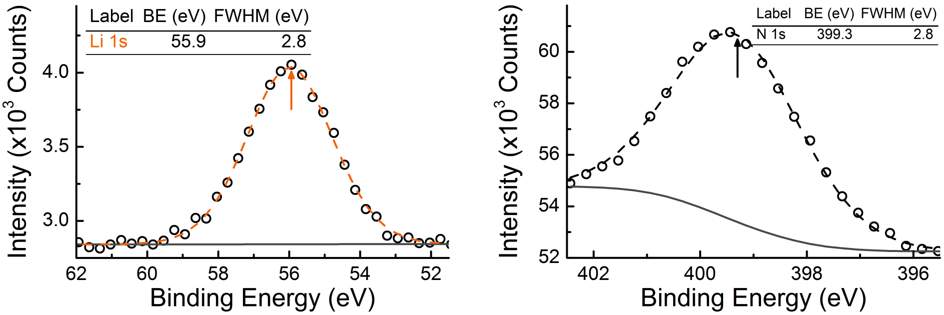

(a) (b)

Figure 3.16: Fitted XPS of the Li 1s peak **(a)** and the N 1s peak **(b)** of Li-TEGO. The centers, marked by arrows, and FWHM of the GL(30) fits are denoted in corresponding tables.

Nickel decorated graphene can be studied accordingly and a survey scan is depicted in the top of figure 3.17. Neither a signal for the copper sample holder, nor for nitrogen can be detected. The latter is not surprising since no nitrogen was used during synthesis, but $Ni(acac)_2$, and the lack of copper in the spectrum is evidence for the full coverage of the sample holder by the pelleted Ni-TEGO. The calculated relative abundance of oxygen is with 5 %At Conc. low compared to metal decorated TEGOs commonly reported in literature [61, 40, 75]. Unlike the Li-TEGO O 1s peak the oxygen signal of Ni-TEGO can again be modeled by the same three components that were used for TEGO. However, the C 1s peak can not be fitted by the previously discussed three components and at least one additional line-shape is necessary as can be seen in the bottom of figure 3.17. The origin of this component, defined as CX, becomes apparent when investigating the nickel signal in the Ni 2p peak (see bottom figure 3.18). Ni 2p is a doublet peak and shows up as Ni 2p 1/2 and 2p 3/2 due to spin-orbit splitting. The center of the nickel 2p doublet is shifted to higher binding energies and a two component fit for the 2p 3/2 peak is presented in the bottom of figure 3.18, with one component centered at the expected position for nickel and the other one shifted to higher binding energies, related to $Ni(acac)_2$ [29]. This explains not only the shift to higher B.E., compared to pure nickel, but additionally accounts for the CX feature in the C 1s spectrum. Thus, residual nickel acetylacetonate could be responsible for the differences measured between the TEGO and Ni-TEGO sample and consequently it appears, that there are small amounts of residual, unreacted, $Ni(acac)_2$ present in the sample. For hydrogen sorption measurements the samples were baked out under vacuum, above 425 K for more than 12 h. It is thus feasible to believe that after the bake-out the measured traces of $Ni(acac)_2$ decomposed.

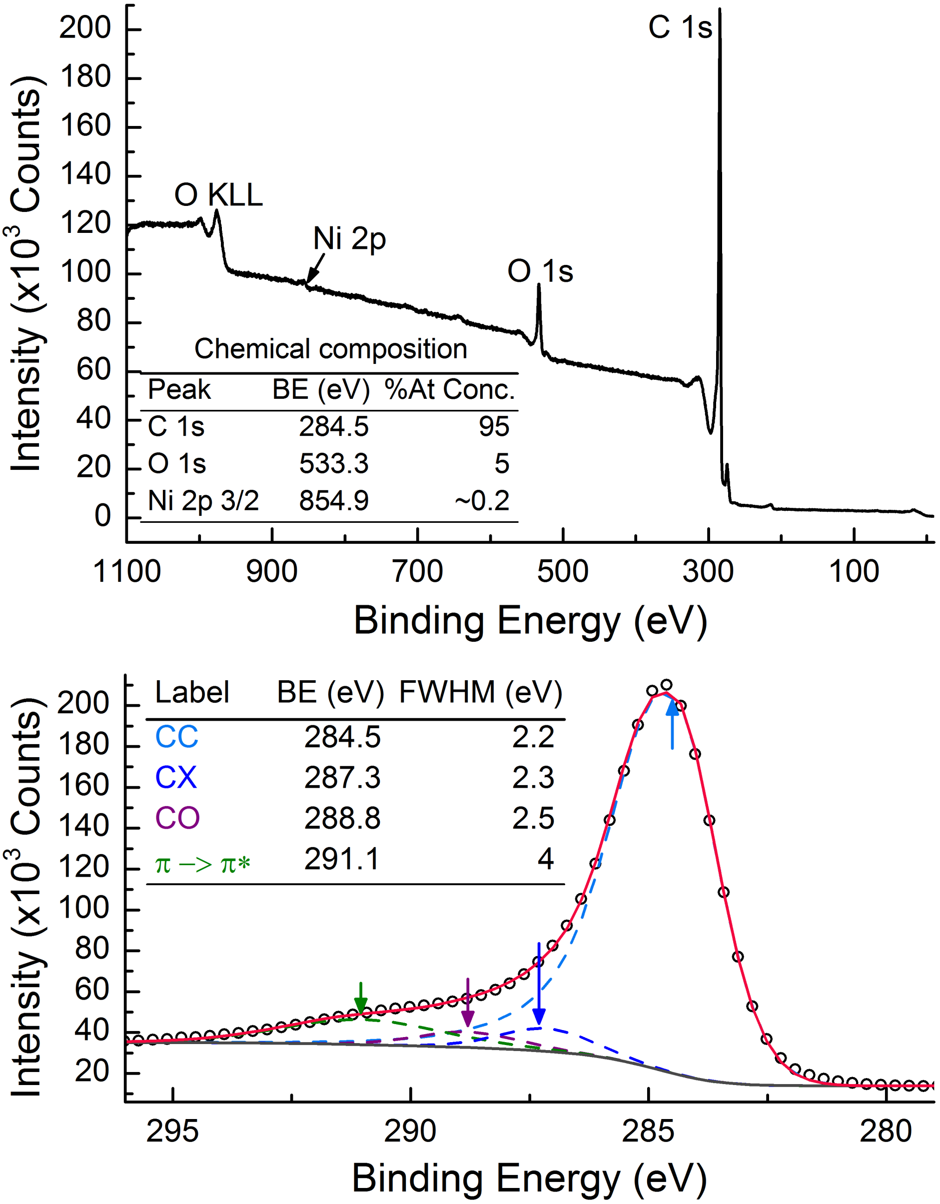

Figure 3.17: **(top)** A full survey spectrum of nickel decorated graphene with indicated peak positions of the different detected elements. In the lower left corner a quantification table is depicted, indicating the average binding energies of the peaks and the relative atomic concentration of the corresponding elements. **(bottom)** Fitted XPS of the C 1s peak of Ni-TEGO. In contrast to the C 1s peak of TEGO and Li-TEGO four components are necessary to model the peak. In the top left corner a table denotes the proposed peak origin and the center and FWHM of the corresponding line-shapes. The fitted components are depicted in dashed lines, the colors correspond to the labels in the table, centers are marked by arrows.

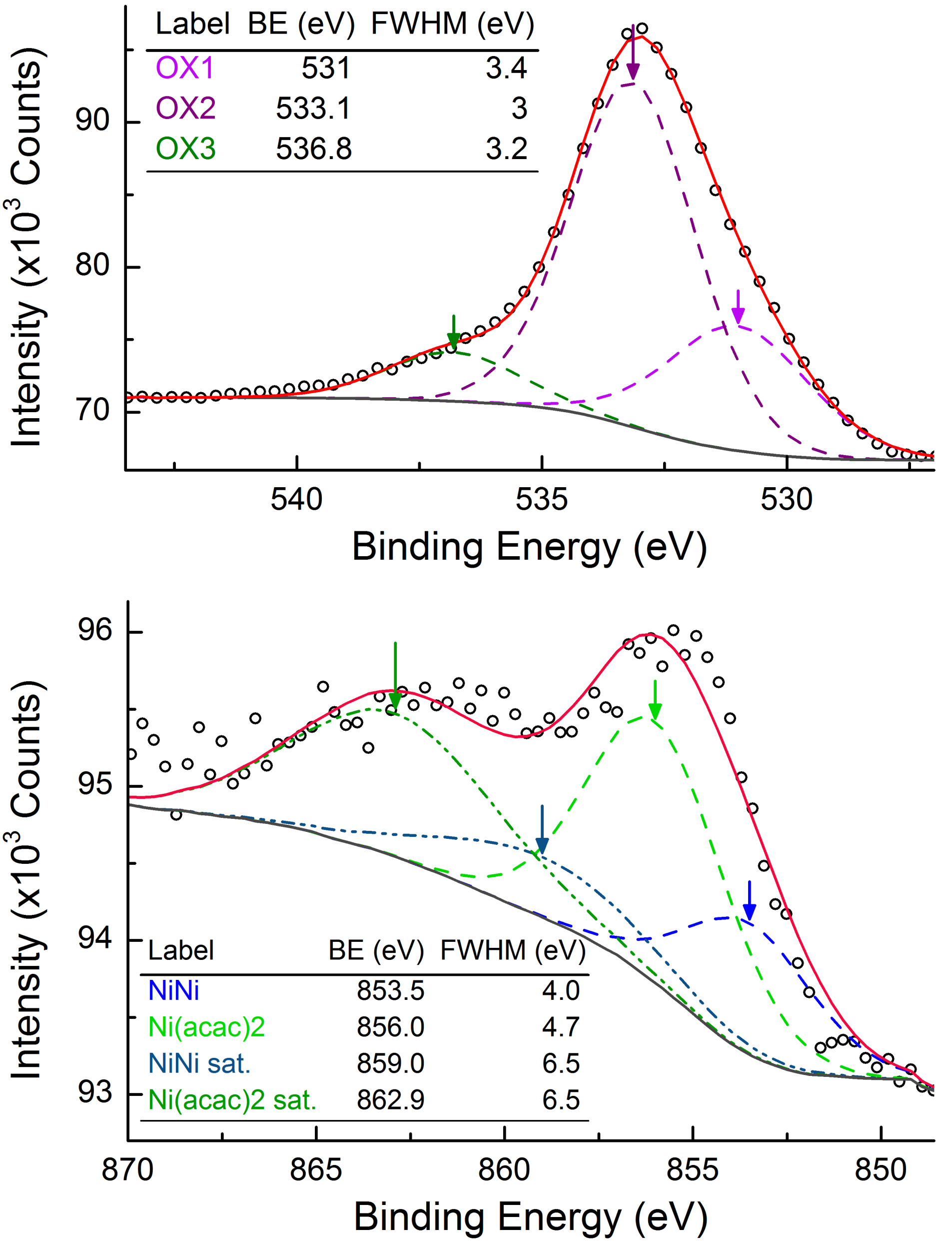

Figure 3.18: Fitted XPS of the O 1s (top) and the Ni 2p 3/2 (bottom) peaks of Ni-TEGO. The fitted components are depicted in dashed lines, the colors correspond to the labels in the tables where the centers, marked by arrows, and FWHM of the fitted line-shapes are denoted. **(top)** In contrast to the O 1s peak of Li-TEGO, and in accordance with the TEGO sample, three components are needed to fit the data satisfactory. **(bottom)** Ni 2p 3/2 component of Ni-TEGO. The fitted components for nickel and Ni(acac)$_2$ are depicted in dashed blue and green lines respectively. For their satellite peaks dashed-dotted lines in different blue and green shades are used.

Table 3.1: *Summary of the XPS C 1s peaks of TEGO, Li-TEGO and Ni-TEGO. All fitted features are denoted with their binding energies (B.E.), the line-shapes used in CasaXPS, the FWHM of the line-shapes and their relative concentration (Rel.Conc.).*

		Carbon 1s peak			
		CC^a	CX^b	CO^c	$\pi \rightarrow \pi *$
TEGO	B.E. (eV)	284.5		288.2	291.0
	Line-shape	GL(30)T(1.6)		GL(30)	GL(30)
	FWHM	2.4		2.2	4.0
	Rel. Conc. (%)	89		3	8
Li-TEGO	B.E. (eV)	284.5		288.0	290.8
	Line-shape	GL(30)T(1.6)		GL(30)	GL(30)
	FWHM	2.3		2.5	3.9
	Rel. Conc. (%)	88		4	8
Ni-TEGO	B.E. (eV)	284.5	287.3	289.4	291.4
	Line-shape	GL(30)T(1.6)	GL(30)	GL(30)	GL(30)
	FWHM	2.2	2.1	2.6	4.0
	Rel. Conc. (%)	85	5	4	6

[a]: CC can be assigned to carbon in sp^2 and sp^3 configuration. The sp^2 fraction clearly dominates, as has been indicated by EELS and Raman, leading to an asymmetric tail towards higher binding energies. This has been accounted for by a tail modifier of the form GL(30)T(1.6). When used to quantify chemical states, the need to calibrate the intensity of asymmetric line-shapes becomes important. TEGO was used as a calibration for the other samples.

[b]: CX most likely models carbon bound in residual Ni(acac)$_2$ as it has not been observed in any other sample and a corresponding feature can be seen in the nickel peaks [29].

[c]: CO can be assigned to carbon bound to oxygen in carbonyl and phenol groups. Due to the low oxygen content the peak appears weak and constitutes generally for only about 4% of the C 1s intensity. It is not feasible to model the different oxygen species separately in the C 1s peak.

Table 3.2: *Summary of the XPS O 1s peaks of TEGO, Li-TEGO and Ni-TEGO. The nomenclature is analogous to that used in table 3.1.*

		Oxygen 1s peak			
		OX1[a]	OLi[b]	OX2[c]	OX3[d]
TEGO	B.E. (eV)	531.1		533.4	537.2
	Line-shape	GL(30)		GL(30)	GL(30)
	FWHM	3		2.9	3
	Rel. Conc. (%)	16		73	11
Li-TEGO	B.E. (eV)	531.3	532.2	533.6	537.3
	Line-shape	GL(30)	GL(30)	GL(30)	GL(30)
	FWHM	2.9	3.3	2.7	2.9
	Rel. Conc. (%)	5	73	20	2
Ni-TEGO	B.E. (eV)	530.6		533.	536.8
	Line-shape	GL(30)		GL(30)	GL(30)
	FWHM	2.9		3	3.2
	Rel. Conc. (%)	19		71	10

[a]: OX1 most likely models oxygen attached to carbon by a double bond as is the case for carbonyl groups (>C=O).
[b]: Based on the XRD data shown in figure 3.7 and the exclusive appearance in the Li-TEGO XP spectrum, OLi is believed to model oxygen bound to lithium. It can be assumed that OLi is a superposition for the different lithium-oxygen species, seen in XRD, with a majority of the signal originating from Li_2O.
[c]: OX2 is the main feature in the O 1s spectrum for TEGO and Ni-TEGO. It is believed to originate from oxygen bound to carbon in phenol groups (C-OH) [40, 4].
[d]: OX3 has a chemical shift of about 6 eV from the lowest bound feature (OX1) in the O 1s spectrum. This corresponds well to the 6 eV shift recorded for the $\pi \rightarrow \pi *$ transition seen in C 1s and has probably the same origin.

3.3.3 Magnetic properties

Evidence for the presence of metallic fcc nickel nanoparticles, with an averaging diameter of 17 nm, on the Ni-TEGO sample was detected by means of HAADF-STEM and HRTEM investigations. As mentioned above, both measurement techniques are local measurements of a small part of the investigated sample while the bulk data of XRD shows no signal of nickel crystallites at all. To verify the absence of larger grains or NP agglomerates and to get information on the magnetic properties of the whole Ni-TEGO system zero-field-cooled (ZFC) and field-cooled (FC) SQUID measurements were performed and the results are presented in figure 3.19. Additionally hysteresis was measured at 2 K between $[-5,5]$ T and parts of the corresponding data can be seen in the inset in figure 3.19. The measured coercive field at low temperatures is about 120 Oe and can be attributed to randomly distributed nanoparticles of soft magnetic material. The absence of a measurable exchange bias shift suspends the existence of a thick nickel oxide layer around the NP, however, it is not possible to fully exclude the presence of very thin layers below a few nanometers from this, as has been shown by Seto et al.[106]. For the ZFC measurement the sample was cooled down to 2 K in the absence of an applied external magnetic field. The total magnetization of the system equals zero since the magnetic moments of the particles are randomly oriented. A probing field of $\mu_0 H = 3 \cdot 10^{-3}$ T was subsequently applied and the magnetization was measured versus temperature during heating from $T = 2 \rightarrow 400$ K. The applied field induces reorientation of the magnetic moments parallel to the field and results in a net magnetic moment increasing with temperature as a growing number of particles have enough thermal energy to overcome the energy barrier E_B pinning the magnetic moments along the easy axis. The magnetic moments of particles with a thermal energy above E_B will be enabled to randomly fluctuate. This type of magnetic behavior is described in detail in section 2.1.1 and a schematic of the particles can be seen in figure 2.1 and 2.2. The measurement points of a ZFC measurement represent, for a certain temperature, the magnetization of particles with a certain volume for which their relaxation time τ is equal to the experimental time window t. Particles with $\tau \gg t$, at fixed T, will continue to be blocked during the observation period. Particles with $\tau \ll t$, at fixed T, behave superparamagnetic and particles with τ in the range of the measurement period will have a certain probability that the magnetic moment is still directed along the applied field and has not yet changed. The mathematical expression for this is the Néel-Brown equation 2.2. The temperature at which most particles align with the probing field is called the blocking temperature T_B. Even though the Ni-NPs show cubic fcc structure and should show cubic anisotropy, nanoparticles have typically uniaxial anisotropy which can be attributed to the large surface to volume ratio and the thus large influence of surface, strain/stress and shape effects on the effective anisotropy constant. Surface anisotropy is explicitly mentioned here since in general the surface anisotropy, normal to the surface, would average to zero for spheres but nanoparticles behave differently and this no longer holds true such that even small changes of shape can lead to relatively large changes in the effective anisotropy [3].

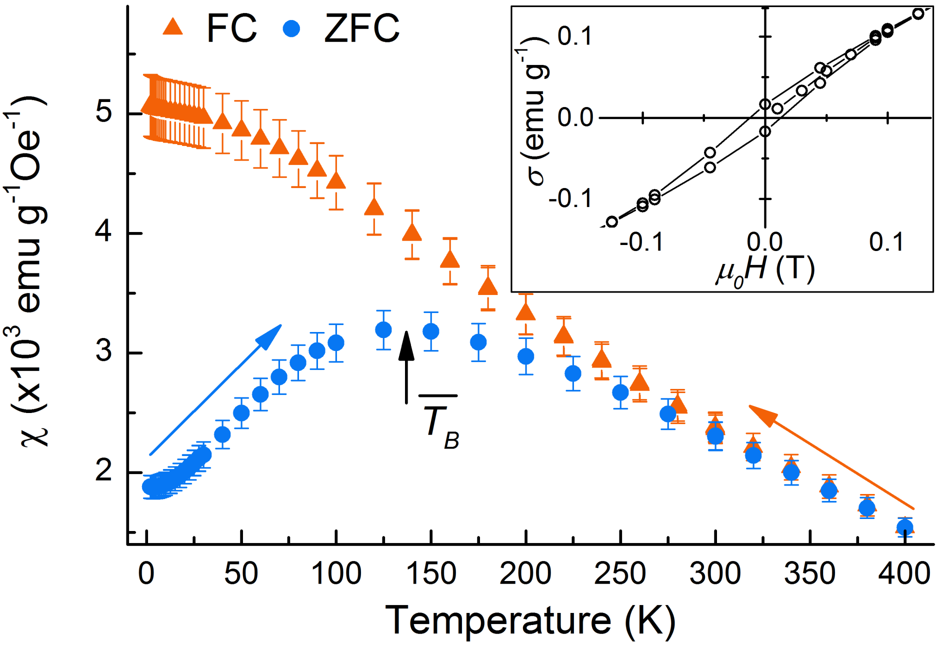

Figure 3.19: ZFC and FC SQUID data of Ni-TEGO is depicted in blue and orange respectively. The average blocking temperature is marked with an arrow at $\bar{T}_B = 137$ K. The Inset shows a hysteresis loop and a coercivity of about 120 Oe. The hysteresis loop was recorded range between $[-5, 5]$ T at 2 K while only the relevant parts are shown.

As seen in figure 3.19 there is a single susceptibility peak in the ZFC measurement of Ni-TEGO at $T_B = 137(\pm 2)$ K, above which the magnetization decreases with increasing temperature, a clear display of superparamagnetic behavior. The absence of additional peaks in the ZFC measurement is proof for monodispersity, or in other words proof for a single particle size distribution. The weak Curie like trend at very low temperatures, i.e. the reduced incline in the ZFC curve, is believed to be caused by $S = 1/2$ paramagnetic defects found in pure TEGO, that are usually in the order of approximately 10^{18} g^{-1}.

The FC measurement followed the ZFC process. The magnetization was measured versus temperature during cool down from $400 \rightarrow 2$ K with the field of $\mu_0 H = 3 \cdot 10^{-3}$ T still applied. The non equal behavior of the system of ZFC and FC measurements is typical for superparamagnetic nanoparticles. The absence of a plateau, in particular below T_B, and the overall negative slope is a clear indicator for the absence of strong particle-particle interactions [5].

Taking the average diameter $\bar{d} = 17$ nm from the HRTEM measurements, the measured blocking temperature of $T_B = 137$ K and plugging this into equation 2.3 one gets an effective anisotropy of $K_{\text{eff}} = 18.6(\pm 4) \cdot 10^3$ Jm^{-3}. To see if the initial assumptions were correct this value was compared to literature. The K_1 component of the magnetocrystalline anisotropy constant of bulk Ni exhibits a strong temperature dependence. This dependence is depicted in figure 3.20 and can be expressed as [132]:

$$K_1 = K_0 e^{-aT^2}$$
$$K_1 = 42.3 \cdot 10^3 \text{ J m}^{-3}$$

with $K_0 = 8 \cdot 10^5$, $a = -3.4 \cdot 10^{-5}$ and $T = T_B = 137$ K. K_1 and the effective anisotropy for cubic crystals can be compared by [42]:

$$K_{\text{eff}} = \frac{|K_1|}{12} = 3.5 \cdot 10^3 \text{ J m}^{-3} \tag{3.3}$$

The large difference between the literature value for the cubic magnetocrystalline anisotropy and the measured anisotropy $\left((3.5 \text{ vs. } 18.6) \cdot 10^3 \text{ Jm}^{-3}\right)$ comes as no surprise and is proof of the large influence of shape anisotropy.

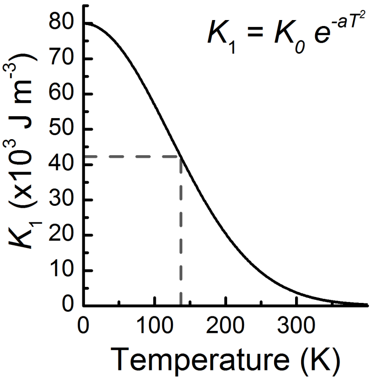

Figure 3.20: Strong temperature dependence of the K_1 component of bulk nickel [132]. At $T_B = 137$ K the anisotropy constant $K_1 = 3.5 \cdot 10^3$ J m^3.

In section 2.1.1 the Stoner-Wohlfarth model and its applicability for particles similar to the Ni-NPs present on Ni-TEGO has been discussed. However, equation 2.7 has the drawback, that an accurate measurement of the anisotropy constants N_a and N_c proves cumbersome and is for a system composed of particles of various sizes and shapes unpractical. Rearranging equation 2.7 and solving for $(N_a - N_c)$ gives:

$$(N_a - N_c) = 2\frac{K_s}{M^2}. \tag{3.4}$$

With the effective anisotropy value calculated by means of the Néel-Brown expression one can calculate $(N_a - N_c)$ by means of equation 3.4. Included in Stoner and Wohlfarth paper they have given a list of values for $(N_a - N_c)$ that can be directly compared to the axes ratio $m = c/a$ of the corresponding prolate spheroid [112]. A graphical illustration can be seen in figure 2.1. Taking the literature value of the saturation magnetization M_s for bulk nickel at 139 K $\left(M_s = 57.8 \text{ emu g}^{-1}\right)$ [28] and a nickel density of $\rho_{\text{Ni}} = 8.908$ g cm^3 one gets $M_s = 514.9$ emu cm^{-3}. Plugging this and the measured $K_{\text{eff}} = 186 \cdot 10^3$ erg cm^{-3} for K_s into equation 3.4 gives a value for $(N_a - N_c)$ of 1.403. This corresponds to an axis ratio of $m \approx 1.3 - 1.4$ which is in excellent agreement with the slight elongation seen with HRTEM.

3.3.4 Specific surface area and skeletal density

In this section measurements of the BET specific surface area (SSA) and skeletal density of Ni-TEGO are presented. While the latter is of use in hydrogen adsorption measurements the SSA of Ni-TEGO will be important for the comparison of the over all hydrogen adsorption of Ni-TEGO with different carbon-based systems since the hydrogen uptake is in good approximation correlated with the specific surface area of the adsorber $\left(\sim 1.5 \text{ mass\%} / 1000 \text{ m}^2\text{g}^{-1}\right)$ [149]. Measurements were conducted on a BELSORP-max, a Sievert-type apparatus, commercially available from BEL JAPAN INC.. The sample handling and basics in BET theory are discussed in section 2.2.3.2. Figure 3.21 shows the N_2 adsorption data on Ni-TEGO at 77 K. A linear fit was performed in the interval $p/p_0 \approx [0.05, 0.35]$ and from the slope and intercept the BET specific surface area can be calculated according to equation 2.20 with $a_{\text{BET}} = 515 \pm 3$ m^{2}g^{-1}. The theoretical surface area of pure graphene lies with 2630 m^{2}g^{-1} considerably higher but is seldomly achieved by graphene produced on a gram scale.

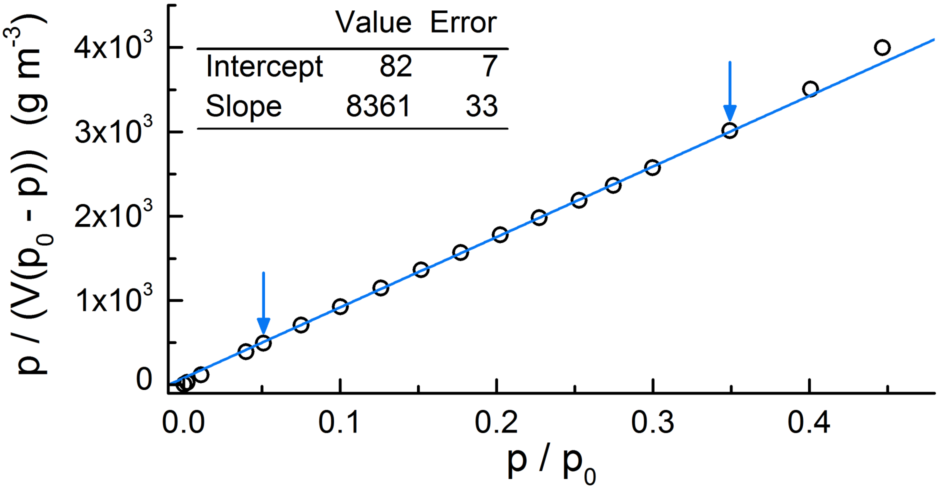

Figure 3.21: BET adsorption isotherm of N_2 on Ni-TEGO at 77 K. The blue line depicts a linear fit of the data within the range spanned by the two blue arrows $\left(p/p_0 \approx [0.05, 0.35]\right)$. For values below and above this interval the data starts to deviate in a type II isotherm fashion, typical for N_2 adsorption. The table in the top left corner indicates the slope, intercept and standard error of the linear fit.

Helium adsorption was performed to determine the skeletal density of nickel decorated TEGO. The skeletal density is, in distinction from other density definitions, the weight of the material divided by the sum of the volumes of the solid material including all closed and blind pores within the pieces but without all accessible pores. It is assumed that helium does not physisorb on Ni-TEGO at room temperature and due to its size even small pores and folds are penetrated and thus accounted for. The volume of the sample holder and the inner volumes of the instrument were carefully measured as well as the corresponding temperatures to be able account for thermal gas expansion. By measuring the pressure difference after helium expansion from a known volume (inner volume of the instrument) into the sample holder, once empty and once filled with the sample, the volume difference can be calculated and thus the volume of the sample accessible by helium. This volume divided by the sample weight gives a skeletal density of 2.1 ± 0.1 g/cm^3, which is comparable to the density of bulk graphite with a calculated density of 2.26 g/cm^3.

3.4 Interaction with hydrogen

As described in the introduction of this chapter it is believed that metal decorated TEGO readily stores large quantities of hydrogen under favorable conditions. After the extensive structural investigations presented in section 3.3 Ni-TEGO is well characterized. The unknowns of the system have been reduced to a level enabling investigations of the interaction with hydrogen. In a first step the adsorption experiments of molecular hydrogen at cryogenic temperatures (77 K) will be presented. In a second step the findings from Longitudinal Field Muon Spin Repolarization (LF-μ-SR) will be discussed, which in turn is an indication for the interaction of atomic hydrogen with Ni-TEGO.

3.4.1 Hydrogen at cryogenic temperatures

Sorption experiments of gaseous molecular hydrogen were conducted on two different instruments with different underlying measurement principles (see section 2.2.3). Due to the higher accuracy of the Sieverts-type BET instrument at low pressures, sorption data up to 0.1 MPa of hydrogen pressure was only taken from this instrument while the data from the dynamic pcT apparatus was omitted for this region. Figure 3.22 shows the concentrated hydrogen sorption data at 77 K. A solid red line depicts the corresponding Langmuir-Freundlich isotherm fit of the form:

$$N = \frac{N_t K p^m}{1 + K p^m}. \tag{3.5}$$

Equation 3.5, also known as generalized Sips, Bradley's or generalized Freundlich isotherm, describes a combination of the Freundlich and Langmuir isotherms. The expression has a finite limit at high pressures and all coefficients have physical meaning. N is the amount of hydrogen adsorbed on a gramm of sample at a certain pressure p, N_t is the adsorbed amount at saturation and thus related to the total amount of binding sites, K and m are constants. m is called the heterogeneity index and can vary between 0 and 1. At $m = 1$ equation 3.5 reduces to the Langmuir equation. K is related to the binding affinity. It is believed, that the Langmuir-Freundlich isotherm is a more accurate description of hydrogen sorption and in particular, that it is likely giving a more accurate value for N_t than the Langmuir or Freundlich equation correspondingly [120, 32].

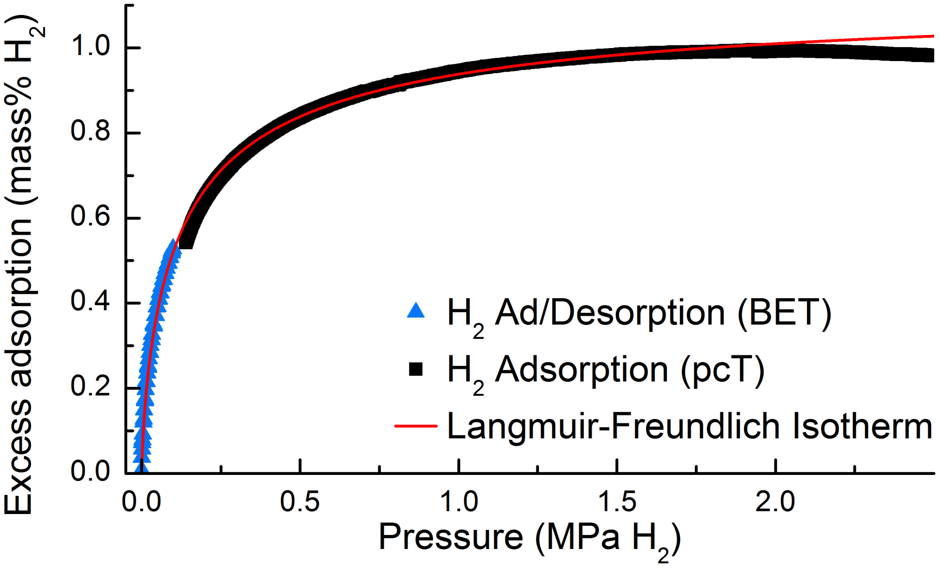

Figure 3.22: Hydrogen adsorption of Ni-TEGO at 77 K. The blue triangles are data recorded with the BELSORP-max BET, the black squares are measured with the in-house build dynamic pcT instrument. Due to the high density of measurement points recorded with the dynamic pcT instrument only about 4 % of the them are shown for better visibility. The red line is a Langmuir-Freundlich isotherm fit which starts to deviate from the data at a hydrogen pressure of about 1.8 MPa.

The curve fit results in a value of $N_t = 1.14$ mass% H_2, while the error is estimated to be not more than 0.1 mass%. At a hydrogen pressure of about 1.8 MPa the fit diverges from the data and while the fit shows asymptotic behavior and reaches a plateau at high pressures, the recorded adsorbed hydrogen seems to decrease.

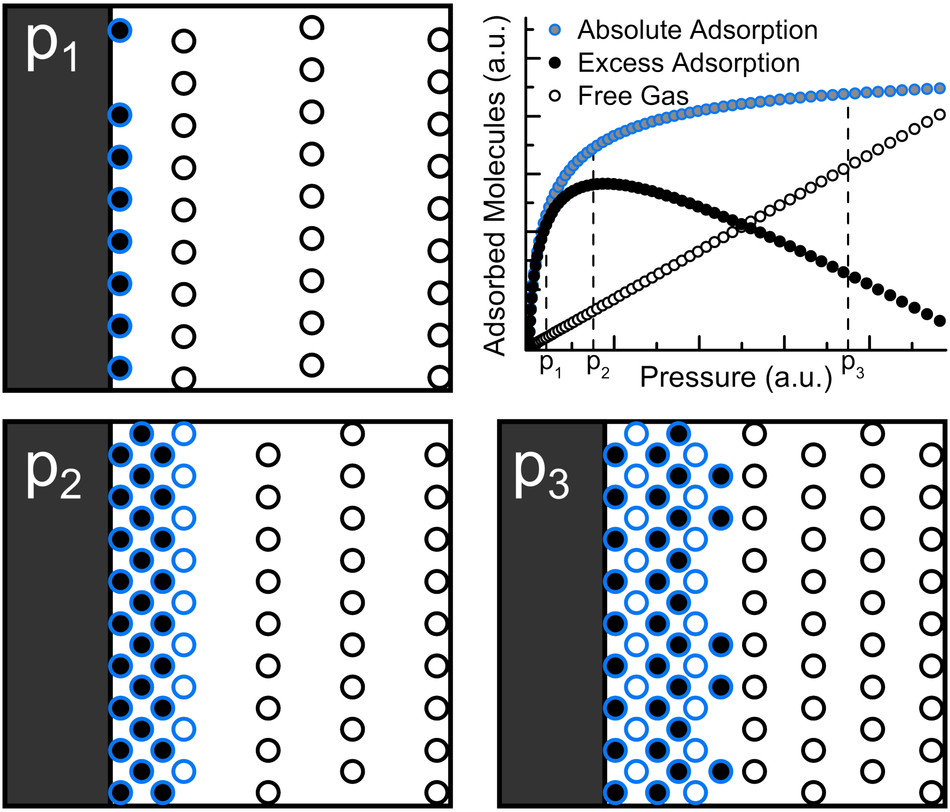

Figure 3.23: Schematic representation of the relation between excess and absolute adsorption. The dark gray region to the left of p_1–p_3 symbolizes the surface, the circles represent gas molecules and the different colors distinguish them from each other. All blue rings, filled black or white, are constituting to the absolute amount of adsorbed gas molecules. The black circles filled in white illustrate free gas molecules and with rising pressure from p_1–p_3 their numbers increases proportionally. The blue circles filled with black are the difference between absolute absorbed gas molecules and free gas molecules in the region before the surface where gas adsorption takes place. With increasing gas pressure the probability to find gas molecules in the region of adsorption increases until at high enough pressure the density of molecules in the free gas phase is non negligible compared to the density of molecules adsorbed on the surface. At that point the two different phases of molecules become indistinguishable for many instruments and a decrease in the recorded adsorption takes place. This can be seen in the graph in the top right corner where the excess adsorption shows a maximum unto which it starts to decrease with increasing pressure.

The decrease is not a physical property as the system is not desorbing hydrogen, rather, the dynamic pcT measures excess adsorption while the fit model describes absolute adsorption. As indicated in figure 3.23 the trend of excess and absolute adsorption diverges at higher pressures (or concentrations). In addition the hydrogen uptake at higher temperatures, i.e. 93 K and 103 K, was measured and while the overall hydrogen adsorption clearly decreases as expected, the data quality is not satisfactory enough to draw unambiguous conclusions. The over all hydrogen adsorption of carbon-based systems is in good approximation correlated with the specific surface area of the adsorber. The relation holds that per 1000 m^2/g^{-1} about 1.5 mass% H_2 can be stored at 77 K [149]. With a BET specific surface area of 515 m^2g^{-1} Ni-TEGO should therefor store only about 0.77 mass% H_2. The measured value of 1.14 mass% H_2 for Ni-TEGO indicates a dramatic increase of almost 50 %. The hydrogen adsorption and desorption cycles for all tested temperatures and loading pressures where fully reversible and hydrogen desorbed under medium vacuum conditions (0.1 Pa).

3.4.2 Longitudinal field muon spin repolarization

For the investigation of the interaction of a material with atomic hydrogen, the source of hydrogen is always molecular hydrogen. Prior to chemisorption the molecule has to dissociate and consequently there are several processes involved, i.e. dissociation, thermalization, adsorption and subsequent absorption. By using muons, and regarding them as light isotopes of hydrogen, one can decouple the dissociation from chemisorption and gain inside in atomic-hydrogen-like processes at conditions that are not accessible with H_2 as hydrogen source. To do this zero field and longitudinal field muon spin repolarization (ZF-μSR and LF-μSR) was performed on Ni-TEGO at the EMU spectrometer at the ISIS pulsed muon source, Rutherford Appleton Laboratory in England. The basic theory behind the particle and how it is produced was reported in 2.1.2; for a description on the experimental realization see section 2.2.4.

Previous ZF-μSR studies on TEGO show a strong influence of lattice defects on the asymmetry signal [97]. The results indicate that dipolar interaction between a single proton and the muon spin causes the precession of the muons spin rather than being induced by long-range magnetic order. In other words, the more defects a TEGO sample shows, the higher the amount of trapped muons that subsequently are subject to local dipolar interaction. These dipolar interactions force the precession of the muons spins and thus causes a larger amplitude in the asymmetry measurement. A similar ZF-μSR measurement was conducted with nickel decorated TEGO and both can be seen in the inset in figure 3.24. The TEGO and Ni-TEGO measurement data has been normalized to the corresponding maximum value A_{max} which depends on the intrinsic asymmetry of the weak decay (see 2.3), the initial polarization of the muon pulse and the positron detectors and is typically around $A_{\text{max}} \approx 0.21 - 0.25$. For the muons implanted in Ni-TEGO two components for the repolarization of the muon spin polarization can be identified. A slowly decreasing fraction, fitted with a Lorentzian, comprises about 52 % of the signal and a Gaussian component, making up about 10 %. The Lorentzian decrease is a typical signal for μ^+ diffusing on a carbon surface [124] while the Gaussian component can be explained by local dipolar interaction of the same kind as reported for TEGO. The most notable feature becomes apparent when comparing the measurements of pure TEGO to Ni-TEGO. While for the pure TEGO a full initial polarization is observed the Ni-TEGO measurement shows a large missing fraction of about 38 % in zero applied field. This missing fraction is indicative of strong interactions of the implanted μ^+ with electrons through hyperfine coupling and can occur either by the creation of isotropic muonium or after the formation of a radical by external addition [9]. In case of a radical formation the electrons wavefunction is not localized on the muon, as is the case for muonium, and thus the hyperfine coupling is measurably reduced. By applying a longitudinal magnetic field, parallel to the muons initial spin, one can decouple the muon spins from the electron spins and thus, through unraveling the hyperfine interaction, gradually repolarize the muon spins. For isotropic muonium the repolarization has the form

$$P = \frac{1}{2}\left(1 + \frac{x^2}{x^2+1}\right), \tag{3.6}$$

where $x = B/B_{\text{hyp}}$, B is the applied field and $B_{\text{hyp}} = 158$ mT is the characteristic hyperfine field for free isotropic muonium [126]. If the hyperfine interaction is anisotropic the zero field polarization is quenched from 50 % to 0 % and equation 3.6 reduces to approximately $P = x^2/\left(x^2+1\right)$. The LF-$\mu$SR repolarization experiment is plotted in figure 3.24 with the measured polarized fraction against the externally applied magnetic field. Already a comparably low field is sufficient to fully repolarize the muon spins, hence ruling out the hyperfine interaction of free muonium where B_{hyp} is expected to be 158 mT. Reacquiring the 100 % spin polarization with a longitudinal field additionally proves that other thermalization processes than the discussed one do not contribute to the observed missing fraction. With P_{diam} the diamagnetic fraction of muons and A_{rad} the amplitude of the missing fraction, observed in the ZF-μSR experiment, one can fit the data by [100]:

$$P_{\text{exp}} = P_{\text{diam}} + A_{\text{rad}}\left(\frac{x^2}{x^2+1}\right). \tag{3.7}$$

$$B_{\text{hyp}} = A_{\mu}(|\gamma_e| + \gamma_{\mu}) \tag{3.8}$$

The resulting hyperfine field has a value of $B_{\text{hyp}} = 7.1 \pm 0.7 \cdot 10^{-3}$ T and with equation 3.8 the field corresponds to a hyperfine frequency of approximately 200 MHz. It is important to note, that due to the low amount of data points and the probability of anisotropy in the hyperfine coupling this evaluation is only an estimation and a more precise determination is denied.

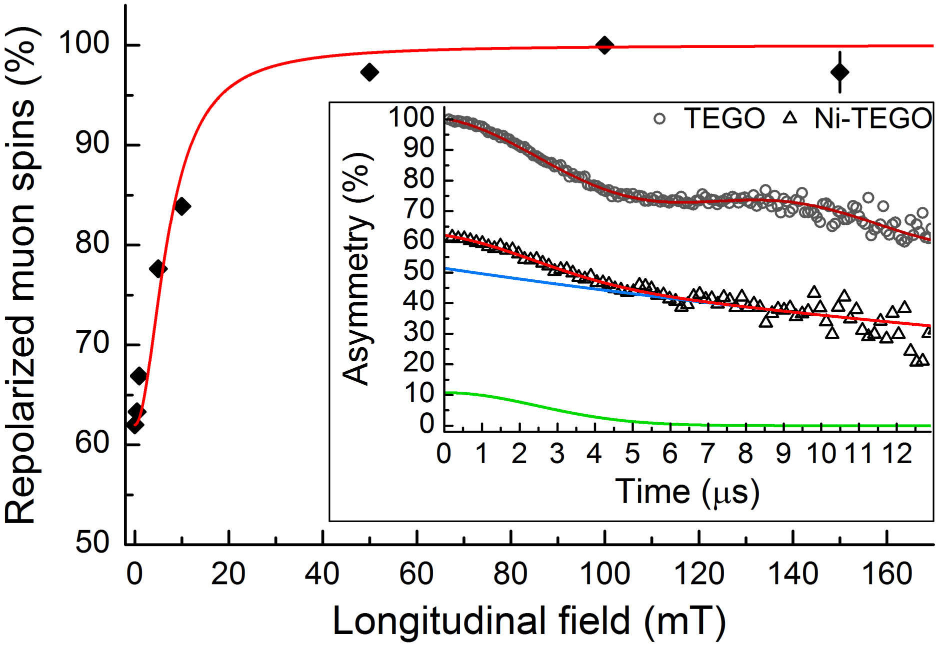

Figure 3.24: Muon spin repolarization experiment in Ni-TEGO at 300 K. The repolarization asymmetries have been fitted by equation 3.7 and the fit is shown as a solid red line. The inset shows zero field muon spin relaxation of TEGO (grey circles) and Ni-TEGO (black triangles) at 300 K. The latter was fitted by a Gaussian (green solid line) and a Lorentzian (red solid line). For TEGO the combined fit of Gaussian and Lorentzian is shown as a dark red solid line as described in [97].

Such a low value for the hyperfine field can only be explained by the formation of adduct radicals which, however, have not been observed on pure TEGO. The small amount of nickel in the sample can not account for the large radical fraction of 38 %, moreover a muonium radical formation is not expected on metal nanoparticles [6, 27]. The radicals must thus form on carbon which again is not expected. The reason why in-plane bonding on pure graphene is questionable is that the unpaired electron of muonium, subsequent to the sp^2 to sp^3 hybridization of carbon, delocalizes and becomes part of the π-derived conduction band of graphene. The stronger localization of the paramagnetic electron in case of Ni-TEGO can be ascribed to local perturbations of the graphene π-orbitals caused by the nickel nanoparticles and a subsequently allowed radical formation. As for atomic hydrogen the results indicate a strong increase in bonding of hydrogen in case of Ni-TEGO, compared to pure TEGO, with hydrogen favorably bonded in vicinity to the nickel nanoparticles.

3.5 Summary and conclusion

Throughout this chapter extensive investigations have been presented, conducted on a novel class of materials, i.e. lithium and nickel decorated thermally exfoliated graphite oxide (Li-/Ni-TEGO). The backbone of all synthesized samples is TEGO which can be viewed as a defective graphitic matrix with monolayer-graphene like areas of on average 9 nm diameter surrounded by a slim network of graphite multilayers. This was confirmed by HRTEM imaging, SAED, XRD and Raman measurements as reported in section 3.3.1. The majority of carbon is bound as sp^2 carbon, with a small fraction of sp^3 which was additionally underpinned by the asymmetric peak shape seen in XPS and the large fraction of $\pi \rightarrow \pi*$ transition in the C 1s peak (see 3.3.2). A low oxygen content of only about 3 %At Conc. and marginally more for the metal decorated samples shows the thorough deoxygination by thermal exfoliation and the subsequent appropriate conditions for sample handling and analysis. The skeletal density of TEGO is, within the instrumental sensitivity, equivalent to that of other graphite like materials $\rho_{\text{skeletal}} \approx 2.1\ \text{g/cm}^3$ and the samples have a BET specific surface area of $a_{\text{BET}} \approx 515\ \text{m}^2\text{g}^{-1}$ (see 3.3.4).

In the case of lithium decoration the resulting samples are extremely sensitive to oxidation and even common techniques such as handling under inert conditions in Ar-filled gloveboxes $\left(O_2 < 0.5\ \text{ppm}, H_2O < 0.5\ \text{ppm}\right)$, sealed airtight containers and under vacuum did not prevent the formation of oxidized lithium species. It is thus highly questionable if a future thorough investigation of this type of material is feasible. The samples decorated with nickel proved less reactive towards oxygen and their structure and interaction with hydrogen were subsequently studied.

The synthesis conditions lead to the formation of dilute, monodisperse nickel nanoparticles, of slightly prolonged prolate spheroid shape and an approximate diameter of 17 nm. The nickel remains metallic and due to the nanometer size the particles display superparamagnetic behaviour above their average blocking temperature of $T_B = 137$ K (see sections 3.3.3 and 3.3.1). The overall nickel content of the sample is relatively low and XPS gives only a value of less than 1 mass%. The fact that the ejected photoelectrons can only be recovered from the first few nanometers of the nickel nanoparticles will lead to a somewhat higher actual stoichiometry. The investigation of hydrogen sorption at cryogenic temperatures shows that the presence of Ni-NPs significantly enhance the physisorption of hydrogen and an increased hydrogen capacity of almost 50 %, compared to carbon with the same specific surface area, was reported in section 3.4.1. Additionally muon spin repolarization measurements, reported in section 3.4.2, show the formation of a large fraction of radicals. About 38 % of the implanted muon spins can be recovered with a longitudinal field of a dimension easily explainable with muonium-adduct radical formation. This is a clear fingerprint of a strong interaction with atomic hydrogen and can not be seen for undecorated TEGO.

While these findings demonstrate the dramatic enhancement of the carbon hydrogen interaction for both molecular as well as atomic hydrogen, no evidence for Kubas interaction or hydrogen spillover, as has been predicted by theory, was found.

Decorated graphenes demonstrate the high versatility of carbon materials. Their chemical and physical properties can be altered on demand according to the decorated atoms. Even the very low amount of nickel deposited onto the TEGO support changed the interaction towards hydrogen dramatically. The advantage of the chosen synthesis path opens up the possibility to additionally alter characteristic parameters like the nanoparticle size and distribution, the structure of TEGO as well as the deposition material. This enables the investigation of the influence of each of the named parameters separately and might elucidate the origin of the discovered metal mediated hydrogen-carbon interaction enhancement. Furthermore sorption measurements at higher temperatures might enable the dissociation of hydrogen and therewith increase the overall capacity through a different type of hydrogen bond.

4 Metal intercalated fullerene

4.1 Introduction

The common hydrogenation of pristine C_{60}, forming so-called hydrofullerenes $C_{60}H_x$, is an energy demanding process and can only be achieved via high hydrogen pressures and elevated temperatures (5–12 MPa and 573–673 K). During hydrogenation H_2 is added at a C=C double bond resulting in the formation of two C−H bonds, a transformation of $sp^2 \rightarrow sp^3$ and a corresponding severe distortion of the carbon cage. For neutral hydrofullerenes ($C_{60}H_x$) only even numbers for x are expected and typically between $2 < x < 44$; with the two most abundant stoichiometries $C_{60}H_{18}$ and $C_{60}H_{36}$ [116]. This type of hydrogenation of fullerenes is non-reversible and prolonged hydrogenation and dehydrogenation results in the collapse into polycyclic aromatic hydrocarbons but also in a fragmentation of the C_{60} cage structure [118, 117].

The strong influence of metal decoration on the hydrogen-graphene interaction was discussed above in chapter 3. Comparably metal intercalated fullerenes show great potential as solid hydrogen storage materials. Of all fullerenes C_{60} is of distinct interest, owing to its high electron affinity (2.65 eV) and the easiness of reversible addition of up to 6 electrons on its triply degenerate t_{1u}-LUMO [131, 44]. This is widely exploited in the synthesis of charge transfer salts (fullerides) were alkali, alkaline earth and transition metals donate electrons in an ionic bond to the fullerene. The next higher molecular orbital of C_{60} is t_{1g}; also triply degenerate and energetically close to t_{1u}. Based on this it is widely suggested that C_{60} can accept even higher charges, up to 12 electrons, however, even for heavy doping no metal-intercalated compounds have been reported that would exhibit a 12 e^- saturated state. At higher intercalation the charge transfer is not fully provided to C_{60} any more. One explanation indicates that, subsequent to an intercalation leading to a charge transfer of 6 e^-, interstitial electron states are induced; probably originating at the centers of metal aggregates around the interstitial octahedral site (see figure 4.1) [2]. This filling of interstitial electron states limits the charge transfer to C_{60}. Nevertheless, a high loading of 6, with an estimation as high as 8 e^-, is reported for different intercalated fullerene compounds [79, 2].

Enhanced electrostatic interactions between H_2 and C_{60}, depending on the amount of additional charge transferred to the fullerene cage, is proposed by first principle DFT calculations [141]. The binding energy increase for physisorbed H_2, typically around 5 kJ mol^{-1}, is expected to be up to 17–31 kJ mol^{-1}, with a hydrogen storage capacity of up to 8 mass% [141]. Analogous to the Kubas interactions predicted for metal decorated graphene, first principle calculations indicate possible Kubas interactions for metal intercalated fullerenes. The increased binding energy of the H_2 molecule leads to a calculated hydrogen storage capacity increase of up to 6.8, 7.5, 8.4, 9.5 and 13.5 mass% for Ni_3C_{60}, $Ti_{12}C_{60}$, $Ca_{32}C_{60}$, Na_8C_{60} and $Li_{12}C_{60}$ respectively [107, 138, 140, 18, 113]. Both mentioned approaches leave the dihydrogen molecule intact and facilitate hydrogenation under moderate conditions, due to binding energies in the desired range of 20–40 kJ mol^{-1} H_2; conditions under which the fullerene molecules stay intact. During their research on hydrogen sorption of alanates Teprovich et al. found that when they used C_{60} as a catalyst they formed metal fullerenes during desorption and simultaneously facilitated desorption at reduced temperatures [122]. Subsequently they reported that Li_xC_{60} reversibly stores up to 5 mass% of hydrogen [121].

The following chapter reports on the hydrogen and deuterium absorption and desorption properties of $Na_{10}C_{60}$ and $Li_{12}C_{60}$. In the course of the underlying scientific project (SNSF - Smart carbon-based materials for hydrogen storage) various different samples have been investigated and the here discussed selection are the most promising of a wide range of synthesized materials. As part of a bigger project most of the conducted experiments have been performed by various different laboratories. The fullerides were investigated by means of X-ray powder diffraction and in situ neutron powder diffraction, Fourier transformed infrared (FT-IR) spectroscopy, Raman spectroscopy and volumetric gas absorption measurements (pcT, pressure-composition-temperature).

4.2 Experimental

4.2.1 Sample synthesis

For the synthesis of metal intercalated fullerenes high purity (> 99.9 %), polycrystalline C_{60} was purchased from MER Corporation. Prior to further use the powder was degassed in dynamic high vacuum (10^{-3} Pa) at 523 K for 12 h.

To synthesize Na_xC_{60} the degassed C_{60} was mixed with anhydrous sodium azide (NaN_3, Sigma-Aldrich) in stoichiometric amounts within the inert atmosphere of an Ar-glove box. The material was subsequently hand-ground with agate mortar and pestle, for thorough homogenization and the resulting fine powder was pelletized (80–120 mg per pellet). The pellets were placed in tantalum foil bags and then sealed in Pyrex vials. The solid state reaction was performed under dynamic high vacuum and slow heating (≈ 10 K h^{-1}) up to 723 K at which the sample was held for 5 h. The decomposition of NaN_3 and the subsequent diffusion of Na onto the fullerene cages started around 638 K and followed the formula:

$$C_{60} + x \cdot NaN_3 \Longrightarrow Na_xC_{60} + \frac{3}{2}x \cdot N_2$$

While from pure stoichiometric considerations the resulting compound should have been $Na_{10}C_{60}$ further investigations, which are reported below, evidence a slightly lower sodium amount. The final compound is nevertheless simply called $Na_{10}C_{60}$. Analogously, the synthesis of $Li_{12}C_{60}$ was performed by mixing stoichiometric amounts of previously degassed C_{60} with flakes of high purity granular lithium (99 %, Sigma-Aldrich). Approximately 500–600 mg of the mixture was transferred to a 3 sphere agate ball mill and milled at 30 Hz for 1 h. The resulting material appeard as a uniform black powder which was pelletized (≈ 100 mg per pellet) and placed in tantalum foil bags; sealed in Pyrex vials in high vacuum. The vials were slowly heated up to 543 K and kept at this point for 36 h to facilitate the diffusion of lithium onto C_{60}.

To avoid contamination and oxidation the synthesized samples were exclusively handled in the inert atmosphere of argon filled glove boxes (H_2O and $O_2 < 1$ ppm). Sample synthesis was performed by Dr. Mattia Gaboardi at the University of Parma, Italy.

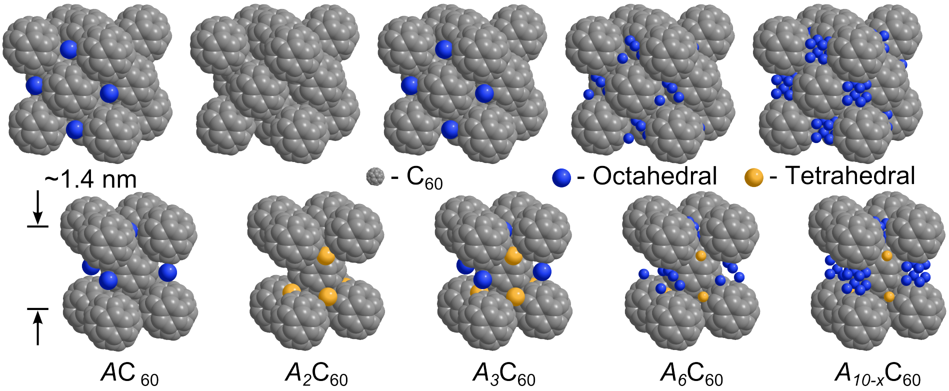

Figure 4.1: Schematic visualization of metal intercalated C_{60} on the basis of undoped fcc, $Fm\bar{3}m$ (255), C_{60}. Colored spheres indicate possible interstitial sites, octahedral (blue) and tetrahedral (yellow), where the intercalated metal atoms can reside. The lower row shows tetragonal cuts of the cubic structures above and serve as a different field of vision with visible tetrahedral sites. A_n stands for the dopand and the respective stoichiometry n, e.g. Li_{12} or Na_{10}. Depending on the size of the doped element it is possible that multiple atoms occupy one classical interstitial site [38]. Metal intercalated C_{60} can furthermore crystallize in different structures, e.g. cubic bcc or polymeric sheets [95].

4.2.2 Experimental procedure and setups

Sample synthesis and subsequent handling was conducted exclusively under inert atmosphere to prevent oxidation and contamination. Hydrogen (99.999 % H_2) and deuterium (99.8 % D_2) sorption was measured volumetrically with a pcT instrument (see experimental paragraph 2.2.3.1). For $Na_{10}C_{60}$ approximately 100–200 mg of sample were introduced to about 20 MPa H_2 and a subsequent temperature ramp increased the sample temperature at 0.5 K min^{-1} up to 473 and 673 K depending on the experiment. At the final temperature the samples were kept between 1 and 67 h. The amount of absorbed hydrogen was determined by the changes in pressure at known volumes and temperatures and corrected with a non absorbing silicon sample occupying the same volume as the active material. Dehydrogenation was measured either in an applied vacuum (< 0.1 Pa) or at a back pressure of 0.1 MPa H_2 and with a temperature ramp of 1 K min^{-1}.

In case of $Li_{12}C_{60}$ 375 mg of sample was used and in a first absorption step 19 MPa D_2 were applied to the sample. The sample temperature was ramped at 0.5 K min^{-1} up to 498 K were it was kept for 45 h. In a second step only 10 MPa D_2 were applied but the temperature was ramped up to 623 K for 24 h. The amount of absorbed deuterium was again determined by the changes in pressure at known volumes and defined temperatures.

For Raman spectroscopy and X-ray diffraction the samples were filled into $\varnothing = 0.5$ mm quartz capillaries with a wall thickness of 0.01 mm. The capillaries were sealed by melt off. The X-ray diffractometer and the Raman spectrometer are explained in sections 2.2.1.1 and 2.2.6 respectively.

Fourier transform infrared spectroscopy (FT-IR) (see section 2.2.6) was performed within an argon glove box to prevent contamination. Depending on the sample FT-IR grade potassium bromide (KBr) was used to decrease the attenuation of the sample and improve the spectra.

In situ neutron powder diffraction measurements were carried out at the HRPT beamline of the Swiss Spallation Neutron Source (SINQ) at the Paul Scherrer Institute (PSI) in Villingen, Switzerland. The available neutrons in high-intensity mode had a wavelength of $\lambda_n = 0.18857$ nm. The $Na_{10}C_{60}$ was measured in a $\varnothing = 6$ mm steel sample holder with a wall thickness of 1 mm. This resulted in strong reflections of the steel sample holder and subsequently $Li_{12}C_{60}$ was measured in sample holders made of vanadium ($\varnothing = 6.3$ mm and a wall thickness of 0.25 mm). Diffraction patterns were recorded between $2\theta = 5$–$165°$ and acquisition times of 3 h and 4.25 min for $Na_{10}C_{60}$ and $Li_{12}C_{60}$ respectively. In case of lithium fulleride typically 10 individual patterns were summed to enhance the statistics. The sample temperature was controlled by a radiation-type furnace.

The majority of pcT, XRD, Raman and FT-IR measurements were conducted with or by Dr. Philippe Mauron at Empa in Dübendorf, Switzerland. The FT-IR spectrum of $Li_{12}C_{60}$ was measured by Dr. Pietro Galinetto at the Dipartimento di Fisica “A. Volta” in Pavia, Italy. In situ neutron powder diffraction measurements were carried out by a varying group of scientists that, apart from myself, included Dr. Philippe Mauron, Dr. Mattia Gaboardi, Dr. Denis Sheptyakov, Dr. Mohammad Choucair and Fabio Giglio. The data discussion and analysis presented in this chapter was conducted in the course of this thesis if not otherwise stated.

4.3 Results and discussion

Prior to any sorption experiments the amount of transferred charge to the fullerene was investigated by means of Raman spectroscopy. As reported in literature there is a close empirical relation between the $A_g(2)$ Raman mode of C_{60} and the amount of charge transferred to the fullerene. While for pristine C_{60} $A_g(2) = 1469\ \mathrm{cm}^{-1}$ the mode is shifted to lower wavenumbers by 6–7 cm^{-1} per transferred electron [62, 45, 128]. Correspoding Raman spectra of $Na_{10}C_{60}$ and $Li_{12}C_{60}$ are depicted in figure 4.2.

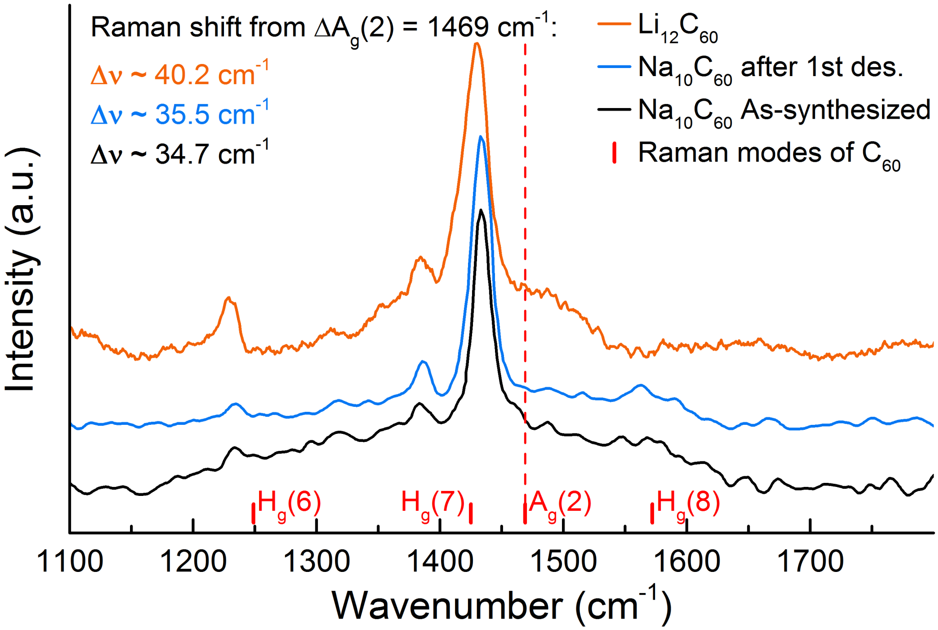

Figure 4.2: Normalized and y-axis shifted Raman spectra of as-synthesized $Na_{10}C_{60}$, $Na_{10}C_{60}$ after the first hydrogen sorption cycle and $Li_{12}C_{60}$. All spectra were recorded at room temperature; the sodium samples with a 532 nm laser at a power of 0.2 mW; the lithium sample with a He-Ne laser at 632.8 nm, 1 mW power and a 0.6 optical density filter to prevent polymerization. The red bars indicate Raman modes of pristine C_{60} [62]. The peaks have been fitted by Gaussian functions and the shift of their respective centers from 1469 cm^{-1} is indicated in the top left corner.

The sodium intercalated fullerene has initially a shift of about 35 cm^{-1} which shifts lower after the first hydrogen sorption cycle to about 36 cm^{-1}. With approximated 6 cm^{-1} per transferred electron this corresponds to a charge transfer of 6 electrons. For $Li_{12}C_{60}$ a shift of about 40 cm^{-1} was measured, corresponding to a charge transfer of 6.7 electrons. These charge transfers are lower than expected for such doping levels and might be an indication of a lower stoichiometry than the synthesis predicts. In particular the downshift after hydrogen sorption seen for $Na_{10}C_{60}$ indicates a change in structure. X-ray powder diffraction conducted on these samples will solidify these results and is discussed below.

Hydrogen and deuterium sorption experiments build the basis of the here reported investigations on $Na_{10}C_{60}$ and $Li_{12}C_{60}$. While the sodium intercalated sample was investigated both with hydrogen as well as deuterium gas the lithium fulleride was only investigated with deuterium due to an upcoming neutron diffraction experiment at that point in time.

An initial hydrogen absorption experiment of the as-synthesized sodium intercalated fullerene was conducted at 20 MPa H_2 and with a temperature ramp of 0.5 K per minute up to 673 K (see figure 4.3(a)). Absorption started around 423 K; which is about 200 K below pristine C_{60} [104]. A maximum of 2.2 mass% H_2 was reached at 573 K after which the sample started to desorb hydrogen with increasing temperature. As a result only 1.1 mass% of stored H_2 was retained after the measurement ended. The subsequent desorption experiment is shown in figure 4.3(b). Two distinct desorption peaks can be seen; the first one starting around 423 K and a second peak, sharper and larger than the first, with an onset temperature of about 523 K. The full 1.1 mass% H_2 were recovered via thermal desorption at a temperature of 673 K with the majority already released 100 K below the final temperature. Multiple absorption and desorption experiments on $Na_{10}C_{60}$ followed and all proved fully reversible. A typical absorption can be seen in figure 4.4 and in figure 4.3(c) the fifth desorption of $Na_{10}C_{60}$ is presented. The sample was hydrogenated at 623 K and 25 MPa for an extended period of time during which the maximum of 3.5 mass% hydrogen was stored. The desorption reveals a single sharp desorption peak with an onset temperature of 450 K.

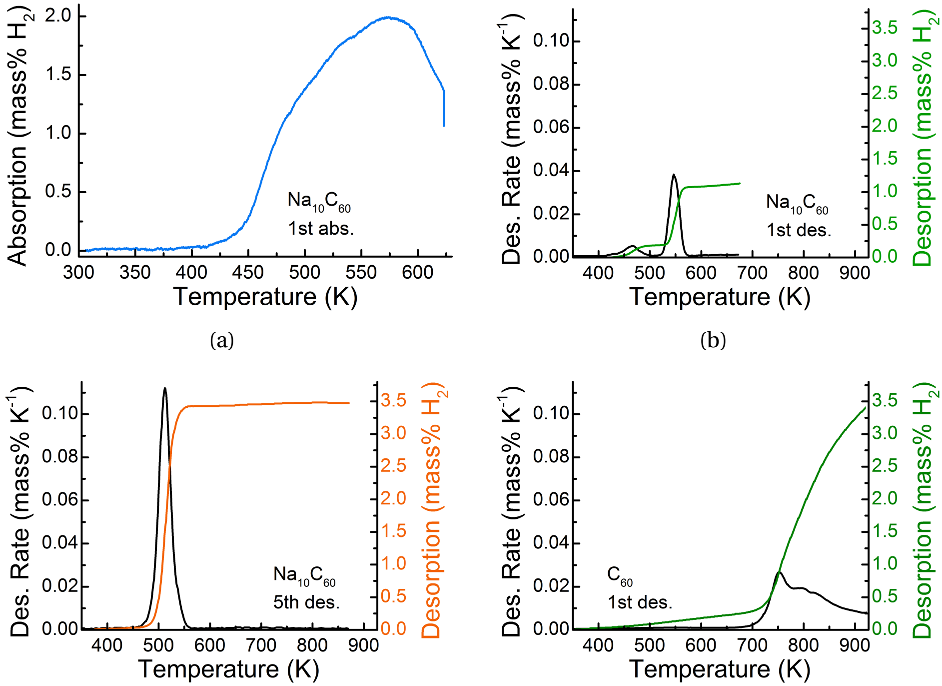

(a) (b) (c) (d)

Figure 4.3: **(a)** First hydrogenation of $Na_{10}C_{60}$ with an applied H_2 pressure of 20 MPa and a heating ramp of 0.5 K min^{-1}. The absorption onset temperature is reached at about 423 K and desorption begins at 573 K. **(b)** Desorption rate and desorbed hydrogen in mass% as a function of temperature for the first desorption of $Na_{10}C_{60}$ with a hydrogen back pressure of 0.1 MPa (corresponding absorption depicted to the left). Two distinct peaks during desorption can be seen at 423 K and 523 K; the temperature is ramped at 1 K min^{-1}. **(c)** Isochoric hydrogen desorption after the 5th absorption (623 K and 25 MPa) with a temperature ramp of 1 K min^{-1}. The pressure increased from vacuum to about 0.18 MPa and the full 3.5 mass% H_2 are recovered. The desorption onset temperature lies around 450 K. **(d)** First dehydrogenation of ball milled $C_{60}H_y$ as a function of temperature (heating ramp of 2 K min^{-1}). The sample was hydrogenated at 673 K and 12 MPa for 50 h. The desorption was not complete even at 973 K when the experiment was stopped and only 3.8 of 7.2 mass% H_2 are recovered.

In case of $Li_{12}C_{60}$ an isochoric deuterium absorption measurement was conducted prior to a scheduled neutron diffraction experiment. In a first step the temperature was ramped up at 0.5 K min^{-1} to 498 K at 19 MPa H_2 pressure, followed by a 45 h lasting isothermal absorption process which is presented in figure 4.4. The absorption onset temperature was below 373 K, even lower than for the sodium intercalated fullerene and more than 200 K below pristine C_{60}. At the end of this first step about 4.5 mass% H_2 were stored and upon cooling retained within the sample. A second absorption with a hydrogen pressure of

10 MPa at 623 K for 24 h resulted in an additional absorption of 0.5 mass% H_2 giving a total equivalent of 5 mass% H_2. Very similar to what Teprovich et al. reported for their mixed lithium intercalated fullerene [121]. At this elevated temperature the sodium sample already started to decompose and desorb hydrogen, indicating a higher stability of the lithium intercalated derivative.

In comparison to the two fullerides desorption data of ball milled and hydrogenated C_{60} is presented in figure 4.3(d). The fullerene sample was hydrogenated at 673 K and 12 MPa H_2 pressure and kept there for 50 h after which the sample had absorbed about 7.2 mass% H_2. Already upon hydrogen absorption the sample showed signs of degrading and X-ray diffraction revealed a strong amorphization (see figure 4.5). After the corresponding desorption, which started above 673 K and continued up to 973 K, when the experiment was stopped, no signs of crystallinity remained in the XRD pattern. Furthermore only around 3.8 mass% H_2 were released. The C_{60} sample turned from deep black to red, post-hydrogen absorption and showed up as an inhomogeneous powder suspended in liquid after the final desorption step. While no further analysis of the liquid was conducted it is reasonable to assume that via fragmentation of C_{60} not only gaseous but also liquid hydrocarbons are formed. A schematic illustration of the proposed mechanism for the irreversible hydrogenation and dehydrogenation of C_{60} can be seen in figure 4.10.

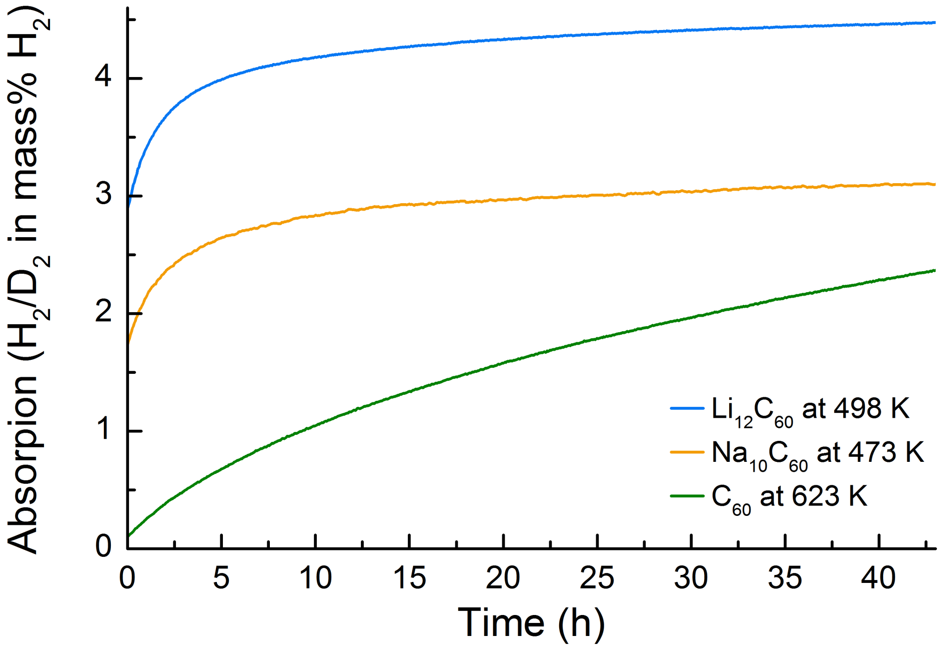

Figure 4.4: Isothermal hydrogen uptake of ball milled C_{60} (623 K and 18.5 MPa H_2) and $Na_{10}C_{60}$ (473 K at 20 MPa H_2); deuterium uptake of $Li_{12}C_{60}$ (498 K at 19 MPa D_2)

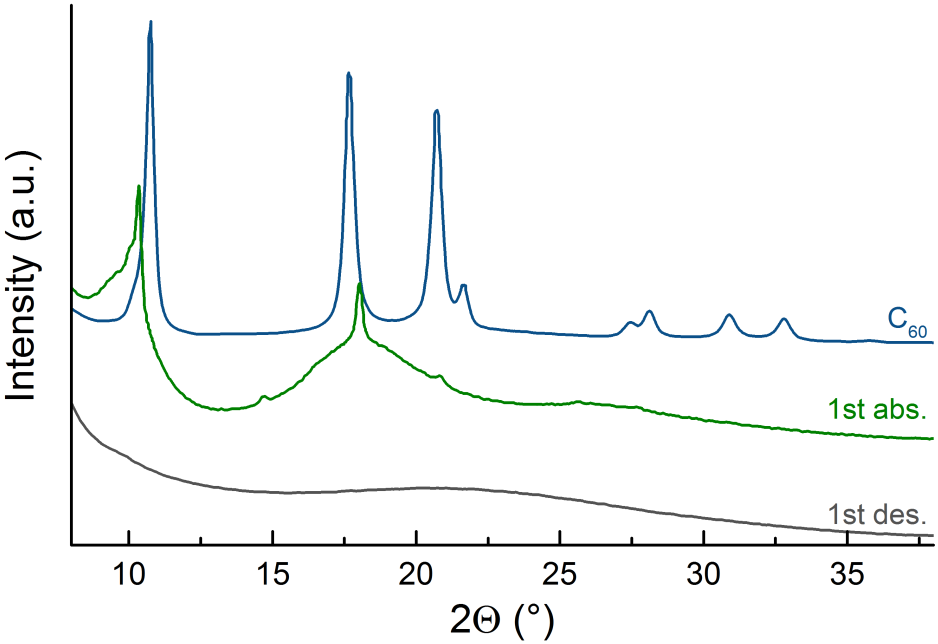

Figure 4.5: Normalized and y-axis shifted X-ray diffraction patterns of ball milled C_{60} (blue); after absorption $C_{60}H_x$ (green) and after desorption (grey). Hydrogenation took place at a temperature of 673 K and 12 MPa H_2 pressure where the sample was kept for 50 h. About 7.2 mass% of H_2 were absorbed. The reflection intensity and sharpness dramatically decreased upon hydrogenation indicating the destruction of the fullerene crystallites. Hydrogen desorption started around 673 K and continued up to 973 K when the experiment was stopped. During desorption only 3.8 mass% H_2 were recovered and no x-ray reflections remained.

Analogous to the hydrogenation and dehydrogenation of C_{60} the sorption processes for sodium and lithium fullerides have been followed via x-ray diffraction. Corresponding patterns are presented in figure 4.6.

As-synthesized $Na_{10}C_{60}$ exhibit multiple phases when compared to similar structures published in literature. Two phases in particular seem to make up most of the measured diffraction pattern. The main phase is in good agreement to an fcc phase of $Na_{9.28}C_{60}$ with space group $Fm\bar{3}$ (202) as published by Yilderim et al. [139]. The second and minor phase coincides well with the base-centered monoclinic phase of $Na_{3.82}C_{60}$, with space group C 1 2/m 1 (12), that Kubozono et al. found for their single phase sample [60]. Rietveld refinement of as-synthesized $Na_{10}C_{60}$ with the structural data for the main phase gives a lattice parameter of $a = 1.449$ nm [79]. This does not fit to either of the lattice parameters found in literature. By linear interpolation of the data for Na_3C_{60} (1.4191 nm [98]), Na_6C_{60} (1.4359 nm [98]) and $Na_{9.28}C_{60}$ (1.459 nm [139]) the Rietveld refined lattice parameter of 1.449 nm corresponds to an intercalation quantity of approximately $Na_{7.8}C_{60}$. After the first hydrogen sorption cycle the

XRD patterns of before and after do not coincide any longer. An irreversible process occurred and most of the reflections, corresponding to the monoclinic phase, vanished. This can be explained by a hydrogen assisted annealing process. This structural reformation and the lower than expected stoichiometry are in good agreement with the measured charge transfer by means of Raman spectroscopy. Upon hydrogenation the fcc lattice structure measurably expands, reflections move to smaller angles, and desorption causes the lattice to contract again. A strong indication of hydrogen absorption by the fulleride structure [103]. A remarkable feature is seen around 32°, 37° and 53° for the pattern recorded after the second hydrogenation. Strong reflections emerged that can be assigned to NaH, probably originating from sodium deintercalated from the $Na_{10}C_{60}$ [145]. Upon dehydrogenation the NaH reflections disappear completely and the XRD pattern equals the one before hydrogenation. A possibility for the hydrogen uptake could thus have been the formation of NaH but even if all sodium would deintercalate during hydrogenation to form

$$\mathrm{Na_{10}C_{60}} + 5\,\mathrm{H_2} \Rightarrow 10\,\mathrm{NaH} + \mathrm{C_{60}} \tag{4.1}$$

only about 1 mass% hydrogen could be absorbed. Furthermore the lattice expansion upon hydrogenation and subsequent contraction after desorption as well as that the strong reflection at $\approx 11°$ shows shoulders on both sides, are strong reasons against this explanation. While for pristine C_{60} a sharp reflection at a similar position is typical the shoulders around $\approx 11°$ indicate additional phases besides C_{60}. It is thus likely that just parts of the sodium deintercalates from the fulleride structure with the remaining sodium assisting hydrogenation of the carbon matrix. A possible hydrogenation can follow a process like

$$\mathrm{Na_{10}C_{60}} + x\,\mathrm{H_2} \Rightarrow a\,\mathrm{NaH} + \mathrm{Na}_{10-a}\mathrm{C}_{60}\mathrm{H}_{2x-a} \tag{4.2}$$

The fact that the NaH reflections disappear during dehydrogenation is particularly interesting since the process occurs at a temperature were NaH is generally stable (decomposition temperature of NaH = 698 K [43]). The lack of other sodium reflections after desorption and the resemblance of the patterns before and after the hydrogenation cycle can be explained by a subsequent reintercalation of Na into the fulleride structure.

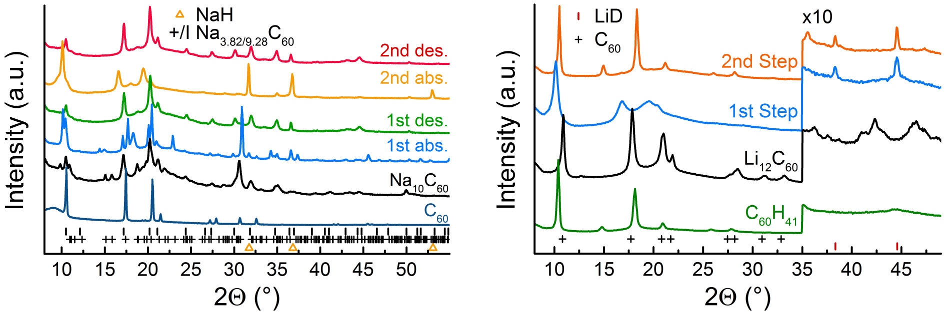

(a) (b)

Figure 4.6: Normalized and y-axis shifted X-ray powder diffraction patterns measured at room temperature. **(a)** $Na_{10}C_{60}$ before and after the first and second hydrogenation and subsequent dehydrogenation. A reference ball milled C_{60} sample is depicted at the bottom. Furthermore the reflections of NaH (yellow triangles, [145]), $Na_{3.82}C_{60}$ (black plus, [60]) and $Na_{9.28}C_{60}$ (black bar, [139]) are indicated by their respective symbols. **(b)** $Li_{12}C_{60}$ as-synthesized and after the first (498 K, 19 MPa) and second (623 K, 10 MPa) deuteration step. A commercially available reference sample of $C_{60}H_{41}$ from MER Corporation is depicted at the bottom. Reflections of LiD (red bars, [146]) and the fcc structure of C_{60} (black pluses, [13]) are indicated by their respective symbols.

The XRD patterns of $Li_{12}C_{60}$, presented in figure 4.6(b), show a similar feature. The dominant reflections of $Li_{12}C_{60}$ can be ascribed to the fcc structure of C_{60}. Upon the first deuteration step (498 K and 19 MPa D_2) these reflections broaden and shift towards smaller angles indicating a deuterium induced expansion of the lattice. After the second step of deuteration (623 K and 10 MPa D_2) the fcc structure disappeared and the reflections resemble a bcc type structure, very similar to commercially available $C_{60}H_{41}$ (MER Corporation). Since no structural data is available at this time Rietveld refinement was not performed. In addition to this bcc structure a second phase is visible with reflections around 38.4° and 44.6° which completely vanish after desorption (see figure 4.9). Analogous to NaH this phase can be ascribed to deintercalated LiD [146]. Would the entire lithium content deintercalate to form LiH, during hydrogenation instead of deuteration, only about 1.5 mass% H_2 would be stored (see equation 4.3). If additionally the fullerene structure would hydrogenate and form $C_{60}H_{36}$ the summed up capacity would be around 5.6 mass% H_2 (see equation 4.4). In comparison $C_{60}H_{36}$ has a hydrogen content of around 4.8 mass%.

$$Li_{12}C_{60} + 6\,H_2 \Rightarrow 12\,LiH + C_{60} \tag{4.3}$$

$$Li_{12}C_{60} + 24\,H_2 \Rightarrow 12\,LiH + C_{60}H_{36} \tag{4.4}$$

The reintercalation of LiD during desorption is remarkable since pristine LiD has a melting point close to 1000 K, almost 400 K higher than the temperature at which reintercalation takes place.

XRD indicates that a fraction of the absorbed hydrogen, equivalently deuterium, is bound by deintercalated Na and Li. It was shown that the intercalated amount of alkali metals does not account for the large quantity of stored hydrogen as seen by volumetric absorption measurements. In this respect infrared spectroscopy is used to verify the existence of hydrogen covalently bound to carbon which can account for the additional hydrogen absorbed by the samples. In figure 4.7 infrared spectra of C_{60}, $Na_{10}C_{60}$ and $Li_{12}C_{60}$ are depicted. The hydrogenated sodium samples show clear bands around 2800–3000 cm^{-1}. This corresponds to typical C–H stretching bands of hydrofullerenes and as a reference pristine C_{60} and $C_{60}H_{41}$ are shown [103]. Since $Li_{12}C_{60}$ was deuterated rather than hydrogenated the corresponding C–D vibrations are at lower wavenumbers [103, 119]. After desorption the C–H and C–D bands disappeared entirely. In addition to the previously conducted analysis the infrared spectra are a clear indication that the majority of hydrogen is bound covalently to the carbon scaffold rather than to the dopand alkali metal.

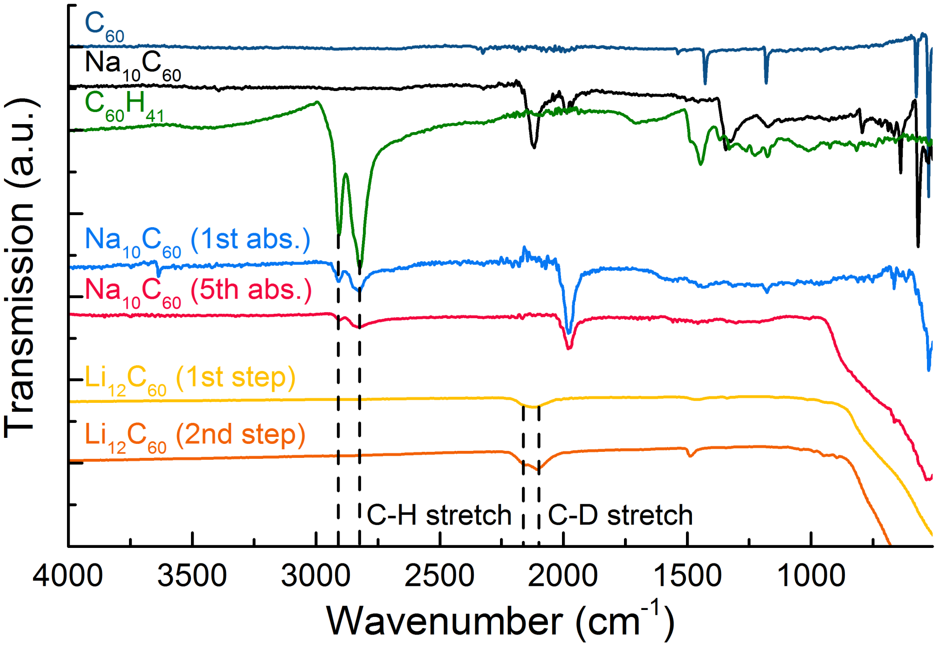

Figure 4.7: Normalized and y-axis shifted fourier transform infrared spectra of C_{60}, $C_{60}H_{41}$ (MER Corporation), $Na_{10}C_{60}$ (as-synthesized and after the first and fifth hydrogenation) and $Li_{12}C_{60}$ (after the first and second step of deuteration). C_{60}, as-synthesized $Na_{10}C_{60}$, and $Na_{10}C_{60}$ after the first absorption have been diluted in KBr to increase transmission and thus improve the spectra. Typical C–H and C–D stretch vibration bands, as published in literature have been indicated by dashed lines [103] C–D [103, 119].

To further support the proposed sorption processes for sodium and lithium intercalated fullerenes new batches of $Na_{10}C_{60}$, without traces of $Na_{3.82}C_{60}$, and of $Li_{12}C_{60}$ were synthesized. Subsequently deuterium absorption and desorption was followed by means of in situ neutron powder diffraction respectively. The recorded diffraction patterns of sodium fulleride are presented in figure 4.8. The sample was initially kept at room temperature and 0.1 MPa helium pressure. The reflections coincide well with the previously discussed fcc (Fm$\bar{3}$ (202)) structure of $Na_{9.28}C_{60}$ and Rietveld refinement yields a lattice parameter of 1.454 nm [79]. This corresponds to $Na_{8.6}C_{60}$, in analogy to the linear interpolation conducted for the XRD data. The most intense reflections around 53.8° and 63.1° originate from the steel of the sample holder and have not been included in the further discussion. The application of 10 MPa D_2 has no visible impact on the pattern. The temperature was stepwise increased and patterns at 423, 523 and 623 K are plotted in figure 4.8. The temperature increase leads to a linear thermal expansion, however, at 523 K an abrupt increase of the lattice parameter a was recorded and is depicted in the inset of figure 4.8). The lattice expansion is coincidental with the emergence of a new phase that was identified as NaD. Further heating to 623 K results in the disappearance of the NaD phase and the dramatic decrease of the lattice parameter. The patterns before deuteration and at 623 K overlap very well, indicating that a majority of deuterium desorbed at this temperature. The intercalation of C_{60} does not only lead to Pauli repulsion, ultimately leading to a lattice expansion, but the ionic interaction between the anion C_{60}^{n-} and the A^+ cations can lead to a lattice contraction. Upon deintercalation this ionic interaction decrease and can lead to an effective expansion of the lattice. At the same time Somenkov et al. have measured a for different stoichiometries of $C_{60}D_x$ and a linear fit on their published data gives a relation between a and x following [110]:

$$a = 0.0024\ \mathrm{nm} \cdot x + 1.4098\ \mathrm{nm} \tag{4.5}$$

With a measured deviation from the thermal lattice expansion at 523 K of $\Delta a \approx 0.03$ nm equation 4.5 yields a deuteration corresponding to $C_{60}D_{17}$. With a full deintercalation of Na and subsequent deuteration to form 10 NaD + $C_{60}D_{17}$ an equivalent of 2.8 mass% H_2 can be stored. However, the measured XRD data indicates that a fraction of sodium remains within the lattice. This excess sodium will give an additional lattice contraction and higher loadings could thus be possible without such a dramatic expansion as seen for pure C_{60}. While it was not possible to undoubtedly determine the precise sorption mechanism of $Na_{10}C_{60}$ a tentative proposition of the process can be seen in figure 4.10.

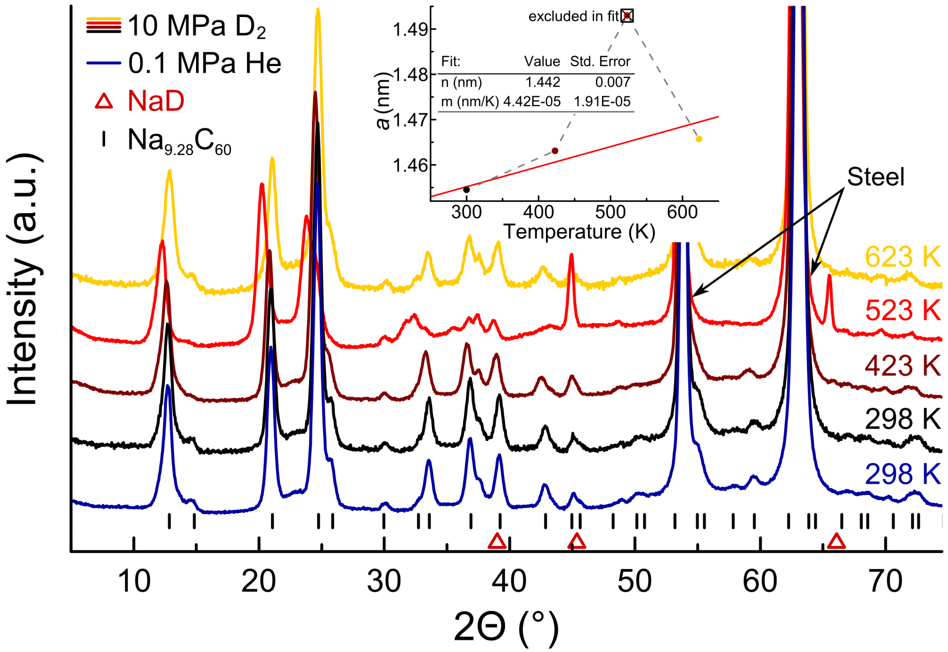

Figure 4.8: Neutron powder diffraction patterns of $Na_{10}C_{60}$ at different temperatures. The blue line represents data for an applied 0.1 MPa helium; all other data corresponds to an applied pressure of 10 MPa deuterium. Reflections of $Na_{9.28}C_{60}$ are plotted at the bottom as black bar [139]; NaD reflections are marked with red triangles and appear at 523 K [109]. The strong reflections at 53.8° and 63.1° originate from the steel-sample holder and have not been included in the further discussion. The inset shows the results of the refined lattice constant a as a function of temperature [79]. A linear fit (red line) was performed for the points at 300, 423 and 623 K and the results are presented in the table.

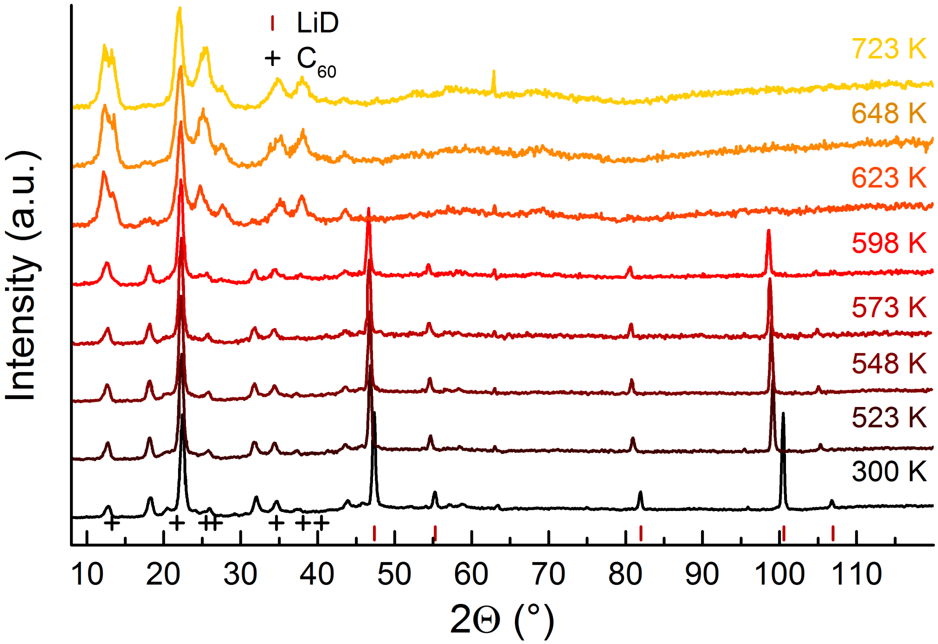

Figure 4.9: Neutron powder diffraction patterns of deuterated $Li_{12}C_{60}$ at different temperatures. The sample was deuterated beforehand at 623 K and 10 MPa D_2, corresponding to the second step in figure 4.6(b). Reflections of LiD are indicated with red bars and start to vanish with increasing temperature with the onset at 598 K [146]. Coincident with the apparent reintercalation of LiD and the desorption of deuterium, the bcc type structure reforms and starts to resemble that of fcc C_{60} again (black plus sings, [13]); analogously to the XRD data. The sharp reflection at 62.9° does not change position with temperature and shows irregular variation in intensity marking it as a possible artifact.

In case of in situ neutron powder diffraction of $Li_{12}C_{60}$ a vanadium sample holder was used instead of the one made of steel. This dramatically reduced the influence of the sample holder on the measurement. The deuterated sample shows strong reflections for LiD [146] and the bcc type structure that was discussed for the XRD experiment. Following the temperature ramp the recorded patterns equal one another apart from the typical thermal expansion. At a temperature of 598 K, however, the intensities of the LiD reflections start to decrease and vanish for the pattern at 623 K. While for the deuteration recorded with XRD the sample underwent a structural reformation from an fcc to a bcc type structure the reverse process is seen for the desorption and the patterns at 623, 648 and 723 K show reflections that can be ascribed to the fcc structure of C_{60} [13]. A reaction pathway similar to that one of $Na_{10}C_{60}$ can be proposed:

$$Li_{12}C_{60} + x\,H_2 \Rightarrow a\,LiH + Li_{12-a}C_{60}H_{2x-a} \qquad (4.6)$$

Due to the current lack of knowledge concerning the structural changes between hydrogenated and unhydrogenated $Li_{12}C_{60}$ no illustration of the reaction pathway is proposed. However, the above discussed results indicate that it is probable that the reaction is closely resembling that of $Na_{10}C_{60}$ with the difference of an intermediate reformation to a bcc structure during hydrogenation.

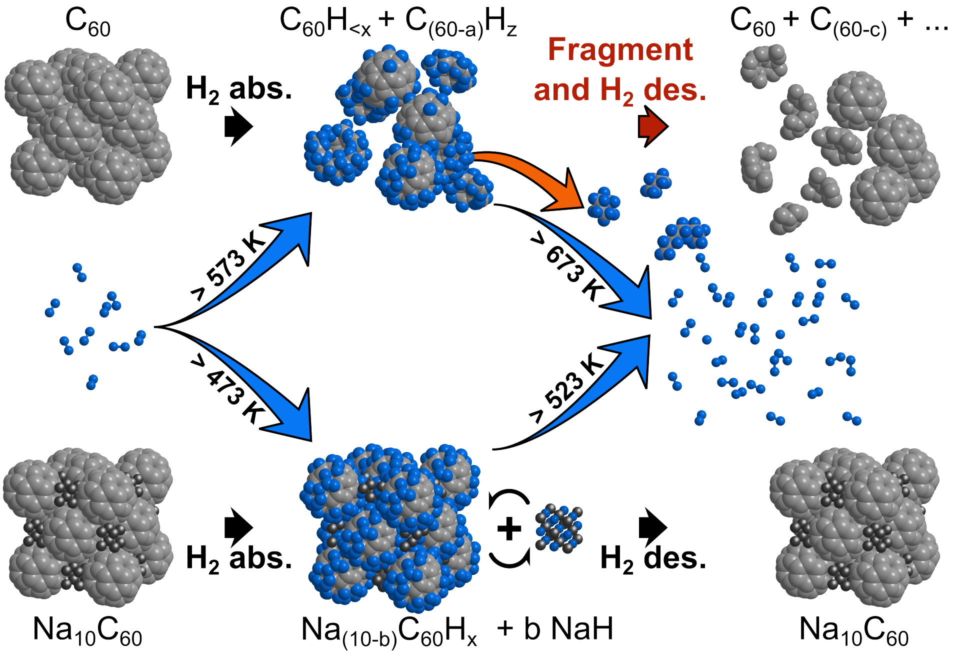

Figure 4.10: **(Top)** The irreversible hydrogen sorption cylce of C_{60}. After absorption with an onset temperature 573 K already a small fragmentation of the fullerene cages is visible. Prolonged hydrogenation at elevated temperatures further reduces crystallinity of the fullerene structure. Desorption starts above 673 K and only parts of the hydrogen is released from the fullerenes. A larger part fragments further to form various hydrocarbons releasing the hydrogen at much higher temperatures. **(Bottom)** The reversible hydrogen sorption cycle of $Na_{10}C_{60}$. Hydrogen sorption starts at an onset temperature of 473 K. During hydrogenation parts of the intercalated sodium deintercalates from the fulleride structure to form NaH. The majority of hydrogen is, however, covalently bound to the fulleride. At a temperature above 523 K hydrogen desorps again and sodium reintercalates into the fulleride structure. This sorption cylce is fully reversible and can store up to 3.5 mass% H_2.

5

Corannulene as anode material for Li-ion batteries

5.1 Introduction

Lithium-ion batteries have become one of the most important energy storage technologies on today's market. Their market penetration reaches from small portable devices such as smartphones, tablets and portable PC's to larger stationary solutions like short term storage of renewables and uninterruptible power supplies (UPS) and are even up to the most challenging task of electric mobility. The huge success of past R&D endeavors have lead to the presently most common form of Li-ion batteries with an anode based on carbonaceous materials. The positive electrode is commonly based on a transition metal oxide such as $LiCoO_2$ or $LiMn_2O_4$. Both are connected via an electrolyte, typically a lithium containing salt (e.g. lithium hexafluorophosphate $LiPF_6$) dissolved in a carbonate-based organic, non-aqueous liquid solvent absorbed in a porous plastic separator. During discharging and charging Li^+-ions are intercalated and deintercalated into the active materials of anode and cathode respectively. Throughout the existence of commercial Li-ion batteries, carbonaceous materials have been studied and used as anode materials. In particular the low cost, high abundance and low mass of carbon as well as the potential safety and reliability of carbon-based materials are advantages of these systems. Most commercially available products utilize naturally or industrially available carbon materials such as natural graphite, cokes, carbon fibers, non-graphitizable carbon, and pyrolitic carbon. These, however, are by origin not specially tailored as Li-ion storage materials and in recent years tremendous efforts have been undertaken to enhance critical properties, such as specific surface area,

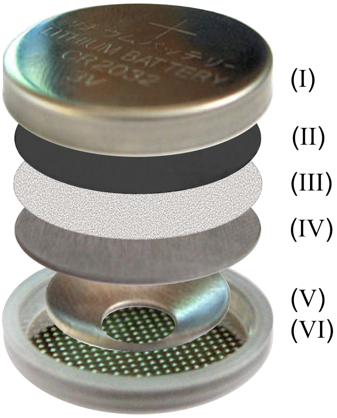

Figure 5.1: Schematic of a typical coin-type half cell setup made of stainless steel (SS) with integrated polypropylen (PP) sealing O-ring. (I) SS-can. (II) Coated Cu foil. (III) Cellguard seperator (PP). (IV) SS-Spacer with Li foil. (V) SS-Cone spring. (VI) SS-Lid with gasket (PP).

porosity and monodispersity, amongst others, to achieve higher capacities, a longer cycle life and overall stability.

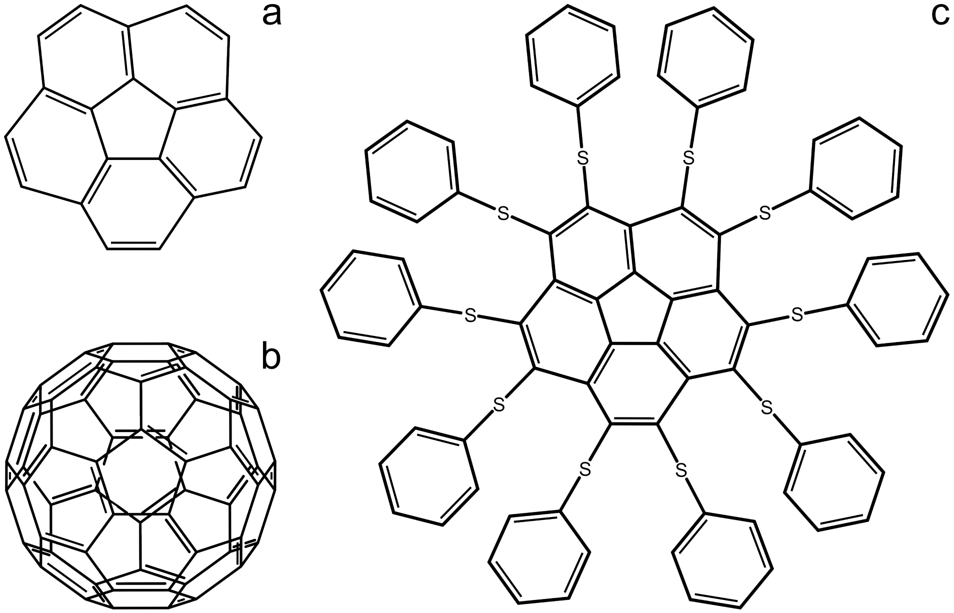

Figure 5.2: (a) Schematic top view of corannulene. (b) Schematic of a C_{60} buckminsterfullerene. (C) Schematic top view of decakis(phenylthio)corannulene.

In capter 4 the hydrogen sorption of $Li_{12}C_{60}$ fullerides was addressed. It was shown that, even under conditions for hydrogen sorption, lithium partly intercalated and deintercalated into the fulleride crystals. It naturally follows to address the Li-ion sorption characteristics of this class of materials. Depending on the hydrogenation state, $C_{60}H_x$-based anodes can achieve stunning capacities as high as 1100 Ah/kg ($Li_{y\leq x}C_{60}H_x$) [71] and it was proposed that the curvature of the aromatic carbon system can have a strong influence on the lithium storage capacity [99]. A recent paper elucidated the lithium-coordination in lithiated corannulene ($Li_4C_{20}H_{10}$), which can be thought of as the smallest subunit of C_{60} still retaining such a curvature that none of the five benzene rings are coplanar [142]. In contrast to C_{60}, corannulene can accept one electron per five carbon atoms (${C_{60}}^{6-}$ accepts one electron per 10 carbon atoms) and is thus more electron rich in its highest reduction state. The mentioned paper presents single-crystal x-ray diffraction evidence for five Li^+ ions, sandwiched between two anionic corannulene decks, two more Li^+ ions externally bound to the top and bottom of the sandwich and a remaining Li^+ cation solvent-separated [142]. It remains to be proven if the, in this way stored, lithium is accessible and can easily intercalate and deintercalate from corannulene-based anode systems. While some results on corannulene half cells have been published some time ago, with reversible capacities of 464 Ah/kg and 602 Ah/kg for at least 5 cycles, research indicates that the full storage potential of the material has not been reached [99, 57]. Here we want to present preliminary results of the investigation of this promising carbonaceous material for Li-ion battery anodes.

5.2 Experimental

Prior to the electrode fabrication corannulene ($C_{20}H_{10}$) and decakis(phenylthio)corannulene (D-corannulene, $C_{80}S_{10}H_{50}$) was hand-ground with agate mortar and pestle to homogenize the active material (structure models in figure 5.2). Subsequently a mixture of 63.75 mass% corannulene, 21.25 mass% carbon black (Super C65, TIMCAL) and 15 mass% carboxymethyl cellulose binder (CMC, grade:2200, Daicel Fine Chem Ltd.) was suspended in purified water (91 mass% liquid to 9 mass% solid) and ball milled for 1 h at 600 rpm. CMC binder was used as a chemical adhesive and since it is well known to effectively enhance capacity retention and is commonly used for carbon-based systems [143, 67, 20]. In this context it is important to note that, since the choice of binder has a critical impact on the performance of the electrode performance, the CMC binder was chosen purely on the basis of previous research on other active materials and may not represent the optimum for corannulene and decakis(phenylthio)corannulene. One batch of corannulene current collectors was thus prepared with a different binder, polyvinylidene fluoride (PVDF), which, however, yielded very similar results to CMC. Well dispersed carbon black ensured good and homogenous electrical conductivity over the entire electrode. The resulting aqueous slurry was evenly cast onto, previously weighed, copper foils. The foils were dried under air at room temperature for 3 h, to remove the solvent, and subsequently placed in a vacuum oven where they continued to dry under moderate vacuum conditions and 345 K for an additional 12 h. For a consecutive measurement of the mass of the active electrode material the dried current collectors were weighed again whereafter they were transferred in a Ar-filled glovebox $\left(O_2 < 1\ \text{ppm}, H_2O < 1\ \text{ppm}\right)$ at which point standard 2025-sized coin-type cells were assembled (see figure 5.1). A Li metal foil served as both reference and counter electrode. The electrodes were separated by Celgard separators (Celgard 2400, 25 μm microporous monolayer polypropylene membrane, Celgard Inc. USA). The electrolyte was 1 M $LiPF_6$ in ethylene carbonate:diethylcarbonate (EC:DEC 1:1 by weight, Novolyte) with an additional 3 mass% fluoroethylene carbonate (FEC). $LiPF_6$ and EC:DEC is often regarded as the standard, first choice solution for Li-ion battery systems [143]. Non-aqueous, polar aprotic electrolyte systems can be used in moisture-sensitive materials and have the advantage of high ionic conductivity, anodic stability and that EC and DEC form dense solid-electrolyte-interface layers (SEI). FEC was added to additionally enhance and stabilize the SEI formation to increase cyclic stability and capacity retention [46, 22].

Electrochemical cycling tests were conducted using a multichannel workstation from Astrol between (0.02–2 V) versus the Li metal foil and a maximum current density of 50 A/kg. Capacities were normalized to the mass of corannulene/D-corranulene while possible contributions from the amorphous carbon were neglected. A total of two sets of 4 corannulene-based cells (one with CMC and one with PVDF binder) and one set of 3 D-corannulene (with CMC) based cells were measured.

5.3 Results and discussion

All assembled half-cells were measured versus metallic lithium at room temperature, as described above in section 5.2. As expected a slight distribution in the measured capacities for the different assembled cells was observed and is caused by variations in the relative ratios of electrolyte, electrode material, thicknesses et cetera. Representative profiles of discharge and charge curves for corannulene and D-corannulene are presented in the figures 5.4 and 5.6 respectively. For the corannulene cell an initial discharge capacity of 407 Ah/kg was observed with a following second discharge capacity of only 144 Ah/kg. An irreversible fraction of the total capacity is common and stems from the formation of a solid-electrolyte interface layer, a lower value is favored [130]. The measured initial discharge capacity of corannulene is surprisingly low compared to 802 Ah/kg as previously published in literature [99]. Further cycling of the cell slowly recovered part of the initial capacity with a maximum of 208 Ah/kg to 197 Ah/kg for discharge and charge profiles after the 18th cycle (fully lithiated graphite LiC_6 shows ≈ 372 Ah/kg [137, 127]). The similarity in charge and discharge capacity corresponds to a good coulombic efficiency of about 95 % that even increased for higher cycling numbers. Reversible Li^+ capacities of corannulene of 464 Ah/kg and 602 Ah/kg can be found in literature [99, 57] and are substantially higher than the measured 208 Ah/kg. The comparison shows that not only the initial capacity but also the reversible capacity are much lower than expected. However, none of the cited capacity values are underpinned by presented measurement data and might thus be taken with a grain of salt. A final conclusion about what caused the large difference between literature and the gathered experimental data can not be drawn as of yet. Probable but not exclusive reasons for the poor cell performance include non optimal choice of binder, electrolyte, addition of FEC and unfavorable cycling conditions.

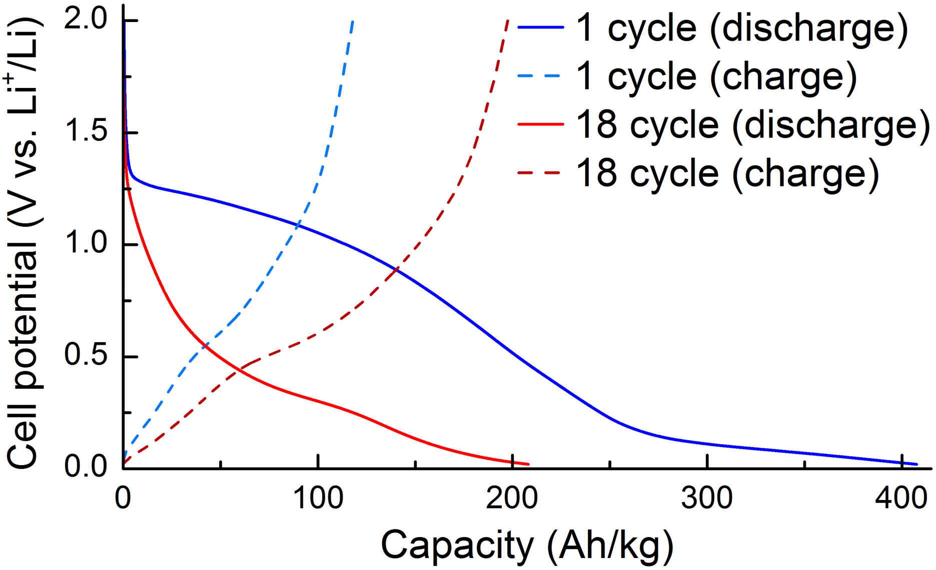

Figure 5.3: Galvanostatic charge-discharge cycling potential versus capacity for the coin-type cell based on 63.75 mass% corannulene. The first discharge cycle shows two plateaus with the first originating from the formation of the SEI. The second plateau is also present in discharge cycle 18 and corresponds to an intercalation of Li ions into the active material. Equivalently the small plateaus present in the charge cycles originate from deintercalation of lithium from the corranulene electrode.

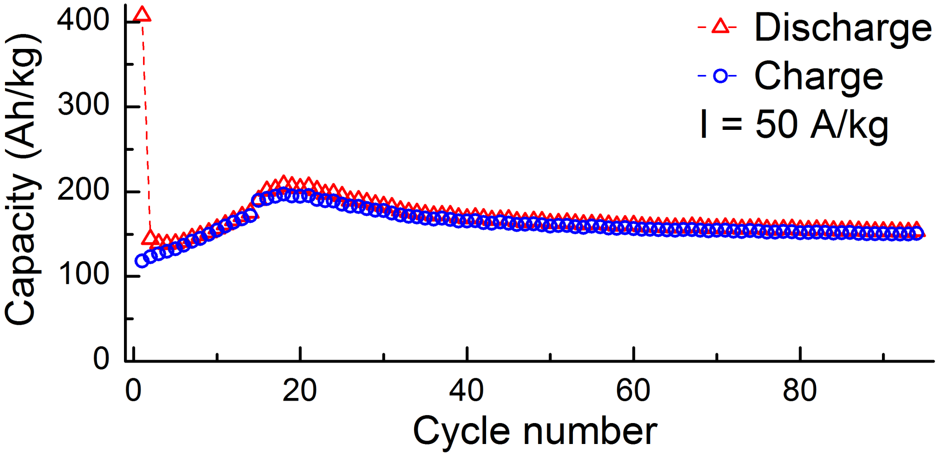

Figure 5.4: Discharge and charge capacities for an anode containing 63.75 mass% corannulene. The cycles were run between 0.02–2 V and with a current density of 50 A/kg. The capacities are normalized to the corannulene content. After the sixth cycle an average coulombic efficiency of 98 % was reached.

For the coin-type cell based on D-corannulene a high initial capacity of 741 Ah/kg was observed. After the formation of the typical solid-electrolyte-interface layer during the first cycle the measured capacity for the subsequent cycles is even lower than for the corannulene cell. Only an average of about ≈ 60 Ah/kg was reached. At such poor capacities it might not longer be feasible to neglect the influence of carbon black on the overall capacity of the cell. It is thus possible that carbon black is, at least partly, responsible for the measured capacity while D-corannulene does not contribute. Figure 5.5 shows the cell potential versus the measured capacity. Contrary to the equivalent measurement for corannulene (see figure 5.3) no plateau is observed during charging. With this and the poor capacity in mind it is conceivable that the required cell potential, necessary to deintercalate the Li-ions, was not reached during the experiment. At higher voltages a charging might takes place which in turn could recover capacity. However, this is speculative and has to be investigated in further measurements with particular attention placed on the stability of all cell components at such high proposed potentials. After these preliminary tests it is nevertheless evident that a more careful selection of every single element in the battery has to be made to succeed in the approach of the theoretically high lithium storage capacity of corannulene and D-corannulene.

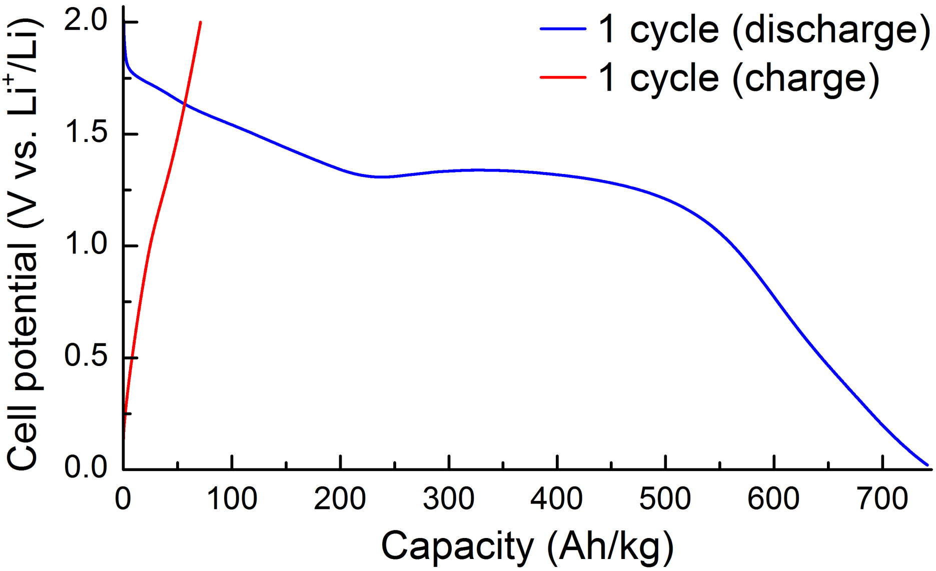

Figure 5.5: Galvanostatic charge-discharge cycling potential versus capacity for the coin-type cell based on 63.75 mass% decakis(phenylthio)corannulene. The broad plateau in the discharge cycle is caused by the formation of a solid-electrolyte interface layer.

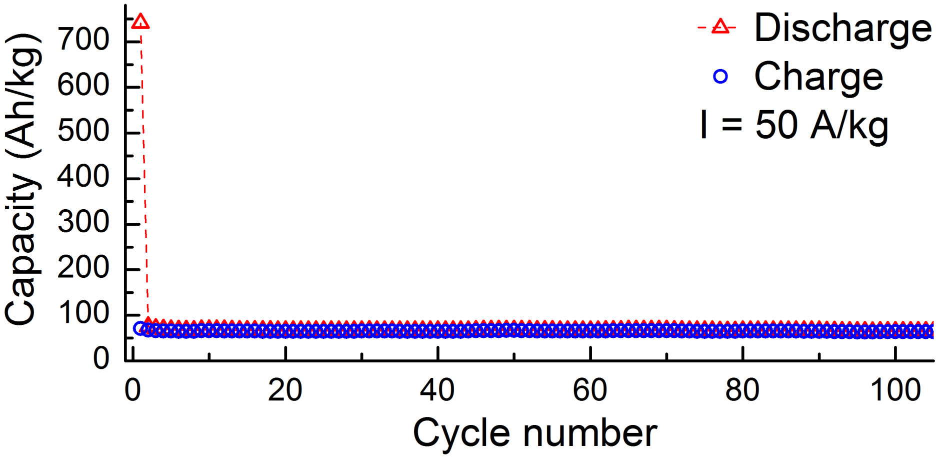

Figure 5.6: Discharge and charge capacities for an anode containing 63.75 mass% decakis(phenylthio)corannulene. The cycles were run between 0.02–2 V and with a current density of 50 A/kg. The capacities are normalized to the decakis(phenylthio)corannulene content. After the sixth cycle an average coulombic efficiency of 98 % and a capacity of ≈ 60 Ah/kg was reached.

6

Summary of results

The studies reported on in this thesis were aimed for a better understanding of novel, nanoscale, carbon-based materials with respect to their structure and the resulting effects on energy storage related properties. The driving force behind carbon as a basis for energy storage materials is the low atomic weight, high abundance and accessibility in addition to carbons valency, making it extremely versatile with respect to structural modification. In this context three different classes of materials were selected for further investigation; namely metal decorated thermally exfoliated graphites, metal intercalated fullerenes and corannulene derivatives.

Metal decorated graphenes, in particular lithium and nickel decorated TEGO, were produced in a two step synthesis and under inert conditions. The resulting carbon backbone was identified as a defective graphitic matrix with monolayer-graphene like areas surrounded by a slim network of graphite multilayers. The majority of carbon is bound as sp^2 carbon, with only fractional quantities of sp^3. The meticulous care that was taken ensured a low oxygen content of only about 3 %At Conc. and marginally more for the metal decorated samples. While the skeletal density of TEGO was measured to be close to that of graphite the BET specific surface area proved larger than 500 m^2g^{-1} with the possibility of significant increase. Results on the lithium decorated samples and their extreme sensitivity towards oxidation call a possible applicability as a storage material into question. On the other hand the samples decorated with nickel proved less reactive towards contamination, conserving the possibility of a whole zoo of materials that can be deposited onto TEGO and subsequently be tested in a likewise manner. The chosen synthesis conditions produced monodispersed nickel nanoparticles of slightly prolonged prolate spheroid shape and an approximate diameter of 17 nm. The nickel remains metallic and due to the nanometer size the particles display superparamagnetic behaviour above their average blocking temperature. While the main motivation of this thesis lies in the sector of energy storage it is important to note that especially nickel nanoparticles are proposed to find use in many other areas; amongst others for catalysis, medical applications, as electrochemical capacitors or as sensor materials. A viable synthesis approach is therefor appreciated in a broad context. Concerning energy storage the presence of nickel nanoparticles significantly enhances the physisorption of hydrogen and an increase in hydrogen storage capacity of almost 50 % (at 77 K), compared to carbon with the same specific surface area, can be reported. For muon spin repolarization measurements a large missing fraction of close to 40 % is seen. The signal was recovered with a longitudinal field easily assignable to muonium-adduct radical formation; a clear fingerprint of a strong interaction with atomic hydrogen that has not been seen for undecorated TEGO. While these findings demonstrate the dramatic enhancement of the carbon hydrogen interaction for both molecular as well as atomic hydrogen, no evidence for Kubas interaction or hydrogen spillover, as has been predicted by theory, was found. The characteristics of the chosen synthesis path opens up the possibility to additionally alter determining parameters like the nanoparticle size and distribution, the structure of TEGO as well as the deposition material. This implements the possibility to investigate the influence of each of the named parameters separately and might elucidate the origin of the discovered hydrogen-carbon interaction enhancement. Furthermore sorption measurements at higher temperatures might enable the dissociation of hydrogen and therewith increase the overall capacity through a different type of hydrogen bond.

Hydrogen and deuterium sorption measurements were conducted on $Na_{10}C_{60}$ and $Li_{12}C_{60}$. At a hydrogen pressure of 20 MPa and a temperature of 473 K a hydrogen content of 3.5 mass% is reversibly stored. Desorption starts at an onset temperature of 523 K with a back pressure of 0.1 MPa H_2. In case of $Li_{12}C_{60}$ deuteration starts already below 373 K, while desorption takes place at around 573 K with an equal back pressure. At the optimal conditions $Li_{12}C_{60}$ stores an equivalent of 5.5 mass% H_2, fully reversible. Both absorption and desorption for the sodium as well as lithium fulleride take place at significantly lower temperatures than for pure C_{60} and have dramatically increased kinetics; indicative of a lower stability of the fullerides. The appearance of NaD and LiD, upon deuteration of $Na_{10}C_{60}$ and $Li_{12}C_{60}$ respectively, was observed by means of powder X-ray diffraction and in situ neutron powder diffraction. Reflections of both compounds disappear entirely during desorption. This has been explained by the deintercalation and subsequent reintercalation of sodium and lithium during sorption of the fullerides. While both alkali metal hydrides are known to store hydrogen readily the stoichiometry of the intercalated metal is to low to accommodate the measured amounts of absorbed D_2. Additionally FT-IR measurements show C–D stretching vibration bands of covalently bound deuterium revealing that a majority is stored on the fullerene rather than the deintercalated metal clusters. What is remarkable in this context is that the reintercalation takes place at temperatures several hundred Kelvin below the melting points of both NaD and LiD. Future investigations will need to address the influence of the intercalation induced charge of the fullerenes and if it remains upon deintercalation of the metal atoms. The sorption mechanism, tentatively explained in this thesis, is furthermore not undoubtedly determined and needs clarification to fully understand this apparent interplay of mutual destabilization of all involved compounds.

Besides work on hydrogen as an ideal intermediate energy storage medium the investigations conducted during this thesis work delved into a more conventional field of energy storage, that of Li-ion battery storage systems. The research on $Li_{12}C_{60}$ demonstrated the reduced stability of LiD in the presence of fullerenes, where the intercalation and deintercalation of lithium took place at temperatures well below that typically necessary to decompose the compound. The desire for a thorough investigation of the Li-ion sorption characteristics of this class of materials was clearly propelled by these findings. However, while C_{60} accepts one electron per 10 carbon atoms corannulene can accept one electron per five carbon atoms and thus demonstrates a much higher electron affinity than even C_{60}. Since lithium is ionically bound to the carbon scaffold a higher number of accepted electrons should enable a higher lithium doping level. In this context corannulene and decakis(phenylthio)corannulene have been investigated for their reversible lithium storage capacity by means of room temperature electrochemical cycling tests. Preliminary tests revealed poor storage capacities for both derivatives. While these results are by no means conclusive they give strong impulses for future measurements and in particular call for a careful selection of every single element in the assembled electrochemical cells. This is paramount if one wishes to succeed in the approach of the theoretically high lithium storage capacity of corannulene and decakis(phenylthio)corannulene.

List of scientific presentations

The following is an excerpt of the given scientific presentations and publications directly related to the research presented in this thesis.

1. **Hydrogen Adsorption Properties of Metal Decorated Graphene**
   Poster presentation, International Symposium on Metal-Hydrogen Systems (23.10.2012) Kyoto, Japan
   http://www.mh2012.jp/

2. **Reversible Hydrogen Absorption in Sodium Intercalated Fullerenes**
   Talk, International Symposium on Metal-Hydrogen Systems (23.10.2012) Kyoto, Japan
   http://www.mh2012.jp/

3. **Enhancing the Hydrogen Graphene Interaction by Metal Decoration**
   Poster presentation, 11th Young Researcher's Conference: Materials Science and Engineering (04.12.2012) Belgrade, Serbia
   http://www.cost-mp1103.eu/

4. **Enhancing the Hydrogen Carbon Interaction**
   Invited Talk, 11th Young Researcher's Conference: Materials Science and Engineering (05.12.2012) Belgrade, Serbia
   http://www.cost-mp1103.eu/

5. **Hydrogen Adsorption Properties of Metal Decorated Graphene**
   Poster presentation, 7th International Symposium Hydrogen & Energy (21.01.2013) Stoos, Switzerland
   http://www.empa.ch/plugin/template/empa/*/50343/

6. **Nickel decorated graphene Synthesis and study of the interaction with hydrogen**
   Poster presentation, Empa PhD Students' Symposium 2013 (23.10.2013) Dübendorf, Switzerland
   1st Place at the Poster Award
   http://www.empa.ch/phd-symposium/

7. **Synthesis of Ni TEGO and study of its interaction with hydrogen**
   Poster presentation, 30th Annual SAOG Meeting (24.01.2014) Dübendorf, Switzerland
   http://www.saog-gssi.ch/

Published, peer-reviewed, paper

I **Reversible hydrogen absorption in sodium intercalated fullerenes**
Ph. Mauron, A. Remhof, **A. Bliersbach**, A. Borgschulte, A. Züttel, D. Sheptyakov, M. Gaboardi, M. Choucair, D. Pontiroli, M. Aramini, A. Gorreri and M. Riccò
International Journal of Hydrogen Energy, **37**, 14307 (2012)
http://dx.doi.org/10.1016/j.ijhydene.2012.07.045

II **Hydrogen Sorption in $Li_{12}C_{60}$**
Ph. Mauron, M. Gaboardi, A. Remhof, **A. Bliersbach**, D. Sheptyakov, M. Aramini, G. Vlahopoulou, F. Giglio, D. Pontiroli, M. Riccò and A. Züttel
The Journal of Physical Chemistry C, **44**, 117 (2013)
http://dx.doi.org/10.1021/jp408652t

III **Decoration of graphene with nickel nanoparticles: study of the interaction with hydrogen**
M. Gaboardi†, **A. Bliersbach**†, G. Bertoni, M. Aramini, G. Vlahopoulou, D. Pontiroli, Ph. Mauron, G. Magnani, G. Salviati, A. Züttel and M. Riccò
†: These authors contributed equally to this work
Journal of Materials Chemistry A, **2**, 1039 (2014)
http://dx.doi.org/10.1039/C3TA14127F

Comments on my participation

The degree of my involvement in the conducted research and subsequent writing of the peer reviewed papers, that were published during the cause of this thesis, is as follows:

I Participated in various X-ray diffraction, Raman, FT-IR and pcT measurements. Contributed to the manuscript.
Reprinted with permission from [79]. Copyright (2012) *International Journal of Hydrogen Energy.*

II Carried out the in situ neutron powder diffraction measurements and contributed to the analysis and interpretation. Involved in various X-ray diffraction, Raman and FT-IR measurements. Contributed to the manuscript.
Reprinted with permission from [80]. Copyright (2013) *American Chemical Society.*

III Carried out all the X-ray diffraction, Raman, pcT, BET and XPS measurements and made the analysis and interpretation. Strongly involved in the analysis and interpretation of all other measurements. Shared responsibility in writing of the manuscript and wrote corresponding sections of the paper.
Reproduced from [39], 2014, with permission from *The Royal Society of Chemistry.*

It was stated in the above chapters that the analysis presented in this thesis was done, with very few exceptions, in the course of this thesis work. This also includes data that has been published in the here mentioned papers. The data has been analyzed, evaluated and discussed anew in this thesis.

INTERNATIONAL JOURNAL OF HYDROGEN ENERGY 37 (2012) 14307–14314

Available online at www.sciencedirect.com

SciVerse ScienceDirect

journal homepage: www.elsevier.com/locate/he

Reversible hydrogen absorption in sodium intercalated fullerenes

Philippe Mauron [a,*], *Arndt Remhof* [a], *Andreas Bliersbach* [a], *Andreas Borgschulte* [a], *Andreas Züttel* [a], *Denis Sheptyakov* [b], *Mattia Gaboardi* [c], *Mohammad Choucair* [c], *Daniele Pontiroli* [c], *Matteo Aramini* [c], *Alessandra Gorreri* [c], *Mauro Riccò* [c]

[a] *Empa. Swiss Federal Laboratories for Materials Science and Technology, Division "Hydrogen and Energy", Überlandstrasse 129, 8600 Dübendorf, Switzerland*
[b] *Laboratory for Neutron Scattering, Paul Scherrer Institute, 5232 Villigen PSI, Switzerland*
[c] *Dipartimento di Fisica, Università di Parma, Via G. Usberti 7/a, 43124 Parma, Italy*

ARTICLE INFO

Article history:
Received 1 June 2012
Received in revised form
9 July 2012
Accepted 10 July 2012
Available online 28 July 2012

Keywords:
Hydrogen storage
Sodium fulleride

ABSTRACT

The hydrogen absorption of sodium intercalated fullerenes (Na_xC_{60}) was determined and compared to pure fullerenes (C_{60}). Up to 3.5 mass% hydrogen can reversibly be absorbed in Na_xC_{60} at 200 °C and a hydrogen pressure of 200 bar. The absorbed amount of hydrogen is significantly higher than for the case when only the sodium would be hydrogenated ($\sim$1 mass% for $x = 10$). At 200 bar the onset of hydrogen absorption is observed at 150 °C. At a pressure of 1 bar hydrogen the major desorption starts at 250 °C and is completed at 300 °C (heating rate 1 °C min^{-1}). This absorption and desorption temperatures are significantly reduced compared to pure C_{60}, either due to a catalytic reaction of hydrogen on sodium or due to the negatively charged C_{60}. The hydrogen ab/desorption is accompanied by a partial de/reintercalation of sodium. A minor part of the hydrogen is ionically bonded in NaH and the major part is covalently bonded in $C_{60}H_x$. The sample can be fully dehydrogenated and no NaH is left after desorption. In contrast to C_{60}, where the fullerene cages for high hydrogen loadings are destroyed during the sorption process, the Na_xC_{60} sample stays intact. The samples were investigated by X-ray, *in-situ* neutron powder diffraction and infrared spectroscopy. Na_xC_{60} was synthesized by reacting sodium azide (NaN_3) with C_{60} (molar ratio of Na:C_{60} is 10:1).

1. Introduction

Due to its low atomic weight carbon exhibits a high gravimetric hydrogen storage capacity of up to 25.1 mass% in the form of methane (CH_4) and >14.4 mass% in alkanes (C_nH_{2n+2}). In hydrocarbons hydrogen is covalently bonded to carbon. The standard enthalpy of formation of methane is $\Delta_f H^0(CH_4) = -37.3$ kJ mol^{-1} H_2 [1] but due to the high dissociation energy of the C–H bonds ($E_{dis.} = 439$ kJ mol^{-1} [1]) non-catalytic thermal cracking requires temperatures higher than 1200 °C to dissociate CH_4 at a reasonable rate [2]. By using appropriate catalysts the temperature can be significantly reduced to 850–900 °C [3], which is still too high for mobile hydrogen storage applications.

The heat of adsorption of molecular hydrogen on high surface area carbon materials is in the range of 4–6 kJ mol^{-1}

---

[*] *Corresponding author*. Tel.: +41 58 765 4099.
E-mail address: philippe.mauron@empa.ch (P. Mauron).

0360-3199/$ – see front matter Copyright © 2012, Hydrogen Energy Publications, LLC. Published by Elsevier Ltd. All rights reserved.
http://dx.doi.org/10.1016/j.ijhydene.2012.07.045

H_2 [4]. Liquid nitrogen temperatures are thus required for the adsorption of hydrogen. The hydrogen storage capacity depends on the specific surface area of the carbon sorbent and approximately 1.5 mass% of hydrogen is absorbed per 1000 $m^2\ g^{-1}$ of specific surface area at a temperature of 77 K [5].

Hydrogen absorption in C_{60} has been extensively investigated [6–10]. As in the case of hydrocarbons, hydrogen in hydrofullerenes ($C_{60}H_x$) is covalently bonded to carbon. Based on theoretical calculations and literature values, Karpushenkava et al. [11] determined the standard enthalpy and entropy for the hydrogenation of fullerenes ($C_{60}(s) + 18H_2(g) \rightarrow C_{60}H_{36}(s)$) to $\Delta_rH^0 = -74.1$ kJ mol^{-1} H_2 and $\Delta_rS^0 = -126.2$ J mol^{-1} H_2 K^{-1}) (isomer mixture) leading to a decomposition temperature of 314 °C at a pressure of 1 bar hydrogen. This enthalpy is comparable to hydrides such as MgH_2 [12] and $LiBH_4$ [13]. The C–H bond energies in $C_{60}H_{36}$ were calculated to be 295.8 and 293.7 kJ mol^{-1} [14] for the isomer with T and T_h symmetry, respectively, which would be significantly lower than typical C–H bond energies [1].

An intermediate binding energy of 20–40 kJ mol^{-1} H_2 [15] would be an ideal value for practical applications. Additional attracting forces between the hydrogen molecule and the host materials, originating from a quantum-mechanical orbital interaction (e.g. Kubas interaction [16]) or by electrostatic interaction (dipolar or quadrupolar) could realize the desired intermediate binding energy [15]. Theoretical studies predict that some metal-decorated C_{60} can absorb up to 8.4, 9.5 and 13.5 mass% of hydrogen in $Ca_{32}C_{60}$ [17], Na_8C_{60} [18] and $Li_{12}C_{60}$ [19] respectively, due to Kubas interaction with a binding energy in the appropriate range (20–40 kJ mol^{-1} H_2 [15]). For the electrostatic interaction, Yoon et al. [20] have calculated that the binding energy of molecular hydrogen on either positively or negatively charged fullerenes C_n of different size ($20 \leq n \leq 82$) is substantially increased to 17–31 kJ mol^{-1} H_2 with a hydrogen storage capacity of up to 8 mass%.

Charged fullerenes can be realized by alkali or alkali earth metal intercalation, due to a charge transfer from the metal to the fullerenes, forming charge transfer salts, so called fullerides. As the electronic structure of the C_{60} is changed by the electron transfer a catalytic effect on the covalent hydrogenation of the charged C_{60} is expected. Stable Na_xC_{60} exist with continuous stoichiometries. For $x > 4$ Na_xC_{60} has a face-centered cubic (*fcc*) structure [21,22] as pristine C_{60} [23] and Na clusterizes inside the unit cell, whereas for $x = 4$ a body-centered cubic (*bcc*) structure is present and forms a 2D polymer [24].

In particular, arguments based on the filling of one-electron orbitals suggest that a C_{60} can accept up to 12 electrons. For high level ($x > 6$) doped Na_xC_{60} the charge transfer is not fully provided to the C_{60} and a maximal charge transfer to the C_{60} of 8 e^- is estimated for $Na_{10}C_{60}$ [25]. The formation of new interstitial states accommodate a part of the additionally donated charge ($6 < x \leq 8$) [25]. $Na_{10}C_{60}$ is therefore a promising system in which hydrogen interacts with C_{60} through Na atoms that partially donate their charge to C_{60}.

Na_xC_{60} can be synthesized basically by three methods. In the first method stoichiometric quantities of C_{60} and NaN_3 are mixed, placed in a quartz tube and heated between 370 and 390 °C for 20 min to decompose the NaN_3, while keeping the pressure below $1 \cdot 10^{-3}$ mbar. Subsequently, the temperature is raised to 410 °C to complete the reaction [26]. In the second method C_{60} is reacted with the appropriate quantity of sodium dissolved in liquid ammonia. The ammonia is distilled, the sample treated in vacuum and annealed at 300 °C for several days [27]. In the third synthesis method NaH is reacted with C_{60} at 350 °C for nine days with two intermediate regrindings [28,29]. If the sample is only heated to 280 °C for 1 h NaH intercalates into C_{60} [30].

Previous work on hydrogen absorption in metal intercalated C_{60} has been performed by Wang et al. [31] who investigated the hydrogen absorption in a PtC_{60} compound. The hydrogen amount absorbed up to 200 °C under a hydrogen pressure of 20 bar was 1.6 mass% and at 1 bar hydrogen pressure only 0.3 mass% were released. The authors estimated the reversible hydrogen absorption between 0.5 and 0.6 mass%.

Goldshleger et al. [32] investigated the interaction of PtC_{60} with deuterium (D_2). For samples treated at a temperature of 100 °C and 10–20 bar D_2 they observed C-D absorption bands in the infrared spectra. PtC_{60} deuterated at 100–275 °C released D_2 at ~427 °C whereas samples deuterated at 350–450 °C released D_2 at 510–530 °C. By mass spectroscopy, $C_{60}D_x$ ($x = 2$–26) was identified to be the high-temperature product.

Teprovich et al. [33] reported on the reversible hydrogen uptake of alkali metal fullerides (Na_6C_{60}, Li_xC_{60}) synthesized by dehydrogenation of a C_{60} plus $NaAlH_4$ and $LiAlH_4$ mixture of (1:6), respectively. C_{60} was also used as a catalyst for the hydrogen desorption of $NaAlH_4$ [34], $LiAlH_4$ [33] and $LiBH_4$ [35]. The authors found that NaH, formed during desorption of $NaAlH_4$, was reacting with C_{60} to form sodium fulleride Na_6C_{60}. For hydrogen absorption the sample ($Na_6C_{60} + 6Al$) was held under 120 bar hydrogen at 250 °C for 12 h. A subsequent desorption showed a single desorption event with onset temperature ~150 °C and a 1.5 mass% reduction. The observation of C–H stretching vibrations at ~3000 cm^{-1} by Fourier Transform Infrared (FT-IR) spectroscopy is consistent with hydrofullerene formation.

Teprovich et al. [36] also investigated lithium doped fullerenes (Li_x-C_{60}-H_y). For a 6:1 M ratio of Li:C_{60} they could reversibly store up to 5 mass% of hydrogen with a desorption onset temperature of ~270 °C. By mass spectroscopy they could identify hydrofullerenes up to $C_{60}H_{48}$.

In this paper we investigate the hydrogen absorption and desorption properties of pure Na_xC_{60} without any byproducts. The sodium fulleride was synthesized with sodium azide. This method has the advantage that the hydrogenation can be performed on a pure and Na_xC_{60} compound without possible educt residues as e.g. NaH used in the reaction of C_{60} with NaH or unwanted reaction products such as Al, obtained in the reaction of C_{60} with $NaAlH_4$. Sodium azide completely reacts with C_{60} under evolution of volatile nitrogen gas.

The hydrogen amount was determined volumetrically and the samples were investigated by x-ray, *in-situ* neutron powder diffraction, Raman and FT-IR spectroscopy.

2. Experimental

To produce $Na_{10}C_{60}$, a stoichiometric amount of sodium azide (NaN_3, Sigma–Aldrich) was homogenously mixed with C_{60}

(MER Corp., 99.9%) in a mortar inside a glove box. This material was pelletized (80–120 mg pellets) and placed in tantalum foil bags. The bags were then transferred to a Pyrex vial and placed continuously pumped at a pressure below $1 \cdot 10^{-3}$ mbar. The vial was heated to 250 °C at 50 °C h^{-1} then to 450 °C at 10 °C h^{-1} at which point the sample was held for 5 h. Subsequently the sample was cooled down to 20 °C at 250 °C h^{-1}.

Hydrogen absorption of the samples was measured volumetrically in a pcT (pressure, composition, temperature) instrument [37]. Approximately 200 bar of hydrogen was applied on the sample (100–200 mg) and subsequently a heating ramp of 0.5 °C min^{-1} was applied up to a temperature between 200 and 400 °C, depending on the experiment. The sample was kept at the final temperature between 1 and 67 h. The amount of hydrogen absorbed was determined by the pressure change at known volumes and defined temperatures. In order to correct for the pressure increase in the heated sample holder a measurement consisting of a non-absorbing silicon sample, occupying the same volume as the sample, was subtracted. After each hydrogenation experiment the hydrogen pressure was released from the samples. Hydrogen desorption was carried out either in vacuum ($<1 \cdot 10^{-3}$ mbar) or at 1 bar of hydrogen by applying a heating ramp of 1 °C min^{-1} and by measuring the amount of desorbed hydrogen with a flow meter. Alternatively the pressure increase in a known volume was used to determine the amount of hydrogen.

The samples were solely handled in an argon glove box (H_2O and O_2 levels < 1 ppm) to avoid contamination. For the subsequent x-ray diffraction (XRD) and Raman measurements, the samples were filled in to quartz capillaries with a diameter of 0.5 mm and a wall thickness of 0.01 mm.

The XRD measurements were performed with a Bruker D8 Advanced diffractometer equipped with a Cu target and Göbel x-ray mirror, preparing a parallel incident beam. The patterns were recorded with a one-dimensional position sensitive detector (VÅNTEC).

Raman spectra at room temperature were measured with a Bruker Senterra instrument with 3.5 cm^{-1} spectral resolution in combination with a 10× objective using a 532 nm laser. The laser power was limited to 0.2 mW in order to avoid polymerization of the C_{60} samples [38]. The same quartz capillaries as for the XRD measurements were used.

Infrared measurements were made with a Bruker Alpha FT-IR spectrometer with an ATR (Attenuated Total Reflectance) module equipped with a diamond crystal suitable for powder samples. The measurements were performed in an Argon glove box to protect the sample from air. Some samples were diluted with KBr in order to improve the spectra.

In-situ neutron powder diffraction measurements of $Na_{10}C_{60}$ were performed under 100 bar of deuterium (D_2) at the HRPT beam line at the Swiss Spallation Neutron Source (SINQ) at the Paul Scherrer Institute (PSI) in Villigen, Switzerland. The samples were measured in a 6 mm diameter steel sample holder with a wall thickness of 1 mm with neutron wavelength $\lambda = 1.8857$ Å in a high intensity mode. Diffraction patterns were collected in the angular range $2\theta = 5–165°$ with a typical acquisition time of ~3 h. During D_2 treatment the temperature was increased up to 350 °C using a radiation-type furnace.

3. Results and discussion

3.1. *Hydrogen absorption and desorption*

To determine suitable working conditions, the synthesized Na_xC_{60} was exposed to a hydrogen pressure of 200 bar, the temperature was increased up to 400 °C by a temperature ramp of 0.5 °C min^{-1} and kept at this temperature for 80 min. The absorbed amount of hydrogen is plotted as a function of temperature in Fig. 1. The absorption starts at a temperature of approximately 150 °C which is significantly lower than for pure C_{60} [8,10]. A maximum of 2 mass% hydrogen is reached at a temperature of 300 °C. At temperatures above 300 °C hydrogen desorbs again. As the experiment was stopped the sample still contained 1.1 mass%. The hydrogen desorption of this sample at 1 bar of hydrogen is shown in Fig. 2a. Two desorption processes can be identified, the first starting around 150 °C and a second, with a relatively sharp peak, starting at 250 °C. Up to a temperature of 400 °C the total amount of desorbed hydrogen reaches 1.1 mass%, indicating that the entire hydrogen content was desorbed at a relatively low temperature. In comparison hydrogenated C_{60} (400 °C, 120 bar, 50 h) desorbs hydrogen in vacuum above 400 °C (Fig. 2c). XRD showed some amorphization of the C_{60} sample after hydrogenation and after desorption only an amorphous phase was present, indicating the destruction of the C_{60} cages. A second absorption performed on the sodium fulleride was done by heating the sample up to 200 °C (0.5 °C min^{-1}) and holding this temperature for 67 h at a hydrogen pressure of 200 bar. As shown in Fig. 3, 3.2 mass% were absorbed, with half of the amount already absorbed during the temperature ramp.

3.2. *X-ray diffraction*

In Fig. 4 the XRD patterns of the synthesized Na_xC_{60} and the sample after the first and second hydrogenation/dehydrogenation cycles are shown. The starting Na_xC_{60} shows diffraction peaks correspondingto a major phase of face-centered cubic(*fcc*) Na_xC_{60} [22] and body-centered cubic (*bcc*) Na_4C_{60} [24,39]. The peak at $2\theta < 10°$ indicate a minor phase of

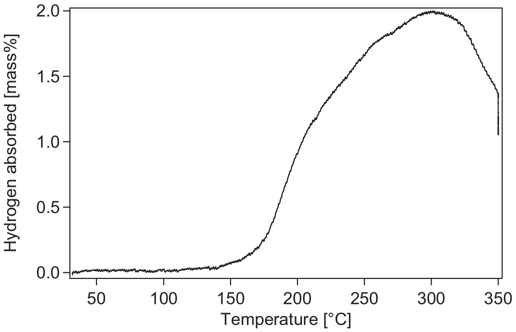

Fig. 1 – Absorbed hydrogen amount in $Na_xC_{60}H_x$ as a function of the temperature (heating rate 0.5 °C min^{-1}) during first absorption at 200 bar hydrogen.

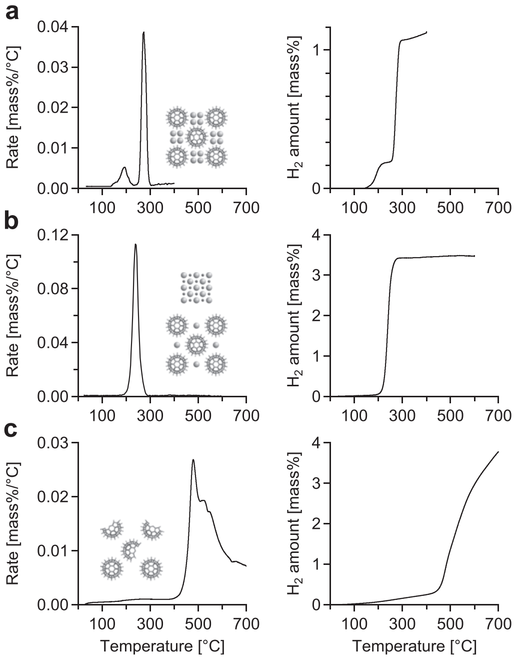

Fig. 2 – a) Desorbed hydrogen amount (right) and desorption rate (left) during first dehydrogenation of $Na_xC_{60}H_x$ at 1 bar hydrogen as a function of temperature up to 400 °C (heating rate 1 °C min^{-1}), b) 5th desorption of $Na_xC_{60}H_x$ up to a temperature of 600 °C in a constant volume from vacuum to 1.8 bar (heating rate 1 °C min^{-1}), c) First dehydrogenation of $C_{60}H_x$ in vacuum as a function of temperature (heating rate 2 °C min^{-1}).

a hexagonal distortion of Na_xC_{60} ($x > 4$) [40]. By Rietveld refinement of the data with the $Na_{9.3}C_{60}$ structure model [22] a lattice parameter of $a = 14.49$ Å was found. This corresponds to $Na_{7.7}C_{60}$ when linearly interpolated [25] with lattice parameter values of Na_6C_{60} [21] and $Na_{9.3}C_{60}$ [22]. The two reflections at 2θ between 10 and 11° correspond to the (111) reflection of the *fcc* and the (110) reflection of the *bcc* structure. After the first absorption (1.1 mass% hydrogen) this reflections are shifted to lower angles due to the expansion of the crystal lattice. After the first dehydrogenation the Na_4C_{60} peaks almost completely disappeared and the main phase corresponds to an *fcc* phase ($a = 14.49$ Å, $Na_{7.7}C_{60}$). After the second hydrogenation (3.2 mass%) an intense reflection at ~11° is seen with shoulders on the right and left side, indicating various phases. Additionally NaH is present which probably originates from deintercalation of sodium from the sodium fulleride ($Na_8C_{60}(s) \rightarrow Na_{(8-y)}C_{60}(s) + yNa(l)$) reacting with hydrogen to form NaH. The XRD pattern of the sample dehydrogenated for the second time looks very similar to the one after the first dehydrogenation and no NaH is visible. Although NaH is very stable ($\Delta_f H^0(NaH) = -112.6$ kJ mol^{-1} H_2 [1]) it seems to decompose during desorption. The NaH decomposition could be favored by reintercalation of the sodium into the fulleride ($Na_{(8-y)}C_{60}(s) + yNaH(s) \rightarrow Na_8C_{60}(s) + y/2H_2(g)$) as suggested by previous works on sodium fulleride synthesis [28]. This interpretation is supported by *in-situ* neutron powder diffraction investigations.

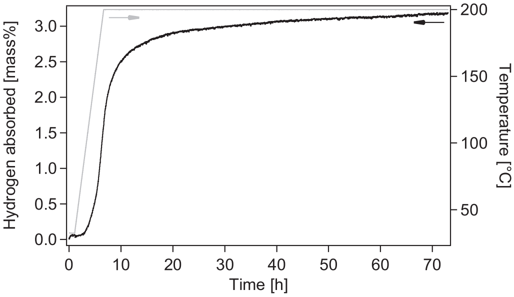

Fig. 3 – Absorbed hydrogen amount in $Na_xC_{60}H_x$ as a function of time during the second hydrogen absorption (heating rate 0.5 °C min^{-1}).

3.3. *Neutron powder diffraction*

Patterns of $Na_{10}C_{60}$ heated from 25 to 350 °C at 100 bar deuterium are shown in Fig. 5. This sample does not contain Na_4C_{60} (another batch). At room temperature the structure of the sample, in presence of 100 bar of deuterium, appears unchanged if compared to the pattern of the same sample under 1 bar He atmosphere. All the peaks can be indexed with an *fcc* structure (space group Fm-3) and LeBail analysis at 25 °C gives a lattice constant of $a = 14.542(2)$ Å with an agreement factor of $R_{wp} = 5.18\%$. The strongest peaks in the diffraction pattern are due to contribution of the steel sample holder and were not taken into account during the analysis. The pattern recorded at $T = 250$ °C shows an abrupt change in the lattice constant of the cubic structure and contemporaneously new reflections in the diffraction profile appeared. These new peaks could be ascribed to a minor fraction of sodium deuteride (NaD). The formation of the deuteride is accompanied by a leakage of sodium from the cubic structure of fullerene, as can be observed by the decrease of the relative intensities of the families of planes {311} and {222}. The changing in relative intensities could also be explained by the introduction of deuterium inside the cell. However, the decrease of the metal inside the crystal coincides with a sharp increase in the unit cell parameter of Na_xC_{60}. This phenomenon was tentatively explained as due to the decrease of the mutual ionic interaction between the anion C_{60}^{n-} and the Na-cluster cation, arising from Na migration out of the fullerides. However, a comparably large expansion of the unit cell suggests that a part of the deuterium reacts with C_{60} as in hydrogenated phases like $C_{60}H_y$ [41]. The NaD reflections disappear again at 350 °C, although the melting point of NaH is at 425 °C [1]. The inset in Fig. 5 shows the lattice parameter *a* as a function of temperature, derived by Rietveld refinement of the data with *fcc* $Na_{9.3}C_{60}$ [22]. The lattice parameter increases with temperature, reaches a maximum at 250 °C, where the NaD is also

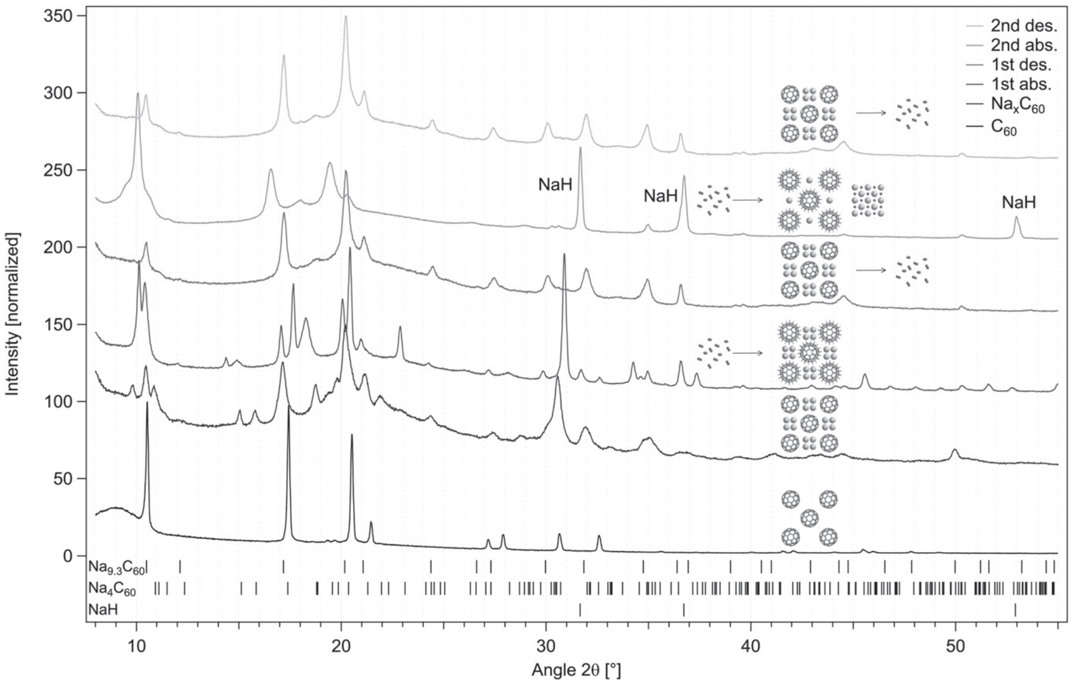

Fig. 4 – XRD patterns of C_{60}, Na_xC_{60} before and after first and second hydrogen ab/desorption measured at room temperature (the patterns are normalized and shifted in y-axis).

observed, and decreases again at higher temperatures. The lattice parameter increases by $\Delta a \approx 0.4$ Å, which is in the same order of magnitude as the increase observed for the hydrogenation of C_{60} to $C_{60}H_{36}$ ($\Delta a \approx 0.5$ Å) determined by a linear extrapolation of data from Schur et al. [9]. They found a linear dependence between the lattice parameter and the hydrogen content in $C_{60}H_x$ measured up to $x = 24$. At 100 bar deuterium and 350 °C, deuterium is desorbed, as indicated by the decrease of the refined unit cell parameter and the disappearance of the diffraction lines of NaD. This is consistent with the performed absorption measurements (see Fig. 1). Fast cooling of the sample at 100 bar deuterium (avoiding reabsorption of deuterium) results in a phase that is very similar to the initial one. This confirms the reversible behavior of the hydrogenation/dehydrogenation process. In summary the mechanism of the Na_xC_{60} hydrogenation compared with pure C_{60} is illustrated in Fig. 6.

3.4. Raman and FT-IR spectroscopy

The Raman spectrum of Na_xC_{60} is shown in Fig. 7. In the literature it is reported that the $A_g(2)$ Raman mode of C_{60} is very sensitive to polymerization and charge transfer [42]. It is shifted to lower wavenumbers by 6–7 cm^{-1} per electron transferred to the C_{60} [42–44] due to the softening of the bond stretching modes as the electrons enter the antibonding molecular orbitals. In polymerized C_{60}, synthesized by pressure- or photo-polymerization, the $A_g(2)$ mode is shifted by 5 cm^{-1} per polymer bond [45,46]. In our sample the $A_g(2)$ mode is shifted from 1468 cm^{-1} for pure C_{60} to 1436 cm^{-1} which corresponds to a charge transfer of 5.3 e^- with an assumed downshift of 6 cm^{-1} per charge. The sample was measured with a low laser intensity (0.2 mW) in order to prevent polymerization. After the first dehydrogenation the $A_g(2)$ mode is shifted down to 1433 cm^{-1} which corresponds to a charge transfer of 5.8 e^-. Barbedette et al. [47] measured modes of 1417 and 1415 cm^{-1} for the Raman spectra of Na_xC_{60} with $x = 9.2$ and 9.8 respectively, indicating that our sample does not reach a doping level of $x = 10$. This is also supported by the presence of Na_4C_{60} and the smaller lattice parameter a in the XRD pattern (Fig. 4).

The infrared spectra of the starting sodium fulleride material and the hydrogenated samples after the first, second and fifth hydrogenation are shown in Fig. 8. All hydrogenated samples show typical C–H stretching bands around 2800–3000 cm^{-1} which are also present in hydrofullerenes [9,41]. After desorption the C–H stretching bands always disappeared entirely.

The 3rd and 4th cycle were performed at 100 bar hydrogen where 1.8 mass% and 0.4 mass% were absorbed at 200 °C (18 h) and 400 °C (12 h) respectively. The 5th absorption was performed at 200 °C and 190 bar hydrogen for 40 h. In order to ascertain that all hydrogen is desorbed up to a temperature of 400 °C, knowing that pure C_{60} desorbs hydrogen only above

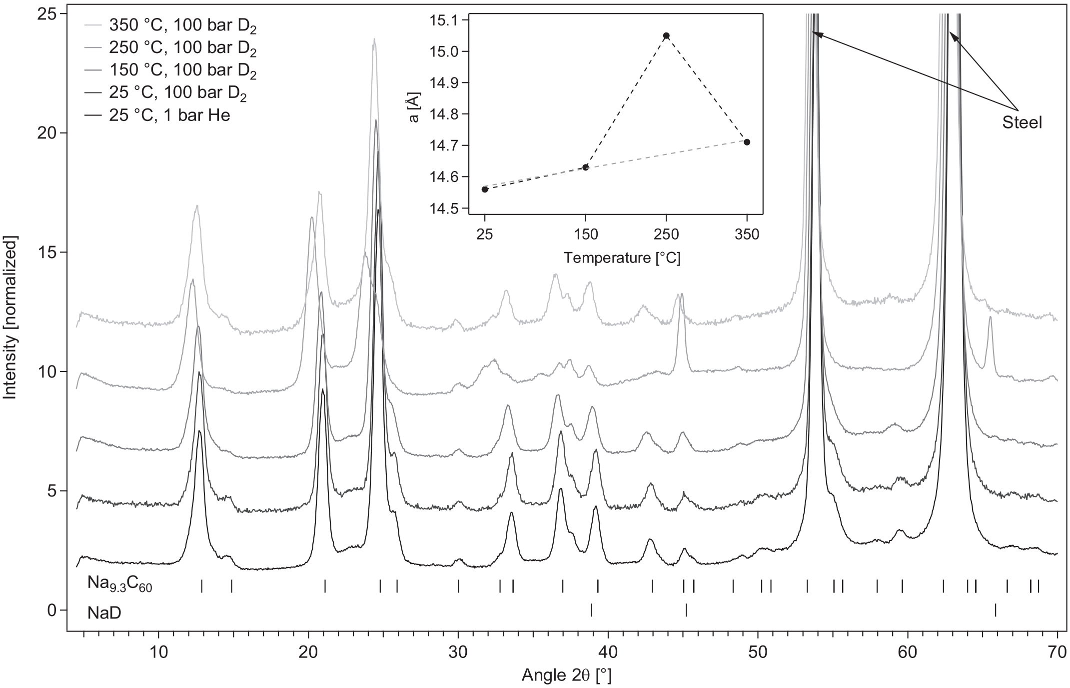

Fig. 5 – Neutron powder diffraction patterns of $Na_{10}C_{60}$ for different temperatures (the patterns are normalized and shifted in *y*-axis), inset: Lattice parameter *a* as a function of temperature for the data fitted with the *fcc* $Na_{9.3}C_{60}$ structure model (dashed lines are guides for the eyes).

400 °C (Fig. 2c), desorption in a constant volume was performed up to 600 °C (Fig. 2b). An amount of 3.5 mass% of hydrogen could be desorbed, whereby the pressure increased from vacuum to 1.8 bar at 600 °C. Only one desorption peak can be seen, which is broader than in the first desorption but mainly due to the fact that the measurement was not done at constant pressure. Despite the sample being heated to 600 °C, a subsequent 6th hydrogen cycle was reversible with 3.4 mass

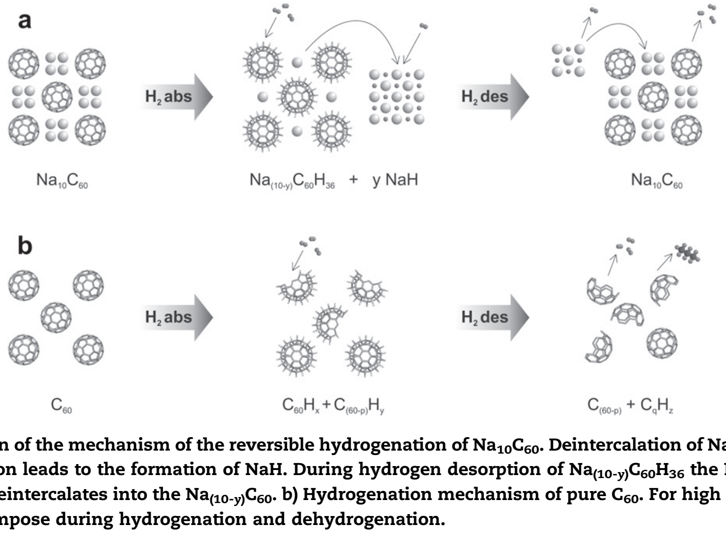

Fig. 6 – a) Illustration of the mechanism of the reversible hydrogenation of $Na_{10}C_{60}$. Deintercalation of Na out of the $Na_{10}C_{60}$ during hydrogenation leads to the formation of NaH. During hydrogen desorption of $Na_{(10-y)}C_{60}H_{36}$ the Na from the decomposing NaH reintercalates into the $Na_{(10-y)}C_{60}$. b) Hydrogenation mechanism of pure C_{60}. For high hydrogen contents the fullerenes decompose during hydrogenation and dehydrogenation.

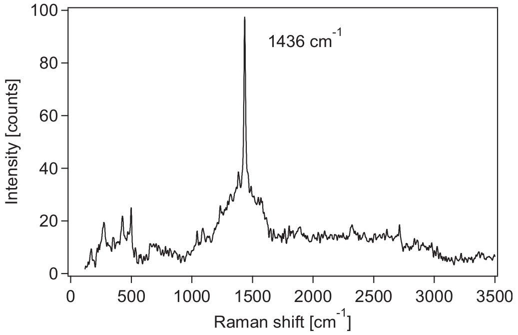

Fig. 7 – Raman spectrum of Na_xC_{60} (532 nm, 0.2 mW, 10× Objective, baseline corrected by concave rubberband correction). The $A_g(2)$ mode shifted from 1468 to 1436 cm^{-1} corresponds to a charge transfer of 5.3 e^-.

% hydrogen (185 bar H_2, 200 °C, 40 h). Our investigations show that up to 3.5 mass% of hydrogen is reversibly absorbed and at least 6 cycles are reversible.

If in the Na_xC_{60} compound *only* the sodium reacted with hydrogen ($Na_{10}C_{60}(s) + 5H_2(g) \rightarrow 10NaH(s) + C_{60}(s)$) then the hydrogen capacity would only be ~1.0 mass%. $C_{60}H_6$, $C_{60}H_{18}$ and $C_{60}H_{36}$ are known to be stable hydrofullerenes [10]. So the measured hydrogen quantities of up to 3.5 mass% hydrogen correspond to the following reaction: $Na_{10}C_{60}(s) + 18H_2(g) \rightarrow Na_{10}C_{60}H_{36}(s)$ corresponding to 3.7 mass%. Supposing there is some deintercalation of sodium: $Na_{10}C_{60}(s) + 20H_2(g) \rightarrow Na_6C_{60}H_{36}(s) + 4NaH(s)$ corresponding to 4.1 mass%, the extra weight of the sodium would be partly compensated. In comparison $C_{60}H_{36}$ has a hydrogen storage capacity of 4.8 mass%.

In all our dehydrogenation experiments of hydrogenated sodium fullerides desorption was completed below 300 °C and desorption at 1 bar hydrogen started at 250 °C, indicating that the stability is lower than for pure $C_{60}H_{36}$ ($T_{dec} = 314$ °C). This is supported by the fact that for conditions where pure C_{60} absorb hydrogen (400 °C, 120 bar) the $Na_xC_{60}H_x$ decomposes (>300 °C, 200 bar).

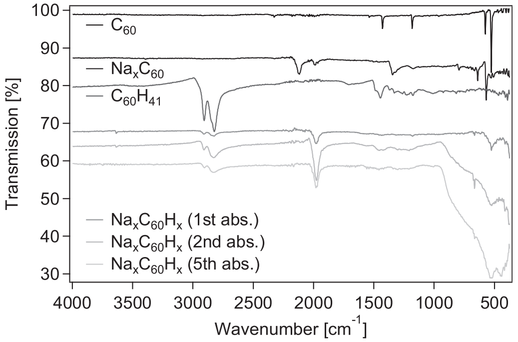

Fig. 8 – FT-IR spectra of C_{60} (KBr), $C_{60}H_{41}$ (MER Corp.), Na_xC_{60} (KBr) and Na_xC_{60} after the first (KBr), second and fifth hydrogenation. The C–H stretching modes are around 2800–3000 cm^{-1} (for clarity the spectra are shifted in y-axis).

4. Conclusion

The hydrogenation and dehydrogenation properties of Na_xC_{60} were investigated volumetrically. At 200 bar hydrogen and a temperature of 200 °C up to 3.5 mass% hydrogen is reversibly absorbed. At 1 bar hydrogen the main desorption shows a sharp peak starting at 250 °C (heating rate 1 °C min^{-1}). FT-IR transmission measurements have shown absorption bands at positions typical for C–H stretching vibrations of covalent hydrogen-carbon bonds. This suggests the formation of hydrofullerenes as e.g. $C_{60}H_{36}$. Therefore neither the Kubas, nor the electrostatic interaction plays the crucial role for the binding of the hydrogen in the final $Na_xC_{60}H_x$. The absorption and desorption occurs at significantly lower temperatures than for pure C_{60}, indicating some catalytic effect of the sodium or the charged C_{60}. Furthermore the stability of $Na_xC_{60}H_x$ seems to be lower than for hydrofullerenes. The occurrence of NaH during hydrogen absorption has been explained by partial sodium deintercalation of the Na_xC_{60} compound and reintercalation during dehydrogenation. An interesting question is how the charge on the C_{60} is changing as a function of the hydrogen and sodium content during hydrogenation.

Acknowledgment

This work was financially supported by the SNF Synergia project “Smart carbon-based materials for hydrogen storage” under the contract number CRSII2_130509/1.

REFERENCES

[1] Lide DR, editor. CRC handbook of chemistry and physics. 89th ed. Boca Raton FL: CRC Press/Taylor and Francis; 2009 (Internet Version).

[2] Hazzim F, Wan Daud WMA. Hydrogen production by methane decomposition: a review. Int J Hydrogen Energ 2010; 35:1160–90.

[3] Muradov N, Smith F, Bockerman G, Scammon K. Thermocatalytic decomposition of natural gas over plasma-generated carbon aerosols for sustainable production of hydrogen and carbon. Appl Catal A 2009;365:292–300.

[4] Schmitz B, Müller U, Trukhan N, Schubert M, Férey G, Hirscher M. Heat of adsorption for hydrogen in microporous high-surface-area materials. Chem Phys Chem 2008;9: 2181–4.

[5] Züttel A, Sudan P, Ph Mauron, Kiyobayashi T, Ch Emmenegger, Schlapbach L. Hydrogen storage in carbon nanostructures. Int J Hydrogen Energ 2002;27:203–12.

[6] Talyzin AV, Tsybin YO, Schaub TM, Mauron P, Shulga YM, Züttel A, et al. Composition of hydrofullerene mixtures produced by C_{60} reaction with hydrogen gas revealed by high-resolution mass spectrometry. J Phys Chem B 2005;109: 12742–7.

[7] Talyzin AV, Tsybin YO, Peera AA, Schaub TM, Marshall AG, Sundqvist B, et al. Synthesis of $C_{59}H_x$ and $C_{58}H_x$ fullerenes stabilized by hydrogen. J Phys Chem B 2005;109:5403–5.

[8] Schur DV, Zaginaichenko SY, Savenko AF, Bogolepov VA, Anikina NS, Zolotarenko AD, et al. Experimental evaluation of total hydrogen capacity for fullerite C_{60}. Int J Hydrogen Energ 2011;36:1143–51.

[9] Schur DV, Tarasov BP, Shul'ga YM, Zaginaichenko SY, Matysina ZA, Pomytkin AP. Hydrogen in fullerites. Carbon 2003;41:1331–42.

[10] Schur DV, Zaginaichnko S, Veziroglu TN. Peculiarities of hydrogenation of pentatomic carbon molecules in the frame of fullerene molecule C_{60}. Int J Hydrogen Energ 2008;33:3330–45.

[11] Karpushenkava LS, Kabo GJ, Diky VV. Thermodynamic properties and hydrogen accumulation ability of fullerene hydride $C_{60}H_{36}$. Fuller Nanotub Car N 2007;15:227–47.

[12] Stampfer JF, Holley CE, Suttle JF. The Magnesium-hydrogen system. J Am Chem Soc 1960;82:3504–8.

[13] Mauron Ph, Buchter F, Friedrichs O, Remhof A, Bielmann M, Zwicky CN, et al. Stability and reversibility of $LiBH_4$. Phys Chem B 2008;112:906–10.

[14] Rathna A, Chandrasekhar J. Theoretical study of hydrogenated buckminsterfullerene derivatives with benzenoid rings, $C_{60}H_{60-6n}$ ($n = 1 - 8$). Chem Phys Lett 1993; 206:217–24.

[15] Lochan RC, Head-Gordon M. Computational studies of molecular hydrogen binding affinities: the role of dispersion forces, electrostatics, and orbital interactions. Phys Chem Chem Phys 2006;8:1357–70.

[16] Kubas GJ, Ryan RR, Swanson BI, Vergamini PJ, Wasserman HJ. Characterization of the first examples of isolable molecular hydrogen complexes, $M(CO)_3(PR_3)_2(H_2)$ ($M = Mo, W; R = Cy$, i-Pr). Evidence for a side-on bonded H_2 ligand. J Am Chem Soc 1984;106:451–2.

[17] Yildirim T, Iniguez J, Ciraci S. Molecular and dissociative adsorption of multiple hydrogen molecules on transition metal decorated C_{60}. Phys Rev B 2005;72:153403.

[18] Chandrakumar KRS, Ghosh SK. Alkali-metal-induced enhancement of hydrogen adsorption in C_{60} fullerene: an *ab Initio* study. Nano Let 2008;8:13–9.

[19] Sun Q, Jena P, Wang Q, Marquez M. First-principles study of hydrogen storage on $Li_{12}C_{60}$. J Am Chem Soc 2006;128:9741–5.

[20] Yoon M, Yang S, Wang E, Zhang Z. Charged fullerenes as high-capacity hydrogen storage media. Nano Let 2007;7:2578–83.

[21] Rosseinsky M, Murphy DW, Fleming RM, Tycko R, Ramirez AP, Siegrist T, et al. Structural and electronic properties of sodium-intercalated C_{60}. Nature 1992;356:416–8.

[22] Yildirim T, Zhou O, Fischer JE, Bykovetz N, Strongin RA, Cichy MA, et al. Intercalation of sodium heteroclusters into the C_{60} lattice. Nature 1992;360:568–71.

[23] Bürgi HB, Restori R, Schwarzenbach D. Structure of C_{60}: partial orientational order in the room-temperature modification of C_{60}. Acta Cryst B 1993;49:832–8.

[24] Oszlányi G, Baumgartner G, Faigel G, Forrò L. Na_4C_{60}: an Alkali intercalated two-dimensional polymer. Phys Rev Lett 1997;78:4438–41.

[25] Andreoni W, Giannozzi P, Armbruster JF, Knupfer M, Fink J. Anomalous electronic behaviour of Na superfullerides: theory and experiment. Europhys Lett 1996;34:699–704.

[26] Imaeda K, Khairullin II , Yakushi K. New superconducting Sodium-Nitrogen-C_{60} ternary compound. Solid State Comm 1993;87:375–8.

[27] Fullagar WK, Reynolds PA, White JW. Lithium and Sodium fullerides prepared in liquid Ammonia. Solid State Comm 1997;104:23–7.

[28] Murphy DW, Rosseinsky MJ, Fleming RM, Tycko R, Ramirez AP, Haddon RC, et al. Synthesis and characterization of Alkali metal fullerides: A_xC_{60}. J Phys Chem Solids 1992;53:1321–32.

[29] Imaeda K, Kröber J, Inokuchi H, Yonehara Y, Ichimura K. Superconductivity in NaH intercalated C_{60}. Solid State Comm 1996;99:479–82.

[30] Imaeda K, Kröber J, Nakano C, Inokuchi H. Recovery and enhancement of superconductivity in the Sodium-hydrogen-C_{60} ternary system. J Phys Chem B 1997;101:10136–40.

[31] Wang XL, Tu JP. Characterization and hydrogen storage properties of Pt-C_{60} compound. Appl Phys Lett 2006;89: 064101.

[32] Goldshleger NF, Tarasov BP, Shul'ga YM, Roschupkina OS, Perov AA, Moravsky AP. Interaction of platinum fulleride C_{60}Pt with deuterium: IR and X-ray photoelectron studies. In: Kadish KM, Kamat PV, Guldi D, editors. Recent advances in the chemistry and physics of fullerenes and related materials, vol. 7. Pennington NJ: The Electrochemical Society; 1999. p. 647–52.

[33] Teprovich JA, Knight DA, Wellons MS, Zidan R. Catalytic effect of fullerene and formation of nanocomposites with complex hydrides: $NaAlH_4$ and $LiAlH_4$. J Alloy Compd 2011; 509:562–6.

[34] Berseth PA, Harter AG, Zidan R, Blomqvist A, Araujo CM, Scheicher RH, et al. Carbon nanomaterials as catalysts for hydrogen uptake and release in $NaAlH_4$. Nano Lett 2009;9: 1501–5.

[35] Wellons MS, Berseth PA, Zidan R. Novel catalytic effects of fullerene for $LiBH_4$ hydrogen uptake and release. Nanotechnology 2009;20:204022.

[36] Teprovich JA, Wellons MS, Lscola R, Hwang SJ, Ward PA, Compton RN, et al. Synthesis and characterization of a lithium-doped fullerane (Li_x-C_{60}-H_y) for reversible hydrogen storage. Nano Lett 2012;12:582–9.

[37] Bielmann M, Kato S, Mauron Ph, Borgschulte A, Züttel A. Characterization of hydrogen storage materials by means of pressure concentration isotherms based on the mass flow method. Rev Sci Instrum 2009;80:082901.

[38] Akselrod L, Byrne HJ, Thomsen C, Roth S. Reversible photochemical processes in fullerenes - a Raman-Study. Chem Phys Lett 1993;215:131–6.

[39] Kubozono Y, Takabayashi Y, Kambo T, Fujiki S, Kashino S, Emura S. Structure and physical properties of Na_4C_{60} under ambient and high pressures. Phys Rev B 2001;63:045418.

[40] Kobayashi M, Kimata N, Heguri S. X-ray diffraction and magnetic susceptibility of sodium fullerides Na_xC_{60}. J Phys Chem Solids 2010;71:689–91.

[41] Molodets AM, Lobach AS, Zhukov AN, Shulga YM, Fortov VE. Stability of crystalline structure and molecules of hydrofullerene $C_{60}H_{36}$ under high shock pressures. Dokl Phys 2008;53:562–5.

[42] Wågberg T, Stenmark P, Sundqvist B. Structural aspects of two-dimensional polymers: Li_4C_{60}, Na_4C_{60} and tetragonal C_{60}. Raman spectroscopy and X-ray diffraction. J Phys Chem Solids 2004;65:317–20.

[43] Haddon RC, Hebard AF, Rosseinsky MJ, Murphy DW, Duclos SJ, Lyons KB, et al. Conducting films of C_{60} and C_{70} by alkali-metal doping. Nature 1991;350:320–2.

[44] Borondics F, Oszlanyi G, Faigel G, Pekker S. Polymeric sheets in Mg_4C_{60}. Solid State Comm 2003;127:311–3.

[45] Wågberg T, Jacobsson P, Sundqvist B. Comparative Raman study of photopolymerized and pressure-polymerized C_{60} films. Phys Rev B 1999;60:4535–8.

[46] Makarova TL, Zakharova IB, Evyatkovskii OE, Buga SG, Vokov AP, Shelankov AL. Experimental realization of high spin states in dilutely hydrogenated fullerenes. Phys Status Solidi B 2009;246:2778–81.

[47] Barbedette L, Lefrant S, Yildirim T, Fischer JE. Raman spectra of sodium saturated doped Na_xC_{60} ($x = 9.2$ and 9.8). In: Kuzmany H, Fink J, Mehring M, Roth S, editors. Physics and chemistry of fullerenes and derivatives. Singapore: World Scientific Publishing Co; 1995. p. 460–6.

THE JOURNAL OF PHYSICAL CHEMISTRY C

Article

pubs.acs.org/JPCC

Hydrogen Sorption in $Li_{12}C_{60}$

Philippe Mauron,*[†] Mattia Gaboardi,[‡] Arndt Remhof,[†] Andreas Bliersbach,[†] Denis Sheptyakov,[§] Matteo Aramini,[‡] Gina Vlahopoulou,[‡] Fabio Giglio,[‡] Daniele Pontiroli,[‡] Mauro Riccò,[‡] and Andreas Züttel[†]

[†]Division "Hydrogen and Energy", EMPA Swiss Federal Laboratories for Materials Science and Technology, Überlandstrasse 129, 8600 Dübendorf, Switzerland

[§]Laboratory for Neutron Scattering, Paul Scherrer Institute, 5232 Villigen PSI, Switzerland

[‡]Dipartimento di Fisica e Scienze della Terra, Università degli studi di Parma, Via G. P. Usberti 7/a, 43124 Parma, Italy

ABSTRACT: The lithium-intercalated fulleride $Li_{12}C_{60}$ was investigated in view of a lightweight hydrogen storage material due to the low molecular weight of its constituents. Deuterium (D_2) absorption in $Li_{12}C_{60}$ shows an uptake of up to 9.5 mass % D_2 (equivalent to ∼5 mass % H_2 for the same stoichiometry). Under a pressure of 190 bar the onset of absorption was observed at a temperature below 100 °C, which is 200 °C lower than that for pure C_{60}. Deuterium desorption was investigated by in-situ neutron powder diffraction, and at a pressure of 1 bar desorption was observed above 300 °C. The ab/desorption is accompanied by a partial de/reintercalation of lithium, observed by the appearance and disappearance of LiD reflections after absorption and during desorption, respectively. A minor part of deuterium is present in ionic form in LiD, and the major part is covalently bound in a Li-depleted compound $Li_{12-x}C_{60}D_{36+y}$.

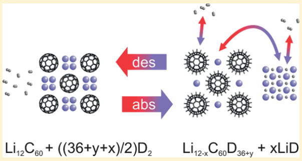

1. INTRODUCTION

C_{60}, theoretically, has the potential to be a carbonaceous hydrogen storage material. A typical stable molecule is $C_{60}H_{36}$,[1] which has a capacity of 4.8 mass % H_2. In $C_{60}H_{60}$ a capacity of 7.7 mass % H_2 is reached at temperatures up to 600 °C and 130 bar,[2] but it also has been observed that prolonged hydrogenation ($T = 400$ °C, $p = 120$ bar, up to 3000 min) can lead to fragmentation of C_{60}.[3,4] Even higher hydrogen absorption amounts have been proposed by theoretical calculations, e.g., $Li_{12}C_{60}$ as an isolated cluster has been studied by Sun et al.,[5] and up to ∼13 mass % H_2 storage capacity was calculated from ab initio simulation.

Yoshida et al.[6] measured the hydrogen absorption of Li_9C_{60} and established that up to ∼2.6 mass % H_2 can be stored at 250 °C and 30 bar H_2. Reversible hydrogen uptake of alkali metal fullerides (Na_xC_{60}, Li_xC_{60}) synthesized by dehydrogenation of C_{60} mixed with $NaAlH_4$ or C_{60} mixed with $LiAlH_4$ each in a molar ratio of 1:6 has been shown by Teprovich et al.[7] For lithium-doped fullerenes (Li_x-C_{60}-H_y) a reversible uptake of 5 mass % H_2 (350 °C, 105 bar H_2) and desorption onset temperature of ∼270 °C was observed when the molar ratio between Li and C_{60} is 6.[8] Hydrogen uptake for Li_{12}-C_{60}-H_y was determined to be 3.5 mass % H_2 at 250 °C and 105 bar H_2. By anelastic spectroscopy measurements Paolone et al.[9] suggested that $Li_6C_{60}H_x$ and $Na_6C_{60}H_x$ are homogeneous materials and cannot be considered as constituted by bulk $C_{60}H_n$ and $Li(Na)H_x$.

In pure sodium-intercalated fulleride $Na_{10}C_{60}$ 3.5 mass % H_2 can reversibly be absorbed at a temperature as low as 200 °C and 200 bar.[10] The ab/desorption kinetics can be significantly improved compared to pure C_{60}, and the stability for dehydrogenation has been lowered. During hydrogenation NaH is formed, leading to partial sodium deintercalation in the compound. It was found that part of hydrogen is ionically bound to NaH and part covalently bond to C_{60}. During dehydrogenation sodium reintercalates into the compound, promoting reformation of $Na_{10}C_{60}$.

In this paper we investigate the deuterium absorption and desorption properties of pure $Li_{12}C_{60}$ without any byproducts by making use of pcT (pressure, composition, and temperature), XRD (X-ray diffraction), FT-IR (Fourier transformed infrared) spectroscopy, and in-situ neutron powder diffraction. Lithium-doped fullerides have a polymeric[11] or monomeric structure[12] depending on the amount of lithium intercalated. $Li_{12}C_{60}$ is a highly doped phase of Li_xC_{60} in which it is established that Li atoms form an incompletely ionized cluster in the central octahedral void of the *fcc* fullerite structure,[12,13] similarly to $Na_{10}C_{60}$.[14] Lithium atoms are, in principle, able to donate up to 6 electrons to the 3-fold degenerate t_{1u} LUMO of C_{60}, and the remainder are expected to delocalize their charge onto the Li cluster. The high negative charge onto C_{60} and the presence of the alkaline cluster in the fulleride has proved to be of fundamental importance in decreasing the energy barrier required for dissociation of hydrogen molecules and formation of $C_{60}H_y$.[15]

Received: August 29, 2013
Revised: October 2, 2013
Published: October 21, 2013

2. EXPERIMENTAL SECTION

Lithium fulleride was synthesized by mixing pure C_{60} (MER Corp., 99.9%) with granular lithium (Sigma-Aldrich 99%) cut in very small flakes. About 500−600 mg of the reagents was ground in 3 spheres agatha ball mill at 30 Hz for 60 min. When the sample became a black and uniform powder it was then pelletized (~100 mg per pellet), placed in tantalum foil bags, sealed in high vacuum ($<1 \times 10^{-5}$ mbar) in a Pyrex vial, and treated in an oven at 270 °C for 36 h. Subsequently, the sample was cooled to 20 °C and recovered in the Ar glovebox. The weight of the sample before and after annealing was unchanged. Samples were synthesized and solely handled in an argon glovebox (H_2O and O_2 levels < 1 ppm) to avoid contamination.

Deuterium absorption of the sample was measured volumetrically in a pcT instrument.[16] In a first step, approximately 190 bar of deuterium (99.8% D_2) was applied on the sample (375 mg) and subsequently heated with a ramp of 0.5 °C min^{-1} up to a temperature of 225 °C. Sample was kept at the final temperature for 45 h in order to achieve a high deuterium absorption. The amount of absorbed deuterium was determined by the pressure change at known volumes and temperatures. In a second step the sample was heated up at 350 °C (in 100 bar D_2) for 24 h. After each absorption step the pressure was released from the sample and the material was investigated by XRD and FT-IR.

XRD measurements were performed with a Bruker D8 Advanced diffractometer equipped with a Cu target and Göbel X-ray mirror, preparing a parallel incident beam. Patterns were recorded with a one-dimensional position-sensitive detector (VÅNTEC). Samples were measured in quartz capillaries with a diameter of 0.5 mm and a wall thickness of 0.01 mm.

Infrared measurements were carried out with a Bruker Alpha FT-IR spectrometer with an ATR (attenuated total reflectance) module equipped with a diamond crystal suitable for powder samples. Measurements were carried out in an argon glovebox to protect the sample from air.

In-situ neutron powder diffraction measurements were performed at the HRPT beamline at the Swiss Spallation Neutron Source (SINQ) at the Paul Scherrer Institute (PSI) in Villigen, Switzerland.[17] Samples were measured in a 6.3 mm diameter vanadium sample holder with a wall thickness of 0.25 mm with neutron wavelength $\lambda = 1.8857$ Å in the high-intensity mode. Individual diffraction patterns were collected in the angular range $2\theta = 5{-}165°$ with an acquisition time of 4.25 min. Typically 10 patterns were summed up to get better statistics. Desorption of deuterated $Li_{12}C_{60}$ was carried out under a pressure of 1 bar of deuterium. From 250 to 450 °C the temperature was increased in steps of 25 °C using a radiation-type furnace. The heating rate was 10 °C min^{-1}, and the sample was stabilized until the normalized total counts of neutrons became constant before measurements were started.

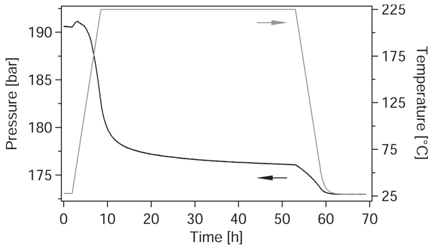

Figure 1. Pressure (black) and temperature (gray) of isochoric deuterium absorption (first step) in $Li_{12}C_{60}$ as a function of time (heating/cooling rate 0.5 °C min^{-1}).

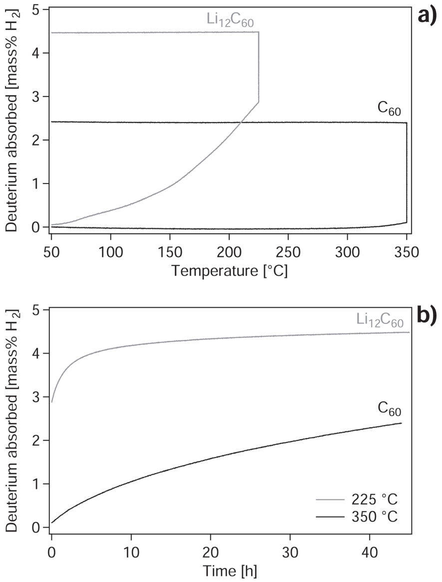

Figure 2. (a) Amount of deuterium (in mass % H_2) absorbed (first step) in $Li_{12}C_{60}$ as a function of temperature (gray) determined from the data of Figure 1 and for comparison hydrogen absorbed in pure C_{60} (black) (heating/cooling rate 0.5 °C min^{-1}). (b) Deuterium (in mass % H_2) uptake for $Li_{12}C_{60}$ (225 °C) and hydrogen uptake for C_{60} (350 °C) as a function of time for the isothermal part.

3. RESULTS AND DISCUSSION

The pressure and temperature of the isochoric deuteration during the first step (225 °C, 190 bar) of $Li_{12}C_{60}$ as a function of time is shown in Figure 1. The corresponding deuterium amount is shown in Figure 2a as a function of temperature (gray). During heating up the absorption already starts below 100 °C, which is 200 °C lower than for pure C_{60}.[2,18] At the final temperature of 225 °C, around 3 mass % H_2 is absorbed. An additional 1.5 mass % H_2 is absorbed during the isotherm (45 h), leading to a total of 4.5 mass % H_2 as shown in Figure 2b (gray). Cooling the sample to room temperature does not change the amount of deuterium absorbed. At the end of the absorption cycle the pressure decreased to 173 bar. In a second step the sample was heated up to 350 °C for 24 h at 100 bar deuterium, leading to an additional absorption of 0.5 mass % H_2. At this temperature and 200 bar, hydrogenated $Na_{10}C_{60}$ is not stable,[10] indicating that the deuterated $Li_{12}C_{60}$ is more stable. The total amount of absorbed deuterium finally sums up to the equivalent of 5 mass % H_2. During the first step in absorption the color of the sample changed from black to bright gray and in the second step to white. For comparison, hydrogen absorption of pure C_{60} (MER Corp.) was also measured at 185 bar and up to a temperature of 350 °C; absorption starts at around 300 °C as shown in Figure 2 (black). A final hydrogen absorption of 2.4 mass % H_2 was reached, and the color of the sample was red. Determination of the *fcc* lattice parameter of hydrogenated C_{60} yields a = 14.394(2) Å, and by comparing with the linear dependence as a function of the hydrogen content given by Shur et al.[19] the absorption was determined to 2.1 mass % H_2 by XRD. The absorption kinetic of $Li_{12}C_{60}$ is much faster compared to pure C_{60}, even at a lower temperature.

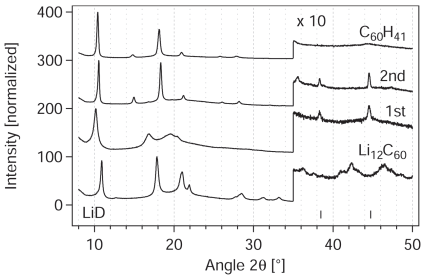

Figure 3. XRD patterns of the as-synthesized $Li_{12}C_{60}$ after the first (225 °C, 190 bar) and second (350 °C, 100 bar) steps of deuterium absorption. For comparison, $C_{60}H_{41}$ from MER Corp. is shown (patterns are normalized and shifted in y axis).

In Figure 3 the XRD pattern of the starting material is plotted: LeBail refinement with the *fcc* structure of C_{60} gives a lattice parameter a = 13.880(9) Å. The structure is contracted with respect to the pure fullerite (a = 14.16(1) Å[20]) due to the high Coulomb interaction arising from lithium atoms inside the lattice, between the charged $C_{60}{}^{n-}$ and Li^+ ions/cluster. No reflections from metallic Li can be identified. After the first deuteration step, two phases can be distinguished: lithium deuteride (LiD) and a less crystallized phase with broad peaks. The shape of the profile of this second phase follows the contour of the *fcc* phase of C_{60} but with a more expanded lattice. At the end of the second absorption step, the LiD phase is still present and a novel *bcc* phase with a lattice parameter of a = 11.79(2) Å can be identified, which is close to the value of a = 11.7(1) Å for $C_{60}D_{36}$[21,22] and similar to a = 11.924(2) Å determined for $C_{60}H_{41}$ (MER Corp.). Given the presence of LiD in the patterns, the deuterated $Li_{12}C_{60}$ phases are partially depleted of Li and can be described as $Li_{12-x}C_{60}D_{36+y}$.

FT-IR spectra of the $Li_{12-x}C_{60}D_{36+y}$ sample after the first and second steps are shown in Figure 4. Peaks around 2100 cm^{-1} (2158 and 2105 cm^{-1} in the second step) can be identified as C−D stretching modes similar to $C_{60}D_{36}$ which are reported to be at 2157 and 2092 cm^{-1},[23] leading to the conclusion that at least part of the deuterium is covalently bound to C_{60} as also seen before for the case of hydrogenated $Na_{10}C_{60}$.[10]

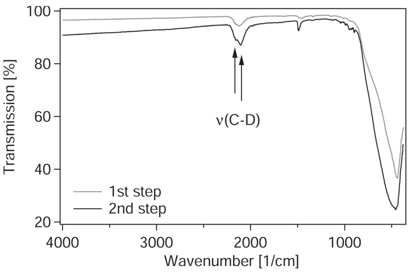

Figure 4. FT-IR spectra of deuterated $Li_{12}C_{60}$ after the first (gray) (225 °C, 180 bar) and second (black) (350 °C, 100 bar) steps. C−D stretching modes appear at 2158 and 2105 cm^{-1} (second step).

Deuterium desorption of the sample deuterated at 350 °C (second step, other batch) was investigated by in-situ neutron powder diffraction. In Figure 5 the neutron patterns are shown for different temperatures during the temperature ramp. At room temperature two phases can be identified: the LiD phase and a *bcc* phase similar to $C_{60}D_{36}$[21,22] as already seen by XRD. There is a linear relationship between the lattice parameter and the amount of hydrogen absorbed in $C_{60}H_x$ for the *fcc* and *bcc* phases.[24] The lattice parameter of a = 11.848(1) Å determined at RT is similar to 11.8(1) Å given by Hall et al.[21,22] for $C_{60}D_{36}$. Up to a temperature of 325 °C the patterns are similar. At 350 °C all LiD reflections disappear, although the melting point and desorption temperature of LiH are at 680[25] and 943 °C (calculated from thermodynamic values[25]), respectively. Up to a temperature of 450 °C there are no significant further changes in the spectra. The pattern at 450 °C evolves to a new structure, which is still under investigation. In Figure 6 the lattice parameters of LiD and $Li_{12-x}C_{60}D_{36+y}$, fitted with the LeBail method from the cubic structures, are plotted as a function of temperature. Due to thermal expansion the lattice parameters increase for LiD and $Li_{12-x}C_{60}D_{36+y}$ by heating up from RT to 325 °C. For $Li_{12-x}C_{60}D_{36+y}$ the lattice expansion deviates from a linear behavior at 325 °C as desorption occurs at this temperature and the lattice parameter decreases again. In the patterns of Figure 5 for one temperature several single patterns are summed up; consequently; part of the kinetic information got lost; therefore, the normalized total counts (S_{tot}) for each pattern as a function of time are plotted in Figure 7. The change of S_{tot} is proportional to the deuterium desorbed from the sample because deuterium is contributing essentially to the total scattering cross section. It can be seen that desorption starts at 300 °C and that it is essentially terminated at 350 °C at a value of S_{tot} = 70%. A calculated value of S_{tot}, considering the sample geometry (cylindrical sample, annular vanadium sample holder) with constant packing and mass densities of the sample,[26] for the formal reaction $C_{60}D_{36}$ + 12 LiD → $Li_{12}C_{60}$ gives S_{tot} = 71% after desorption, which is very close to the measured one.

Since the neutron diffraction of deuterated $Li_{12}C_{60}$ exhibits 2 distinct phases (LiD and a *bcc* phase consistent with $C_{60}D_{36}$) and the FT-IR experiment indicates C−D stretching modes (analogous to $C_{60}D_{36}$), the following reaction mechanism (eq 1) is proposed for absorption

$$\begin{aligned} &Li_{12}C_{60} + ((36 + x + y)/2)D_2 \\ &\quad \leftrightarrow Li_{12-x}C_{60}D_{36+y} + x\text{LiD} \end{aligned} \tag{1}$$

This indicates that during deuteration lithium atoms deintercalate from the $Li_{12}C_{60}$ phase and form LiD in which deuterium is ionically bound to Li and at the same time in the remaining Li-depleted phase $Li_{12-x}C_{60}$ deuterium covalently binds to C_{60}. Due to the fact that the LiD peaks disappear during desorption, it is supposed that the reverse process takes place. LiD reacts with the $Li_{12-x}C_{60}D_{36+y}$ phase by reintercalating Li released from LiD and forming $Li_{12}C_{60}$ again. The exact number of x and y could not be determined by the present experiments and would need further investigations. This reaction pathway is similar to that observed for $Na_{10}C_{60}$.[10] If in the $Li_{12}C_{60}$ compound only the lithium reacted with

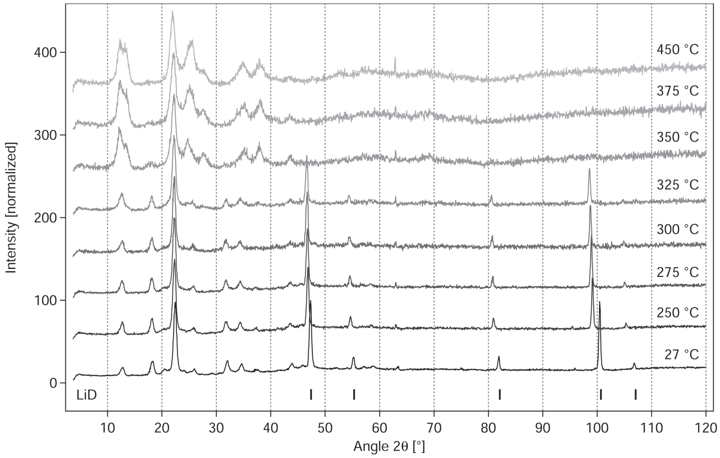

Figure 5. In-situ neutron powder diffraction patterns during desorption of deuterated $Li_{12}C_{60}$ (deuterated at 350 °C, 100 bar D_2, second step) measured at different temperatures (patterns are normalized and shifted in y axis).

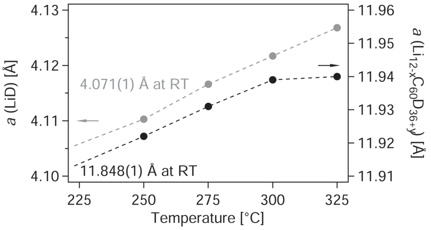

Figure 6. Lattice parameters of LiD (gray) and $Li_{12-x}C_{60}D_{36+y}$ (black) as a function of temperature (values indicated in graph correspond to room-temperature measurements).

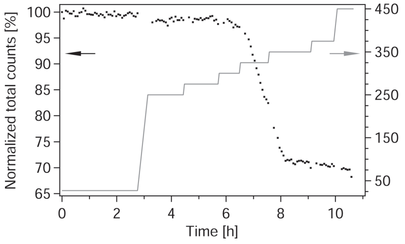

Figure 7. Normalized total neutron counts (proportional to the amount of deuterium) in the deuterated $Li_{12}C_{60}$ (black) and sample temperature (gray) as a function of time during in-situ desorption at a pressure of 1 bar deuterium.

deuterium ($Li_{12}C_{60} + 6D_2 \rightarrow 12LiD + C_{60}$) then the deuterium capacity would be only 1.5 mass % H_2. Assuming that there is a complete lithium deintercalation ($x = 12$) and formation of $C_{60}D_{36}$ ($y = 0$), which is a form of a stable hydrofullerene,[18] then the material would have a total deuterium capacity of 5.6 mass % H_2 ($12LiD + C_{60}D_{36}$). In comparison, $C_{60}H_{36}$ has a hydrogen storage capacity of 4.8 mass % H_2. Interaction of Li improves the sorption properties and at the same time also increases the hydrogen storage capacity.

The $Li_{12}C_{60}$ system (after the second step of absorption) desorbs deuterium above 300 °C compared to 250 °C for $Na_{10}C_{60}$,[10] which is an additional point to the one discussed in the paragraph describing the absorption, indicating that the Li system is more stable than the Na system.

4. CONCLUSION

Deuteration of $Li_{12}C_{60}$ was volumetrically determined, and up to 9.5 mass % D_2 (equivalent to ~5 mass % H_2 for same stoichiometry) was absorbed. Absorption starts below 100 °C, and under a pressure of 1 bar of deuterium desorption starts above 300 °C. During absorption Li deintercalates from the compound to form LiD and a deuterated $Li_{12-x}C_{60}D_{36+y}$ phase with covalent D−C bonds. During desorption LiD reacts with $Li_{12-x}C_{60}D_{36+y}$ under release of deuterium and reintercalation of Li. It has been shown that the absorption and desorption temperature is 200 °C lower than for pure C_{60} and that the amount of deuterium absorbed is higher than that for $Na_{10}C_{60}$ (3.5 mass % H_2).[10] The experimental ab- and desorption conditions (pressure, temperature) indicate that the $Li_{12}C_{60}$ compound is more stable than $Na_{10}C_{60}$.[10]

■ AUTHOR INFORMATION

Corresponding Author

*E-mail: philippe.mauron@empa.ch.

Notes

The authors declare no competing financial interest.

■ ACKNOWLEDGMENTS

This work was financially supported by the SNF Synergia project “Smart carbon-based materials for hydrogen storage” under contract number CRSII2_130509/1.

■ REFERENCES

(1) Haufler, R. E.; Conceicao, J.; Chibante, L. P. F.; Chai, Y.; Byrne, N. E.; Flanagan, S.; Haley, M. M.; O’Brien, S. C.; Pan, C.; Xiao, Z.; et al. Efficient production of C_{60} (buckminsterfullerene), $C_{60}H_{36}$, and the solvated buckide ion. *J. Phys. Chem.* **1990**, *94*, 8634−6.

(2) Schur, D. V.; Zaginaichenko, S. Y.; Savenko, A. F.; Bogolepov, V. A.; Anikina, N. S.; Zolotarenko, A. D.; Matysina, Z. A.; Veziroglu, T. N.; Skryabina, N. E. Experimental evaluation of total hydrogen capacity for fullerite C_{60}. *Int. J. Hydrogen Energy* **2011**, *36*, 1143−51.

(3) Talyzin, A. V.; Tsybin, Y. O.; Schaub, T. M.; Mauron, P.; Shulga, Y. M.; Züttel, A.; Sundqvist, B.; Marshall, A. G. Composition of Hydrofullerene Mixtures Produced by C_{60} Reaction with Hydrogen Gas Revealed by High-Resolution Mass Spectrometry. *J. Phys. Chem. B* **2005**, *109*, 12742−7.

(4) Talyzin, A. V.; Tsybin, Y. O.; Peera, A. A.; Schaub, T. M.; Marshall, A. G.; Sundqvist, B.; Mauron, P.; Züttel, A.; Billups, W. E. Synthesis of $C_{59}H_x$ and $C_{58}H_x$ Fullerenes Stabilized by Hydrogen. *J. Phys. Chem. B* **2005**, *109*, 5403−5.

(5) Sun, Q.; Jena, P.; Wang, Q.; Marquez, M. First-principles study of hydrogen storage on $Li_{12}C_{60}$. *J. Am. Chem. Soc.* **2006**, *128*, 9741−5.

(6) Yoshida, A.; Okuyama, T.; Terada, T.; Naito, S. Reversible hydrogen storage/release phenomena on lithium fulleride (Li_nC_{60}) and their mechanistic investigation by solid-state NMR spectroscopy. *J. Mater. Chem.* **2011**, *21*, 9480−2.

(7) Teprovich, J. A.; Knight, D. A.; Wellons, M. S.; Zidan, R. Catalytic effect of fullerene and formation of nanocomposites with complex hydrides: $NaAlH_4$ and $LiAlH_4$. *J. Alloys Compd.* **2011**, *509*, 562−6.

(8) Teprovich, J. A.; Wellons, M. S.; Lscola, R.; Hwang, S. J.; Ward, P. A.; Compton, R. N.; Zidan, R. Synthesis and Characterization of a Lithium-Doped Fullerane (Li_x-C_{60}-H_y) for Reversible Hydrogen Storage. *Nano Lett.* **2012**, *12*, 582−9.

(9) Paolone, A.; Vico, F.; Teocoli, F.; Sanna, S.; Palumbo, O.; Cantelli, R.; Knight, D. A.; Teprovich, J. A.; Zidan, R. Relaxation Processes and Structural Changes in Li- and Na-Doped Fulleranes for Hydrogen Storage. *Phys. Chem. C* **2012**, *116*, 16365−70.

(10) Mauron, Ph.; Remhof, A.; Bliersbach, A.; Borgschulte, A.; Züttel, A.; Sheptyakov, D.; Gaboardi, M.; Choucair, M.; Pontiroli, D.; Aramini, M.; et al. Reversible hydrogen absorption in sodium intercalated fullerenes. *Int. J. Hydrogen Energy* **2012**, *37*, 14307−14.

(11) Margadonna, S.; Pontiroli, D.; Belli, M.; Shiroka, T.; Riccò, M.; Brunelli, M. Li_4C_{60}: a polymeric fulleride with a two-dimensional architecture and mixed interfullerene bonding motifs. *J. Am. Chem. Soc.* **2004**, *126*, 15032−3 Nov..

(12) Cristofolini, L.; Riccò, M.; De Renzi, R. NMR and high-resolution x-ray diffraction evidence for an alkali-metal fulleride with large interstitial clusters: $Li_{12}C_{60}$. *Phys. Rev. B* **1999**, *59*, 8343−6.

(13) Tomaselli, M.; Meier, B. H.; Ricco, M.; Shiroka, T.; Sartori, A. A multiple-quantum nuclear magnetic resonance study of interstitial Li clusters in Li_xC_{60}. *J. Chem. Phys.* **2001**, *115*, 472−6.

(14) Yildirim, T.; Zhou, O.; Fischer, J. E.; Bykovetz, N.; Strongin, R. A.; Cichy, M. A.; Smith Ill, A. B.; Lin, C. L.; Jelinek, R. Intercalation of sodium hetero-clusters into the C_{60} lattice. *Nature* **1992**, *360*, 568−71.

(15) Aramini, M.; Gaboardi, M.; Vlahopoulou, G.; Pontiroli, D.; Cavallari, C.; Milanese, C.; Riccò, M. Muon spin relaxation reveals the hydrogen storage mechanism in light alkali metal fullerides. *Carbon* **2013**, DOI: 10.1016/j.carbon.2013.09.063.

(16) Bielmann, M.; Kato, S.; Mauron, Ph; Borgschulte, A.; Züttel, A. Characterization of hydrogen storage materials by means of pressure concentration isotherms based on the mass flow method. *Rev. Sci. Instrum.* **2009**, *80*, 082901.

(17) Fischer, P.; Frey, G.; Koch, M.; Könnecke, M.; Pomjakushin, V.; Shefer, J.; Thut, R.; Schlumpf, N.; Bürge, R.; Greuter, U.; Bondt, S.; Berruyer, E. High-resolution powder diffractometer HRPT for thermal neutrons at SINQ. *Physica B* **2000**, *276*, 146−7.

(18) Schur, D. V.; Zaginaichnko, S.; Veziroglu, T. N. Peculiarities of hydrogenation of pentatomic carbonmolecules in the frame of fullerene molecle C_{60}. *Int. J. Hydrogen Energy* **2008**, *33*, 3330−45.

(19) Schur, D. V.; Tarasov, B. P.; Shulga, Y. M.; Zaginaichenko, S. Y.; Matysina, Z. A.; Pomytkin, A. P. Hydrogen in fullerites. *Carbon* **2003**, *41*, 1331−42.

(20) Bürgi, H. B.; Restori, R.; Schwarzenbach, D. Structure of C_{60}: Partial Orientational Order in the Room-Temperature Modification of C_{60}. *Acta Crystallogr., Sect. B* **1993**, *49*, 832−8.

(21) Hall, L. E.; McKenzie, D. R.; Davis, R. L.; Attalla, M. I.; Vassallo, A. M. Structural Determination of the Hydrofullerene $C_{60}D_{36}$ by Neutron Diffraction. *Acta Crystallogr., Sect. B* **1998**, *54*, 345−50.

(22) Hall, L. E.; McKenzie, D. R.; Attalla, M. I.; Vassallo, A. M.; Davis, R. L.; Dunlop, J. B.; Cockayne, D. J. H. *J. Phys. Chem.* **1993**, *97*, 5741−4.

(23) Cataldo, F.; Iglesias-Groth, S.; Manchado, A. Synthesis and FT-IR Spectroscopy of Perdeuterofullerane: $C_{60}D_{36}$ Evidences of Isotope Effect in the Stability of $C_{60}D_{36}$. *Fuller. Nanotub. Car. N.* **2008**, *17*, 378−89.

(24) Talyzin, A. V.; Shulga, Y. M.; Jacob, A. Comparative study of hydrofullerides $C_{60}H_x$ synthesized by direct and catalytic hydrogenation. *Appl. Phys. A: Mater. Sci. Process.* **2004**, *78*, 1005−10.

(25) In *CRC Handbook of Chemistry and Physics*, 89th ed. (Internet Version); Lide, D. R., Ed.; CRC Press/Taylor and Francis: Boca Raton, FL, 2009.

(26) Azuah, R. T.; Kneller, L. R.; Qiu, Y.; Tregenna-Piggott, P. L. W.; Brown, C. M.; Copley, J. R. D; Dimeo, R. M. DAVE: A Comprehensive Software Suite for the Reduction, Visualization, and Analysis of Low Energy Neutron Spectroscopic Data. *J. Res. Natl. Bur. Stand. Technol.* **2009**, *114*, 341−58.

Journal of
Materials Chemistry A

PAPER

View Article Online
View Journal | View Issue

Decoration of graphene with nickel nanoparticles: study of the interaction with hydrogen

Cite this: *J. Mater. Chem. A*, 2014, **2**, 1039

Mattia Gaboardi,†[a] Andreas Bliersbach,†[b] Giovanni Bertoni,[cd] Matteo Aramini,[a] Gina Vlahopoulou,[a] Daniele Pontiroli,[a] Philippe Mauron,[b] Giacomo Magnani,[a] Giancarlo Salviati,[c] Andreas Züttel[b] and Mauro Riccò*[a]

Received 14th October 2013
Accepted 11th November 2013

DOI: 10.1039/c3ta14127f

www.rsc.org/MaterialsA

Graphene obtained from thermal exfoliation of graphite oxide was chemically functionalized with nickel nanoparticles (NPs) without exposing the system to oxidizing agents. Its structural, physical and chemical properties have been studied by means of TEM, X-ray photoelectron and Raman spectroscopies, and SQuID magnetometry. The formation of 17 nm super-paramagnetic (SPM) monodispersed Ni NPs was observed. Nitrogen sorption experiments at 77 K yield a Brunauer–Emmett–Teller specific surface area (BET-SSA) of 505 m^2 g^{-1} and helium adsorption at room temperature gives a skeletal density of 2.1 g cm^{-3}. The interaction with atomic hydrogen was investigated by means of Muon Spin Relaxation (μSR) showing a considerable fraction of captured muonium (~38%), indicative of strong hydrogen–graphene interactions. Hydrogen adsorption has been measured *via* pressure concentration isotherms demonstrating a maximum of 1.1 mass% of adsorbed hydrogen at 77 K and thus a 51% increased hydrogen adsorption compared to other common carbon based materials.

Introduction

The study of carbon-based materials for hydrogen storage experienced a surge in interest after the possibility of gram scale production of graphene and functionalized graphene became possible.[1] Due to the low atomic mass of carbon and the large specific surface area of graphene, with up to 2630 m^2 g^{-1},[2] the largest known for graphitic materials, graphene is ideal for gas adsorption and thus attractive in the field of energy storage and in particular for mobile applications.[3] Pure graphene, however, proves difficult to hydrogenate and only at elevated temperatures the fully hydrogenated graphene (graphane), with a highly desirable hydrogen content of 7.7 mass%, can be obtained. This is indicative of large thermodynamic barriers probably originating from the high activation energy for H_2 dissociation on graphene. Yet, there are several ways to enhance hydrogen sorption which can be utilized. It is well known that defects play a fundamental role in the dissociation of hydrogen molecules and act as trapping centres.[4] Furthermore, metal atoms can support hydrogen dissociation and therewith increase adsorption kinetics dramatically. Experimental studies confirmed that the presence of a metal can additionally increase hydrogen storage properties[5] and CO reduction.[6] In this context, it was suggested by theoretical work that both spillover effects[7] and quantum orbital interactions, like Kubas binding,[8] can occur, *e.g.* curved carbon sheets decorated with single (alkali, alkali-earth, transition metal) atoms, in nanotubes,[9] fullerenes[10–12] and graphene complexes,[13] and enable hydrogenation under preferable conditions. In the case of Kubas interaction the binding energy is thought to fall in the range of 15–30 kJ mol^{-1}, required for room temperature hydrogen storage. It has been previously shown experimentally that alkali–metal intercalation of fullerenes (Li_6C_{60}, $Li_{12}C_{60}$ and $Na_{10}C_{60}$) increases their respective hydrogen storage capacities up to about 5, 4.5 and 3.5 mass% H_2 and lowers the desorption temperature significantly.[14–17] However, finding a suitable synthetic approach, which can be performed in the absence of solvents and without exposing the material to oxidizing agents, is fundamental to prevent undesired reactions like the oxidation of the material or the metal particles. In this manuscript we discuss a novel material, functionalized graphene decorated with Ni nanoparticles (NPs). We present a two-step oxygen and water free chemical methodology for the production of nickel decorated thermally exfoliated graphene oxide (Ni–TEGO) and the characterization of its structural and chemical properties. The sample was investigated by means of transmission electron microscopy (TEM), Raman spectroscopy and X-ray diffraction (XRD) for structural properties, SQuID magnetometry for magnetic information, X-ray photoelectron spectroscopy (XPS) for their chemical composition, and muon spin relaxation (μSR)

---

[a] *Dipartimento di Fisica e Scienze della Terra, Università di Parma, via G.P. Usberti 7/A, 43124 Parma, Italy. E-mail: mauro.ricco@fis.unipr.it*

[b] *Empa. Swiss Federal Laboratories for Materials Science and Technology, Division "Hydrogen and Energy", Überlandstrasse 129, 8600 Dübendorf, Switzerland*

[c] *IMEM-CNR, Parco Area delle Scienze 37/A, 43124 Parma, Italy*

[d] *Nanochemistry Department, Istituto Italiano di Tecnologia, via Morego 30, 16163 Genova, Italy*

† These authors contributed equally to this work.

to determine the interaction of Ni–TEGO with atomic hydrogen. Adsorption experiments with He, N_2 and H_2 were conducted to measure the skeletal density, Brunauer–Emmet–Teller specific surface area (BET-SSA) and the hydrogen physisorption properties.

Experimental

Materials

RW-A grade graphite was purchased from SGL Carbon group. Anhydrous Ni(acac)$_2$ 95% was purchased from Sigma Aldrich. Anhydrous tetrahydrofuran (THF 99.9% inhibitor free, Sigma-Aldrich) was degassed before use. As a reference for a multi-layer graphene sample (about 6 layers thick) we used a commercial graphene on a copper grid purchased from Graphene Supermarket.

Methods

For TEM analysis, a small amount of Ni–TEGO was exposed to air, quickly dispersed in isopropanol and a droplet was deposited onto carbon coated copper grids. The morphology and structure were determined by High Resolution Transmission Electron Microscopy (HRTEM) and by High Angle Annular Dark Field (HAADF) Scanning Transmission Electron Microscopy (STEM). The latter was used to reveal the possible different species of the particles, due to the high contrast (proportional to Z^α, with $\alpha \sim 2$, Z being the atomic number of the element in the sample) of this technique. Selective area electron diffraction (SAED) patterns were acquired on the films to verify the presence of single layers of graphene. STEM observations were carried out on a JEOL JEM-2200FS microscope with a Schottky gun working at 200 kV (point resolution 0.19 nm) at IMEM-CNR in Parma, equipped with an in-column energy filter (Ω-type), a CCD high resolution camera, STEM detectors, and an EDS detector. HRTEM images were acquired on a similar machine at IIT in Genova, equipped with a CEOS 3rd order aberration corrector in the objective lens, capable of 0.10 nm resolution. EEL spectra were acquired using a STEM at IIT in Genova on a FEI Tecnai G2 microscope equipped with a Gatan Enfinium SE spectrometer (model 976). Raman measurements were conducted on a Bruker Senterra Raman spectrometer with a 532 nm laser and an output power of 10 and 20 mW. The spectral resolution was 3.5 cm^{-1} measured using a 10× objective and the samples were filled into quartz capillaries with a 0.7 mm diameter and a wall thickness of 0.01 mm. DC SQuID magnetometry was carried out on about 12 mg of powder sample, sealed in a 5 cm long quartz tube under a 1 mbar He atmosphere without exposing it to air. The experiment was performed on a MPMSXL-5 SQUID magnetometer, in the temperature range of 2–400 K and field range of 0–5 T. The Zero Field Cooling (ZFC) and Field Cooling (FC) measurements were made with a magnetic field of $\mu_0 H = 3 \times 10^{-3}$ T. Hysteresis loops were measured at 2 and 300 K between a field range of ±5 T. The Muon Spin Rotation (μSR) experiment was carried out on the EMU spectrometer at the ISIS-Rutherford Appleton Laboratory, UK. The 100% spin-polarized pulsed beam of this setup is optimized for the study of the muon spin evolution at long timescales (about 15 μs); about 350 mg of Ni–TEGO was pressed and sealed in an air tight silver coated aluminium cell closed with kapton windows. The Transversal Field (TF) measurement was performed at 300 K on a pure silver plate and the full asymmetry was estimated to be 21.7(1)%. A similar measurement was performed on a quartz sample (in which 100% of the muons form muonium) in order to obtain the value of the baseline: 9.25(6)%. To investigate the hydrogen sorption characteristics of the sample we used an in-house build dynamic pcT (pressure-composition Temperature) instrument at 77 and 103 K from 0–40 bar.[18] Due to the exceedingly low bulk density of Ni–TEGO the sample was carefully compressed inside an airtight, stainless steel, sample holder to achieve higher loading weights of up to 100–200 mg. After outgassing for 16 h at 523 K a base pressure of 7.3×10^{-4} mbar was reached. The sample was subsequently cooled down to 77 K in a bath of liquid nitrogen (LN_2) while constantly pumping vacuum. To be able to control the temperature the sample holder was imbedded in an oven, capable of heating the sample while submerged in LN_2. The temperature was monitored *in situ* and hydrogen was only introduced to the system upon reaching thermal equilibrium. The filling level of LN_2 was kept constant over the entire measurement time. The effective adsorbed and subsequently desorbed amount of hydrogen was determined *via* the mass flow method[18] where the hydrogen mass, supplied to or from the sample, is measured with a thermal mass flow controller. As a reference sample a commercial, non-absorbing, silicon (Sigma-Aldrich) was used. Desorption was performed under vacuum (<1×10^{-3} mbar). In addition measurements at 77 K, up to 1 bar of hydrogen, were performed using a Sieverts apparatus (BET), BELSORP-max (BEL, Japan). The BET has the advantage of being able to measure very accurately even under low pressure. The same apparatus was used to extract the BET surface area from nitrogen adsorption at 77 K and the skeletal density *via* expansion of helium from a known volume into the sample volume, once with and once without the sample, at room temperature. X-ray diffraction (XRD) was performed with a Bruker D8 Advanced diffractometer. The Bruker D8 is equipped with a Cu target and Göbel X-ray mirror, to parallelize the incident beam, and a one-dimensional position sensitive detector (VÅNTEC) to record the diffracted photons. XRD samples were filled in 0.5 mm quartz capillaries, with a wall thickness of 0.01 mm. However, even for measurement times exceeding 12 h for $\Delta 2\theta = 105^\circ$ no diffraction peak could be assigned. XPS was performed on a modified VG EscaLab spectrometer with a base pressure of <1×10^{-9} mbar. The load lock of the XPS system is connected to an Ar filled glove box, such that samples can be transferred directly from inert conditions to vacuum and *vice versa*. Samples were pelletized and firmly placed on Cu sample holders with a diameter smaller or equal to the pellet size in order to reduce the signal of the sample holder. As an X-ray light source the 1486.7 eV Al Kα_1 was used and recorded using a Specs PHOIBOS 100 analyser. The spectra were fitted with Gaussian–Lorentzian product functions with fixed (70/30) components after subtraction of a Shirley background and using a Marquardt–Levenberg optimization algorithm. The main C1s peak shows at a binding energy of 284.06 eV and all spectra were calibrated to this peak position. The peak positions have been restrained to maximum and minimum values found in the literature for similar materials and only small deviations from these values were allowed. The main source for peak positions was the NIST XPS database and other experimental and theoretical studies.[19,20] Relative surface compositions were calculated from the spectral peaks of C(1s), O(1s) and Ni(2p) using the CasaXPS software.

Synthesis

Graphene was synthesized *via* thermal exfoliation of graphite oxide (GO) which in turn was produced using Brodie's method.[21] Subsequently, the GO was dried in air at 60 °C for 1 day. In order to exfoliate GO it is necessary to form a propellant gas between neighbouring layers (generated by functional groups detached from the GO). This can be done by increasing the heating rate or increasing the temperature. Reducing the heating rate or lowering the temperature would increase the number of multilayers thus decreasing the specific surface area.[22] Moreover, the efficiency of the exfoliation is amplified if the difference between the pressure of propellant gas and the external pressure is higher. Taking into account these considerations, the GO was placed at the end of a long quartz tube, abruptly heated to 1150 °C under dynamic high vacuum conditions (10^{-5} mbar) and kept for 30 minutes before quickly cooling down to room temperature. The as-prepared Thermally Exfoliated Graphite Oxide (TEGO) was then removed from the quartz tube under anaerobic conditions in an Ar glove box with <0.5 ppm of O_2 and H_2O. The synthesis of Ni decorated TEGO was performed as follows: TEGO was mixed with $Ni(acac)_2$ on the bottom of a 2 way pyrex Rotaflo vial together with a Teflon magnetic stirrer. The vial was closed, brought out of the glove box and connected, by making use of a T-tube, with another vial containing previously degassed anhydrous tetrahydrofuran (THF, Alfa Aesar). The T-tube and the sample containing vial were evacuated until the pressure was lower than 10^{-5} mbar. The synthesis vial was then slowly immersed in liquid nitrogen and THF was condensed in it. After the THF completely soaks the reagents, the vial was removed from liquid nitrogen and the mixture was kept for 12 hours at 50 °C under continuous stirring to ensure the impregnation of TEGO with the metal–organic precursor. The solvent was then removed and the uniform black product was heated up to 300 °C in a high dynamic vacuum (10^{-6} mbar, ramp rate of 60 °C h^{-1}), in order to thermally decompose $Ni(acac)_2$, and rapidly quenched at room temperature. The as-prepared Ni–TEGO composite shows up as a uniform black powder.

Results and discussion

Microscopy and Raman spectroscopy

To verify the presence of few layer graphene (FLG) and even single layers after exfoliation, we performed SAED on different regions of the as-prepared TEGO, and took different diffraction patterns at various tilt angles. We measured the ratio of the {1100} and {2110} spot intensities of 1.5(1) at 0° tilt with respect to the basal plane and almost constant ($\delta < 12\%$) by changing the tilting angle (20° range), while a thin AB stacked multilayer should have a ratio lower than one at 0° tilt, and showing oscillations by varying the angle.[23] The results are in good agreement with literature values for single layer graphene.[24] A cross-check with the reference sample gave a ratio of {1100} and {2110} spots of 0.5(1) as expected from a multilayer. HRTEM, performed at 80 kV to assure no beam damage or modification to the sample, reveals very thin flat domains surrounded by a thicker defective network (Fig. 1(a–c)). The Electron Energy Loss (EEL) spectrum of the whole area is compatible with FLG with $n \leq 5$ indicating that the flat domains are indeed single layers with the thicker parts resulting from residual defective GO few layers thick (see Fig. 1(d)).[25]

For bulk information on the crystallinity and the average sp^2 domain size we performed Raman spectroscopy on the TEGO samples. Raman spectra of carbon based materials, recorded with a laser excitation wavelength of 532 nm, show several remarkable features denoted the D band, at about 1350 cm^{-1}, the G band at around 1582 cm^{-1}, the D′ band at about 1620 cm^{-1} and the 2D band at around 2700 cm^{-1}. The D and D′ bands are associated with structural defects and disorder and will thus not be recorded for highly crystalline graphite. The G

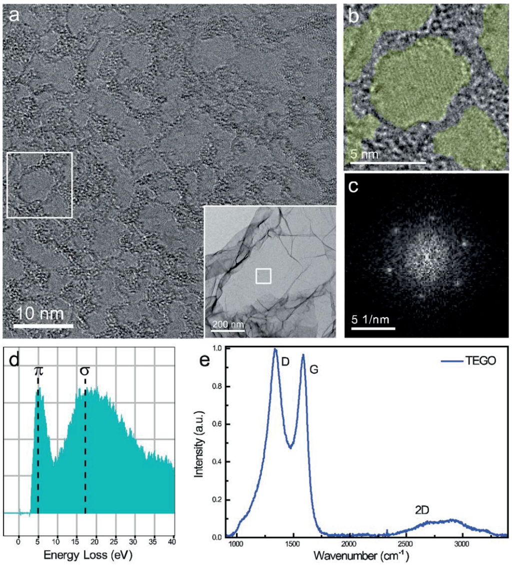

Fig. 1 (a) 80 kV HRTEM image from a flat TEGO region (as indicated in the inset). Small very thin domains are visible, which are surrounded by a thicker network due to residual GO after exfoliation. (b) Zoom of a portion of the film, in which the thin domains (mostly single layers) are highlighted in yellow. (c) FFT from the central domain, with sharp {1100} spots from an ordered hexagonal graphene pattern. (d) Average EEL spectrum from the whole region in (a). The position of the σ plasmon is in agreement with the results from FLG (1–5 layers) resulting from the superposition of the thin TEGO domains and the thicker GO residual. (e) Raman spectrum of as-synthesised TEGO.

band originates from the E_{2g} phonon mode of sp^2 domains at the centre of the Brillouin zone and is a measure of the degree of graphitization. Together with the intensity ratio, the integrated peak area of D and G bands is used to determine the defectiveness of graphitic materials and it was shown that the inverse ratio of I_D/I_G is proportional to the crystallite size for nanographite materials. The relationship can be written as:[26]

$$L_a(\text{nm}) = \left(2.4\cdot 10^{-10}\right)\lambda_{\text{laser}}{}^4\left(\frac{I_D}{I_G}\right)^{-1} \quad (1)$$

The spectrum of the as-synthesized TEGO can be seen in Fig. 1(e). Integrating the area under the D and G band peaks yields $I_D/I_G = 1.56$ and thus average sp^2 domains of $L_a = 12.3$ nm. This stands in excellent agreement with the measured size of the ordered domains, imaged by HRTEM of 10–15 nm (Fig. 1(a) and (b)).

TEM images from Ni–TEGO are shown in Fig. 2: HAADF-STEM images (Fig. 2(a) and (c)) reveal that the graphene films are indeed decorated by nanometer sized particles. The average diameter of the particles is 17(4) nm as obtained from statistical analysis of about 350 particles (Fig. 2(b)). The HRTEM images have atomic columns at positions (see the fast Fourier transforms (FFT) in the insets of Fig. 2(c) and (d)) compatible with the cubic structure of Ni (space group $Fm\bar{3}m$) with the (200) reflection corresponding to the 0.18 nm plane distance in the real space. FFT analysis and geometrical phase analysis (GPA) of HRTEM images of single NPs do not show the presence of Ni-oxide.[27] Fig. 2(e) and (f) show the EEL spectrum from a Ni particle of about 20 nm diameter. The C–K signal originates from the graphene substrate (TEGO). A signal of the O–K ionization edge is hardly detectable, confirming that the oxidation of the particles, if present, is confined to a very thin layer (<1 nm) at the surface and can derive from exposure to air during the TEM sample preparation. Moreover, the fine structure of the Ni-$L_{2,3}$ edge (Fig. 2(f)) resembles the one from metallic fcc Ni.[28] Other spectra collected from different particles show the same features.

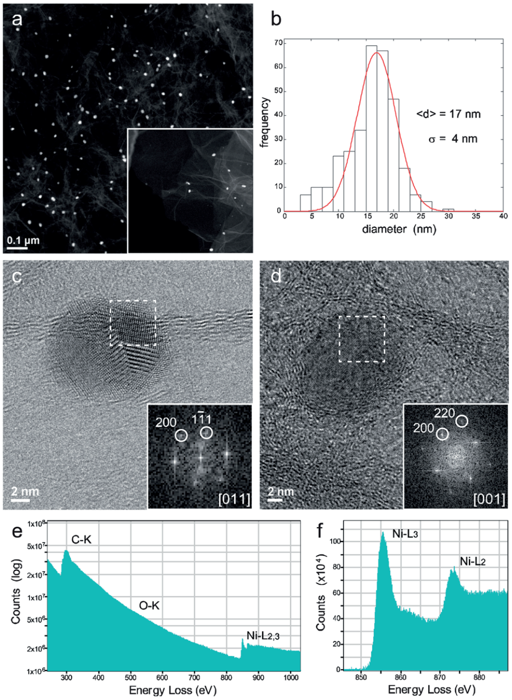

Fig. 2 (a) HAADF-STEM image of the Ni decorated TEGO. The Ni particles show up very bright in the image (dark field) due to the higher atomic number of Ni ($Z = 28$) with respect to carbon atoms ($Z = 6$). Inset: HAADF-STEM image of a single layer graphene region of the sample. (b) Histogram of size distribution from about 350 Ni particles as measured from the STEM images. (c and d) Representative HRTEM (*bright field*) images of the Ni particles, with the FFTs in the insets showing reflections compatible with cubic fcc Ni. (e) EEL spectrum (in log-scale) from a Ni particle on TEGO, showing the C-K ionization edge of TEGO, a low O-K ionization edge, and the Ni-$L_{2,3}$ ionization edge from the particle. (f) Ni-$L_{2,3}$ edge similar to the one from metallic fcc Ni.[28]

Magnetometry

Although electron imaging supports the formation of nickel nanoparticles, TEM is not a bulk measure and cannot be representative of the whole investigated sample. In fact, aggregates of nanoparticles or microscopic grains of Ni could be present which are not seen in the little amount of sample investigated by means of TEM. In this case, the well known magnetic properties of nickel can be exploited in a SQuID measurement in order to have statistics on the entire material. The ZFC and FC measurements of Ni–TEGO are shown in Fig. 3. The behaviour is typical of a system composed of super-paramagnetic (SPM) NPs. The peak in susceptibility in the ZFC measurement corresponds to an average blocking temperature of $\langle T_B\rangle = 137(2)$ K. The total magnetization of the NPs is under thermally induced rotation at 400 K and starts to freeze beneath 300 K. The cubic magnetocrystalline anisotropy constant of

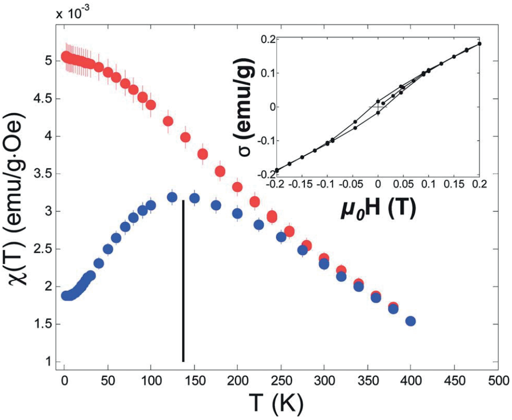

Fig. 3 (a) ZFC (blue) and FC (red) of Ni–TEGO. Inset: hysteresis loop at 2 K shows a coercivity of about 100 Oe.

bulk Ni at low temperature is $K_1 = -8 \times 10^4$ J m^{-3}.[29] Since K_1 is negative, the effective uniaxial anisotropy is $K_{\text{eff}} = |K_1|/12$ and corresponds to a value of 6.67×10^3 J m^{-3}.[30] TEM experiment shows the presence of monodispersed 17(4) nm diameter Ni NPs. If we consider a population of spherical and non-interacting cubic Ni nanoparticles with $T_{\text{B}} = 137(2)$ K and a diameter of 17 nm, the anisotropy constant could be expressed as $K_{\text{eff}} = \ln(\tau/\tau_0)k_{\text{B}}T_{\text{B}}/\beta V$, where $\beta = 1$ when the diameter distribution function is $g(D) = \delta(D - D_0)$; τ is related to the measurement technique (for DC SQuID in the order of 10^2 s); τ_0 is the time-scale of magnetic relaxation (in the order of 10^9 to 10^{12} s) and k_{B} is the Boltzmann factor. Taking $D = 17$ nm, $\beta = 1$ and $T_{\text{B}} = 137$ K, the corresponding value of K_{eff} is about $18.6(4) \times 10^3$ J m^{-3}. An increase in anisotropy can be originating from the presence of shape and surface effects but neither are expected from TEM analysis. In contrast, using $K_{\text{eff}} = 6.67 \times 10^3$ J m^{-3} and $T_{\text{B}} = 137(2)$ K, the estimated size of NPs is $\langle D \rangle = 24(6)$ nm which is however still compatible with the NP size observed with TEM.

This is a rough estimate of $\langle D \rangle$, but since SQuID magnetometry is a bulk measurement, it indicates that Ni is only present in the form of nanoparticles. Moreover, the overall negative slope in the FC susceptibility below $\langle T_{\text{B}} \rangle$ suggests that the NPs responsible for the signal are magnetically non-interacting.[31] This is indicative of a diluted regime of non-aggregated NPs. The weak Curie-like trend detectable at very low temperature is partially attributed to the sum of the $S = 1/2$ paramagnetic defects of pure graphene (in our TEGO usually in order of $\sim 10^{18}$ g^{-1}) and to the smaller SPM NPs. The hysteresis loop at 2 K (see the inset of Fig. 3) shows a coercitive field of about 100 Oe, typical of soft magnetic materials and easily attributed to randomly oriented magnetic NPs. The absence of a measurable exchange bias shift in the hysteresis loop excludes the formation of a thick shell of Ni oxide on Ni NPs when the sample is never exposed to air.[32] The formation of a thin oxide shell, however, cannot be excluded. For example, Seto *et al.* found a shift of 30 Oe for core–shell Ni–NiO NPs with a core diameter similar to our case (17.4 nm) and 2.1 nm shell.[33]

X-ray photoelectron spectroscopy

As a quantitative spectroscopic technique, able to measure electrons which have escaped from the first few nanometers of the investigated material, XPS is a well suited method to study the composition of a material like Ni–TEGO, with its structure closely resembling a 2D surface. The XPS spectra and the respective fits are depicted in Fig. 4. The relative abundance of chemical elements and the chemical shifts for the fitted peaks can be found in Table 1.

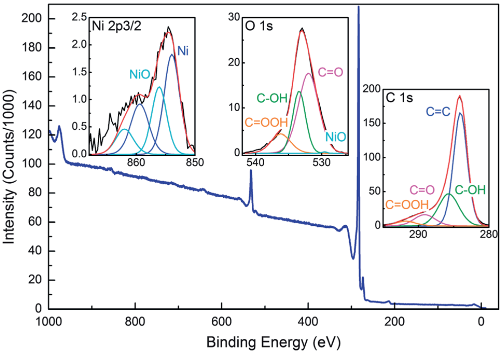

Fig. 4 XPS spectra of Ni–TEGO. The insets show the spectra of the Ni 2p3/2 including the corresponding satellite peaks, O 1s and C 1s peaks (from left to right).

Table 1 Results of the peak analysis of the Ni–TEGO XPS data and relative abundance of carbon, oxygen and nickel calculated from the total area under the respective peaks

	Binding energies and chemical shifts (eV)		
Functional group	C–/=C (284.06)	C=O (532)	Ni 2p3/2 (853.95)
C–OH	1.65	1.42	—
C=O	5.06	0	—
C=OOH	7.77	4.2	—
NiO 2p3/2	—	−2.45	2.16
Relative abundance (%)	C – 94.66	O – 5.2	Ni – 0.14

The limited resolution of the XPS spectrometer does not allow a separate analysis of the carbon–carbon single and double bonded peaks and a one peak fit was performed. This main C1s peak shows at a binding energy of 284.06 eV and all spectra were calibrated to this peak position. Ni constitutes to about 0.14% relative abundance. A minor contribution of NiO can be seen for the Ni 2p3/2 peak. This can be interpreted by a core–shell structure with a thin layer of NiO encapsulating a Ni core. TEM measurements, not showing significant NiO, underpin this interpretation of merely a thin layer of oxidized Ni. Another reason for this chemical shift could be the presence of unreacted Ni(acac)$_2$, which is known to have a very similar chemical peak shift as NiO and was used as a precursor.[34,35] Oxygen constitutes to about 5.2%. With roughly 3% O measured for the pure TEGO and only 0.14% Ni, the additional oxygen can originate from either partly unfinished annealing of the TEGO or precursor, *e.g.* non-decomposed Ni(acac)$_2$.[36] The low oxygen content, particularly for TEGO, and the absence of significant impurities are evidential for a high quality synthesis.

Muon spin rotation

Positive muons (μ^+) are spin 1/2 particles with about one ninth of the mass of the proton. By implanting μ^+ into insulating samples and observing the formation of muonium (Mu $= \mu^+e^-$), a light isotope of hydrogen, one can probe the interaction of hydrogen with its host system, thus studying the two steps of the H_2 absorption process separately, in order to discern the dissociation of the molecule from the binding of atomic hydrogen.[37] Zero Field (ZF) relaxation of the muon polarization (see the inset of Fig. 5) highlighted two different components: a slowly decaying fraction fitted with a Lorentzian relaxation

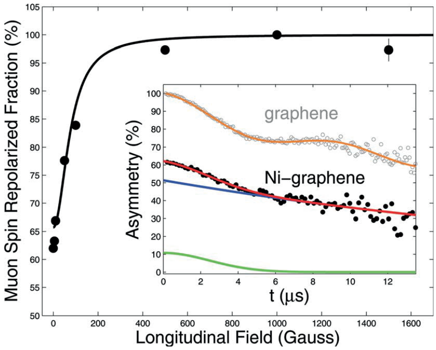

Fig. 5 Muon spin repolarization experiment of Ni–TEGO at 300 K fitted with the simple model for muonium radical (eqn (1)). Inset: zero field muon spin relaxation (at 300 K) of Ni-graphene (black dots) fitted (red line) with the sum of Gaussian (green line) and Lorentzian (blue line) decays. A constant contribution is added to Lorentzian decay, due to diamagnetic muons. As comparison, pure TEGO is reported (grey dots) and fitted (orange line) as described in M. Riccò *et al.*[4]

(~52%) and a small Gaussian component (~10%). The Lorentzian decay is typical for μ^+ diffusing through a carbon surface. The Gaussian component can be assigned to the small fraction of μ^+ attached to edges and undergoing local dipolar interaction with nearby protons. However, if we compare the observed signal with that obtained from pure graphene (TEGO), where the full initial asymmetry is observed,[4] an evident missing fraction appears, which significantly lowers the signal amplitude. In metal decorated graphene ~38% of the implanted muons were not revealed by the detector which indicates that the frequency of the precession signal exceeds the instrument cut-off of 13 MHz. Such a phenomenon can occur when the positive muon strongly interacts with an electron (hyperfine interaction) either due to the formation of muonium or after the adduction reaction of muonium to form a radical.[38] In the latter case the electron wavefunction is no longer localized on the muon and the hyperfine interaction is thus sensibly reduced. The application of longitudinal fields, which decouple the muon spin from the electron spin, allows discrimination between these two cases and estimation of the intensity of the hyperfine interaction. It is well known that the free muonium signal is recovered by the application of a longitudinal field of 1580 G while a much lower value is generally required to recover a muonium-adduct radical signal.[39] The muon spin repolarized fraction of the sample, as a function of longitudinal field, has the functional behavior of the simple model for isotropic muonium: $P = 1/2[1 + x^2/(x^2 + 1)]$, where $x = B/B_{\text{Hyp}}$ and B_{hyp} is the hyperfine field for free muonium.[37] Assuming an isotropic interaction, our repolarization curves have been fitted with the function

$$P_{\text{exp}} = P_{\text{diam}} + A_{\text{rad}}\left[\frac{x^2}{x^2+1}\right], \tag{2}$$

where P_{diam} is the diamagnetic fraction of muons observed in the ZF experiment and A_{rad} is the amplitude of the radical fraction. As shown in Fig. 5, the flex of the fitting function is localized at the field of 77(1) G, corresponding to a hyperfine frequency of 212(4) MHz. Such a low value clearly demonstrates the formation of a radical complex which was not detected in bare graphene.[4] The radical site must be on the graphene plane as no radical formation is expected from the interaction of muonium with metal nanoparticles[40] and moreover, the small volume fraction of metal in our sample could hardly account for such a large fraction of radical signal observed. Therefore, the large amplitude of the observed radical signal witnesses the large reactivity of the Ni decorated graphene with atomic hydrogen.

Hydrogen sorption

Hydrogen sorption was measured both with a Sieverts type apparatus up to 1 bar H_2 pressure and on an in-house build dynamic pcT apparatus. Due to the higher accuracy of the Sieverts measurements at low pressure the pcT data were omitted in this region and only the BET data were taken into account. The experimental data can be seen in Fig. 6. The solid, red line depicts an isotherm, fitted to the data, with the following form:

$$n = \frac{N_t(K_0p)^m}{1+(K_0p)^m}, \tag{3}$$

where n is the relative amount of hydrogen adsorbed on a gram of sample, N_t the adsorption capacity of the system and related to the total number of binding sites, p the hydrogen pressure and thus related to the concentration under equilibrium conditions, K_0 is the binding affinity parameter and m is the heterogeneity index.[41] It is noteworthy that at hydrogen pressures above 20 bar the data start to deviate from the isotherm model. This can be explained by the difference between absolute adsorption, as calculated by the fit model in eqn (3), and excess adsorption, which is measured with the pcT apparatus. While the fit model shows an asymptotic behavior the measured excess adsorption reaches a maximum value and decreases subsequently, due to the non-negligible bulk density of the high pressure gas. The isotherm fit indicates that at 77 K a maximum of about 1.15 mass% of hydrogen can be adsorbed on Ni–TEGO.

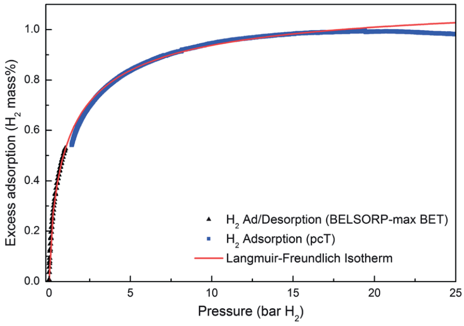

Fig. 6 Hydrogen adsorption measured with the BET (black triangles) and the dynamic pcT setups (blue squares).

As expected, higher temperatures during adsorption resulted in lower hydrogen uptake. With a BET specific surface area of 505 $m^2 g^{-1}$ Ni–TEGO adsorbs and desorbs about 51% additional hydrogen as compared to previous results on hydrogen physisorption with roughly 1.5 mass%/1000 $m^2 g^{-1}$ at 77 K.[42] Hydrogen adsorption proved fully reversible during numerous cycles.

Discussion

As previously discussed, hydrogen is not chemisorbed on pure graphene under desirable conditions (only at elevated temperatures around 800 °C or under high pressure). Recent measurements of Inelastic Neutron Scattering (INS) and ^1H Nuclear Magnetic Resonance (^1H-NMR) demonstrated the diffusion of chemisorbed hydrogen on graphene planes, with an activation energy barrier of about 30 meV.[43] This led us to decorate graphene with a catalyst known to be efficient in dissociating H_2, *e.g.* nickel. The μSR experiment clearly shows the formation of a radical on the graphene plane. The production of a radical proves the chemisorption of hydrogen which is however still perturbed by an unpaired electron. This is not expected for an isolated "in plane" chemisorbed hydrogen for which the unpaired π electron, following the sp^2 to sp^3 hybridization of carbon, gets diluted in the graphene π-derived conduction band. The localization of the paramagnetic electron can be, in our case, attributed to the local perturbation of the nickel NP on the π-orbitals. The locally modified graphene around the Ni NP shows thus a larger affinity to hydrogen (muonium) with respect to the unperturbed plane which enhances its chemisorption. The BET and pcT measurements, on the other hand, do not show evidence of the Ni catalyzed dissociation of hydrogen at 77 K. The measured adsorbed–desorbed hydrogen is however about 51% above expectation and this is probably due to Ni activated physisorption, in the proximity of graphene planes facing a Ni NP. These results suggest that a further improvement of the system is required to achieve the hydrogen dissociation: either by reducing the size of the nanoparticles or by decorating TEGO with atomic nickel.

Conclusions

Ni decorated graphene has been synthesized following a two step process under oxygen/water free conditions. The TEM analysis demonstrates the formation of monodispersed nickel nanoparticles, of 17 nm diameter, decorating the single layer graphene sheets. SQuID magnetometry confirms the production of diluted superparamagnetic nickel with an average blocking temperature of 173 K, consistent with the estimated average dimension of the NPs. The presence of oxidized species of Ni on the surface is detected by XPS. We attribute this to a non-reacted fraction of $Ni(acac)_2$ or to the existence of a thin layer of Ni oxide, present on the surface of nanoparticles. The appearance of a radical state in the μSR experiment can be considered a clear fingerprint of atomic hydrogen capture, not seen in bare graphene. Moreover, the presence of Ni on graphene seems to significantly increase the amount of molecular hydrogen adsorbed at 77 K as seen in dynamic pcT and BET isotherm measurements.

Acknowledgements

The authors would like to acknowledge financial support from the SNSF "HyCarBo" project (Grant no. CRSII2-130509), ISIS Rutherford Appleton laboratory for beam time allocation and local contact Dr Sean Giblin for support during the experiment.

Notes and references

1 M. Choucair, P. Thordarson and J. Stride, *Nat. Nanotechnol.*, 2008, **4**, 2–5.
2 A. Peigney, C. Laurent, E. Flahaut, R. R. Bacsa and A. Rousset, *Carbon*, 2001, **39**, 507–514.
3 L. Schlapbach and A. Züttel, *Nature*, 2001, **414**, 353–358.
4 M. Riccò, D. Pontiroli, M. Mazzani, M. Choucair, J. A. Stride and O. V. Yazyev, *Nano Lett.*, 2011, **11**, 4919–4922.
5 Y. Wang, C. X. Guo, X. Wang, C. Guan, H. Yang, K. Wang and C. M. Li, *Energy Environ. Sci.*, 2011, **4**, 195.
6 C. Zhang, W. Lv, Q. Yang and Y. Liu, *Appl. Surf. Sci.*, 2012, **258**, 7795–7800.
7 A. Singh, M. Ribas and B. Yakobson, *ACS Nano*, 2009, **3**, 1657–1662.
8 G. J. Kubas, *J. Organomet. Chem.*, 2001, **635**, 37–68.
9 T. Yildirim and S. Ciraci, *Phys. Rev. Lett.*, 2005, **94**, 175501.
10 T. Yildirim, J. Íñiguez and S. Ciraci, *Phys. Rev. B: Condens. Matter Mater. Phys.*, 2005, **72**, 153403.
11 K. R. S. Chandrakumar and S. K. Ghosh, *Nano Lett.*, 2008, **8**, 13–19.
12 M. Yoon, S. Yang, C. Hicke, E. Wang, D. Geohegan and Z. Zhang, *Phys. Rev. Lett.*, 2008, **100**, 206806.
13 H. Lee, J. Ihm, M. L. Cohen and S. G. Louie, *Nano Lett.*, 2010, **10**, 793–798.
14 J. A. Teprovich, M. S. Wellons, R. Lascola, S. Hwang, P. A. Ward, R. N. Compton and R. Zidan, *Nano Lett.*, 2012, **12**, 582–589.
15 P. Mauron, M. Gaboardi, A. Remhof, A. Bliersbach, A. Züttel, D. Sheptyakov, M. Aramini, G. Vlahopoulou, F. Giglio, D. Pontiroli and M. Riccò, *J. Phys. Chem. C*, 2013, **117**, 22598–22602.
16 M. Aramini, M. Gaboardi, G. Vlahopoulou, D. Pontiroli, C. Cavallari, C. Milanese and M. Riccò, *Carbon*, 2013, **7**, 2–7.
17 P. Mauron, A. Remhof, A. Bliersbach, A. Borgschulte, A. Züttel, D. Sheptyakov, M. Gaboardi, M. Choucair, D. Pontiroli, M. Aramini, A. Gorreri and M. Riccò, *Int. J. Hydrogen Energy*, 2012, **37**, 14307–14314.
18 M. Bielmann, S. Kato, P. Mauron, A. Borgschulte and A. Züttel, *Rev. Sci. Instrum.*, 2009, **80**, 083901.
19 D. Yang, A. Velamakanni, G. Bozoklu, S. Park, M. Stoller, R. D. Piner, S. Stankovich, I. Jung, D. A. Field, C. A. Ventrice and R. S. Ruoff, *Carbon*, 2009, **47**, 145–152.
20 T. Szabó, O. Berkesi, P. Forgó, K. Josepovits, Y. Sanakis, D. Petridis and I. Dékány, *Chem. Mater.*, 2006, **18**, 2740–2749.
21 B. C. Brodie, *Ann. Chim. Phys.*, 1860, **59**, 466–472.

22 M. J. McAllister, J. Li, D. H. Adamson, H. C. Schniepp, A. A. Abdala, J. Liu, M. Herrera-Alonso, D. L. Milius, R. Car, R. K. Prud'homme and I. A. Aksay, *Chem. Mater.*, 2007, **19**, 4396–4404.
23 J. C. Meyer, A. K. Geim, M. I. Katsnelson, K. S. Novoselov, T. J. Booth and S. Roth, *Nature*, 2007, **446**, 60–63.
24 Y. Hernandez, V. Nicolosi, M. Lotya, F. M. Blighe, Z. Sun, S. De, I. T. McGovern, B. Holland, M. Byrne, Y. K. Gun'Ko, J. J. Boland, P. Niraj, G. Duesberg, S. Krishnamurthy, R. Goodhue, J. Hutchison, V. Scardaci, A. C. Ferrari and J. N. Coleman, *Nat. Nanotechnol.*, 2008, **3**, 563–568.
25 T. Eberlein, U. Bangert, R. Nair, R. Jones, M. Gass, A. Bleloch, K. Novoselov, A. Geim and P. Briddon, *Phys. Rev. B: Condens. Matter Mater. Phys.*, 2008, **77**, 233406.
26 M. A. Pimenta, G. Dresselhaus, M. S. Dresselhaus, L. G. Cançado, A. Jorio and R. Saito, *Phys. Chem. Chem. Phys.*, 2007, **9**, 1276–1291.
27 S. D'Addato, V. Grillo, S. Altieri, S. Frabboni and S. Valeri, *Appl. Surf. Sci.*, 2012, **260**, 13–16.
28 G. A. Botton and C. J. Humphreys, *Intermetallics*, 1999, **7**, 829–833.
29 H. Williams and R. Bozorth, *Phys. Rev.*, 1939, **56**, 837.
30 J. Gittleman, B. Abeles and S. Bozowski, *Phys. Rev. B: Condens. Matter Mater. Phys.*, 1974, **9**, 3891–3897.
31 S. Bedanta and W. Kleemann, *J. Phys. D: Appl. Phys.*, 2009, **42**, 013001.
32 L. Del Bianco, F. Boscherini, A. Fiorini, M. Tamisari, F. Spizzo, M. Antisari and E. Piscopiello, *Phys. Rev. B: Condens. Matter Mater. Phys.*, 2008, **77**, 094408.
33 T. Seto, H. Akinaga, F. Takano, K. Koga, T. Orii and M. Hirasawa, *J. Phys. Chem. B*, 2005, **109**, 13403–13405.
34 J. SCHREIFELS, P. C. Maybury and J. W. E. Swartz, *J. Catal.*, 1980, **65**, 195–206.
35 M. Chigane and M. Ishikawa, *J. Chem. Soc., Faraday Trans.*, 1998, **94**, 3665–3670.
36 J. Von Hoene, R. G. Charles and W. M. Hickam, *J. Phys. Chem.*, 1958, **62**, 1098–1101.
37 A. Schenck, *Muon spin rotation spectroscopy*, 1985.
38 S. F. J. Cox, *Rep. Prog. Phys.*, 2009, **72**, 116501.
39 E. Roduner, M. Schwager and M. Shelley, *Mol. Eng.*, 1994, **4**, 259–276.
40 R. Bewley and R. Cywinski, *Phys. Rev. B: Condens. Matter Mater. Phys.*, 1998, **58**, 11544–11551.
41 D. G. Kinniburgh, *Environ. Sci. Technol.*, 1986, **20**, 895–904.
42 A. Züttel, P. Sudan, P. Mauron, T. Kiyobayashi, C. Emmenegger and L. Schlapbach, *Int. J. Hydrogen Energy*, 2002, **27**, 203–212.
43 D. Pontiroli, M. Aramini, M. Gaboardi, M. Mazzani and M. Riccò, *J. Phys. Chem. C*, submitted.

Bibliography

[1] H. F. Abbas and W. M. A. Wan Daud. **Hydrogen production by methane decomposition: A review.** *International Journal of Hydrogen Energy*, 35(3):1160–1190, 2010.

[2] W. Andreoni, P. Giannozzi, J. F. Armbruster, M. Knupfer and J. Fink. **Anomalous electronic behaviour of Na superfullerides: theory and experiment.** *EPL (Europhysics Letters)*, 34(9):699, 1996.

[3] F. Bødker, S. Mørup and S. Linderoth. **Surface effects in metallic iron nanoparticles.** *Phys. Rev. Lett.*, 72:282–285, Jan 1994.

[4] G. Beamson and D. Briggs. ***High resolution XPS of Organic Polymers - The Scienta ESCA300 Database***. John Wiley and Sons Ltd, 1992.

[5] S. Bedanta and W. Kleemann. **Supermagnetism.** *Journal of Physics D: Applied Physics*, 42(1):013001, 2009.

[6] R. I. Bewley and R. Cywinski. **Muon spin relaxation in a superparamagnet: Field dynamics in $Cu_{98}Co_2$.** *Phys. Rev. B*, 58:11544–11551, Nov 1998.

[7] R. Bhandari and I. Stadler. **Grid parity analysis of solar photovoltaic systems in Germany using experience curves.** *Solar Energy*, 83(9):1634 – 1644, 2009.

[8] M. Bielmann, S. Kato, Ph. Mauron, A. Borgschulte and A. Züttel. **Characterization of hydrogen storage materials by means of pressure concentration isotherms based on the mass flow method.** *Review of Scientific Instruments*, 80(8), 2009.

[9] S. J. Blundell. **Spin-polarized muons in condensed matter physics.** *Contemporary Physics*, 40(3):175–192, 1999.

[10] S. J. Blundell. ***Magnetism in Condensed Matter.*** Oxford University Press, 2001.

[11] G. A. Botton and C. J. Humphreys. **Determining the bonding in intermetallics using electron energy loss spectroscopy and density functional theory.** *Intermetallics*, 7(7):829 – 833, 1999.

[12] K. Branker, M. J. M. Pathak and J. M. Pearce. **A review of solar photovoltaic levelized cost of electricity.** *Renewable and Sustainable Energy Reviews*, 15(9):4470 – 4482, 2011.

[13] H. B. Bürgi, R. Restori and D. Schwarzenbach. **Structure of C_{60}: partial orientational order in the room-temperature modification of C_{60}.** *Acta Crystallographica Section B*, 49(5):832–838, Oct 1993.

[14] B. C. Brodie. **Sur le poids atomique du graphite.** *Ann.Chim.Phys.*, 59:466–472, 1860.

[15] W. Fuller Brown. **Thermal Fluctuations of a Single-Domain Particle.** *Phys. Rev.*, 130:1677–1686, Jun 1963.

[16] S. Brunauer, P. H. Emmett and E. Teller. **Adsorption of Gases in Multimolecular Layers.** *Journal of the American Chemical Society*, 60(2):309–319, 1938.

[17] L. G. Cançado, K. Takai, T. Enoki, M. Endo, Y. A. Kim, H. Mizusaki, A. Jorio, L. N. Coelho, R. Magalhães-Paniago and M. A. Pimenta. **General equation for the determination of the crystallite size L_a of nanographite by Raman spectroscopy.** *Applied Physics Letters*, 88(16):–, 2006.

[18] K. R. S. Chandrakumar and S. K. Ghosh. **Alkali-Metal-Induced Enhancement of Hydrogen Adsorption in C_{60} Fullerene: An ab Initio Study.** *Nano Letters*, 8(1):13–19, 2008. PMID: 18085807.

[19] T. Chen, F. Deng, J. Zhu, C. Chen, G. Sun, S. Ma and X. Yang. **Hexagonal and cubic Ni nanocrystals grown on graphene: phase-controlled synthesis, characterization and their enhanced microwave absorption properties.** *J. Mater. Chem.*, 22:15190–15197, 2012.

[20] Z. Chen, V. Chevrier, L. Christensen and J. R. Dahn. **Design of Amorphous Alloy Electrodes for Li-Ion Batteries: A Big Challenge.** *Electrochemical and Solid-State Letters*, 7(10):A310–A314, 2004.

[21] I. Childres, L. A. Jauregui, W. onjun Park, H. Cao and Y. P. Chena. ***Raman Spectroscopy of Graphene and Related Materials.*** Purdue University, West Lafayette, IN, US.

[22] N.-S. Choi, K. H. Yew, K.Y. Lee, M. Sung, H. Kim and S.-S. Kim. **Effect of fluoroethylene carbonate additive on interfacial properties of silicon thin-film electrode.** *Journal of Power Sources*, 161(2):1254–1259, 2006.

[23] J. Chontanawat, L. C. Hunt and R. Pierse. **Causality between Energy Consumption and GDP: Evidence from 30 OECD and 78 Non-OECD Countries.** Surrey Energy Economics Centre (SEEC), School of Economics Discussion Papers (SEEDS) 113, Surrey Energy Economics Centre (SEEC), School of Economics, University of Surrey, June 2006.

[24] M. Choucair, P. Thordarson and J. A. Stride. **Gram-scale production of graphene based on solvothermal synthesis and sonication.** *Nat Nano*, 4(1):30–33, 2009.

[25] J. Clarke and A. I. Braginski, editors. ***The SQUID Handbook: Fundamentals and Technology of SQUIDs and SQUID Systems, Volume I.*** WILEY-VCH Verlag, 2004.

[26] S. F. J. Cox. **Muonium as a model for interstitial hydrogen in the semiconducting and semimetallic elements.** *Reports on Progress in Physics*, 72(11):116501, 2009.

[27] S. F. J. Cox, S. P. Cottrell, M. Charlton, P. A. Donnelly, C. Ewels, M. Heggie and B. Hourahine. **A molecular radical model for hydrogen and muonium in graphite.** *Journal of Physics: Condensed Matter*, 13(10):2169, 2001.

[28] J. Crangle and G. M. Goodman. **The Magnetization of Pure Iron and Nickel.** *Proceedings of the Royal Society of London. A. Mathematical and Physical Sciences*, 321(1547):477–491, 1971.

[29] M. O. de Souza, F. M. T Mendes, R. F. de Souza and J. H. Z. dos Santos. **XPS characterization of nickel-acetylacetonate impregnated in NaX and NaY zeolites.** *Microporous and Mesoporous Materials*, 69(3):217 – 221, 2004.

[30] M. A. Delucchi and M. Z. Jacobson. **Providing all global energy with wind, water, and solar power, Part II: Reliability, system and transmission costs, and policies.** *Energy Policy*, 39(3):1170 – 1190, 2011.

[31] P. Divya and S. Ramaprabhu. **Hydrogen storage in platinum decorated hydrogen exfoliated graphene sheets by spillover mechanism.** *Phys. Chem. Chem. Phys.*, 16:26725–26729, 2014.

[32] D. D. Do. ***Adsorption Analysis: Equilibria and Kinetics*, Volume 2.** Imperial College Press, 1998.

[33] T. Eberlein, U. Bangert, R. R. Nair, R. Jones, M. Gass, A. L. Bleloch, K. S. Novoselov, A. Geim and P. R. Briddon. **Plasmon spectroscopy of free-standing graphene films.** *Phys. Rev. B*, 77:233406, Jun 2008.

[34] B. Elliston, I. MacGill and M. Diesendorf. **Least cost 100% renewable electricity scenarios in the Australian National Electricity Market.** *Energy Policy*, 59(0):270 – 282, 2013.

[35] E.ON. **E.ON examines options for storing wind power in the German gas grid.** E.ON company website, November 2011.

[36] V. Fernandes, R. J. O. Mossanek, P. Schio, J. J. Klein, A. J. A. de Oliveira, W. A. Ortiz, N. Mattoso, J. Varalda, W. H. Schreiner, M. Abbate and D. H. Mosca. **Dilute-defect magnetism: Origin of magnetism in nanocrystalline $\mathbf{CeO_2}$.** *Phys. Rev. B*, 80:035202, Jul 2009.

[37] M. A. Fetcenko, S. R. Ovshinsky, K. Young, B. Reichman, C. Fierro, J. Koch, F. Martin, W. Mays, T. Ouchi, B. Sommers and A. Zallen. **High catalytic activity disordered VTiZrNiCrCoMnAlSn hydrogen storage alloys for nickel-metal hydride batteries.** *Journal of Alloys and Compounds*, 330 - 332(0):752 – 759, 2002.

[38] L. Forro and L. Mihaly. **Electronic properties of doped fullerenes.** *Reports on Progress in Physics*, 64(5):649, 2001.

[39] M. Gaboardi, A. Bliersbach, G. Bertoni, M. Aramini, G. Vlahopoulou, D. Pontiroli, Ph. Mauron, G. Magnani, G. Salviati, A. Züttel and M. Riccò. **Decoration of graphene with nickel nanoparticles: study of the interaction with hydrogen.** *J. Mater. Chem. A*, 2:1039–1046, 2014.

[40] A. Ganguly, S. Sharma, P. Papakonstantinou and J. Hamilton. **Probing the Thermal Deoxygenation of Graphene Oxide Using High-Resolution In Situ X-ray-Based Spectroscopies.** *The Journal of Physical Chemistry C*, 115(34):17009–17019, 2011.

[41] Y. Gao, N. Zhao, J. Li, E. Liu, C. He and C. Shi. **Hydrogen spillover storage on Ca-decorated graphene.** *International Journal of Hydrogen Energy*, 37(16):11835–11841, 2012.

[42] J. I. Gittleman, B. Abeles and S. Bozowski. **Superparamagnetism and relaxation effects in granular Ni-SiO_2 and Ni-Al_2O_3 films.** *Phys. Rev. B*, 9:3891–3897, May 1974.

[43] W. Grochala and P. P. Edwards. **Thermal Decomposition of the Non-Interstitial Hydrides for the Storage and Production of Hydrogen.** *Chemical Reviews*, 104(3):1283–1316, 2004.

[44] R. C. Haddon. **Electronic structure, conductivity and superconductivity of alkali metal doped (C_{60}).** *Accounts of Chemical Research*, 25(3):127–133, 1992.

[45] R. C. Haddon, L. F. Schneemeyer, J. V. Waszczak, S. H. Glarum, R. Tycko, G. Dabbagh, A. R. Kortan, A. J. Muller, A. M. Mujsce, M. J. Rosseinsky, S. M. Zahurak, A. V. Makhija, F. A. Thiel, K. Raghavachari, E. Cockayne and V. Elser. **Experimental and theoretical determination of the magnetic susceptibility of C_{60} and C_{70}.** *Nature*, 350(6313):46–47, 1991.

[46] G.-B. Han, M.-H. Ryou, K. Y. Cho, Y. M. Lee and J.-K. Park. **Effect of succinic anhydride as an electrolyte additive on electrochemical characteristics of silicon thin-film electrode.** *Journal of Power Sources*, 195(11):3709–3714, 2010.

[47] Y. Hernandez, V. Nicolosi, M. Lotya, F. M. Blighe, Z. Sun, S. De, I. T. McGovern, B. Holland, M. Byrne, Y. K. Gun'Ko, J. J. Boland, P. Niraj, G. Duesberg, S. Krishnamurthy, R. Goodhue, J. Hutchison, V. Scardaci, A. C. Ferrari and J. N. Coleman. **High-yield production of graphene by liquid-phase exfoliation of graphite.** *Nat Nano*, 3(9):563–568, September 2008.

[48] O. H. Hohmeyer and S. Bohm. **Trends toward 100% renewable electricity supply in Germany and Europe: a paradigm shift in energy policies.** *Wiley Interdisciplinary Reviews: Energy and Environment*, 2014.

[49] Z. Hu, Y. Chen, Q. Hou, R. Yin, F. Liu and H. Chen. **Characterization of graphite oxide after heat treatment.** *New J. Chem.*, 36:1373–1377, 2012.

[50] A. W. Hull. **A New Method of X-Ray Crystal Analysis.** *Phys. Rev.*, 10:661–696, Dec 1917.

[51] A. W. Hull. **Structure of graphite.** *Physical Review*, 10:661–696, 1917.

[52] J. Huscher and D. Smith. ***The Unpaid Health Bill - How coal power plants make us sick.*** Health and Environment Alliance (HEAL), 2003.

[53] T. Hussain, B. Pathak, M. Ramzan, T. A. Maark and R. Ahuja. **Calcium doped graphane as a hydrogen storage material.** *Applied Physics Letters*, 100(18):183902, 2012.

[54] T. Hussain, A. De Sarkar and R. Ahuja. **Strain induced lithium functionalized graphane as a high capacity hydrogen storage material.** *Applied Physics Letters*, 101(10):103907, 2012.

[55] Y. Idemoto, J. W. jr. Ricardson, N. Koura, S. Kohara and C.-K. Loong. **Crystal structure of $(Li_xK_{1-x})_2CO_3$ $(x = 0, 0.43, 0.5, 0.62, 1)$ by neutron powder diffraction analysis.** *Journal of Physics and Chemistry of Solids*, 59:365–376, 1998.

[56] Hydrogen Co-Ordination Group IEA. **Hydrogen Production and Storage**, 2006.

[57] R. E. Gerald II, C. S. Johnson, J. W. Rathke, R. J. Klingler, G. Sandi and L. G. Scanlon. **^{7}Li NMR study of intercalated lithium in curved carbon lattices.** *Journal of Power Sources*, 89(2):237 – 243, 2000.

[58] D. Klemm, B. Heublein, H.-P. Fink and A. Bohn. **Cellulose: Fascinating Biopolymer and Sustainable Raw Material.** *Angewandte Chemie International Edition*, 44(22):3358–3393, 2005.

[59] G. J. Kubas, R. R. Ryan, B. I. Swanson, P. J. Vergamini and H. J. Wasserman. **Characterization of the first examples of isolable molecular hydrogen complexes, $M(CO)_3(PR_3)_2(H_2)$ (M = molybdenum or tungsten; R = Cy or isopropyl). Evidence for a side-on bonded dihydrogen ligand.** *Journal of the American Chemical Society*, 106(2):451–452, 1984.

[60] Y. Kubozono, Y. Takabayashi, T. Kambe, S. Fujiki, S. Kashino and S. Emura. **Structure and physical properties of Na_4C_{60} under ambient and high pres-sures.** *Phys. Rev. B*, 63:045418, Jan 2001.

[61] A. Kumar, A. L. M. Reddy, A. Mukherjee, M. Dubey, X. Zhan, N. Singh, L. Ci, W. E. Billups, J. Nagurny, G. Mital and P. M. Ajayan. **Direct Synthesis of Lithium-Intercalated Graphene for Electrochemical Energy Storage Application.** *ACS Nano*, 5(6):4345–4349, 2011.

[62] H. Kuzmany, M. Matus, B. Burger and J. Winter. **Raman Scattering in C_{60} fullerenes and fullerides.** *Advanced Materials*, 6(10):731–745, 1994.

[63] H. Lee, J. Ihm, M. L. Cohen and S. G. Louie. **Calcium-Decorated Graphene-Based Nanostructures for Hydrogen Storage.** *Nano Letters*, 10(3):793–798, 2010.

[64] S. Li, H. Zhao and P. Jena. **Ti-doped nano-porous graphene: A material for hydrogen storage and sensor.** *Frontiers of Physics*, 6(2):204–208, 2011.

[65] D. R. Lide, editor. *CRC Handbook of Chemistry and Physics.*

[66] Y. Lin, F. Ding and B. I. Yakobson. **Hydrogen storage by spillover on graphene as a phase nucleation process.** *Phys. Rev. B*, 78:041402, Jul 2008.

[67] W.-R- Liu, M.-H. Yang, H.-C. Wu, S. M. Chiao and N.-L. Wu. **Enhanced Cycle Life of Si Anode for Li-Ion Batteries by Using Modified Elastomeric Binder.** *Electrochemical and Solid-State Letters*, 8(2):A100–A103, 2005.

[68] Y. Liu, L. Ren, Y. He and H.-P. Cheng. **Titanium-decorated graphene for high-capacity hydrogen storage studied by density functional simulations.** *Journal of Physics: Condensed Matter*, 22(44):445301, 2010.

[69] Y. Liu, Z. Lockman, A. Aziz and J. MacManus-Driscoll. **Size dependent ferromagnetism in cerium oxide (CeO_2) nanostructures independent of oxygen vacancies.** *Journal of Physics: Condensed Matter*, 20(16):165201, 2008.

[70] R. C. Lochan and M. Head-Gordon. **Computational studies of molecular hydrogen binding affinities: The role of dispersion forces, electrostatics, and orbital interactions.** *Physical Chemistry Chemical Physics*, 8(12):1357–1370, 2006.

[71] R. O. Loutfy and S. Katagiri. **Fullerene Materials for Lithium-ion Battery Applications.** In Eiji Osawa, editor, *Perspectives of Fullerene Nanotechnology*, pages 357–367. Springer Netherlands, 2002.

[72] J. Lu, K. P. Loh, H. Huang, W. Chen and A. T. S. Wee. **Plasmon dispersion on epitaxial graphene studied using high-resolution electron energyloss spectroscopy.** *Phys. Rev. B*, 80:113410, Sep 2009.

[73] A. E. Lutz, R. S. Larson and J. O. Keller. **Thermodynamic comparison of fuel cells to the Carnot cycle.** *International Journal of Hydrogen Energy*, 27(10):1103 – 1111, 2002.

[74] G. MacKerron. **Nuclear costs: Why do they keep rising?** *Energy Policy*, 20(7):641 – 652, 1992. The first 50 years of nuclear power: legacy and lessons - Part 1.

[75] N. Mahmood, C. Zhang, H. Yin and Y. Hou. **Graphene-based nanocomposites for energy storage and conversion in lithium batteries, supercapacitors and fuel cells.** *J. Mater. Chem. A*, 2:15–32, 2014.

[76] S. L. Mair. **The electron distribution of the hydroxide ion in lithium hydroxide.** *Acta Crystallographica A*, 34:542–547, 1978.

[77] J. P. Marco-Lozar, M. Kunowsky, J. D. Carruthers and A. Linares-Solano. **Gas storage scale-up at room temperature on high density carbon materials.** *Carbon*, 76(0):123 – 132, 2014.

[78] B. V. Mathiesen, H. Lund and K. Karlsson. **100% Renewable energy systems, climate mitigation and economic growth.** *Applied Energy*, 88(2):488 – 501, 2011.

[79] Ph. Mauron, A. Remhof, A. Bliersbach, A. Borgschulte, A. Züttel, D. Sheptyakov, M. Gaboardi, M. Choucair, D. Pontiroli, M. Aramini, A. Gorreri and M. Riccò. **Reversible hydrogen absorption in sodium intercalated fullerenes.** *International Journal of Hydrogen Energy*, 37(19):14307–14314, 2012.

[80] Ph. Mauron, M. Gaboardi, A. Remhof, A. Bliersbach, D. Sheptyakov, M. Aramini, G. Vlahopoulou, F. Giglio, D. Pontiroli, M. Riccò, and A. Züttel. **Hydrogen sorption in $Li_{12}C_{60}$.** *The Journal of Physical Chemistry C*, 117(44):22598–22602, 2013.

[81] M. Mazzani. ***Muons and Hydrogen in Graphene.*** PhD thesis, Universita' Degli Studi Di Parma, 2011.

[82] McPhy. **Solid hydrogen storage with magnesium hydride systems.** McPhy company website.

[83] J. C. Meyer, A. K. Geim, M. I. Katsnelson, K. S. Novoselov, T. J. Booth and S. Roth. **The structure of suspended graphene sheets.** *Nature*, 446(7131):60–63, March 2007.

[84] M. R. Nadler and C. P. Kempter. **Lithium.** *Analytical Chemistry*, 31:2109–2109, 1959.

[85] S. Nagakura. **Study of metallic carbides by electron diffraction Part II. Crystal structure analysis of nickel carbide.** *Journal of the Physical Society of Japan*, 13:1005–1014, 1958.

[86] L. Néel. *Ann. Geophys.*, 5:99, 1949.

[87] United States Department of Energy. **2014 Annual Progress Report.** Annual progress report, 2014.

[88] United States Department of Energy Hydrogen Analysis Resource Center. **Lower and Higher Heating Values of Hydrogen and Fuels.** Comparison chart on governmental website, 2008.

[89] L. A. Openov and A. I. Podlivaev. **Thermal desorption of hydrogen from graphane.** *Technical Physics Letters*, 36(1):31–33, 2010.

[90] S. Pacala and R. Socolow. **Stabilization Wedges: Solving the Climate Problem for the Next 50 Years with Current Technologies.** *Science*, 305(5686):968–972, 2004.

[91] V. B. Parambhath, R. Nagar, K. Sethupathi and S. Ramaprabhu. **Investigation of Spillover Mechanism in Palladium Decorated Hydrogen Exfoliated Functionalized Graphene.** *The Journal of Physical Chemistry C*, 115(31):15679–15685, 2011.

[92] A. Peigney, Ch. Laurent, E. Flahaut, R. R. Bacsa and A. Rousset. **Specific surface area of carbon nanotubes and bundles of carbon nanotubes.** *Carbon*, 39(4):507 – 514, 2001.

[93] R. Prins. **Hydrogen Spillover. Facts and Fiction.** *Chemical Reviews*, 112(5):2714–2738, 2012.

[94] G. M. Psofogiannakis and G. E. Froudakis. **DFT Study of Hydrogen Storage by Spillover on Graphite with Oxygen Surface Groups.** *Journal of the American Chemical Society*, 131(42):15133–15135, 2009.

[95] D. Quintavalle, F. Borondics, G. Klupp, A. Baserga, F. Simon, A. Janossy, K. Kamaras and S. Pekker. **Structure and properties of the stable two-dimensional conducting polymer Mg_5C_{60}.** *Phys. Rev. B*, 77:155431, 2008.

[96] A. Rathna and J. Chandrasekhar. **Theoretical study of hydrogenated buckminsterfullerene derivatives with benzenoid rings, $C_{60}H_{6-n}(n = 1\text{–}8)$.** *Chemical Physics Letters*, 206(1-4):217–224, 1993.

[97] M. Riccò, D. Pontiroli, M. Mazzani, M. Choucair, J. A. Stride and O. V. Yazyev. **Muons Probe Strong Hydrogen Interactions with Defective Graphene.** *Nano Letters*, 11(11):4919–4922, 2011.

[98] M. J. Rosseinsky, D. W. Murphy, R. M. Fleming, R. Tycko, A. P. Ramirez, G. Dabbagh and S. E. Barrett. **Structural and electronic properties of sodium-intercalated C_{60}.** *Nature*, 356(6368):416–418, 1992.

[99] G. Sandi, R. E. Gerald, C. S. Johnson, R. J. Klingler and J. W. Rathke. **Molecular orbital and Li-7 NMR investigation of the influence of curved lattices in lithium intercalated carbon anodes.** *Journal of New Materials for Electrochemical Systems*, 3(1):13–19, January 2000.

[100] A. G. E. Schenck. ***Muon Spin Rotation Spectroscopy Principles and Applications in Solid State Physics.*** CRC Press, 1985.

[101] B. Schmitz, U. Müller, N. Trukhan, M. Schubert, G. Ferey, and M. Hirscher. **Heat of adsorption for hydrogen in microporous high-surface-area materials.** *ChemPhysChem*, 9(15):2181–2184, 2008.

[102] B. J. Schultz, R. V. Dennis, J. P. Aldinger, C. Jaye, X. Wang, D. A. Fischer, A. N. Cartwright and S. Banerjee. **X-ray absorption spectroscopy studies of electronic structure recovery and nitrogen local structure upon thermal reduction of graphene oxide in an ammonia environment.** *RSC Adv.*, 4:634–644, 2014.

[103] D. V. Schur, B. P. Tarasov, Y. M. Shul'ga, S. Y. Zaginaichenko, Z. A. Matysina and A. P. Pomytkin. **Hydrogen in fullerites.** *Carbon*, 41(7):1331 – 1342, 2003.

[104] D. V. Schura, S. Yu. Zaginaichenkoa, A. F. Savenkoa, V. A. Bogolepova, N. S. Anikinaa, A. D. Zolotarenkoa, Z. A. Matysinab, T. N. Vezirogluc and N. E. Skryabinad. **Experimental evaluation of total hydrogen capacity for fullerite C_{60}.** *International Journal of Hydrogen Energy*, 36:1143–1151, 2011.

[105] M. S. Seehra and A. S. Pavlovic. **X-Ray diffraction, thermal expansion, electrical conductivity, and optical microscopy studies of coal-based graphites.** *Carbon*, 31(4):557 – 564, 1993.

[106] T. Seto, H. Akinaga, F. Takano, K. Koga, T. Orii and M. Hirasawa. **Magnetic Properties of Monodispersed Ni/NiO Core-Shell Nanoparticles.** *The Journal of Physical Chemistry B*, 109(28):13403–13405, 2005.

[107] W. H. Shin, S. H. Yang, W. A. Goddard and J. K. Kang. **Ni-dispersed fullerenes: Hydrogen storage and desorption properties.** *Applied Physics Letters*, 88(5), 2006.

[108] R. Shipra, N. Kumar and A. Sundaresan. **Surface ferromagnetism and superconducting properties of nanocrystalline niobium nitride.** *Materials Chemistry and Physics*, 139(2 – 3):500 – 505, 2013.

[109] C. Shull, E. Wollan, G. Morton and W. Davidson. **Neutron Diffraction Studies of NaH and NaD.** *Phys. Rev.*, 73:842–847, Apr 1948.

[110] V. A. Somenkov, V. P. Glazkov, S. Sh. Shil'shtein, V. P. Zhukov, V. N. Bezmel'nitsyn and A. I. Kurbakov. **Neutron diffraction study of the structure of deuterated and fluorinated fullerene C_{60}.** *Metal Science and Heat Treatment*, 42(8):319–325, 2000.

[111] Magna Steyr. **Storage of Compressed Hydrogen.** Company website.

[112] E. C. Stoner and E. P. Wohlfarth. **A Mechanism of Magnetic Hysteresis in Heterogeneous Alloys.** *Philosophical Transactions of the Royal Society of London. Series A, Mathematical and Physical Sciences*, 240(826):599–642, 1948.

[113] Q. Sun, P. Jena, Q. Wang and M. Marquez. **First-Principles Study of Hydrogen Storage on $Li_{12}C_{60}$.** *Journal of the American Chemical Society*, 128(30):9741–9745, 2006.

[114] A. Sundaresan, R. Bhargavi, N. Rangarajan, U. Siddesh and C. N. R. Rao. **Ferromagnetism as a universal feature of nanoparticles of the otherwise nonmagnetic oxides.** *Phys. Rev. B*, 74:161306, Oct 2006.

[115] H. E. Swanson and E. Tatge. **Standard x-ray diffraction powder patterns.** *National Bureau of Standards (U.S.)*, (1):1–95, 1953.

[116] A. V. Talyzin, Y. O. Tsybin, J. M. Purcell, T. M. Schaub, Y. M. Shulga, D. Noreus, T. Sato, A. Dzwilewski, B. Sundqvist and A. G. Marshall. **Reaction of Hydrogen Gas with C_{60} at Elevated Pressure and Temperature: Hydrogenation and Cage Fragmentation.** *The Journal of Physical Chemistry A*, 110(27):8528–8534, 2006.

[117] A. V. Talyzin, Y. M. Shulga and A. Jacob. **Comparative study of hydrofullerides $C_{60}H_x$ synthesized by direct and catalytic hydrogenation.** *Applied Physics A*, 78(7):1005–1010, 2004.

[118] A. V. Talyzin, B. Sundqvist, Y. M. Shulga, A. A. Peera, P. Imus and W. E. Billups. **Gentle fragmentation of C_{60} by strong hydrogenation: a route to synthesizing new materials.** *Chemical Physics Letters*, 400(1â€"3):112 – 116, 2004.

[119] B. P. Tarasov, Y. M. Shul'ga, V. N. Fokin, V. N. Vasilets, S. N. Yu., D. V. Schur and V. A. Yartys. **Deuterofullerene $C_{60}D_{24}$ studied by XRD, IR and XPS.** *Journal of Alloys and Compounds*, 314(1–2):296 – 300, 2001.

[120] S. Tedds, A. Walton, D. P. Broom and D. Book. **Characterisation of porous hydrogen storage materials: carbons, zeolites, MOFs and PIMs.** *Faraday Discuss.*, 151:75–94, 2011.

[121] J. A. Teprovich, M. S. Wellons, R. Lascola, S.-J. Hwang, P. A. Ward, R. N. Compton and R. Zidan. **Synthesis and Characterization of a Lithium-Doped Fullerane (Li_x-C_{60}-H_y) for Reversible Hydrogen Storage.** *Nano Letters*, 12(2):582–589, 2012.

[122] J. A. Teprovich, D. A. Knight, M. S. Wellons and R. Zidan. **Catalytic effect of fullerene and formation of nanocomposites with complex hydrides: $NaAlH_4$ and $LiAlH_4$.** *Journal of Alloys and Compounds*, 509, Supplement 2(0):S562 – S566, 2011.

[123] Toyota. Toyota Ushers in the Future with Launch of Mirai Fuel Cell Sedan, 2014.

[124] Y. J. Uemura. **Probing spin glasses with zero-field muSR.** *Hyperfine Interactions*, 8(4-6):739–748, 1981.

[125] N. A. Usov and J. M. Barandiaran. **Magnetic nanoparticles with combined anisotropy.** *Journal of Applied Physics*, 112(5), 2012.

[126] C. G. Van de Walle. ***Protons and muons in materials science.***, Volume 3. WILEY-VCH Verlag GmbH, 1997.

[127] M. W. Verbrugge and B. J. Koch. **Electrochemical Analysis of Lithiated Graphite Anodes.** *Journal of The Electrochemical Society*, 150(3):A374–A384, 2003.

[128] T. Wagberg, P. Stenmark and B. Sundqvist. **Structural aspects of two-dimensional polymers: Li_4C_{60}, Na_4C_{60} and tetragonal C_{60}. Raman spectroscopy and X-ray diffraction.** *Journal of Physics and Chemistry of Solids*, 65:317 – 320, 2004.

[129] J. Walton, P. Wincott, N. Fairley and A. Carrick. **Peak Fitting with CasaXPS.**

[130] C. Wang, A. J. Appleby and F. E. Little. **Irreversible capacities of graphite anode for lithium-ion batteries.** *Journal of Electroanalytical Chemistry*, 519(1–2):9 – 17, 2002.

[131] L.-S. Wang, J. Conceicao, C. Jin, and R. E. Smalley. **Threshold photodetachment of cold C_{60}.** *Chemical Physics Letters*, 182(1):5 – 11, 1991.

[132] H. J. Williams and R. M. Bozorth. **Magnetic Anisotropy of Nickel at 20° K.** *Phys. Rev.*, 56:837–837, Oct 1939.

[133] D. Wilson. **Power-to-Gas: Utility Scale Energy Storage.** U.S. Department of Energy Publications, May 2012.

[134] R. Wüstenhagen and M. Bilharz. **Green energy market development in Germany: effective public policy and emerging customer demand.** *Energy Policy*, 34(13):1681 – 1696, 2006.

[135] D. Yang, A. Velamakanni, G. Bozoklu, S. Park, M. Stoller, R. D. Piner, S. Stankovich, I. Jung, D. A. Field, C. A. Ventrice and R. S. Ruoff. **Chemical analysis of graphene oxide films after heat and chemical treatments by X-ray photoelectron and Micro-Raman spectroscopy.** *Carbon*, 47(1):145 – 152, 2009.

[136] Z. Yang, Y. Xia and R. Mokaya. **Enhanced Hydrogen Storage Capacity of High Surface Area Zeolite-like Carbon Materials.** *Journal of the American Chemical Society*, 129(6):1673–1679, 2007.

[137] R. Yazami. ***Materials for Lithium-Ion Batteries.*** Kluwer Academic Publishers, 1999.

[138] T. Yildirim, J. Iniguez and S. Ciraci. **Molecular and dissociative adsorption of multiple hydrogen molecules on transition metal decorated C_{60}.** *Phys. Rev. B*, 72:153403, Oct 2005.

[139] T. Yildirim, O. Zhou, J. E. Fischer, N. Bykovetz, R. A. Strongin, M. A. Cichy, A. B. Smith III, C. L. Lin and R. Jelinek. **Intercalation of sodium heteroclusters into the C_{60} lattice.** *Nature*, 360(6404):568–571, 1992.

[140] M. Yoon, S. Yang, C. Hicke, E. Wang, D. Geohegan and Z. Zhang. **Calcium as the Superior Coating Metal in Functionalization of Carbon Fullerenes for High-Capacity Hydrogen Storage.** *Phys. Rev. Lett.*, 100:206806, May 2008.

[141] M. Yoon, S. Yang, E. Wang and Z. Zhang. **Charged Fullerenes as High-Capacity Hydrogen Storage Media.** *Nano Letters*, 7(9):2578–2583, 2007.

[142] A. V. Zabula, A. S. Filatov, S. N. Spisak, A. Yu. Rogachev and M. A. Petrukhina. **A Main Group Metal Sandwich: Five Lithium Cations Jammed Between Two Corannulene Tetraanion Decks.** *Science*, 333(6045):1008–1011, 2011.

[143] W.-J. Zhang. **A review of the electrochemical performance of alloy anodes for lithium-ion batteries.** *Journal of Power Sources*, 196(1):13 – 24, 2011.

[144] M. Zhou, Y. Lu, C. Zhang and Y. P. Feng. **Strain effects on hydrogen storage capability of metal-decorated graphene: A first-principles study.** *Applied Physics Letters*, 97(10):103109, 2010.

[145] E. Zintl and A. Harder. **Über Alkalihydride.** *Zeitschrift für Physikalische Chemie, Abteilung B: Chemie der Elementarprozesse, Aufbau der Materie*, (14):p265–p284, 1931.

[146] E. Zintl and A. Harder. **Gitterdimensionen des Lithiumhydrids LiH und Lithiumdeuterids LiD.** *Zeitschrift für Physikalische Chemie, Abteilung B: Chemie der Elementarprozesse, Aufbau der Materie*, (28):p478–p480, 1935.

[147] E. Zintl, A. Harder and B. Dauth. **Gitterstruktur der Oxide, Sulfide, Selenide und Telluride des Lithiums, Natriums und Kaliums.** *Zeitschrift fuer Elektrochemie*, 40:588–593, 1934.

[148] G. Zollo and F. Gala. **Atomistic Modeling of Gas Adsorption in Nanocarbons.** *Journal of Nanomaterials*, page 32, 2012.

[149] A. Züttel, P. Sudan, Ph. Mauron, T. Kiyobayashi, Ch. Emmenegger and L. Schlapbach. **Hydrogen storage in carbon nanostructures.** *International Journal of Hydrogen Energy*, 27(2):203 – 212, 2002.

Acknowledgments

The past three years have been an exciting and intense journey. I was fortunate in meeting and learning from a great variety of completely different people, sharing my enthusiasm for science and research while often approaching questions entirely different.

I owe a great debt of gratitude to my supervisor Karl-Heinz Ernst for giving me the chance of continuing my research in his group. I appreciate the opportunity to wrestle with the old low temperature STM and while countless hours have been spend repairing and evaluating I have learned a great deal more about complex ultra high vacuum systems and STM's.

Thanks go to Andreas Züttel in whose laboratory I was able to conduct large parts of my experiments on promising hydrogen storage materials and their characterization. I thank him for all the international conferences I was able to visit and the doors he opened.

I am indebted to Arndt Remhof for many things; for his teaching and the countless discussions dissecting my arguments, for his guidance around large scale facilities for "Röntgens" and neutrons, for the time well spend together in Switzerland, Greece and Germany and foremost for the friendship shared.

The doctorate committee members Karl-Heinz Ernst, Peter Hamm, Jürg Osterwalder and Anthony Linden are thanked for their challenging questions, support and kind compliments during and after the defense, as well as Arndt Remhof and Torben Jensen for their reports on the thesis manuscript.

The presented work would not have been possible without the work and dedication of my collaborators, in particular Mattia Gaboardi, Philippe Mauron, Giovanni Bertoni and Mauro Riccó. Thank you for the fruitful discussions and every coffee and beer we shared on the way.

I thank Manfred Parschau for sharing his supreme technical knowledge of the inner workings of STM's. Thanks and gratitude go to Andreas Borgschulte, Jörg Patscheider, Hans-Josef Hug and Miguel Marioni for all the help in discussing and analyzing results, challenging me to a deeper understanding of the techniques used and their genuine interest in my research.

I am very grateful to my students, my fellow PhD's and Post-Docs for good times during scientific discussions, coffee breaks, After-Works, conferences, symposia and generally for joining me on this journey; my thanks in random order to Jan Prinz, Alexander Bonk, Elsa Callini, Nicholas Stadie, Johannes Seibel, Meike Schlupp, Giulio Parcianello, Quirin Stöckl, Chrysanthi Karageorgaki, Johannes Schwenk, Annika Maier, Moritz Wehrle, Renaud Delmelle, Jeffrey Gehrig, Mathis Trant, Maria Fischer, Michal Gorbar, Xue Zhao, Alexandra Rieger, Marcos Penedo-Garcia, Anais Mairena, Jingyi Li, Gitika Srivastava, Liying Ma, Cedric Hugelshofer, Urs Frischknecht, Julio Martinez Garcia, Marcus Pohl and many more along the way.

Thanks to my fellow members of the PhD-Symposium organization committee of 2012 and Anne Satir for the enjoyable experience of seeing an event like that grow into a fully fledged scientific symposium.

All members of the Hydrogen and Energy and the Nanoscale Materials Science departments at Empa are thanked for their camaraderie and great spirits. It was good to be one of you!

I would like to thank the University of Zurich Graduate School of Chemical and Molecular Sciences Zurich (CMSZH) for the great winter retreat in Randa and their financial support.

Financial support by the Swiss National Science Foundation (SNSF) for the projects that I was involved in is gratefully acknowledged; *Smart carbon-based materials for hydrogen storage* and *Single molecule surface dynamics induced by inelastic electron tunneling*.

To my friends at home and far and wide, before I forget to name any of you I write this to you all. Thank you, you are the best and now that this feat is done I promise to shed the silence I have wrapped around myself during the last six month of thesis writing and defense preparations to join you again.

An meine großartige Familie in Deutschland und Schweden, vielen Dank für eure Unterstützung, Liebe und die Gewissheit, dass es für mich immer einen Rückzugsort gibt. Till min fantastiska familj i Tyskland och i Sverige; tack så jättemycket för allt ert stöd! Vetskapen att ni alltid finns där är guld värd och jag uppskattar allt ni gjort och gör för mig.

To the loving and supportive Matilda Ekholm, thank you for giving me the time and space to pursue my passion, for moving to this strange but beautiful country with me, for the love shared and being cute as a button and for reminding me that, while tired from work, leaving the house every once in a while is a good thing!

Zurich, January 28, 2015
Andreas Bliersbach

Andreas Bliersbach

Address: Luchswiesenstrasse 170, CH-8051 Zurich
e-mail: andreas.bliersbach@gmail.com
Date of birth: 19 May 1986
Nationality: German

Education

12/2011 – 02/2012 **Doctoral Studies (Dr. sc. nat.) - University of Zurich, Switzerland**
Thesis Title: *"New Carbon-Based Materials for Energy Storage"*
Supervisor: Prof. Dr. K-H. Ernst (University of Zurich)
Examiners: Prof. Dr. P. Hamm (University of Zurich)
Prof. Dr. J. Osterwalder (University of Zurich)
Prof. Dr. A. Linden (University of Zurich)
Reviewer: Dr. A. Remhof (Empa)
Prof. Dr. T.R. Jensen (Aarhus University)

08/2008 – 06/2009 **Academic Studies (M. Sc.) - Uppsala University, Sweden**
07/2010 – 06/2011 Supervisor: Prof. Dr. B. Hjörvarsson (Uppsala University)
Examiners: Prof. Dr. B. Lindgren (Uppsala University)
Prof. Dr. M. Fiebig (University of Bonn)
Grade: 5/5, *Pass with distinction* (ECTS: *Excellent*/A)

10/2005 – 07/2008 **Academic Studies (Dipl.-Phys.) - University of Bonn, Germany**
07/2009 – 07/2011 Thesis Titel: "*Hydrogen diffusion in nano-sized materials investigated by direct imaging*".
Supervisors: Prof. Dr. B. Hjörvarsson (Uppsala University)
Prof. Dr. M. Fiebig (University of Bonn)
Examiner: Priv.-Doz. Dr. E. Soergel (University of Bonn)
Grade: "Sehr Gut" (ECTS: *Excellent*/A)

09/1996 – 06/2005 **Gymnasium - Kaiserin-Theophanu-Schule Cologne, Germany**
Abitur, June 2005

Publications

- **Decoration of graphene with nickel nanoparticles: study of the interaction with hydrogen.**
  M. Gaboardi, A. Bliersbach, G. Bertoni, M. Aramini, G. Vlahopoulou,
  D. Pontiroli, Ph. Mauron, G. Magnani, G. Salviati, A. Züttel and M. Riccò.
  Journal of Materials Chemistry A, 2:1039–1046, 2014.

- **Hydrogen sorption in $Li_{12}C_{60}$.**
  Ph. Mauron, M. Gaboardi, A. Remhof, A. Bliersbach,
  D. Sheptyakov, M. Aramini, G. Vlahopoulou, F. Giglio, D. Pontiroli, M. Riccò and A. Züttel.
  The Journal of Physical Chemistry C, 117(44):22598–22602 , 2013.

- **Reversible hydrogen absorption in sodium intercalated fullerenes.**
  Ph. Mauron, A. Remhof, A. Bliersbach, A. Borgschulte, A. Züttel, D. Sheptyakov,
  M. Gaboardi, M. Choucair, D. Pontiroli, M. Aramini, A. Gorreri and M. Riccò.
  International Journal of Hydrogen Energy, 37(19):14307–14314, 2012.

- **Using light transmission to watch hydrogen diffuse.**
  G. K. Pálsson, A. Bliersbach, M. Wolff, A. Zamani and B. Hjörvarsson.
  Nature Communications, 3, 2012.

About the author

Andreas Bliersbach from Cologne, Germany, was born in 1986. He started studying physics at the University of Bonn, Germany, in 2005 where he received his Dipl. Phys. degree in 2011. During his studies he went abroad to Uppsala University, Sweden, and later joined the Materials Physics department where he received a M. Sc. with distinction in 2011. At Uppsala University he focused his research on hydrogen diffusion in thin films and developed a novel experimental technique, able to record hydrogen concentration profiles resolved in time and space. From December 2011 until July 2013 he joined the Hydrogen and Energy Department of the Swiss Federal Laboratories for Materials Science and Technology (Empa) where he investigated metal enhanced graphene and fullerene, both carbon-based, nanoscale materials, for the purpose of hydrogen storage. Subsequently he finalized his doctoral studies at the department for Nanoscale Materials Science at Empa. While his research continued to be in the field of energy storage he investigated fullerene-fragments as new anode materials for Lithium-Ion batteries and took first steps into gaining fundamental understanding of the catalytically activated Sabatier reaction of CO_2 and H_2 on a model nickel surface.